Modern glacier and climate fluctuations reflected as geodetic mass balance, calculated using historical and UAV imagery at Fannaråkbreen in Jotunheimen, central southern Norway

UNIVERSITY OF BERGEN

Department of Geography

Master thesis in physical geography

Spring 2024

Lina Kaldhussæter

Abstract

Fannaråkbreen, a mountain glacier in southern Norway, presents immediate responses to climatic fluctuations through its mass balance, making such data important for analysing climate change and glacier state. This study estimates the geodetic mass balance of Fannaråkbreen over various periods since 1966 by subtracting surfaces modelled with conventional and Structure-from-Motion photogrammetry from historical aerial and UAV imagery. Uncertainty was addressed using geostatistics. Results indicate an accelerating mass loss, with the annual mass balance from 1966 to 2023 at -0.37 ± 0.02 m w. e., and a 36.6% total area reduction since 1955. Comparisons with Storbreen's glaciological mass balance reveal similar patterns, with discrepancies linked to differences in glacier size, local climates and measurement techniques. Additionally, the results illustrate that Fannaråkbreen exhibits mass loss patterns and rates consistent with other continental glaciers in the region. The study also quantifies winter and summer balances at 1.10 ± 0.05 and -1.71 ± 0.09 m w. e. respectively, based on high-resolution UAV data from 2022 and 2023. These findings underscore how remotely sensed data, combined with precise co-registration methods, can assess and reconstruct glacier changes in detail remotely, offering a method to supplement global mass balance records.

Acknowledgements

The completion of this thesis would not have been possible without the help of knowledgeable people. Therefore, first and foremost, I would like to thank my supervisors Benjamin Aubrey Robson and Svein Olaf Dahl, and acknowledge the ideas and experiences they shared, for joining me during fieldwork and overall being invaluable for the implementation of this project. Another thank you goes to my field assistants who helped me with practicalities and data acquisition – Isaac Dawson, Daniel Jack Thomas, Melanie Stammler and my life partner Joakim Kaldhussæter.

Next, I would like to thank the Meltzer fund and GeoForum Hordaland for scholarships that supported the purchase of images from Kartverket, accommodation, transport for fieldwork, and data storage devices. The contributions of several other individuals are also deeply appreciated: Hardy Buller (Kartverket) who helped obtaining the earliest photographs from 1955, Christian Lussana and Line Båserud who navigated me to the climate data, Liss Marie Andreassen who shared her work data from Storbreen, Mathias Holtedahl Thorp who shared his experiences from his master project and my colleagues from Field Geospatial for helping me with alignment of the 1955 images.

Remarks for the reader

Each figure in this thesis is created by the author unless stated otherwise. All maps provided are referenced to the ETRS 1989 UTM Zone 32N coordinate system, with easting and northing measured in meters. In this thesis, artificial intelligence (OpenAi) was not used for writing text. However, it was employed to customise Python tools provided by the xDEM library and to generate scripts for plotting data.

Table of Contents

List of figures

1. Introduction

1.1 Glaciers in changing climate

Mean global air temperatures have increased by 1.1°C during the last century and this has had a detrimental effect on all ecosystems on Earth (IPCC, 2023, p. 346). Besides implications such as increasing frequency of extreme weather events and loss of biodiversity, increasing warming rates also continue to affect the cryosphere (WMO, 2023). With glaciers playing an important part in geomorphological processes and as terrestrial freshwater reservoirs at a regional level (Vaughan, 2014; Marzeion et al., 2017), they in turn also control seasonal river run-off which is a water source for large populations, increase the risk for geohazards and impact the global mean sea-level (GMSL) (Huss, 2011; Stoffel & Huggel, 2012; Marzeion et al., 2017).

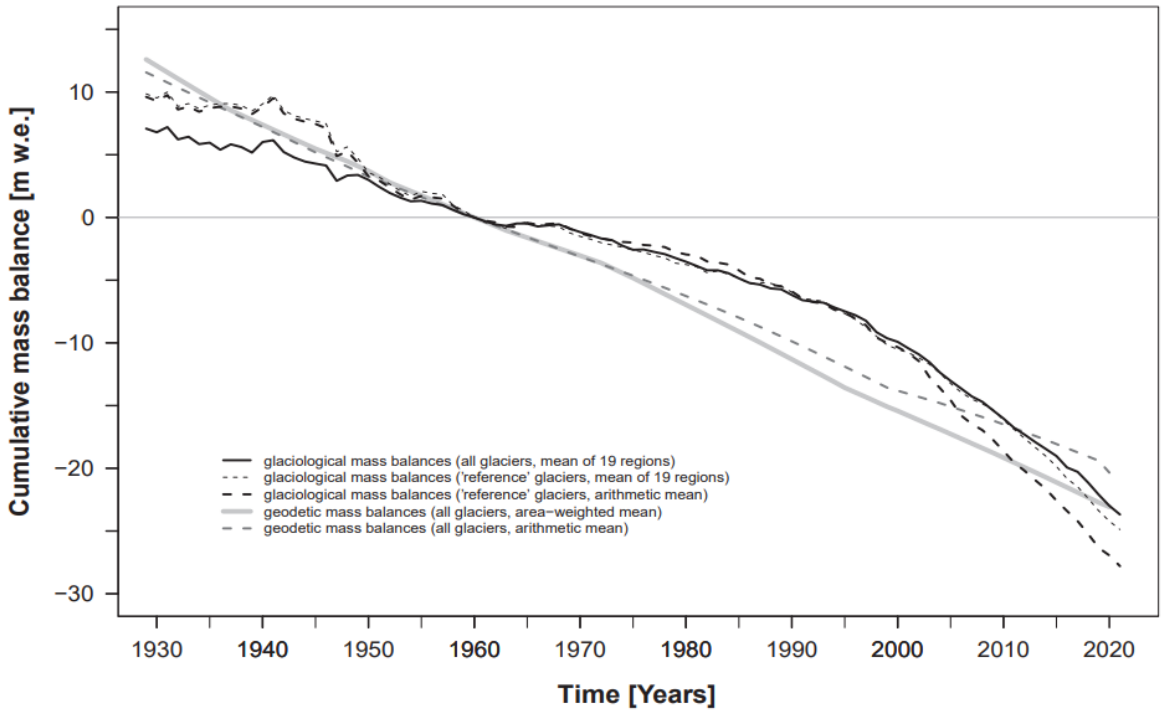

Figure 1.1: Cumulative averaged annual mass balance values form glaciers worldwide measured with two different approaches (1930-2021), compared to the year 1960 (figure from WGMS, 2023).

The adaptability of glacier geometry in response to atmospheric changes makes glaciers well suited for climate research and understanding sea-level variability (Bojinski et al., 2014; Marzeion et al., 2017), with smaller mountain glaciers being especially useful for this due to their exceptional sensitivity to climatic fluctuations (Dyurgerov & Meier, 2000). Therefore, glaciers have been recognized as one of the 55 Essential Climate Variables (ECV) by the

United Nations Framework Convention on Climate Change's (UNFCCC) Global Climate Observing System (GCOS) (Meier, 1984; Zuo & Oerlemans, 1997; Braithwaite & Zhang, 1999; Bojinski et al., 2014; Marzeion et al., 2017). Research has shown that over the last couple of decades, glaciers have been shrinking and losing mass at extraordinary rates, with double the rate compared to the 1990s (Figure 1.1) (Haeberli & Holzhauser, 2003; Zemp et al., 2015; Roe et al., 2017; Hugonnet, McNabb, et al., 2021; Rounce et al., 2023; WGMS, 2023). Globally, there has not been a single year within the last five decades where, on average, glaciers have increased in mass or maintained a positive mass balance (WGMS, 2023). Even if the climate was to stabilize, the retreat would continue due to glaciers being in an extreme disequilibrium with the current climate conditions (Zemp et al., 2015). Such rapid melting is estimated to have contributed to the Global Mean Sea Level (GMSL) changes by 27 ± 22 mm in the period between 1961 and 2016, of which 10 ± 4 mm can be ascribed to the period of 2006-2016 alone (Hugonnet, McNabb, et al., 2021).

A thorough understanding of how glaciers acquire or lose mass with changes in climate can be achieved by frequently (e.g., seasonally) surveying individual glaciers over long periods of time, which according to Dyurgerov and Meier (1999), WMO (2011) and Thibert et al. (2013), should be at least 30 years in order to infer a climatic response. This information, can provide detailed insights on processes involved in glacier mass turnover, what is essential for glacier-climate sensitivity studies in the time of the ongoing climate change, past and future modelling of regional climate, and for inferring glacier health in regions where sampling is scarce (e.g., Haeberli, 2011).

Today there are only 61 "reference" glaciers in the world that have such long mass balance records (WGMS, 2024). Traditionally, long-term glacier mass balance conclusions have been drawn from results obtained using the traditional glaciological method, which involves measurements of surface elevation changes with ablation stakes and snow density measurements of in snow pits (Zemp et al., 2015; Marzeion et al., 2017). Due to the practice being field-based, mass balance records of the reference glaciers are heavily biased towards few regions with accessible glaciers (such as the Alps), resulting in misrepresentation of other, not surveyed regions (Braithwaite, 2009). Small sample sizes also influence the results from the earliest years (WGMS, 2023). However, the more recent geodetic method utilising remote sensing techniques for repeated mapping of glacier surface has been used for surveying glaciers in secluded and isolated regions, as well as to fill temporal and spatial gaps in the glaciological records (e.g., Seehaus et al., 2019; Huber et al., 2020; Hugonnet, McNabb,

et al., 2021; Mukherjee et al., 2023) and to calibrate measurements carried out in a traditional way (e.g., Thibert & Vincent, 2009; Andreassen, Robson, et al., 2023). Thus, this approach is also employed in this study, focusing on how repeated aerial surveys can be used to estimate glacier mass balance.

1.2 Glacier monitoring in the Norwegian context

In Norway, glaciers are not only important as climate proxies but also characterise the landscape and play a significant economic role in tourism and the power industry (Andreassen & Elvehøy, 2021). The hydropower constitutes around 90% of all electricity produced in this country (SSB, 2024) and around 15% of the runoff used for energy generation comes from catchments with glaciers, where meltwater is responsible for high rates of discharge during summer months (Andreassen et al., 2005). The incentive to begin glacier observations stemmed from the demand of improved knowledge about glacier hydrology which would later be utilized for development of hydroelectric power industry (Andreassen, Elvehøy, et al., 2022).

Norwegian glaciers have shrunken substantially since the Little Ice Age (e.g., Winsvold et al., 2014; Leigh et al., 2020; Paul Weber et al., 2020; Carrivick et al., 2022). More recently, according to the inventory of country's glaciers using Sentinel-2 images from 2018 and 2019, a total of 2328 ± 70 km^2 of Norway was glaciated, representing a 15% decrease in glacier-covered area compared to the previous investigation conducted between 1999 and 2006 (Andreassen, Nagy, et al., 2022). In the region of Jotunheimen, the highest glacier retreat rates have been observed in the period between the 1930s and 1965 (Østrem & Haakensen, 1993; Andreassen et al., 2005). For the period of 1965-2003, the glaciated area in the region shrank by 12%, or at a rate of 3,2% per decade measured since the 1930s (Andreassen et al., 2008).

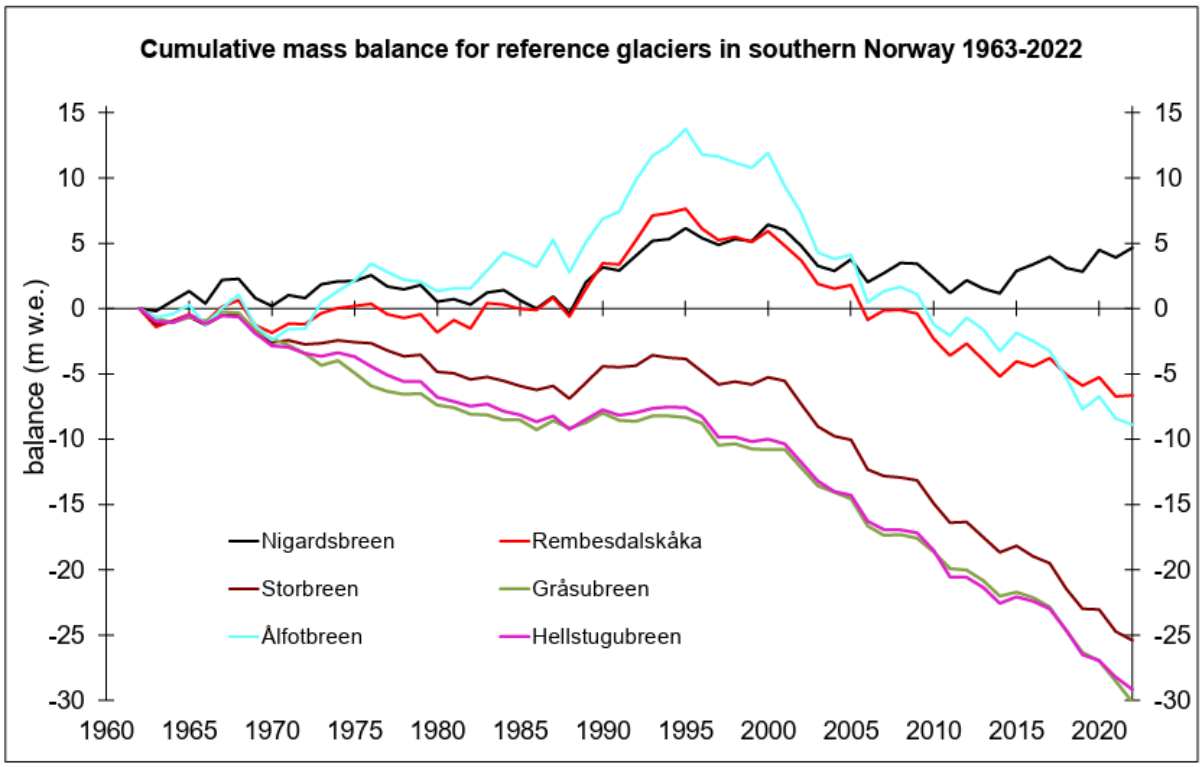

Figure 1.2: Mass balance in meters water equivalent (m w. e.) for the six glaciers in southern Norway with the longest mass-balance series (Ålfotbreen, Nigardsbreen, Rambedalskåka, Storbreen, Hellstugubreen, Gråsubreen - listed based on their location from West to East), measured over the period of 1963-2022 (from Andreassen et al., 2023).

For a long time, the conclusions of long-term glacier mass balance have been drawn from the results based on the traditional glaciological method using ablation stakes for measurements of surface elevation change and snow pits for snow density (Zemp et al., 2015; Marzeion et al., 2017). The total of 43 glaciers are surveyed annually by The Norwegian Water Resources and Energy Directorate (NVE) using the glaciological method, accounting for only 5% of the country's total glacier area (Andreassen et al., 2020; Nesje, 2023; NVE, 2024). However, there are only six glaciers with mass balance records of at least 60 years (Figure 1.2) (Andreassen et al., 2020).

Nonetheless, for at least the last five decades, Norwegian glaciers have been captured in aerial photographs by the NVE (Haug et al., 2009). Today, these images can be photogrammetrically processed to provide detailed information about planimetric and volumetric changes of glaciers (e.g., Andreassen, 1999; Andreassen et al., 2002; Østrem & Haakensen, 1999).

1.3 Glaciological and geodetic mass balances

The glaciological method requires measurements to be carried out being physically on the glacier surface, what can be logistically challenging and require a lot of resources, because

glaciers are innately located in remote areas and often feature steep slopes with large crevasses and sometimes requiring special equipment for access. This often results in sparse measurement networks, as depicted in Figure 1.3, and insufficient amount of samples in avalanche areas, steep slopes or crevasses (e.g., Østrem & Haakensen, 1999; Klug et al., 2018). As a consequence, the method relies on interpolation and extrapolation of data, and fails to capture changes occurring internally and sub-glacially, as stake readings only show the changes of the upper glacier layer (Østrem & Brugman, 1991; Zemp et al., 2015; Marzeion et al., 2017).

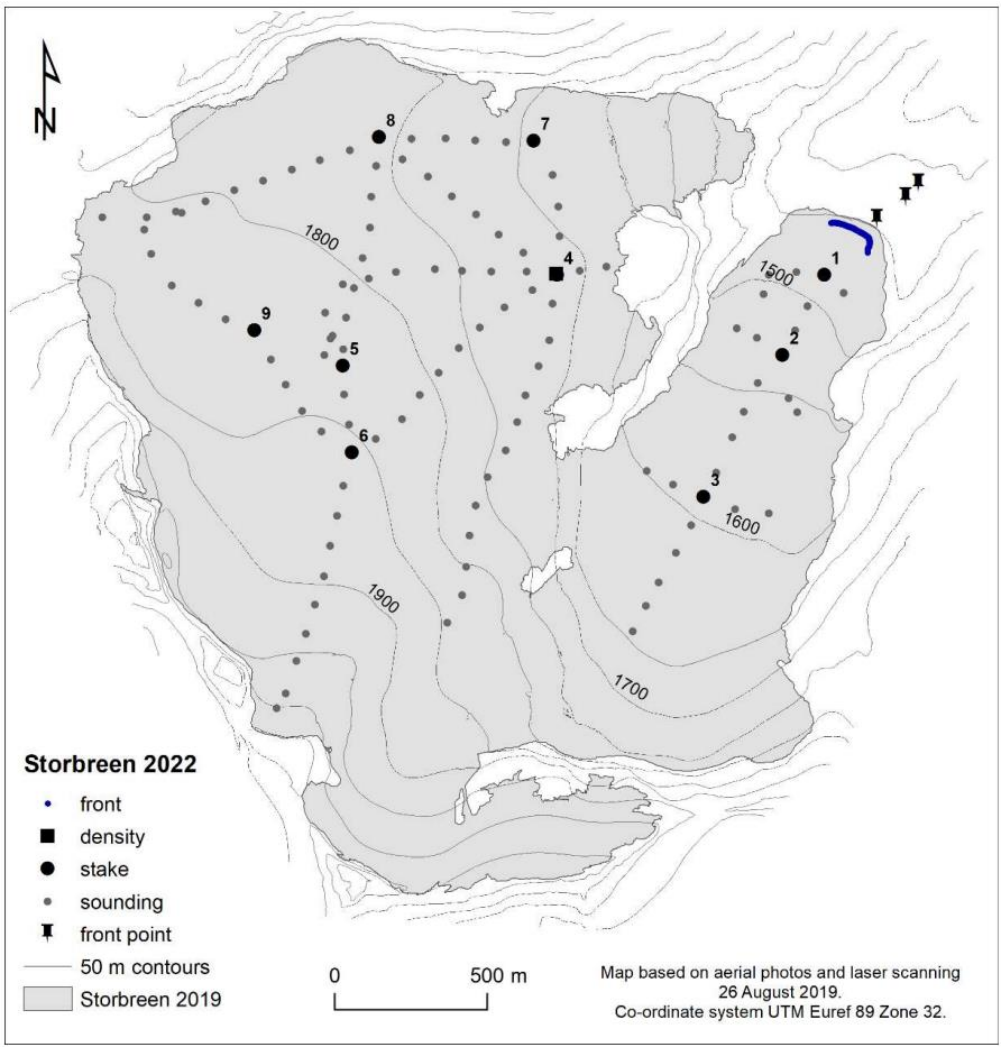

Figure 1.3: A map showing locations of ablation stakes used for glaciological mass balance estimations of Storbreen, Jotunheimen. The figure shows how sparse the measurement network can be, resulting in interpolation of data between the points and extrapolation of data in areas that were not measured (Andreassen, Elvehøy, & Kjøllmoen, 2023).

However, glacier surveying using remote sensing techniques and photogrammetry, which enable the extraction of elevation data from optical images (Fox & Nuttall, 1997), offers significant advantages. It allows for comprehensive measurement of the entire glacier surface

area and can be applied efficiently across large and remote regions using just a few images (e.g., Mertes et al., 2017; Mölg & Bolch, 2017; Robson et al., 2022). Remote sensing has been used in numerous studies for glacier inventories (e.g., Bishop et al., 2004; Raup et al., 2007; Andreassen, Nagy, et al., 2022), velocity estimations (e.g., Krimmel & Meier, 1975; Kääb et al., 2016) and for assessments of geodetic mass balance on different scales, including single glaciers (e.g., Rolstad et al., 2009; Andreassen et al., 2016), larger regions and ice caps (Andreassen, Robson, et al., 2023) as well as globally (Hugonnet, McNabb, et al., 2021). Photogrammetry also allows utilization of archival aerial photographs for reconstruction of past glacier surfaces (Figure 1.4) to learn about decadal trends in glacier response to atmospheric changes. This is especially important for areas that are devoid of observations or have short data records (Mertes et al., 2017). Therefore, geodetic approaches are needed to complement field observations in many mountain regions to assess how glaciers act as freshwater sources, their seasonality and impact on the sea-level (Pelto et al., 2019).

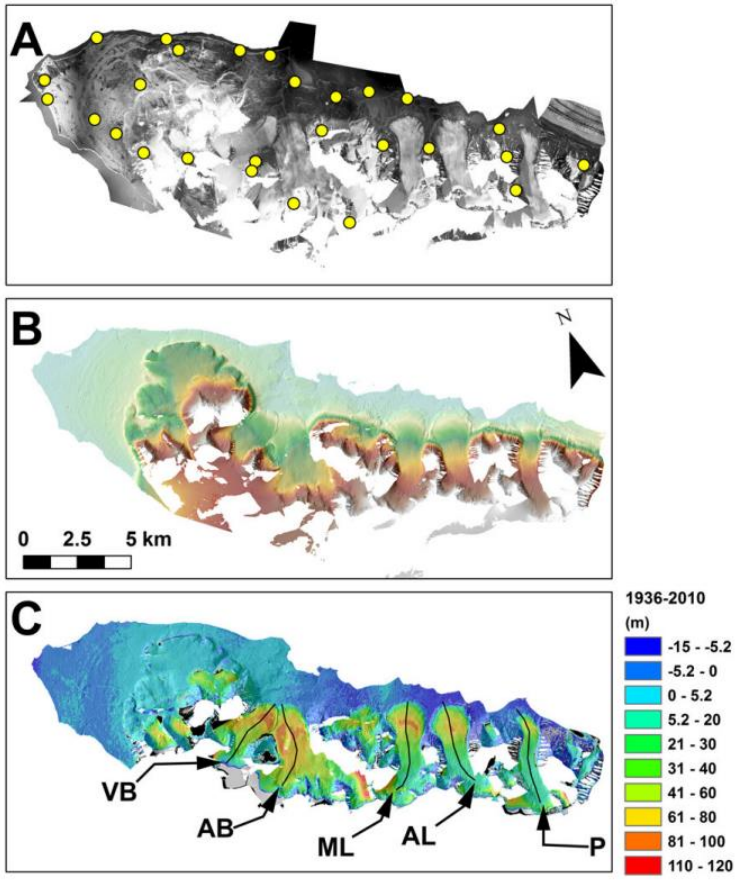

Figure 1.4: A figure showing an example of historical imagery utilization for estimation of glacier surface elevation change. A – Ny Ålesund orthoimage, B – digital elevation model (DEM) from the 1936 image, C – elevation difference between 1936 and 2010. Yellow dots are ground control point (GCP) locations, solid black lines mark elevation profiles that were used in the study. VB - Vestre Brøggerbreen, AB - Austre Brøggerbreen, ML - Midtre Lovénbreen, AL - Austre Lovénbreen and P – Pedersenbreen (figure from Mertes et al., 2017).

1.4 Aims and objectives

This study will reconstruct the area and geodetic mass balance of Fannaråkbreen (2.47 km^2), which due to its size is a sensitive climate indicator in Norway's Jotunheimen national park, dating back to the 1950s. Fannaråkbreen was chosen for its unexamined history and sensitivity to climate due to its size. Its accessibility facilitates Unmanned Aerial Vehicle (UAV) mapping across seasons, filling a regional research gap as no other temperate glacier in Jotunheimen has such extensive records.

The dataset from Fannaråkbreen will enhance the national glacier mass balance database and validate against the long-term glaciological mass balance series from nearby Storbreen. High-resolution seasonal data coupled with past reconstructions of mass balance can be used to describe regional climate dynamics and this glacier's specific climate response, aiding regional mass balance estimation, identification of local variations and future climate modelling (Haeberli, 2011).

Archival aerial photographs (1955, 1966, 2004, 2010, 2017) (Kartverket, 2024b) and a LiDAR (Light Detection and Ranging) Digital Elevation Model (DEM) from 2020 (Kartverket, 2020a) from the Norwegian Mapping Authority will be used for mass balance reconstruction back in time. Recent glacier changes rely on UAV-derived elevation data from photogrammetry, with missions conducted in September 2022, June and September 2023, timed to capture seasonal change in glacier mass and quantify the winter and summer mass balances. No previous such study is known to have taken place. Additionally, two image sets - one with only nadir and another with nadir and oblique angles - will be analysed to determine the most suitable method for mapping steep glacier areas.

The research questions are therefore as follows:

- How did the volume and area of Fannaråkbreen change between the 1955 and 2023 and how does its long-term mass balance compare regionally?
- What are the short-term (seasonal) mass changes and how accurately can they be measured using remotely sensed UAV data?
- How does the geodetic mass balance of Fannaråkbreen compare to the glaciological records of Storbreen?

2. Theoretical background and terminology

To provide better clarity to this study, this section presents the main concepts and key terms forming the basis for this investigation. It will be elaborated on definitions as well as relevant theoretical concepts that support the analysis and discussion of the results.

To begin with, it is essential to clarify the term "*glacier*". H. Ahlman, one of the pioneers of glacier research in Norway, defines it as "a many year old mass of snow and ice in movement" (H. Ahlman in Liestøl, 2000, p. 13). Patterns of glacier distribution on Earth depicts the interaction between topography (aspect and relief), precipitation that can be turned to ice and air temperature, differing in a consistent manner around the globe north-south, east-west as well as proximity to a source of moisture (Benn & Evans, 2010, p. 11). Glaciers form where summers are not warm enough to melt snow fallen during winter, allowing it to accumulate over several years and forming ice underneath (Liestøl, 2000).

Glaciers are characterized by movement initiated by mass accumulation in the higher parts that eventually begins to press the ice down the slope and outwards where air temperature is higher, resulting in melting of the old ice during ablation Figure 2.1 (W. Werenskiold in Liestøl, 2000, p. 13). Normally, glaciers tend to gain more mass than they lose in the upper parts, however, the opposite is true for the parts at a lower altitude (Bakke & Nesje, 2011).

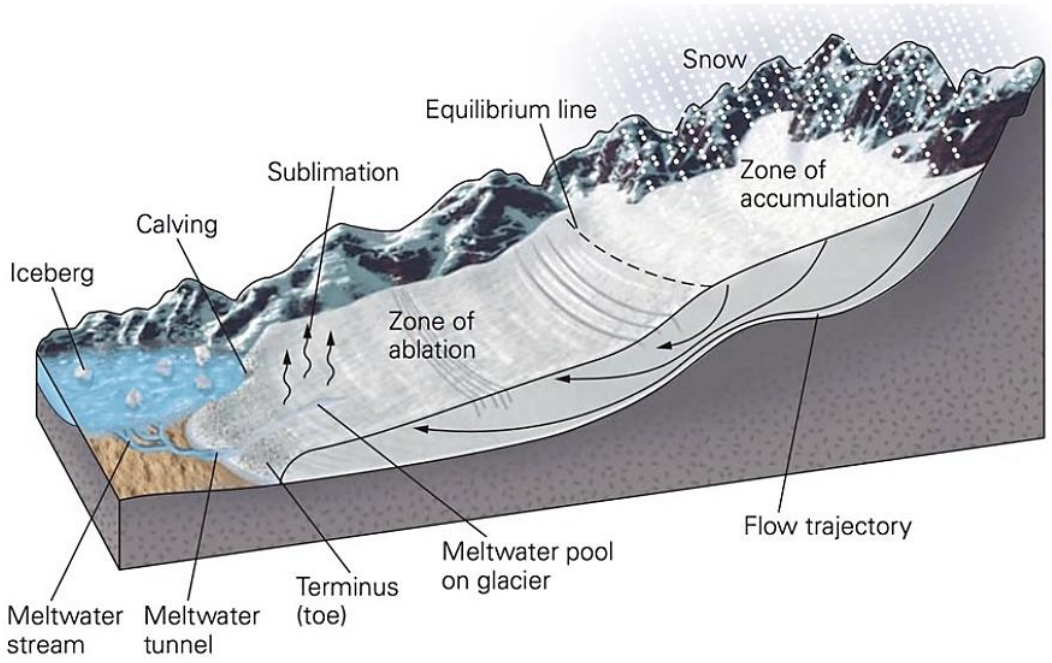

Figure 2.1: An idealized representation of glacier geometry showing processes important for glacier mass balance (figure from Marshak & Repcheck, 2009).

2.1 Remote sensing in glacier studies

In glacier studies, while direct glacier survey techniques can be resource-demanding and spatially limited, remote sensing can bridge gaps in glacier monitoring networks by observations across large areas (Bamber & Rivera, 2007). Remote sensing not only helps in carrying out glacier inventories and mapping glacier area (e.g., Andreassen et al., 2008; Andreassen, Nagy, et al., 2022), but also in estimating volume change and mass balance from stereo-imagery (e.g., Gardelle et al., 2013; Hugonnet, McNabb, et al., 2021).

Nonetheless, today's prevalent satellite data often lacks the precision to capture changes in small glaciers (Leprince et al., 2007; Bash et al., 2018). This was evident in the latest Norwegian glacier inventory (Andreassen, Nagy, et al., 2022), where over 2000 small glaciers were detected using 10 m spatial resolution Sentinel-2 imagery, which were overlooked with the previous inventory that employed three-times coarser Landsat imagery (Andreassen et al., 2012). Furthermore, the quality of space-borne data also depend on cloud coverage and temporal resolution which is predefined, while aerial photography, although more accurate, is usually quite costly (Wigmore & Mark, 2017).

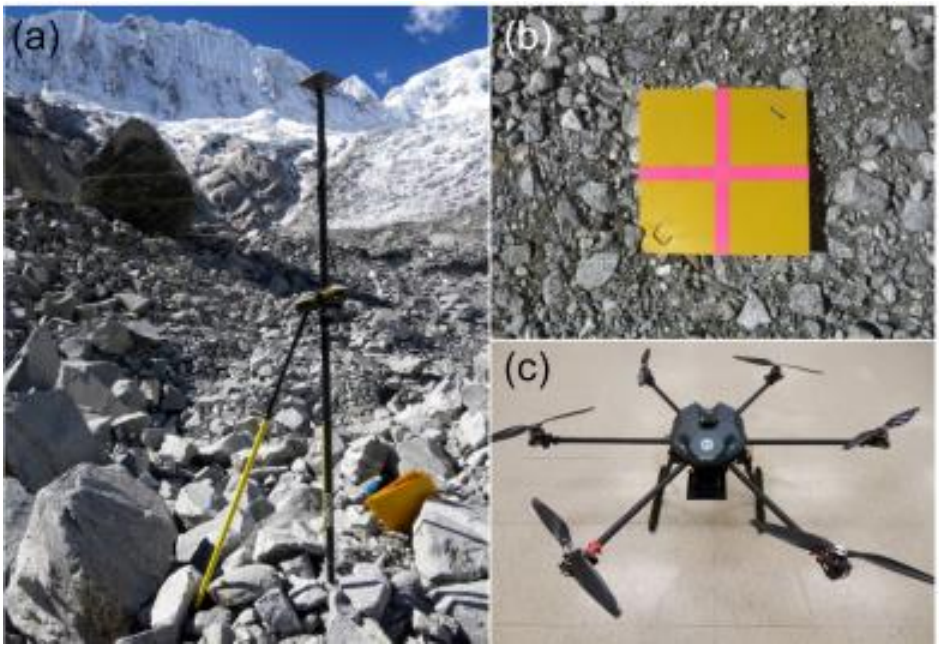

Figure 2.2: A setup used to survey Llaca glacier in Peru. a) dGNSS for direct spatial referencing of images, b) target for ground control and c) the UAV used for mapping (figure from Wigmore & Mark, 2017).

Unmanned Aerial Vehicles (UAVs, commonly called *drones*) have emerged as a solution to these issues, capable of capturing high-accuracy, high-resolution topographical data over time and space, and adaptable to various wavelengths (Bhardwaj et al., 2016). Employing sensors

with precise positioning systems (e.g., differential Global Navigation Satellite System or dGNSS, Figure 2.2a), UAVs facilitate detailed three-dimensional analyses through Structure-from-Motion (SfM) and Multi-View Stereo (MVS, see section 2.4.1) algorithms (Smith et al., 2016). This allows UAVs to capture glacier dynamics with a spatial resolution of a few centimetres, to monitor surface fluctuations over comparatively short time periods, from months to days, (e.g., Wigmore & Mark, 2017; Che et al., 2020; Baurley & Hart, 2022), even for slow moving glaciers (Cao et al., 2021). This resource-efficient technology is increasingly utilised to calculate glacier volume changes, enabling precise assessments of mass balance.

2.2 Glacier parameters

There are several different glacier parameters that can be monitored for learning about climate. The one showing almost immediate glacier response to changes in air temperature or precipitation is glacier mass balance (vertical changes), through a number of processes affecting glacier dynamics and in turn influencing terminus position and total glacier area (horizontal changes) (WGMS, 2008).

2.2.1 Mass balance

Glacier mass balance is regarded as reflecting the immediate and direct response of glaciers to climate changes (Haeberli, 1998; Nesje et al., 2008; Marzeion et al., 2017). It is considered the variable that links glacier changes to climate (Meier, 1965), indicating increasingly unstable atmospheric conditions as mass balance deviations from zero become more pronounced (WGMS, 2023). For around 100 years ago it become an objective of measuring in different regions to determine the overall state of glaciers, initiated by Forel (1895) and today glacier observations from across the world are in coordination by several institutions into the Global Terrestrial Network of Glaciers (GTN-G) (Marzeion et al., 2017), published in "Fluctuations of Glaciers" every five years since 1967 (Kasser, 1967; PSFG 1973, 1977, 1985; WGMS, 1988) with a biannual supplement "Glacier Mass Balance Bulletin" (WGMS, 2023 and earlier issues).

However, methodological research on glacier mass balance did not begin until around 1940s (Ahlmann, 1948). At the beginning, mass balance studies were aimed to help learn about the health of glaciers (Ahlmann, 1948; Braithwaite & Zhang, 1999) and in later years, the advancements in hydropower in Norway, further developed this interest (Collins, 1984). The

longest persisting mass balance and glacier length monitoring has been taking place in northern Sweden, Storglaciären, since 1946 until today (Schytt, 1962; Holmlund et al., 1996).

The state of a glacier in terms of balance is determined by the sum of inputs and outputs to a glacier unit, either measured for the whole or a part of a glacier. The total change in mass is estimated by adding together the amount of ice that forms under accumulation (positive) and the amount of mass lost (negative) during the processes of ablation (schematically presented in Figure 2.3). If ablation has exceeded accumulation, the net mass balance (b_n) will be negative, and if the opposite is true, it will result in a positive value. Normally, mass balance is estimated for one hydrological year and sometimes for a period of several years, however, for mid- and high- latitude glaciers, seasonal winter (b_w, positive) and summer (b_s, negative) balances which signify mass accumulation and ablation respectively, can be defined (Benn & Evans, 2010, p. 37-38).

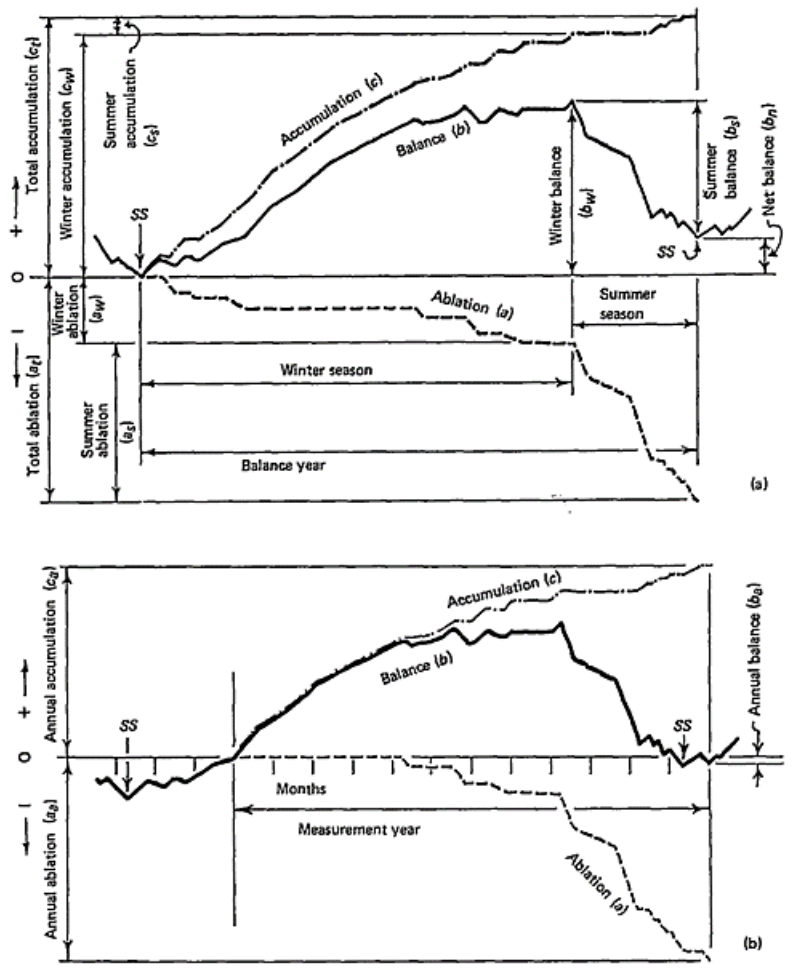

Figure 2.3: The terms describing mass balance measured at a specific point. a) depicts simultaneous occurring of accumulation and ablation throughout one mass balance year; b) represents the total difference in mass occurring during one mass balance year (figure from UNESCO & IAHS report, 1970 in Østrem & Brugman, 1991).

Mass accumulation in mid-latitude glaciers depends on winter precipitation variability, while mass loss (ablation from ice or snow melt) is closely associated to summer temperatures, linking to variations in weather conditions that occur within one year (Huss & Bauder, 2009; Cogley et al., 2011; Wagnon et al., 2013). Therefore, seasonal mass fluctuations are key indicators of climate impacts on glaciers (Vincent et al., 2004; Huss et al., 2008), but more specifically, of the drivers (Andreassen et al., 2005; Marzeion & Nesje, 2012; Trachsel & Nesje, 2015). These measurements not only help detail patterns and tendencies in glacier mass development (Pelto et al., 2019), but also serve as important datasets for the calibration and validation of both global and regional glacier models (Clarke et al., 2015; Huss & Hock, 2018; Maussion et al., 2019), as well as for integration of seasonal changes into regional hydrological models (Schnorbus et al., 2014). However, these two components are not often differentiated from the mass balance estimates (Dyurgerov & Meier, 1999; Ohmura, 2011).

Seasonal mass balance allows estimation of the amount mass gained and lost during one mass-balance year, what is not possible to do if the measurements are performed only once per year. However, as illustrated in Figure 2.3a, ice accumulation can also occur during the summer and melting can happen during the winter months, leading to seasonal mass changes to differ from the values representing accumulation and ablation. For temperate glaciers, snowfall in the summer months is often regarded as rainwater flowing off the glacier. Nonetheless, this does not influence the estimation of total b_n, as showed in equation 2.1, where c_t = total accumulation and a_t = total ablation (Østrem & Brugman, 1991).

$$b_n = c_t + a_t = b_w + b_s \qquad 2.1$$

Annual mass balance is measured as average change in thickness of water layer over glacier area and expressed as meters water equivalent per year (m w. e. a^{-1}), what includes corrections for snow or ice density (Haeberli, 2011, p. 399). The reason usual mass unit kilogram per area (kg m^{-2}) is replaced by meters, is that since the density of water in liquid form is 1000 kg m^{-3}, 1 kg of water if equally spread over 1 m^2, would measure to 1 mm (0.001 m) of depth (Cogley et al., 2011). As snow and ice can have different densities, the density of liquid water is constant, making mass balance values to be comparable.

Surface albedo and debris cover, topography, air temperature and precipitation are the factors that influencing the components of mass balance (Fischer, 2010; Cogley et al., 2011). Typically, the regional distribution of winter precipitation, and local allocation of snow by wind, as well as avalanching from surrounding slopes, influence how glaciers gain mass

(Figure 2.4) (Lie et al., 2003a). During ablation, melting is the biggest contributor to mass loss. Mass reduction can also be caused by evaporation and calving, however, when total mass turnover is considered, their effects are not as significant (Østrem & Brugman, 1991).

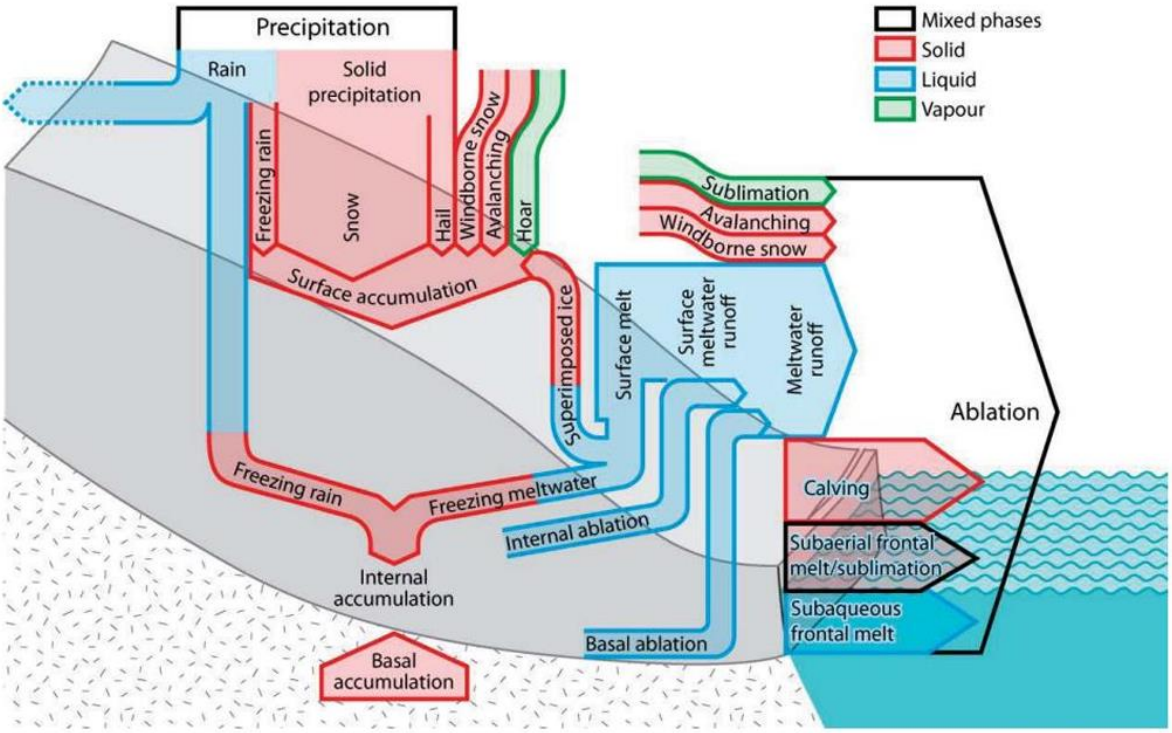

Figure 2.4: A schematic representation of the main mass balance components (figure from Cogley et al., 2011).

Although these components influence mass change for the whole ice body, these changes are not distributed homogeneously. For this reason, mass balance is classified into several types. The first is *surface mass balance*, measured at glaciers' surface, commonly by the traditional glaciological method with the use of stakes. The second is *internal mass balance*, caused by englacial processes such as refreezing of water, normally not detected during surface balance surveys. Next, *basal mass balance* is the change of glacier mass caused by processes influencing glacier sole at the bed, such as ablation due to ice pressure or geothermal heat flux. Lastly, the term *climatic mass balance* has been introduced to address the frequent instances where "surface" mass balance was used to refer to both surface and internal balances (Cogley et al., 2011).

Even though the most mass is exchanged on the glacier's surface, the total balance is the result of sub- and englacial processes, however, being quite difficult to detect and measure using traditional methods. This is especially true for temperate glaciers, where vertical mass allocation happens at the beginning of the ablation season, when meltwater from the surface

percolates down and refreezes, releasing latent heat that and raising temperatures of the whole snow layer to 0°C (Østrem & Brugman, 1991).

2.2.2 Planimetric glacier attributes

Planimetric glacier length variations (front positions) is another glacier parameter that is being reported by WGMS, representing a delayed, filtered but relatively easily observed response to changes in climate (Holmlund et al., 1996; Haeberli, 1998; Roe & O'Neal, 2009; Roe, 2011). The change in glacier length can be described as a function between the observed vertical glacier change (mass balance) and its initial length (Nye, 1960). This also means that if the change of glacier length in a period of time is known, it may be possible to infer the change of its mass. Therefore, length observations provide valuable information about glacier interactions with climate, what is especially beneficial for regions where mass balance has not been measured before, excluding instances of surging or calving glaciers (Haeberli, 1998).

Besides measurements of glacier terminus, the information on change of the total glacier area also provides important insights about the general glacier state within the specific region. Planimetric changes is a form of glacier adjustment to the extent appropriate for equilibrium conditions (where mass balance is zero) (WGMS, 2023). Glacier area measured during glacier inventories carried out on different scales is needed to quantify glacier mass balances, and since mean glacier elevations are some of the results of such inventories, they can also be applied for approximate estimations of regional equilibrium line altitudes (ELAs) (Haeberli, 1998).

2.3 Methods to measure mass balance

2.3.1 Glaciological method

The traditional way for mass balance calculation is glaciological, employing direct stake measurements and excavation of snow pits (Hoinkes, 1970; Braithwaite, 2002). Originally, the technique was developed by Østrem and Stanley in the 1960s (1966, 1969), who built on the foundation provided by H. W. Ahlman (Braithwaite, 2002; Cogley et al., 2011). The emergence of first programs dedicated to monitoring glacier hydrology were the main motivation for this development, as it raised the need for a uniform methodology and a detailed framework for field measurements to estimate glacier mass in the coastal Northern Europe (Thorarinsson, 1940; Ahlmann, 1948; Braithwaite, 2002; Cogley et al., 2011). Typically, this approach is utilized to estimate annual fluctuations and seasonal balances

(Klug et al., 2018). Østrem and Brugman (1991) have produced a user guide based on the instructions of Østrem and Stanley (1966, 1969), which is still often referred to in research articles.

The application of the method, as described by Østrem and Brugman (1991), begins with a choice of a suitable glacier (with regards to accessibility), followed by an establishment of an as evenly distributed stake network as possible (stakes are poles installed on the ice surface (Cogley et al., 2011)). The stakes marked regularly (as seen in Figure 2.5) are used to measure the difference in glacier surface height between two observations. For winter balance at the point where a stake is placed, the thickness of the snow layer is measured at the end of the accumulation period, referencing its thickness to the layer from previous summer. As snow can be distributed heterogeneously across the glacier, the accumulation pattern can be established using probing rods. Conversely, to measure glacier melt, surface lowering in relation to the poles drilled in ice is read directly from stake lengths (Østrem & Brugman, 1991).

Figure 2.5: An ablation stake used in glaciological method on Engabreen. The markings on the pole are used to determine elevation change of the glacier surface (figure from Andreassen, Elvehøy, & Kjøllmoen, 2023).

The equation 2.2 (provided by Dyurgerov, 2002) demonstrates how to derive mass balance (b_i) for a specific point using stake method. With the first member of the equation, the density of solid ice is calculated (normally, 0.90 g cm^{-3}). Here, ρ_0 refers to ice density and Δh the alteration in the ice surface level compared to the top of a measuring pole. The second part is used to account for mass change due to snow or firn, with varying density over time that is measured by weighing a known volume of snow taken form a snow pit. When specific point balance values from several sites (multiple b_i) are known, spatial information can be integrated to derive mass balance for the entire glacier. First, specific mass balances for different altitudes are estimated by multiplying the b_i with area of the respective elevation band it is measured at, then averaged and divided by the total glacier area (Dyurgerov, 2002).

$$b_i = \rho_0 \Delta h + (\rho_2 h_2 - \rho_1 h_1) \qquad 2.2$$

The glaciological method provides accurate point specific mass balance and information on its spatial distribution (Hock & Noezli, 1997). Depending on the frequency of stake readings, the field-based method can be utilized on a relatively high temporal scale making it suitable for detecting shorter term mass balance changes. However, some estimations can have different sources of uncertainties, such as stake relocations or logistical limitations that affect stake distribution (e.g., Klug et al., 2018; Wagnon et al., 2020), outdated glacier area information (Wang et al., 2014), interpolation between data points (Hock & Jensen, 1999), extrapolation of unmeasured glacier areas (such as cliffs and crevasses) (Jansson, 1999; Fischer, 2010) and inability to correctly identify the layer of the previous ablation season (Cox & March, 2004; Andreassen et al., 2016).

2.3.2 Geodetic method

An alternative approach to traditional mass balance assessment is referred to as geodetic (volumetric) method, introduced by S. Finsterwalder for the first time in the 19th century (Braithwaite, 2009). The method is based on repeated surveying of glacier surface and area, building on the comparison of two DEMs from different dates to infer whether the surface had thickened or thinned during that time period (difference DEM) (Figure 2.6) (Rignot et al., 2003). The changes in glacier surface are measured with reference to the surrounding bedrock, assuming that it is not changing (Haug et al., 2009).

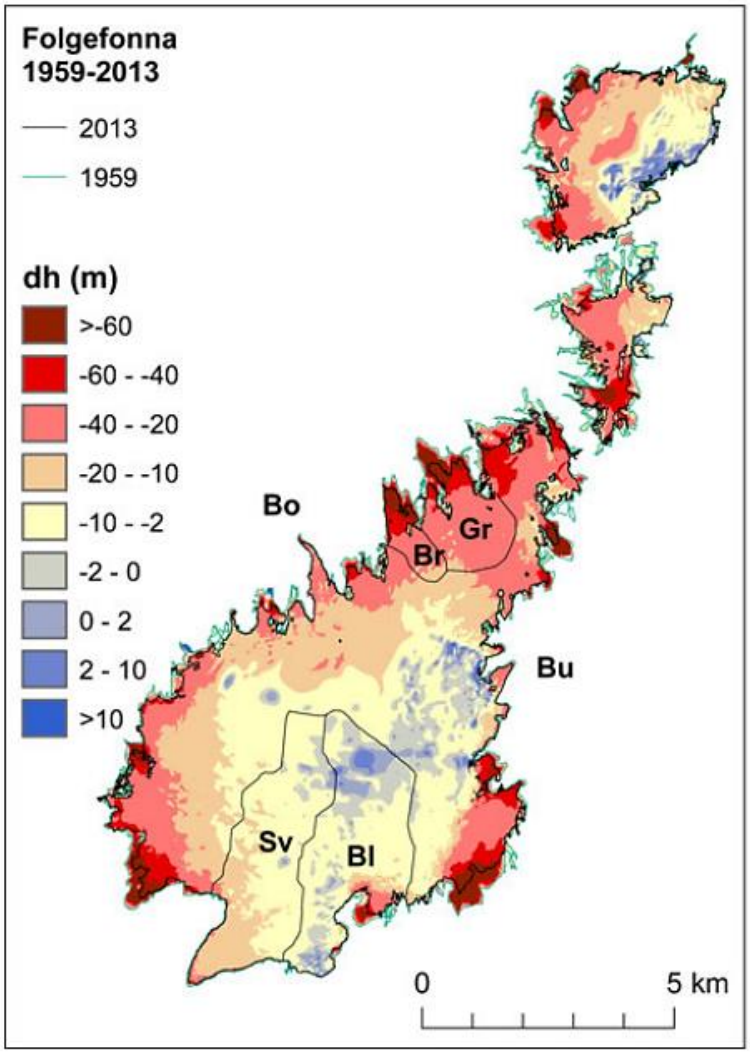

Figure 2.6: The difference in surface elevation between 1959 (aerial photogrammetry) and 2013 (airborne laser scanning), Folgefonna. Elevation change is required for estimation of glacier volume change and its further conversion to mass by integrating ice density values (figure from Andreassen et al., 2020).

Accurate surface elevations with sufficient time period between for the change to be significant, is the main element required to estimate geodetic mass balance (Bamber & Rivera, 2007). This data can be sourced from old topographical maps, terrestrial and aerial photographs (e.g., Krimmel, 1999; Andreassen et al., 2002; P. Weber et al., 2020), satellite imagery (e.g., Larsen et al., 2007; Schiefer et al., 2007; Andreassen et al., 2012; Winsvold et al., 2017), laser point clouds (e.g., Sapiano et al., 1998; Baltsavias et al., 2001; Andreassen, Robson, et al., 2023) and GPS devices for location information. By utilizing a combination of different data from various platforms, mass balance can be estimated over longer time scales, and referenced to higher accuracy data, such as LiDAR or UAV imagery, as compared to sources like aerial photographs or maps (Schenk & Csatho, 2012; Csatho et al., 2014).

Once the average value of elevation change (Δh) for the entire glacier surface is quantified through DEM differentiation, volumetric glacier change can be derived by multiplying it by the glacier area (A). However, this number does not account for the mass of the material whose volume has been gained or lost. Therefore, the density values (ρ) of snow (for estimation of seasonal change) or ice (annual or balance over longer periods) must be incorporated into the estimate, and the result should be converted to water equivalent by dividing by the density of water, which is 1000 kg/m^{-3}, as shown in equation 2.3 (Giesen et al., 2008; Cogley et al., 2011). For conversion of volumetric balance for the entire area of land-terminating glaciers and for periods longer than 5 years, Huss (2013) suggests using the value of 850 ± 60 kg m^{-3} for ice, assuming, stability of mass balance gradients, the presence of firn on the surface and that the difference in volume are significantly larger than zero.

$$B_{geod} = \frac{\Delta h \times A \times \rho_{snow/ice}}{1000\ kg/m^{-3}} \qquad 2.3$$

However, calculation of winter mass requires knowledge of snow density. Accurately estimating snow density can be difficult as it varies considerably with time and space, while acquiring snow samples necessitates physical presence, making it laborious and costly (Pelto et al., 2019). Therefore, besides uncertainties related to DEM production (see section 2.5) and assuming snow layer homogeneity, snow density represents another potential error source (Haug et al., 2009; Huss, 2013; Sold et al., 2013; Belart et al., 2017). Other significant errors can arise from the data itself, especially if the exact date of image acquisition is uncertain or if images from different dates are used to depict the surface conditions for the same time period (Cogley, 1999).

The geodetic method is time and cost-efficient, and with historical data, mass balance can be calculated far back in time (e.g., Haug et al., 2009). It enables mass balance analysis across decades for entire regions (e.g., Wingham et al., 1998; Krabill et al., 2000; Bamber et al., 2004; Larsen et al., 2007; Schiefer et al., 2007; Andreassen, Robson, et al., 2023), covering entire glacier extents (Haug et al., 2009; Basantes-Serrano et al., 2018) and capturing all processes related to surface change, including englacial and basal mass changes, and ice flow effects (Cuffey & Paterson, 2010). It is also effective for assessing winter snowpack depth (Berthier et al., 2014; Nolan et al., 2015), an important aspect of glacier mass balance (Østrem & Brugman, 1991).

2.3.3 Method comparison

The two methods have their own strengths and limitations. Surface point elevations measured geodetically are affected by glacier movement, while this is avoided with point measurements read from ablation stakes which move in tact with the ice mass (Paterson, 1994). Additionally, as opposed to field measurements, the geodetic mass balance does not accumulate systematic errors with time, making it useful for detailing mass balances for longer time periods (Wang et al., 2014). This together with the fact that geodetic mass estimations include internally occurring accumulation and ablation, allow it to be utilised for calibration of glaciological mass balance results and validation of mass change simulations (Jóhannesson et al., 2013; Andreassen et al., 2016; Kronenberg et al., 2016). Therefore, it is suggested to incorporate decadal volumetric measurements alongside with the records based on in-situ measurements (Zemp et al., 2013). However, detailed glaciological point and snow density measurements are also considered valuable, complementing the geodetic method with site-specific density measurements (Braithwaite, 2002).

Which approach to choose, depends on the goal of the study: weather detailed, point-specific data of surface change is needed, or broader insights of the entire glacier (including internal mass change) or assessment on a larger geographical scale is preferred. Nevertheless, the most thorough insights on glacier mass balance can be achieved if both methods are used in combination (Thibert et al., 2008; Fischer, 2011; Huss et al., 2017; Klug et al., 2018).

2.4 Conventional and Structure-from-Motion photogrammetry

Due to increasing popularity of UAVs and increases in computing power, photography has been widely used in recent years to study glaciers (Fox & Nuttall, 1997). Photogrammetry is often used in relation to remote sensing. It aims to extract quantitative information about an object from stereo-images through estimation of parallax – the shift of an object between two overlapping photographs taken from two different angles (Lillesand et al., 2015). This allows an extraction of object's x, y and z coordinates (Schenk, 2005; Gomarasca, 2009).

The first initial motivation behind aerial photographic surveys of the ground and experimental photogrammetry was for military surveillance purposes (Gomarasca, 2009), followed by an invention of a stereoplotter. Further technological progress in computing throughout the late 1960's enabled analytical photogrammetry to develop, along with the first computer programs within the field, optimising aerial triangulation. The field entered a new era in the early 2000's when digital cameras as well as processing microchips and devices for data

preservation and access become more readily available, giving rise to digital photogrammetry (Schenk, 2005). As working with large data volumes became easier, georeferenced digital point datasets emerged as primary products in glacier research for deriving glacier DEMs (Fox & Nuttall, 1997) with a possibility to reconstruct surfaces more than a hundred years back in time utilising historical sources (e.g., Holmlund & Holmlund, 2019; Kavan, 2020; Holmlund, 2021). The following overview of the core photogrammetry principles is informed by Lillesand et al, 2015, p. 146-217.

2.4.1 The parallax

A principle in photogrammetry, describing how stationary objects seem to move relative to each other when looked at from different positions is called a *parallax*. A typical example would be looking through the window of a moving train and seeing objects in far distance to appear moving less than objects closer to the viewer. When applied in photogrammetry, the principle of parallax involves observing how far a terrain feature *A* in Figure 2.7 appears to be shifted in one image relative to another. This shift indicates its relative distance from the camera compared to another feature such as *B*, that also shifts, but by a different amount. Essentially, objects at higher elevations will appear to have moved more than those situated lower. By estimating this difference, it is possible to estimate the latitude (X), longitude (Y) and elevation (*Z*), and generate a DEM (Lillesand et al., 2015, p. 177-178).

To achieve this, a sufficient overlap between images is required together with exact camera locations and camera angle information. These parameters, together with the measured parallax and triangulation methods, can be applied to estimate the distances between the camera and the object (Lillesand et al., 2015). For instance, the parallax of the point *A* in Figure 2.7a can be estimated by subtracting the *x* image coordinate of the point *A* in one image (x_a) and its x coordinate in another image (x'_a) of the stereopair (Figure 2.7b) as shown in the equation 2.4 (Lillesand et al., 2015, p. 178-179).

$$p_a = x_a - x'_a \qquad 2.4$$

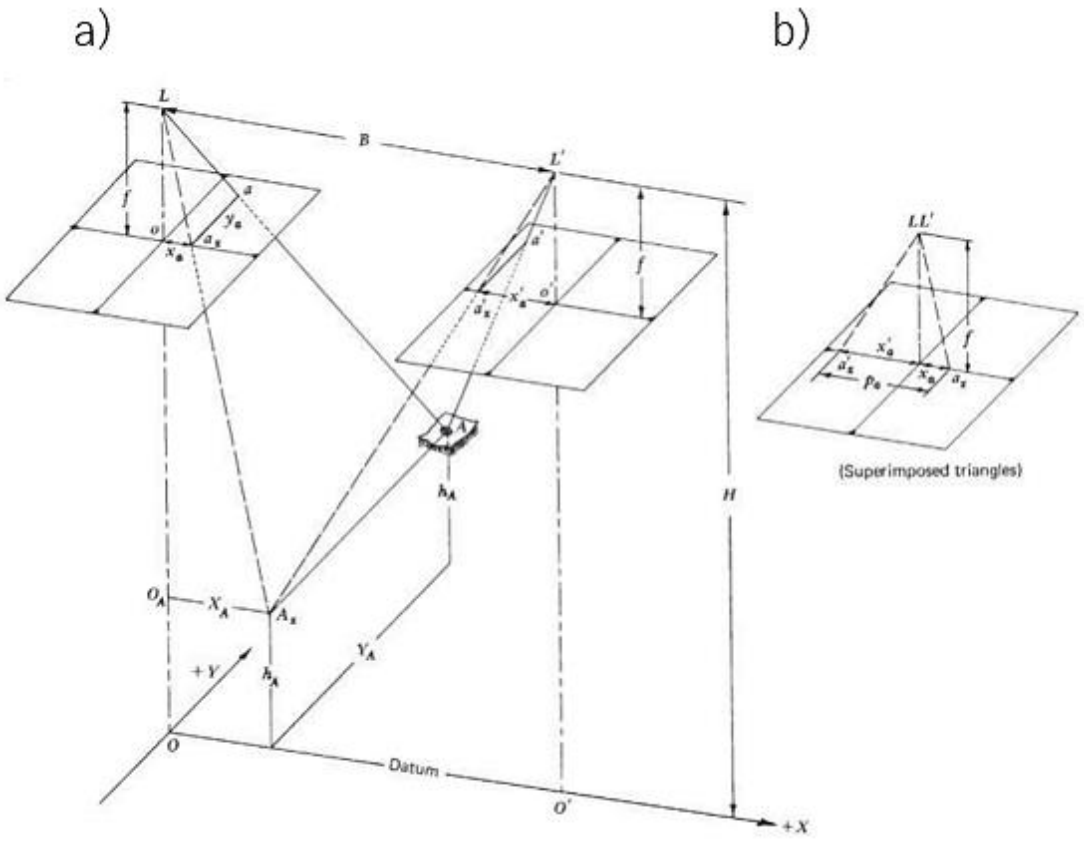

Figure 2.7: Geometric representation of parallax relationships on vertical photos of the same object taken from different positions. a) a stereopair, b) superimposed images (right on left) (figure from Lillesand et al., 2015).

Having estimated the parallax of the point *A* and when the distance of the baseline (*B*) between the exposure stations (*L* and *L'*) is known, it is possible to estimate its X and Y ground coordinates using the equation derived by triangulating (equations 2.5 and 2.6). However, an assumption that that these photographs have been taken from the same height and that they are perfectly vertical, must be made (Lillesand et al., 2015, p. 179-181).

$$X_A = B\frac{x_a}{p_a} \qquad 2.5$$

$$Y_A = B\frac{y_a}{p_a} \qquad 2.6$$

Based on the Figure 2.7a, the baseline (*B*) and the parallax (p_a) forms a right-angled triangle and gives an idea of how far away the point *A* is located from the camera (Z-dimension). With the lengths of baseline and parallax providing two sides of the triangle, the rest can be estimated using the Pythagorean theorem, which, after application of further geometric

principles, can translate the 2D parallax measurements to 3D space and thus, extract the Z-coordinate, a process called *space intersection* (Lillesand et al., 2015, p. 181-182).

2.4.2 Extraction of elevation data using photogrammetry

In digital photogrammetry (including scanned analogue photographs), image point matching is done using numerical image correlations applying different matching techniques on pixel scale. One of the techniques employs an idea of *epipolar* (reprojected to have the same orientation (CATALYST.Earth, 2024b)) geometry to reduce the time needed for computation by moving the search window (e.g., 5x5 pixel area) solely along the straight line where any point parallax occurs. Since digital systems employ a variety of mathematical processing algorithms, it does not rely on the assumptions about images being truly vertical nor their altitude being constant, as they can handle these variations described by collinearity equations, solving the *exterior orientation*, necessary for using aerial images for mapping.

Exterior orientation refers to the relationship between the absolute (ground) and relative (image) coordinate systems, described by several parameters: omega (ω) – rotation about the x-axis, phi (φ) – rotation about the y-axis, kappa (κ) – rotation about the z-axis (Figure 2.8). This geometric relationship is determined by estimation of these parameters, what is done by projecting image 2D coordinates to 3D system (and the other way around), a process called indirect georeferencing. In direct georeferencing, however, these parameters have already been measured for each image with the GPS and IMU (inertial measurement unit), removing the necessity for establishment of ground control points (GCPs) (see section 2.4.4).

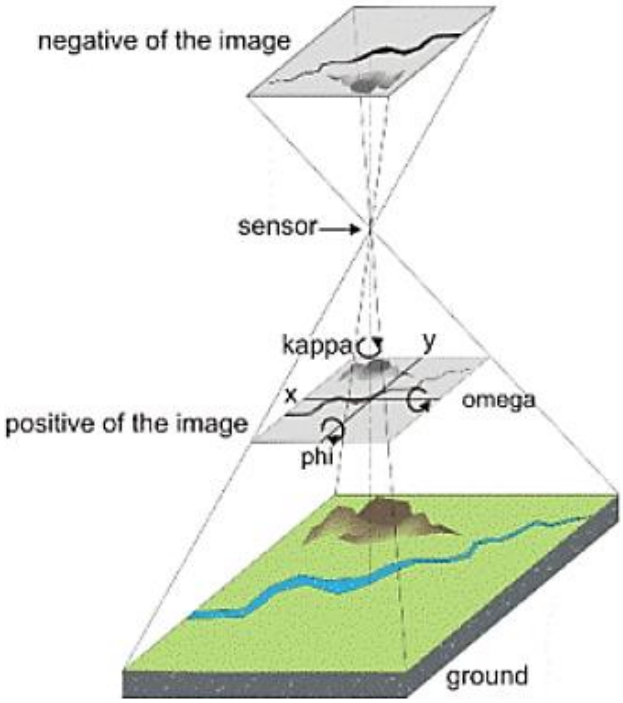

Figure 2.8: Visual representation of the geometric relationship between image (relative) and ground (absolute) coordinate systems, expressed in omega, phi and kappa angles. These angles are crucial for solving exterior orientations (figure from Wolf & Dewitt, 2000).

Thereafter, relative orientation refers to the relationship and overlap between photographs in a block (a set of overlapping images). This is solved by collecting points that are easily identifiable in several images (tie points in Figure 2.9), comparing their photocoordinates from each image and correcting for the differences. Further, bundle adjustment (an estimation of exterior and interior orientations (Ullman & Brenner, 1979) of the whole block can be used to determine how the relative positions of these points relate to the ground coordinates (solving of the absolute orientation). If direct georeferencing has been applied, GPS coordinates have already been acquired, making each image centre (points *o* in Figure 2.7) a GCP. However, additional control points can be established to improve the absolute accuracy of the model and it is common to measure 10 or more of such points for blocks consisting of hundreds of images, even with direct georeferencing (Maune, 2007).

For historical analogue datasets, additional *interior orientations* defined by to the geometry of camera lens need to be established. The goal is to locate the perspective centre (referred to as PPA) and establish the curve of radial lens distortion, what is not needed to be done for modern cameras (Schenk, 2005). The parameters needed to solve this are normally provided in camera calibration report (Wolf & Dewitt, 2000; CATALYST.Earth, 2024c). Once these orientations are solved, one of the main photogrammetric products, a DEM, can be extracted

using highly automated elevation sampling of correlated images in the overlap area (Lillesand et al., 2015).

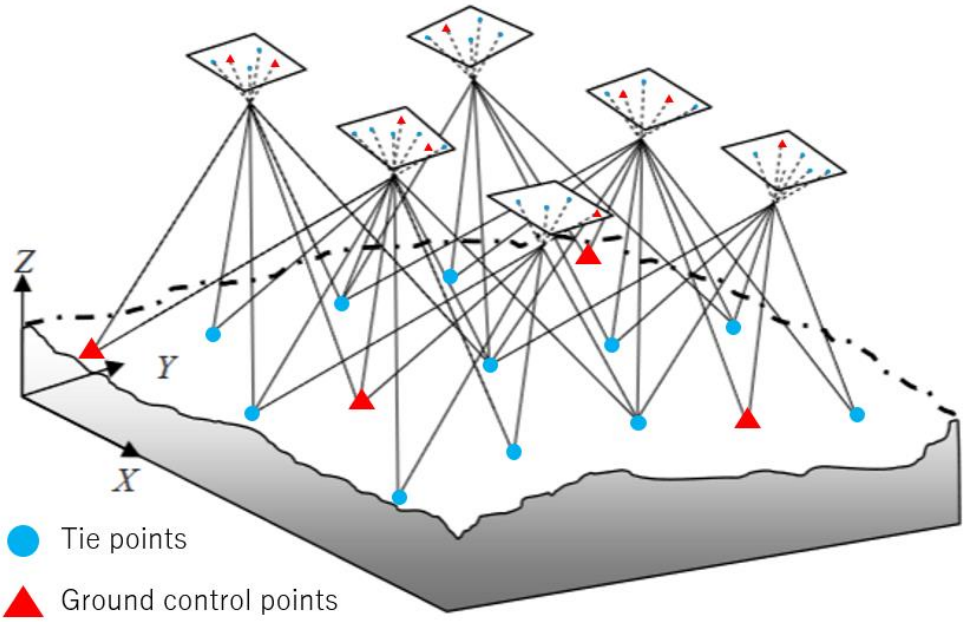

Figure 2.9: An illustration showing how tie points describe relative orientation between a block of images and the fact that ground control points are basically tie points with location attribute (figure adapted from Fig. 5.1 in Yuan, 2009).

2.4.3 Structure-from-Motion with Multi-Stereo View photogrammetry

In contrast to traditional photogrammetric techniques, structure-from-Motion (SfM) photogrammetry does not require parameters set during camera calibration, as they are estimated based on the geospatial information recorded by a GPS and the sensor orientation captured by an IMU unit (Smith et al., 2016; Eltner & Sofia, 2020). This makes SfM photogrammetry suitable for computation of inner image orientations in cases of missing camera calibration reports for the analogue image datasets (e.g., Gonçalves, 2016; Mölg & Bolch, 2017; Vivero et al., 2021).

The method employs computer vision algorithms for automated extraction of 3D point coordinates from a large number of images using bundle adjustment. During this process, the model is optimised through establishment of rays linking image centres with three-dimensional tie points (bundle, Figure 2.9) seeking to find the best fitting non-linear function to minimise the projection error (adjustment) (Granshaw, 1980; Triggs et al., 2000; Szelski, 2011). Lastly, georeferencing of the final point cloud is performed and, if needed, some additional information, such as additional GCPs for improvement of interior and exterior orientation parameters is added, and the model is readjusted (Eltner & Sofia, 2020).

The resulting sparse point cloud is then densified utilising a Multi-View Stereo (MVS) algorithm (Seitz et al., 2006; Remondino et al., 2014). Patch-based MVS developed by Furukawa & Ponce (2010) is the algorithm type that are best suitable for applications in physical geography today (Smith et al., 2016). It uses feature detection to create a set of patches which are then expanded to collect even more patches. After a refinement, the remaining patches constitute a resulting mesh used for modelling.

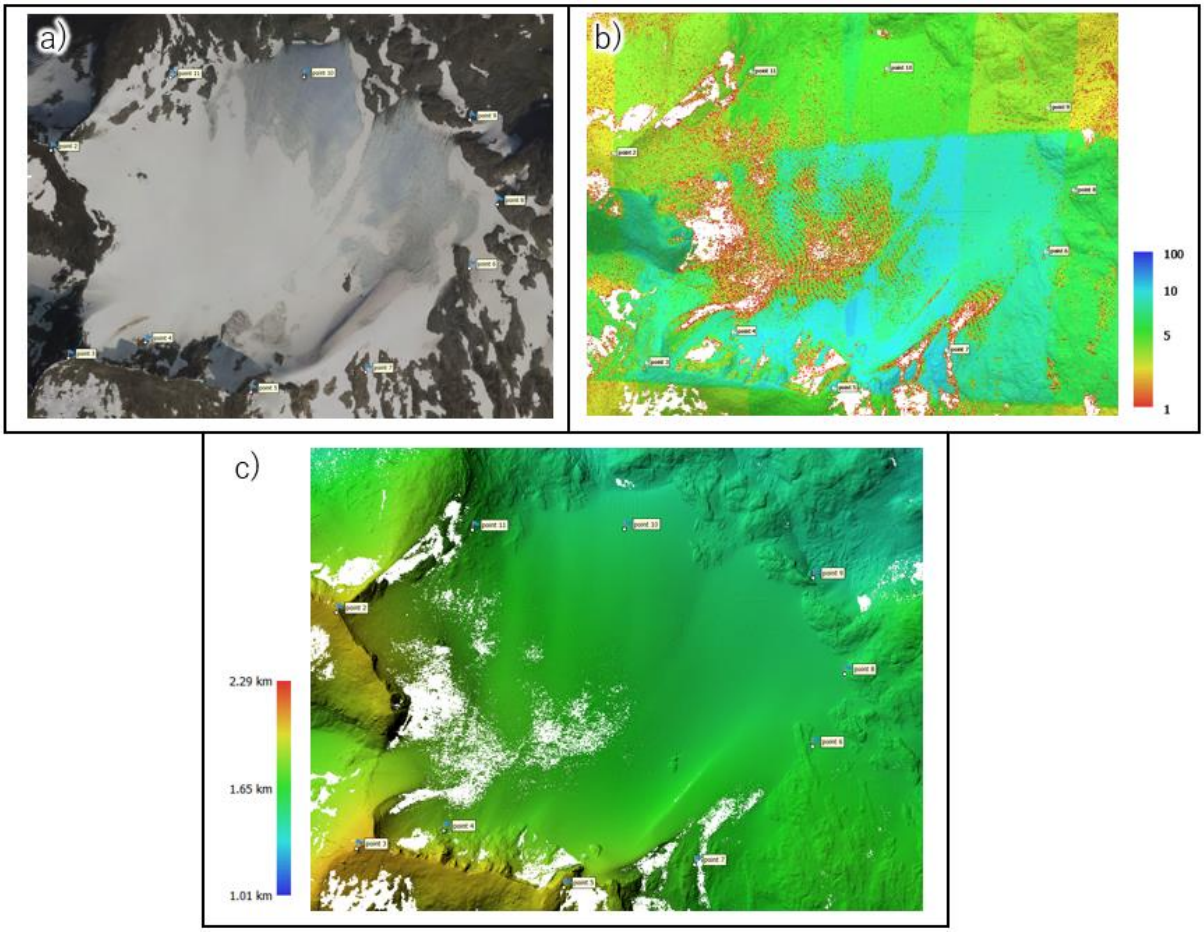

Figure 2.10: The importance of having sufficient surface contrast for quality of a DEM (an example from this study) a) An orthomosaic generated from underexposed photographs from 2017; b) photogrammetric dense point cloud coloured by point confidence, extracted from imagery in a); c) a shaded representation of a DEM extracted from the point cloud in b). As seen from the figure, areas with the lowest surface texture in a) yielded no data in the final output c).

The quality of the final product depends greatly on the quality of images, since the foundation of the SfM photogrammetry is feature detection and their matching (Furukawa & Ponce, 2010; Gruen, 2012). Therefore, sufficient image contrast that is affected by the texture of surface being photographed, is of high importance. For this reason, mapping of homogeneous featureless surfaces such as snow can be challenging, resulting in data gaps within DEMs (Figure 2.10) (Eltner & Sofia, 2020). Other factors such as ground sampling distance (most often corresponding to spatial sensor resolution (Lillesand et al., 2015), surface capturing

from different perspectives and distances (Micheletti et al., 2015; Eltner et al., 2016; Smith et al., 2016), optimal image overlap (not too large and not too small) (Mosbrucker et al., 2017) are also considered having an effect on the quality of the reconstructed photogrammetric model.

Utilisation of SfM photogrammetry with MVS is considered having been revolutionary for surveying topography (e.g., Lucieer et al., 2013; Tuffen et al., 2013; Eltner et al., 2014; Javernick et al., 2014) due to its ability to produce highly accurate spatial products, the versatility of applicable sensors, cost efficiency, feasibility of frequent surveying and point quality that is comparable to LiDAR clouds (Westoby et al., 2012; Carrivick et al., 2016; Smith et al., 2016). These were also the reasons for the choice of this remote sensing data processing method for glacier surface mapping in this study.

2.4.4 Direct and indirect georeferencing of models

Low to medium cost UAVs normally come with cheaper IMUs and GNSS receivers, affecting the accuracy of direct image georeferencing (Ekaso et al., 2020). Therefore, in such cases, it is recommended to improve image location accuracy indirectly, by establishing GCPs surrounding the area of interest prior to the survey. This can be done by marking and accurately measuring the locations of specific points with differential GNSS, which would be easily recognised in the images during conventional photogrammetric processing (e.g., Westoby et al., 2012; Lucieer et al., 2013), what may also be important for improvement of absolute and relative accuracies of elevation models (James et al., 2017). As shown in Figure 2.11, height errors increase with the distance from GCPs (Tonkin & Midgley, 2016), thus it is suggested to distribute them effectively, ensuring they encircle the object or area being modelled (James & Robson, 2012; Eltner et al., 2016; Smith et al., 2016).

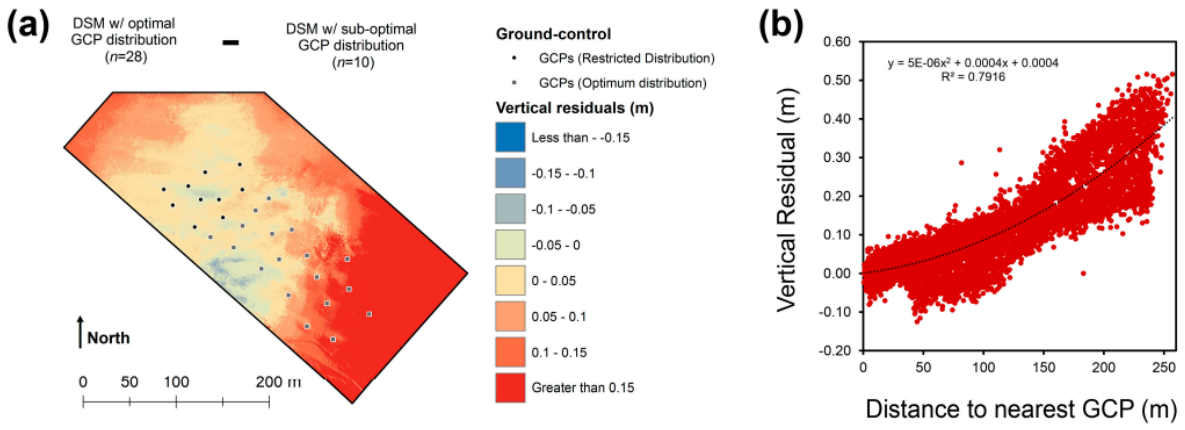

Figure 2.11: a) Elevation difference between a DEM generated using a homogenous ground control point (GCP) distribution and a DEM derived with the use of a less even distribution of GCPs across the same model. b) A plot visualising the trend of increasing elevation errors with larger distances from the GCPs in form of a polynomial regression (figure form Tonkin & Midgley, 2016).

In some cases where sites are less accessible, a proper GCP distribution may not be possible (Ekaso et al., 2020). Therefore, another way to improve absolute accuracy of a model is to manually select a number of tie points that belong to non-moving features such as corners of large boulders. By sampling their X, Y and Z coordinates from a previously georeferenced orthomosaic and DEM, they can be used as virtual ground control points (e.g., Immerzeel et al., 2014).

However, recent advances in the development of methods and hardware for UAVs, specifically designed for earth surface surveys, now enable the acquisition of high-accuracy spatial information. Thus, the reliance on any type of GCPs is for production of high-accuracy models is becoming less crucial, making mapping of inaccessible areas using SfM photogrammetry increasingly more attractive (Eltner & Sofia, 2020). Direct referencing is now possible through techniques such as Real-Time Kinematic (RTK) positioning and Post Processing Kinematic (PPK) technology which are used to correct GPS data. The RTK method involves a fixed base station installed at the survey site sending correction signals to the GNSS receiver (rover) on the aircraft during flight, achieving location accuracy to within a few centimetres (Ekaso et al., 2020; Eker et al., 2021) (Figure 2.12a). In contrast, the PPK technique involves correcting GNSS data recorded by a module on the aircraft against a nearest base station's known location during post-processing, resulting in corrections of positional errors (Wingtra, n.d.) (Figure 2.12b).

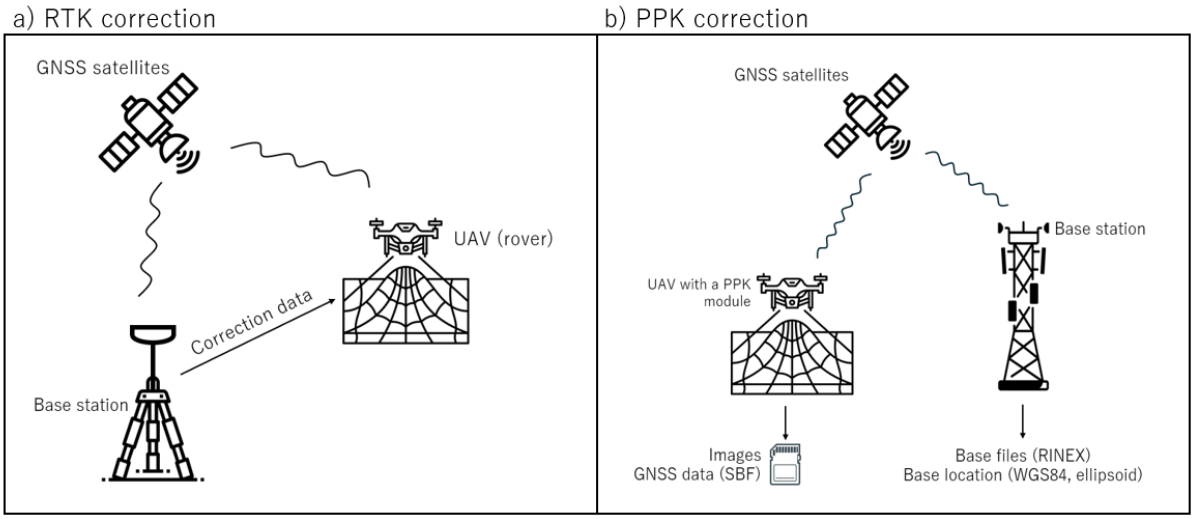

Figure 2.12: Schematic representation of a) Real-time kinematic (RTK) and b) Post processing kinematic correction of location data used for direct image georeferencing under surveying (vector icons sourced from Flaticon, 2024).

2.5 Uncertainties from DEM differencing

The results of glacier volume change, and thus, mass balance are largely affected by the quality of input DEMs (Rolstad et al., 2009). These DEMs are produced through various data acquisition methods and processing techniques, which introduce uncertainties that are carried through to the final results. Therefore, these factors should be addressed.

2.5.1 Error sources

First, it can be distinguished between DEM *accuracy* and *precision*. Accuracy represents how different the recorded (DEM) and the true (reference) elevation values are statistically (Mesa-Mingorance & Ariza-López, 2020). On the one hand, accuracy relates to systematic errors within the entire DEM (affine biases) potentially resulting from horizontal/vertical, rotational DEM adjustments or scaling, tilt alignments and vertical shifts (Mukherjee et al., 2013; Kulp & Strauss, 2019), which were performed in order to correct for any misalignments to the reference dataset. On the other hand, accuracy can vary among specific cells due to various factors. These include specific biases related to different resolutions (Vaze et al., 2010; Gardelle et al., 2012), methods for data acquisition and instruments used which may introduce issues such as inaccurate positioning and lens distortions (Girod et al., 2017; Dehecq et al., 2020). Additionally, factors such as terrain complexity and the quality of the software and algorithms used in data processing can also affect accuracy (Hugonnet et al., 2022) (Figure 2.13).

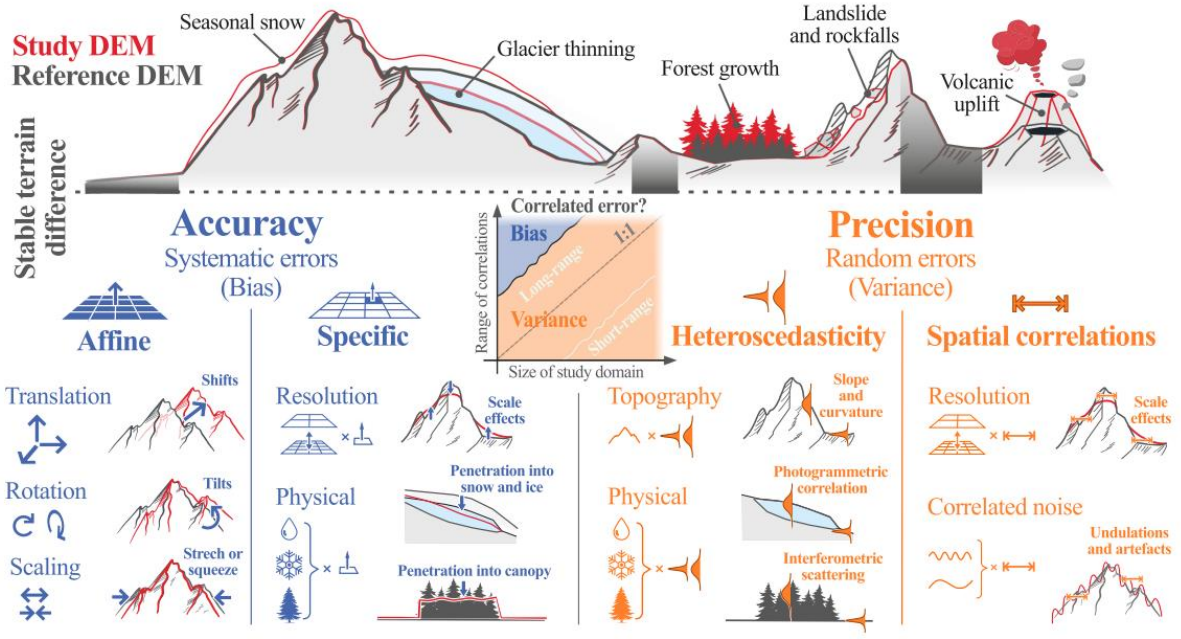

Figure 2.13: An illustration of a framework proposed for DEM uncertainty assessment based on stable terrain. Accuracy can include both affine and specific systematic errors, while precision includes heteroscedasticity and spatial correlations (figure from Hugonnet et al., 2022).

In contrast to accuracy, precision relates to random errors of data acquisition and represents the spread of inaccuracies, indicating how much individual errors vary from the average error value (Mesa-Mingorance & Ariza-López, 2020). This measurement is important for reproducibility, since a high-precision DEM consistently produces similar elevation values for a specific location using the same measurement methods, showing to higher reliability due to less random spread of errors. Precision shows to either a pattern of error variability (spatially correlated errors), or to errors not having a constant variance (heteroscedasticity). The former can for example be influenced by the resolution or spectral range of an instrument and noise that took place under processing which normally correlates with aspect, while the latter can be dependent on a terrain attribute and result in higher errors in areas with e.g., steep slopes (Hugonnet et al., 2022) (Figure 2.13).

2.5.2 Uncertainty assessment

The main approach used to evaluate the quality of a DEM is to compare it to an independent reference dataset over stable areas (bare rocks) and statistically determine the discrepancies between them (Cox & March, 2004; Nuth et al., 2007; Haug et al., 2009). The reference DEM, which should be at least three times more accurate than the DEM under assessment, is considered to approximate true ground values. This is despite the acknowledgement that

obtaining a true elevation value is impossible due to unavoidable uncertainties inherent in measurement techniques (Mesa-Mingorance & Ariza-López, 2020).

However, the differentiation is not always a straightforward process, sometimes requiring application of several different types of 3D alignments, including generic registration techniques (e.g., Zhou et al., 2016), methods considering least squares (e.g., Gruber et al., 2012), or specialised DEM registration incorporating terrain constraints (e.g., Nuth & Kääb, 2011). As mentioned in section 2.3.2, DEM differencing is also employed to estimate changes in glacier surface elevation by comparing co-registered glacier pixels, aiming to deduce changes in glacier volume, and consequently, mass balance. Therefore, the method of differentiation is significant for the results of mass balance and the assessment of uncertainty. The techniques for co-registration and bias correction are elaborated on in section 5.2.

3. Study area

Fannaråkbreen is located in the western part of the national park of Jotunheimen, central South Norway (Figure 3.1). Covering an area of around 3500 km^2, Jotunheimen mountain range belongs to the Scandinavian Caledonides (Winkler et al., 2020, p. 169). Over a hundred peaks which are rising above 2000 m a.s.l. with two of them being Norway's highest (Galdhøpiggen, 2469 m a.s.l. and Glittertinden, 2464 m a.s.l.), resemble "residual massifs" of the initial mountain range in this area (Gjessing, 1978) and the plateaus in between that are mainly above 1500 m a.s.l. are considered being the paleic surfaces from the preglacial period (Reucsh, 1901; Ahlmann, 1919, 1922; Gjessing, 1967).

During the most recent glacier inventory of Norway, it has been estimated that there was a little over 150 km^2 of glaciated area in Jotunheimen national park, including ice remnants and perennial snow fields (Andreassen, Nagy, et al., 2022). Small and very small (> 0.5 km^2) valley and cirque glaciers constitute the majority of all ice bodies within the area, some of them connecting and forming larger glacier systems (Winkler et al., 2020, p. 171). Yet, glaciers larger than 1 km^2 are taking up the most of the total glaciated area (Andreassen et al., 2008). Besides Jotunheimen being the region characterized by glaciers, it also stands as one of the key permafrost areas in Scandinavia (Gisnås et al., 2013; Gisnås et al., 2017).

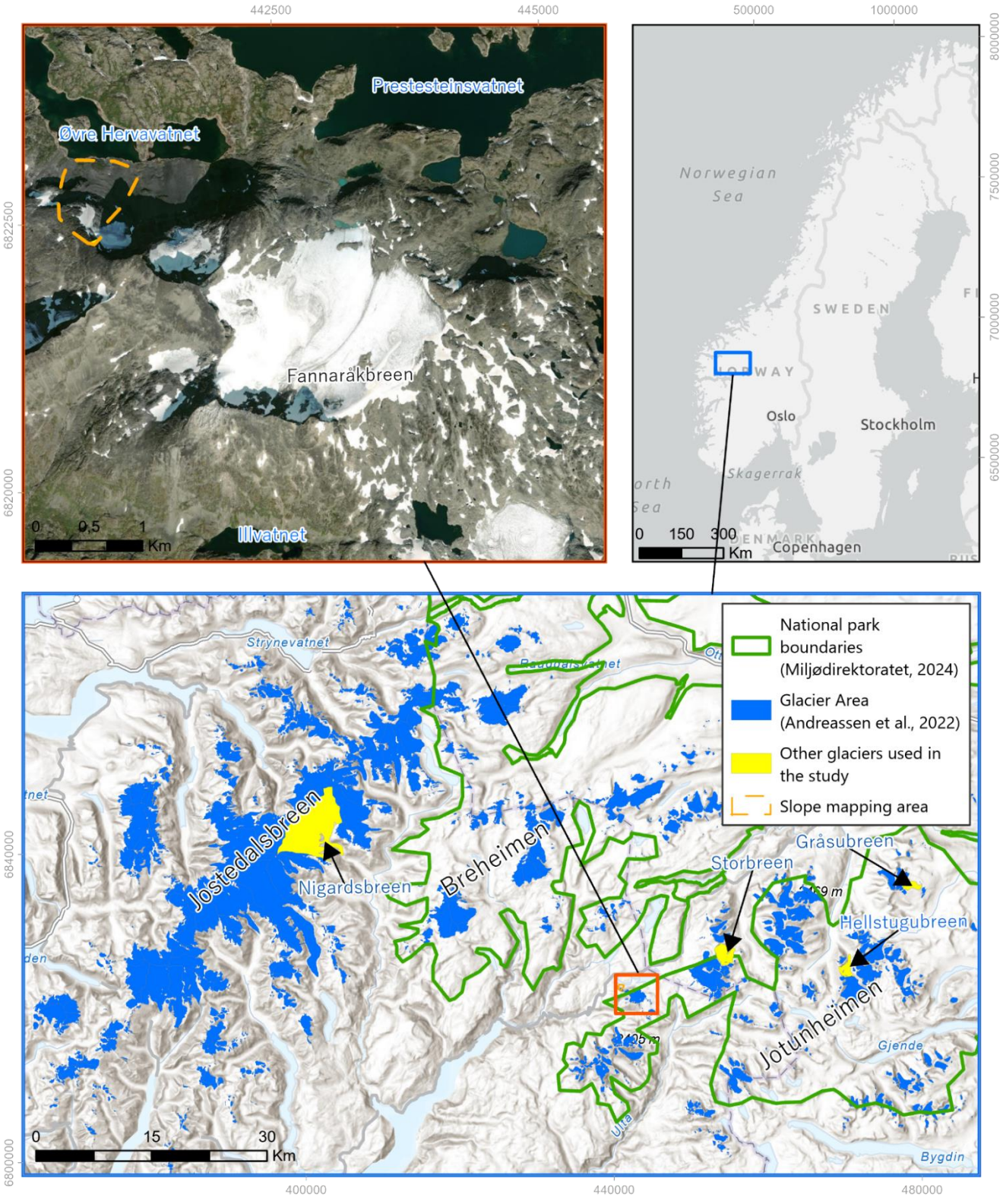

Figure 3.1: A map over the study area in the geographical context of the region in central southern Norway. The measurements of other (yellow) glaciers were used to compare the results of Fannaråkbreen in section 7.2..

3.1 Geographical context

The glacier is located just north-east from the Hurrungane massif, which together with the area of Sognefjellet are referred to as the Western Jotunheimen (Winkler et al., 2020). Situated in the elevation range between 1460 and 2500 m a.s.l, Fannaråkbreen has north-east aspect and is surrounded by steep slopes in the south-west - a typical morphology for cirque glacier erosion. A mid-moraine can be distinguished from the patterns of debris on the surface, following the direction of glacier movement (Figure 3.2).

The surrounding terrain is dominated by undulating surface with aggregations of loose blocks as well as continuous bedrock without the cover of loose material. Orthopyroxene gneiss is the bedrock type that dominates the study area, with pyroxene granulite featuring a composition that varies between gabbroic and quartz-monzonitic, along with the presence of anorthosite and amphibole-rich gneiss pockets (Lutro, 2002).

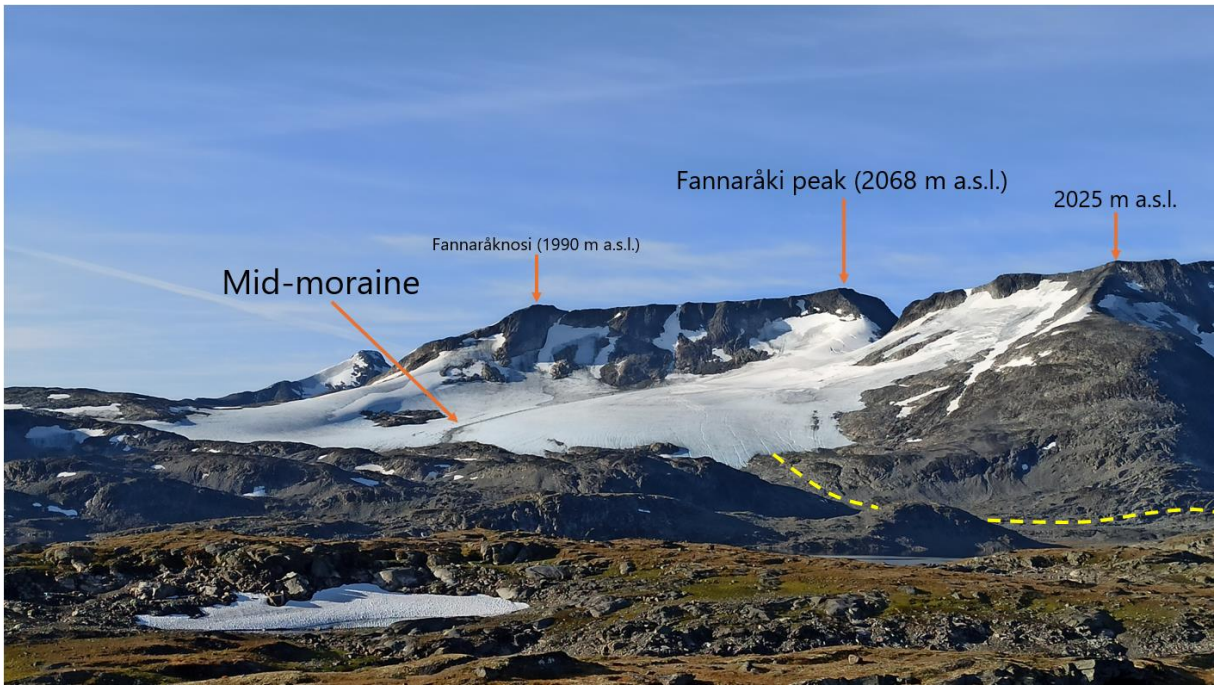

Figure 3.2: Figure showing Fannaråkbreen's mid-moraine and heights of the surrounding peaks. Yellow dashed line marks the route used to access the glacier.

The glacier drains through two main meltwater streams to the dam Prestesteinsvatnet, where water is further directed towards the dam overflow routed towards the Øvre Hervavatnet (Figure 3.1). The first stream drains directly to the dam (in close proximity to the dashed yellow line), the other leading meltwater through the series of smaller lakes.

Fannaråkbreen is located approximately 12,5 km south-west from Storbreen in Leirdalen valley, with an area of 4.9 km^2, at an altitude between 1420 and 2091 m a.s.l. Fannaråkbreen and Storbreen are both of similar size, ranging between similar ranges of altitude and having the same north-east aspect. Storbreen is a Norwegian glacier that has had its length measured since 1902 and annual mass balance series are available since the 1949, making it a glacier with the second longest continuous mass balance records in the world, after Storglaciären in Sweden (NVE, 2023).

3.2 Climate

The local climate in the study area is largely influenced by Norway's general weather patterns that are related to country's coastal position and steep topography, with most of the precipitation being frontal in the autumn and orographic in summers (Andreassen et al., 2012). The North Atlantic (NAO) and Arctic (AO) oscillations, as well as the mountain range called the Scandes and stretching north-south direction, are the main factors influencing this pattern.

The NAO is defined as a variation in difference of the sea level pressure between the Icelandic low and the Azores high in the Atlantic Ocean, not showing any systematic trends in the pattern (Hanssen-Bauer, 2015). High positive NAO or AO index values are higher, they show to high low-pressure activity in the northern seas that bring mild temperatures to the coast and snow to maritime glaciers, while negative values result in the opposite – lower winter temperatures and less precipitation. In Norway, these weather systems influence the main wind direction, which is west (Hanssen-Bauer & Førland, 1998; Nesje et al., 2000).

The mild and moist air masses brought by the westerlies after reaching the coast and the mountain range in south-west (area of Jotunheimen) are orographically lifted, where condensation occurs due to lower temperatures, resulting in 8% more precipitation every 100 meters of elevation (Sælthun, 1973; Haakensen, 1989; Dahl & Nesje, 1992; Dahl & Nesje, 1994). According to the data from period between 1971 and 2000, most of the precipitation (3500-4000 mm annually) is received by lower western areas with more than 5000 mm being modelled to fall within glacier areas at higher elevations (Figure 3.3c). Due to proximity to the ocean, the average temperatures between the coldest and the warmest months differ by only between 10 and 15 °C in coastal areas (Figure 3.3a, b) (Hanssen-Bauer, 2015).

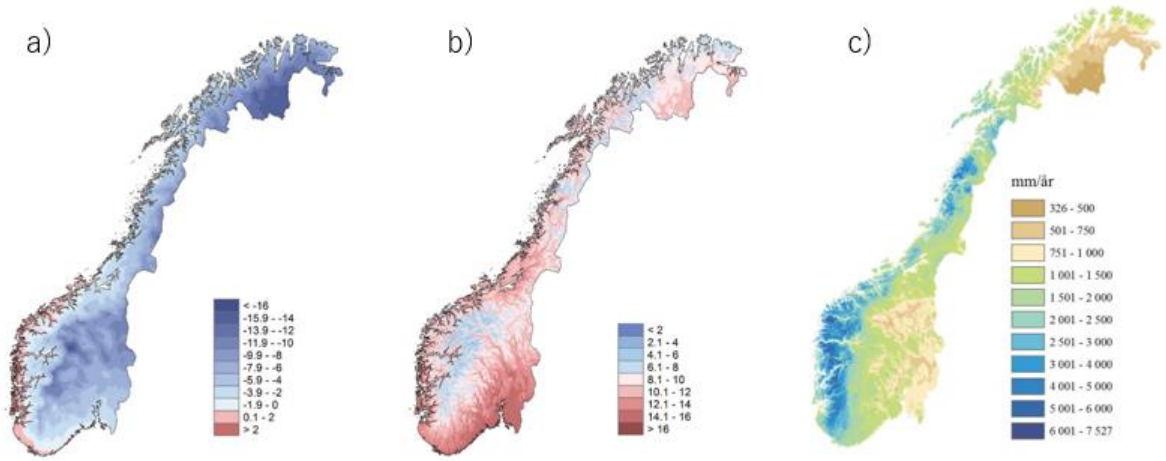

Figure 3.3: Mean annual climatic values for Norway, in the period of 1971-2000. a) mean annual winter temperature (°C), b) mean annual summer temperature (°C) and c) mean annual precipitation (mm) (figures from Hanssen-Bauer et al., 2015).

The conditions in the study area are regarded as transitional, where oceanic climate of the south-west changes towards more continental eastern, with more pronounced differences between the highest and the lowest temperatures throughout the year. This is indicated by the trend in precipitation data showing dryer conditions west-east direction, with Hurrungane massif in the west receiving up to 2000 mm, Galdhøpiggen further east - 1500 mm and Veodalen even further east, only up to 1000 mm of precipitation annually. The temperature and precipitation records also demonstrate Jotunheimen's role in creating a rain shadow effect over eastern areas such as Lom and Skjåk (Winkler et al., 2020).

3.2.1 Implications on glaciers

These climatic patterns, especially the west-east temperature-precipitation gradients that show a transition from strong oceanic conditions towards continental, are of high influence with regards to glacier distribution and the boundary of the regional equilibrium-line altitude (ELA). The distribution of this line where glacier net mass balance is equal to zero, has been modelled for southern parts of Norway based on the relationship established by Liestøl (Figure 3.4a) (Lie et al., 2003b). Considering the factors that the relationship is based on, the regional ELA has been estimated to be located between 1200 m a.s.l. in coastal areas and 2000 m a.s.l. towards Jotunheimen and even higher further east, intersecting with the largest country's plateau glaciers validating this model (Figure 3.4b) (Liestøl, 1967; Lie et al., 2003b).

The west-to-east pattern of the ELA can be explained by the mild westerlies that in combination with orographic uplift, result in sufficient amounts of snow in the winter season

allowing glacier formation at lower altitudes than in more continental areas, while changes in the south-north directions can be ascribed to topography that influences orographic uplift (Lie et al., 2003b). According to the model, the climatic ELA at the study area is at around 1900 m a.s.l.

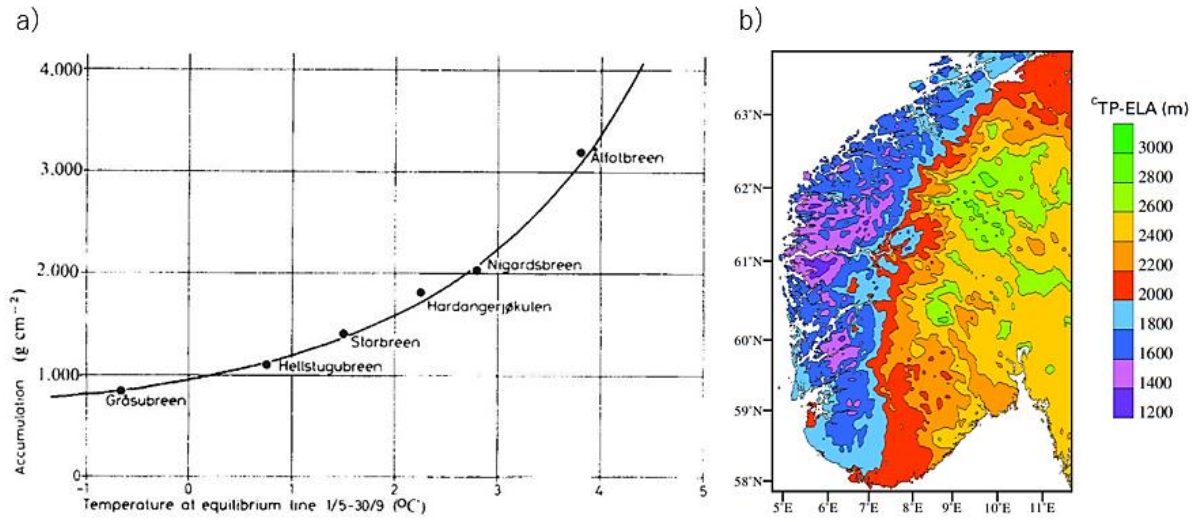

Figure 3.4: a) An exponential relationship between temperature and precipitation of the ablation season at the ELA (Liestøl in Sissons, 1979), b) Map that symbolises the climatic (over 30 years) Temperature-Precipitation ELAs (°TP-ELAs) estimated for southern Norway (figure from Lie et al., 2003b).

3.2.2 Local weather data

Weather stations in the vicinity of the study area as seen in the Figure 3.5 are Fannaråki (2026 m a.s.l.), Sognefjellhytta (1413 m a.s.l.) and Hervavatn (1304 m a.s.l.) (Norsk Klimaservicesenter, 2024). The measurements at Fannaråki summit at the top of the glacier started in 1932 and were terminated in 1978. The data from this station has to be handled with caution due to the fact in mind that it had been influenced by the conditions specific to the area (Winkler, 2001). Three months after the closure of the nearest station, the Sognefjellhytta station just below the glacier was opened and has been recording air temperature and precipitation until today.

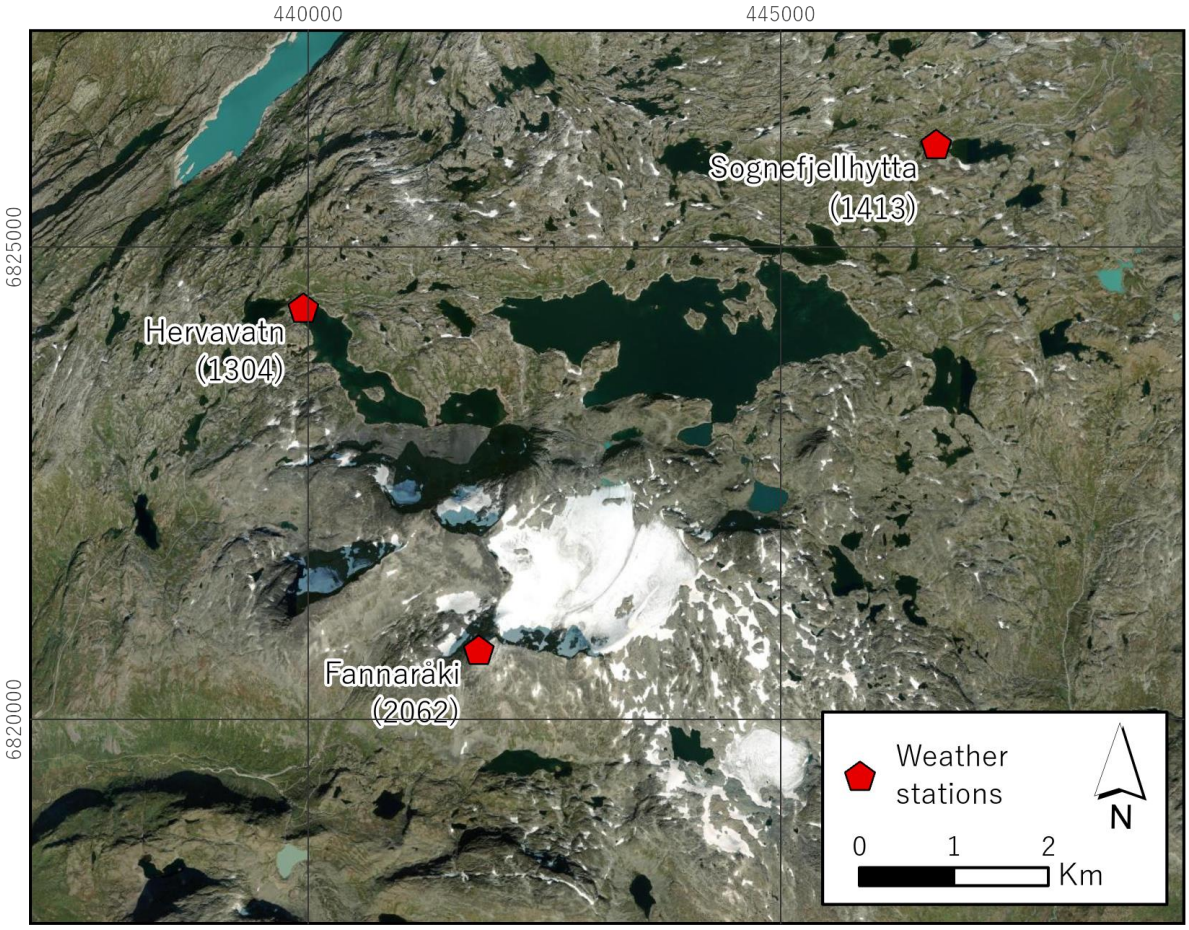

Figure 3.5: A map of the closest weather stations and their altitude (background imagery source from Earthstar Geographics in ArcGIS Pro).

Except for the period from September 2012 to January 2014, there is no overlap in the data from Fannaråkbreen and Sognefjellhytta; this includes extended periods of missing data (Table 3.1). The same situation applies to the Hervavatn station. Thus, instead of utilising data from the local climate stations, weather information for the study area has been extracted from *seNorge_2018* interpolation by Lussana et al. (2019), covering the entire country for the time period between 1957-2023 (see section 4.4). The existing overlap of temperature data from Fannaråkbreen and Sognefjellhytta stations has been used to establish the temperature gradient specific to the study area, which is -0,4°C/100 m, agreeing with the regional laps rate of 0,42 °C decreasing every 100m (Aune, 1993).

Table 3.1: An overview of the local weather stations with elevation, variables measured with regards of temperature and precipitation and time period the data is available for (Norsk Klimaservicesenter, 2024).

Station name	Elevation (m a.s.l.)	Variables	Data from	Data until
Fannaråki	2062	Temperature Precipitation	1932-08-01 / 2012-08-31 1932-08-01	1978-08-31 / 2014-02-05 1978-08-31
Sognefjellhytta	1413	Temperature Precipitation	1978-12-01 1978-12-01	Until now Until now
Hervavatn	1304	Temperature Precipitation	2018-12-04 2022-11-19	Until now 2023-07-31

3.3 Previous research from the area

The study by Matthews et al. (2000) analysed two sediment cores from Smørstabbtinden area in central Jotunheimen (the location of Storbreen) with a goal to learn about glacier fluctuations throughout the deglaciation period of the Holocene. In another study by Matthews (2005) lichens were used to date moraines from the LIA in 16 different areas in Jotunheimen and it was found that the moraines formed during 12 distinct events.

A later study by Hormes et al. (2009) utilised a sediment core from Nedre Hervavatn, one of the lakes in the lake system that Fannaråkbreen drains through. The sediments were used to radiocarbon date utilising a wiggle-match technique to assess minor changes in the environment that took place between 9750 and 1180 cal BP, identifying three episodes of large volumes of meltwater.

The moraines in area of Styggedalsbreen, Hurrungane (just south-west for Fannaråkbreen) has been investigated by Shakesby et al. (2020) to determine climatic fluctuations during the Erdalen Event (approx. 10.2 – 9.7 ka). Three different techniques for dating were applied on several ridges providing chronology of the events, and together with ELA estimations for Styggedalsbreen, showed to high glacier sensitivity to environmental changes. It has been concluded that climatic fluctuations during this event were more complex than previously assumed.

A remote sensing glacier inventory using Landsat imagery for the entire Jotunheimen has been conducted by Andreassen et al. (2008). Glacial changes that occurred between the 1930s and 2003 were assessed, utilising glacier outlines derived from previous investigations in the 1960's and 1980's. The results showed an overall glacier retreat, with an exception being some glaciers, showing to differences being highly individual.

4. Data

In this study, several different data sources were utilised to derive glacier surface information. This includes historical analogue and newer digital photographs from the archives of Norwegian Mapping Authority (Kartverket), a LiDAR derived elevation model and UAV imagery acquired during three fieldwork sessions in the study area. Other data utilised in this analysis encompassed climate values extracted for the study area from the interpolation datasets, information on the geoid height (difference between two datums) and base station corrections used for georeferencing of the field data.

4.1 Historical imagery

The archive of historical aerial imagery owned by Norwegian Map Authority (Kartverket) consists of images with some sets covering just parts or the entire country since the 1930's, acquired with a goal for them to be used for mapping (Kartverket, 2024b). A total of seven sets of archival aerial imagery over the study area have been suitable for this study (Figure 4.1).

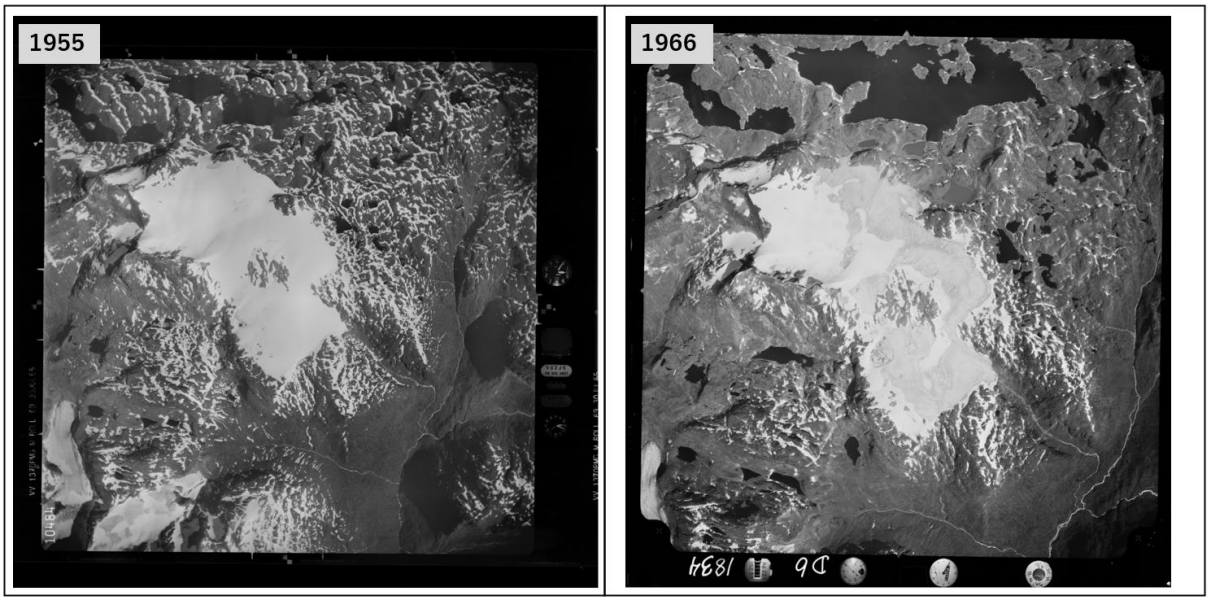

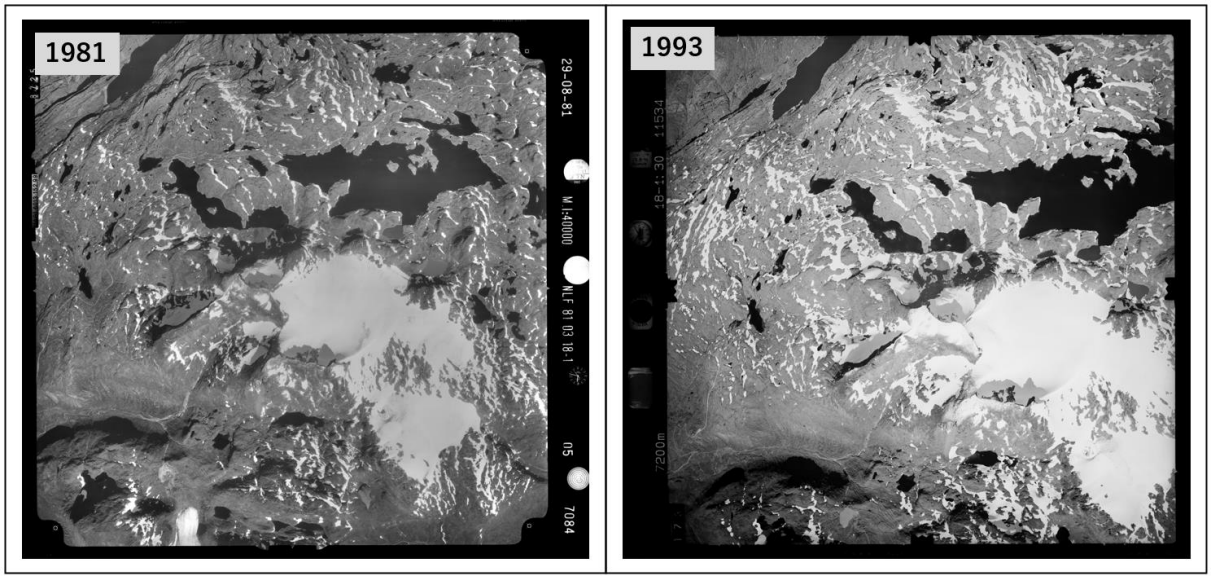
1981
29-08-81
1993
7200m

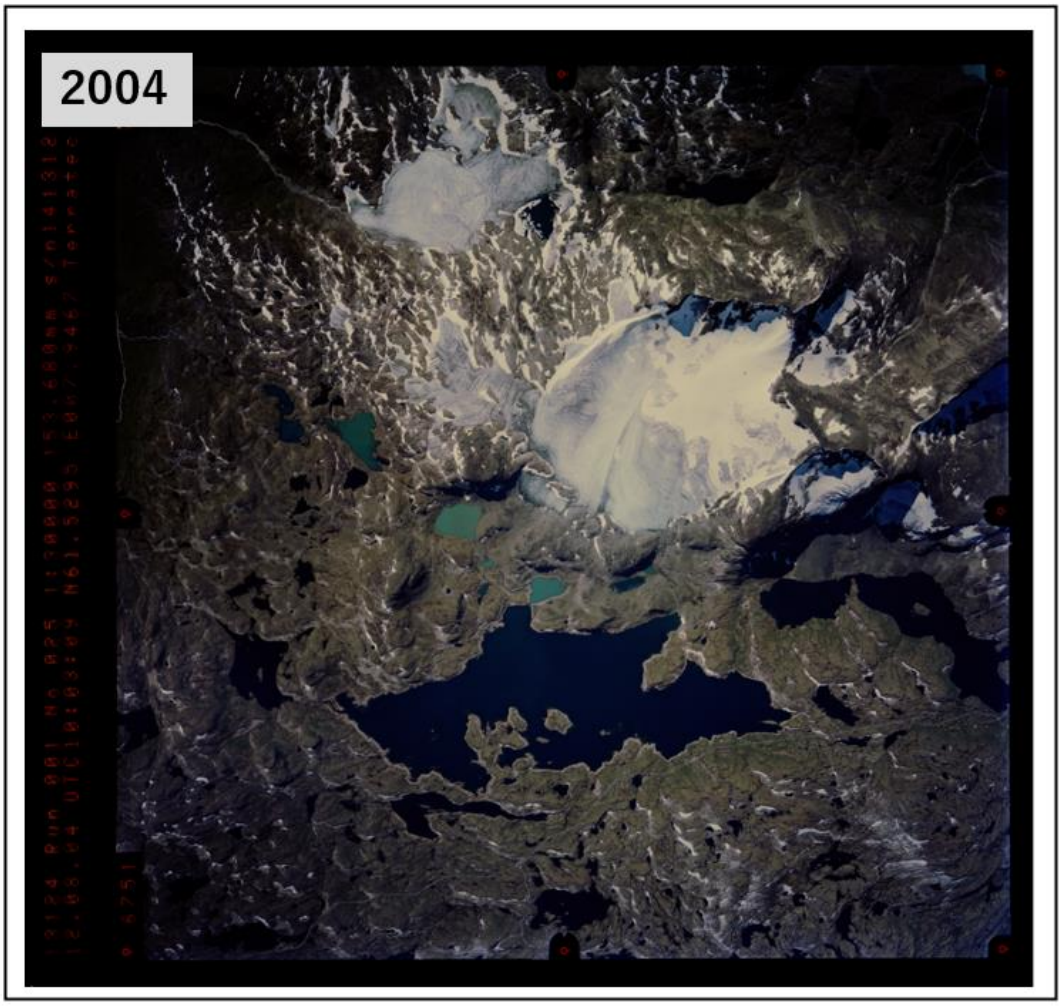
2004

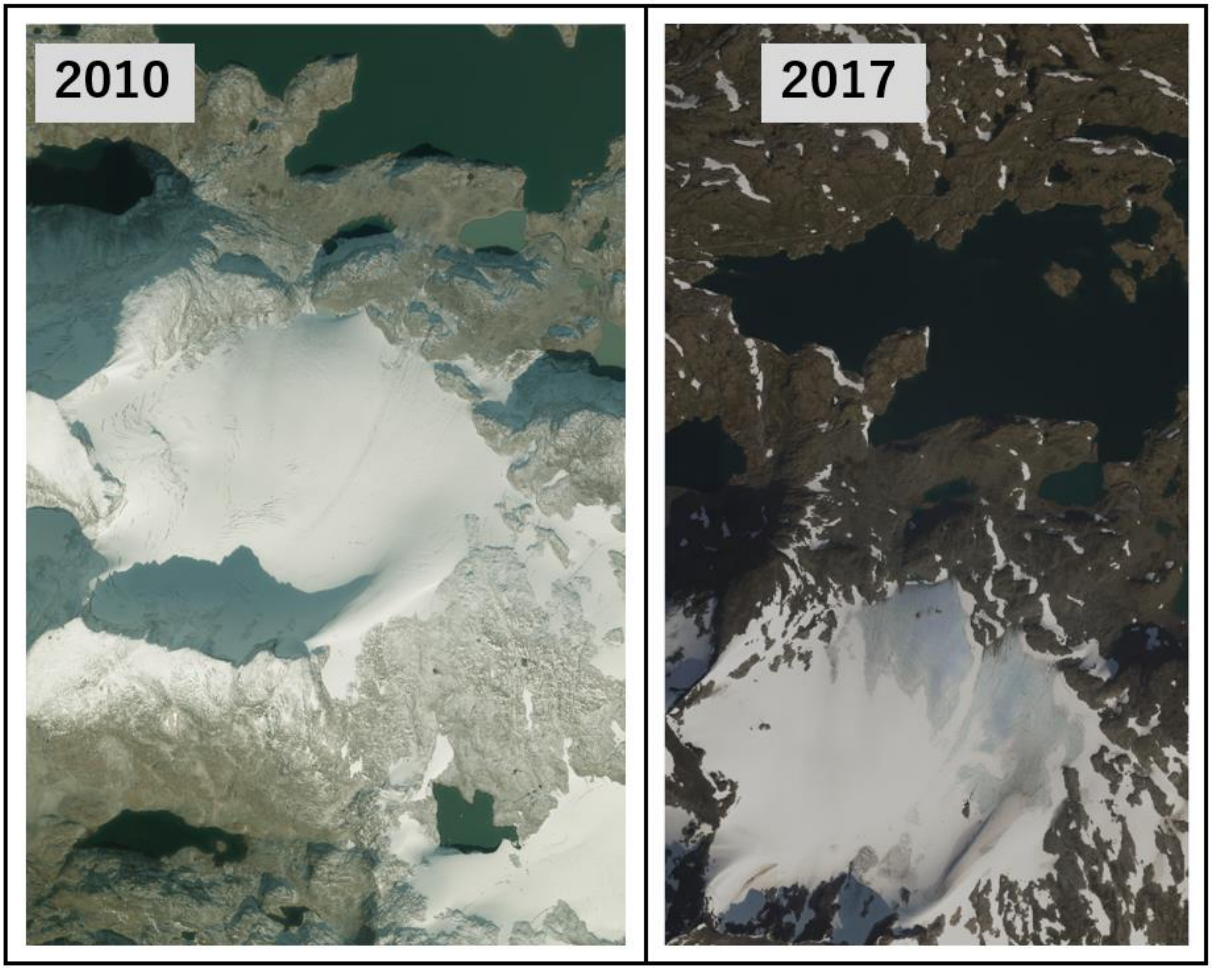

Figure 4.1: Examples from each scanned, raw set of historical aerial imagery over the study area. The scale in these images is not uniform and since they are not orthorectified, distortions are present. Photographs from 1955-2004 (four black and white and one in RGB) have data frames with additional information such as flight altitude or image number on one of the edges and fiducial marks either in corners or on edges, representing image boundaries.

All image sets have calibration reports that include detailed information, such as focal length and radial distortion required for solving image orientations in photogrammetry. The oldest images are from 1955, surveyed by the US Army Map Service (AMS) covering southern parts of the country. Images from 1981, 2004, 2010 and 2017 have been previously digitized and published in Norgeibider (Kartverket, 2024e). However, all images were delivered in raw format, not spatially referenced. Due to high snow and ice albedo, image scans of darker exposure have been provided for the sets from 2004 and 2017. The information of each set is summarized in Table 4.1.

Table 4.1: A summary of the historical aerial photograph sets used in the study with information of the date images were taken, flight operator, amount of images available over the study area, scale or/and spatial resolution, flight and the main products that were extracted during processing.

Date	Project name and operator	Number of photographs	Scale/ Resolution	Product
1955	US Army Map Service (AMS)	3	1:50 000	Orthomosaic
1966-07-26	WF-1834 (Widerøe's Flyveselskap AS)	2	1:28 000	Orthomosaic, DEM
1981-08-28	NLF-07084 (Norsk Luftfoto og Fjernmåling)	2	1:40 000 0.4m	Orthomosaic, DEM
1993	FWG-11534 (Norsk Luftfoto og Fjernmåling)	1	1:40 000 0.4m	Orthoimage
2004-08-12	TT—13124 (TerraTec AS)	3	0.5m	Orthomosaic, DEM
2010-09-27	BG-BNO10044 (Blom AS)	6	0.5m	Orthomosaic, DEM
2017-09-23	TT-14233 (TerraTec AS)	12	0.25m	Orthomosaic, DEM

4.2 Digital Elevation Model from Høydedata

To cover the year 2020, a freely available DTM based on airborne LiDAR data had been downloaded from Høydedata (Kartverket, 2024d), under the project *NDH Jostedalsbreen 2pkt 2020* (2pt/m^2). The data was acquired by TerraTec AS as a part of an undergoing initiative to generate a detailed national elevation model of Norway. The scanning took place in the month of August, with elevation accuracy of 0.1 m being referenced to the Norwegian vertical datum NN2000 (Kartverket, 2020a).

4.3 Field data (UAV)

To capture seasonal glacier surface elevation changes, the area has been visited in total of three times (refer to Table 4.2 for summary). The data collected in field was UAV imagery, acquired over the whole glacier area covering some surrounding stable ground for generation of DEMs and orthoimages of the glacier. To maintain ground sampling distance as constant as possible, terrain following feature was employed for all flights (e.g., Karušs et al., 2022). Automatic camera capturing was used with endlap of at least 70% and sidelap of at least 30% for each acquisition.

The first survey took place at the end of the ablation season, on the 20th of September 2022, the second took place on 17th of June 2023 and the third on the 6th of September 2023. The first flight was carried out automatically using a third part-app Map Pilot Pro (Maps Made

Easy, 2024) with a connection of an iPad, while the other two missions were planned using the software integrated into the UAV controllers. The geospatial information for the data from the first survey was enhanced via a collection of virtual GCPs referenced to the LiDAR dataset form 2020 during processing (further details are found in section 5.1.2). However, due to cold temperatures and slight wind, power became an issue, resulting in incomplete first coverage of the glacier surface at the highest altitudes, with some steepest parts missing. In June 2023, the imagery was referenced employing an RTK (DJI D-RTK base station) (Figure 4.2a, b), while the data from the final acquisition in September 2023 (Figure 4.2c) employed WingrtaHub software for PPK correction (explained in section 2.4.4), based on the data from a base station located in Årdal (Figure 4.3).

Table 4.2: The summary of UAV missions showing flight dates, the type of UAV used, image spatial resolution and number of images taken during each survey.

Flight date	UAV type	Sensor	Resolution (m)	Number of images	Location source
2022-09-20	DJI Mavic 2 Pro	Hasselblad 1" CMOS 20 MP	0.07	1165	GCPs
2023-06-17	DJI Mavic 3 Pro	Hasselblad 4/3 CMOS 20 MP	0.05	1384	RTK
2023-09-06	WingtraOne	RGB61	0.06	1847	PPK
Slope mapping					
2023-09-06	DJI Mavic 3 Pro	Hasselblad 4/3 CMOS 20 MP	0.018 (ortho) / 0.03 (DJI Smart Oblique)	338 (ortho) / 889 (DJI Smart Oblique)	RTK

Image acquisition for the comparison of slope mapping methods took place in June 2023. The location data for the images from this acquisition were corrected with RTK, utilising Continuous Positioning System (CPOS), real-time positioning service for direct referencing provided by Kartverket, accessed via a subscription. Utilising the network of permanent base stations and the user's location, CPOS established a virtual reference station (VRS) which was then used to correct the position information of the UAV for each image captured (Kartverket, 2023). Permanent base station positions are shown in Figure 4.3b.

Figure 4.2: Photographs taken during fieldwork. a) Landing of the DJI Mavic 3 Pro with field assistants in June 2023; b) snow covering large areas, looking down from the glacier; c) the survey UAV Wingtra One used in September 2023 with Fannaråkbreen in the background; d) after the acquisition of slope data with DJI Mavic 3 Pro during the last field visit, the mapped area is marked with dashed yellow line.

4.4 Climate data

Since there were large gaps in in the climate data from local climate stations (the same problem was experienced by Andreassen and Oerlemans (2009)), values for air temperature and precipitation for the period 1957 – 2023 were extracted for the glacier area from the interpolation dataset *seNorge_2018* v. 23.09 instead. This is the latest version, reviewed and updated using the newest datasets and modelling methods (Lussana, 2020, 2021). The average monthly temperature and precipitation datasets for the whole country are available through the Norwegian Meteorological Institute's *Thredds Data Server* (MET, 2023, 2024c, 2024b, 2024a). The datasets were downloaded in the *NetCDF* format and handled in ArcGIS Pro as multidimensional datasets for extraction of the interpolated meteorological values over the study area.

4.5 Elevation reference and base station data

The model of elevation difference between the datums EUREF89 and NN2000 was utilized to correct the values of DEMs derived from UAV data to make them comparable to the LiDAR dataset, referenced using NN2000 vertical datum (orthometric height). The difference model

(Figure 4.3a) was provided via national database for geographic data Geonorge (Kartverket, 2016).

To correct the geospatial information from the last acquisition (as mentioned in section 4.3), data from Årdal base station belonging to Kartverket was used. It is available via a subscription through their service ETPOS (Kartverket, 2024c) and was downloaded from their platform available at https://etpos.kartverket.no/.

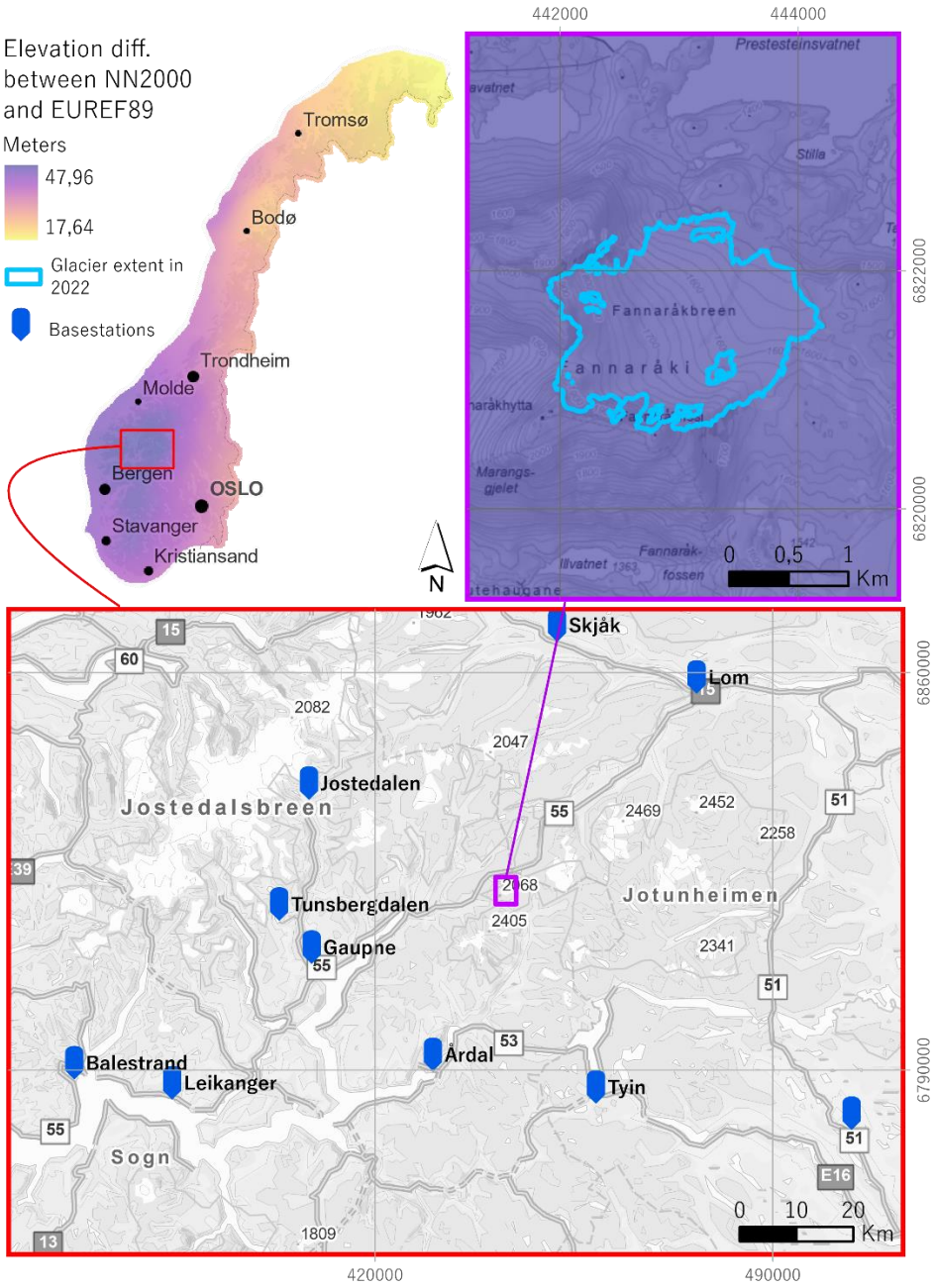

Figure 4.3: a) A map illustrating elevation differences between the two datums used for data acquisition in this study (EUREF89 (ellipsoidal) and NN2000 (orthometric, relative to sea-level)). The area of interest falls within the area of the highest difference; b) a map showing the locations of Kartverket's permanent base stations used along with CPOS service (basemap: Geodata AS, et al. 2024. Data: Andreassen, Nagy, et al., 2022; Kartverket, 2024a).

5. Methods

Several different approaches have been utilized with the goal to assess the mass balance of Fannaråkbreen. The methodology presented in Figure 5.1 includes photogrammetric data pre-processing techniques to extract elevation values and generate glacier elevation models, followed by their utilisation for calculation of mass balance.

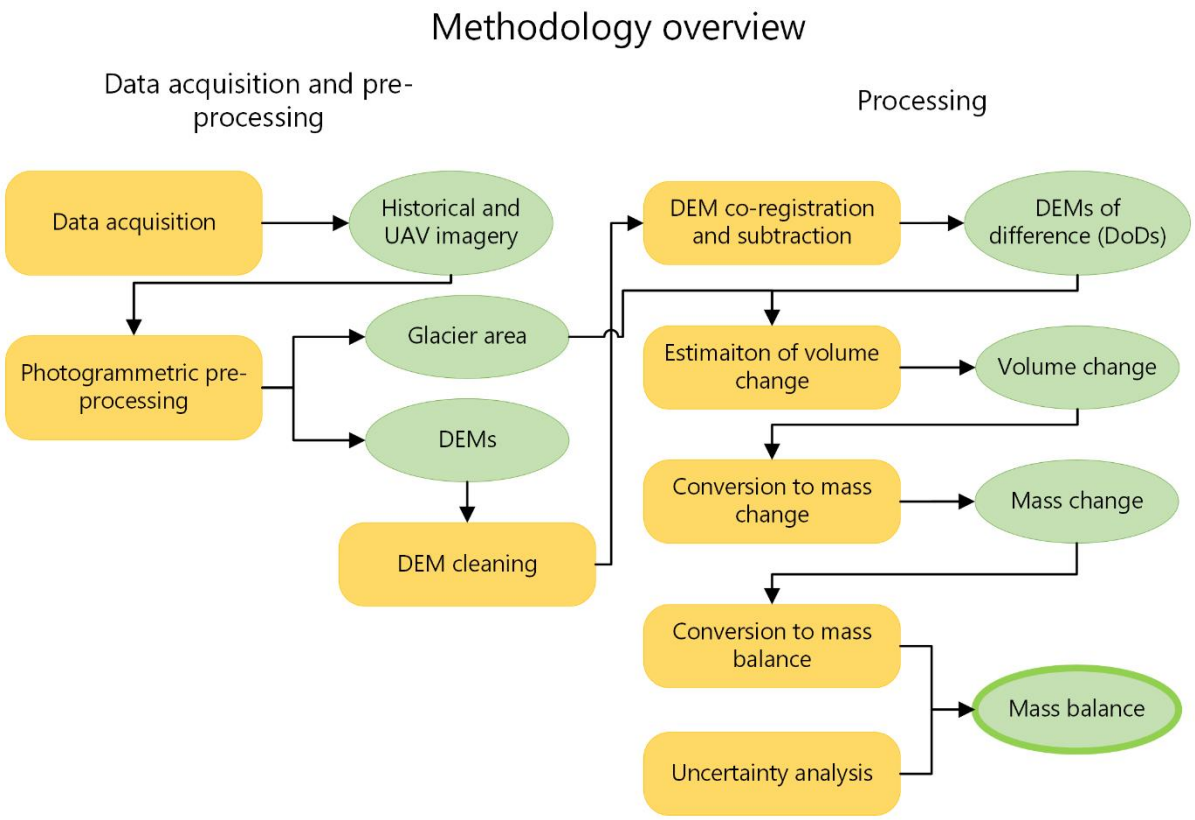

Figure 5.1: Chart representing the methodology and workflow, illustrating the main steps to generate DEMs and further DEM processing for quantification of glacier surface change and mass balance.

5.1 Generation of digital elevation models

In this study, a DEM subtraction method was applied to estimate glacier surface change, requiring several steps. Initially, aerial imagery was acquired from Kartverket and via three UAV missions in the study area (section 4.3). An additional pre-processing step was required for the latest glacier data, during which the image geolocation was corrected using the PPK technique, applied with the software WingtraHub, following the procedure suggested by the producer (Wingtra Knowledge Base, 2024).

The DEMs were generated using photogrammetric (section 2.4) approaches. The main outputs (DEMs of difference) for estimating glacier mass change were produced by differentiating between aligned DEM pairs (section 5.2.1) and removing linear and non-linear biases that

were still present in the surface models after the co-registration. Lastly, the accuracy was quantified to determine the overall uncertainties associated with the outputs.

5.1.1 Photogrammetric image processing

To calculate the mass balance for Fannaråkbreen for the period of 57 years, two photogrammetry approaches were applied to the data. Archival analogue aerial photographs were treated using conventional digital photogrammetry in CATALYST Professional OrthoEngine software, v. 222.0.3 (CATALYST.Earth, 2024a), a workflow summarised in Figure 5.2.

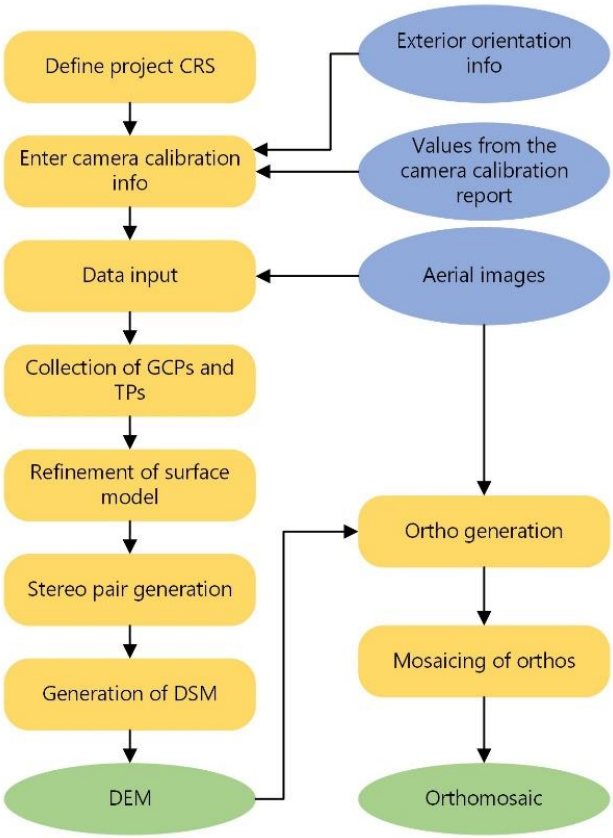

Figure 5.2: The photogrammetry workflow used for analogue images in CATALYST OrthoEngine. Blue and green ovals represent inputs and outputs respectively, while yellow rectangles depict processes.

The inner orientations for all historical images were solved by inserting camera parameters from the calibration reports, such as PPO (Principal Point Offset), PPA (Principal Point of Autocollimation), PPS (Principle Point of Symmetry), FL (Focal Length), lens distortion parameters and coordinates of the fiducial marks (CATALYST.Earth, 2024c). Next, the model's projection was established, and the positions of the fiducials located on image frames were identified, setting the boundaries of the data. In the next step, image tie points (TPs) were acquired automatically using different methods available within the software, allowing alignment of image frames using bundle adjustment. In the following step, image georeferencing took place by sampling GCPs from the georeferenced 2017 orthomosaic and LiDAR DEM from 2020 (both available at Kartverket, 2024d). This was done by pinpointing identical stable terrain features in both the reference materials and the dataset being referenced, entering their horizontal and vertical coordinates to the software, what also improved the relative model orientation. After the collection of virtual GCPs, more tie points were collected and the ones having the highest root mean square error (RMSE) values were

removed, further improving overall model accuracy. The Table 5.1 shows a summary of the number and RMSE values for the TPs and GCPs.

Table 5.1: The summary of tie points (TPs) and ground control points (GCPs) and their horizontal and vertical root mean square error (RMSE) for each dataset processed in CATALYST OrthoEngine (given in meters).

Year	No. of TPs	No. of GCPs	TP RMSE, x-axis	TP RMSE, y-axis	TP RMSE z-axis	GCP RMSE, x-axis	GCP RMSE, y-axis	GCP RMSE z-axis
1955	264	10	1.383	3.238	1.292	4.090	2.924	11.410
1966	285	12	0.036	0.117	0.052	0.639	0.876	5.312
1981	1460	10	0.080	0.173	0.071	0.844	0.834	3.796
1993	25	9	0.055	0.351	0.142	0.791	0.713	-
2004	987	10	0.065	0.083	0.036	0.695	0.866	5.124

CATALYST OrthoEngine uses epipolar images to automatically generate DEMs. Blending was used as mode for combining these epipolar images. Based on visual interpretation, the NCC (Normalised Cross Correlation) method appeared to produce better results than SGM (Semi-Global Matching). All four datasets yielded DEMs with 1 meter of resolution along with a *.tif* file with the information of data quality for each pixel (image score), later used to remove erroneous values (see section 5.1.3).

In the final stage of photogrammetric processing, orthomosaics were generated applying the Ortho and Mosaic tools available at the CATALYST software. The best image merging method appeared to be “Minimum Squared Difference”, while “bundle” worked best for balancing image colours and cubic convulsion appeared to be the most optimal approach for resampling.

With regards to scanning, the photographs from 1955 were of the poorest quality of all historical image sets. In addition to them being of the smallest scale, they did not yield a DEM of sufficient quality for mass balance estimations, however, they were still suitable for mapping of the glacier area. Moreover, the image set from 1993 was not suitable for DEM extraction due to insufficient overlap between the photos over the glacier area and was solely used for digitizing the glacier area for that specific time period (for output summary refer to Table 4.1).

5.1.2 Structure-from-motion photogrammetry

The digital photographs from Kartverket (2010 and 2017) along with UAV imagery from the last two UAV acquisitions were processed with Agisoft Metashape Professional v. 2.0.2 (Agisoft LLC, 2024), while the data from 2022 was processed with Pix4D Matic v. 1.58.1 (Pix4D, 2020) to obtain glacier surface elevation data. Since these datasets contained several more images, the largely automated SfM photogrammetric method proved to be more suitable than conventional photogrammetry that treats each image individually.

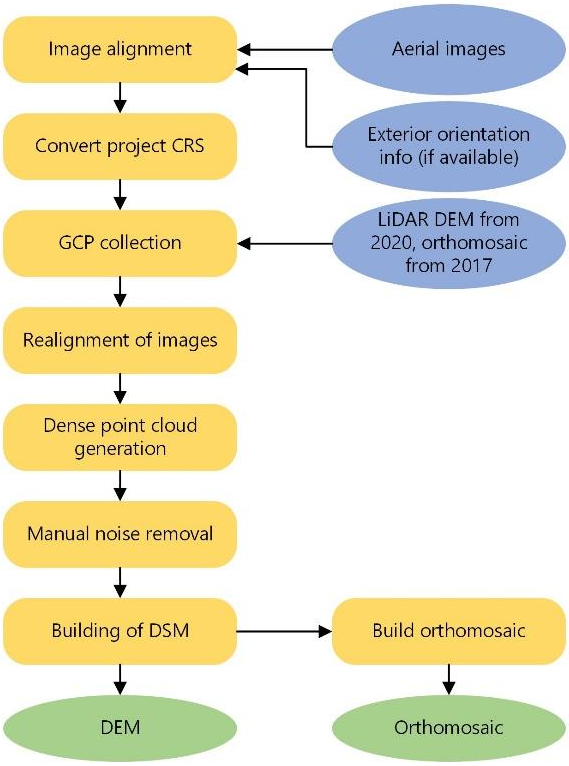

Figure 5.3: The workflow of Structure-from-Motion photogrammetry for digital images processed in Agisoft Metashape Professional. Blue and green ovals represent inputs and outputs respectively, while yellow rectangles depict processes.

This approach reads image metadata containing the geospatial and orientation information automatically. In the first step of the workflow (Figure 5.3), it is utilised for generation of sparse (tie-point) cloud during image alignment (Figure 5.4a) to establish image locations using feature matching across overlapping images. For photographs from 2010 and 2017, this data was input manually from the text files that followed these datasets and additional virtual GCPs were collected in the same manner as described in the previous section 5.1.1 with the goal to improve the absolute accuracy. GCPs, also referenced to the LiDAR DEM were accommodated for the UAV imagery from September 2022, what after performing realignment function, substantially lowered the residuals. Images captured in 2023 were georeferenced directly using dGNSS and PPK, eliminating the necessity for GCPs. In the next step, dense point cloud (Figure 5.4b) was generated for each of the five photosets with the quality parameters set to very high, depth filtering set to mild.

In the last step, DEMs (Figure 5.4c) were extracted automatically from the dense point clouds alongside with orthomosaics (Figure 5.4d). The DEM generation was performed without allowing interpolation to only keep only the measured data points. The resulting voids were later filled using more glacier appropriate methods described in 5.2.3. The imagery from 2010

produced DEMs with 0.3 m, and 2017 with 0.2 m per pixel, while UAV data yielded DEMs between 0.05 and 0.07 m of spatial resolution.

Table 5.2: The summary of tie points (TPs) and ground control points (GCPs) and their horizontal and vertical root mean square error (RMSE), given in meters for each dataset processed using Structure-from Motion photogrammetry. Each surface model was generated in Agisoft Metashape Professional except for the 2022-09, which was produced using the Pix4D Matic software.

Year	No. of TPs	No. of GCPs	TP RMSE, x-axis	TP RMSE, y-axis	TP RMSE z-axis	GCP RMSE, x-axis	GCP RMSE, y-axis	GCP RMSE z-axis
2010	27 086	11	0.11	0.24	0.59	0.61	0.92	0.73
2017	433 384	11	0.88	0.70	0.06	0.54	1.28	0.33
2022-09	7 706 859	16	0.17	0.17	0.17	0.651	1.910	1.177
2023-06	1 620 758	0	0.199	0.159	0.317	-	-	-
2023-09	921 885	0	0.093	0.157	0.259	-	-	-

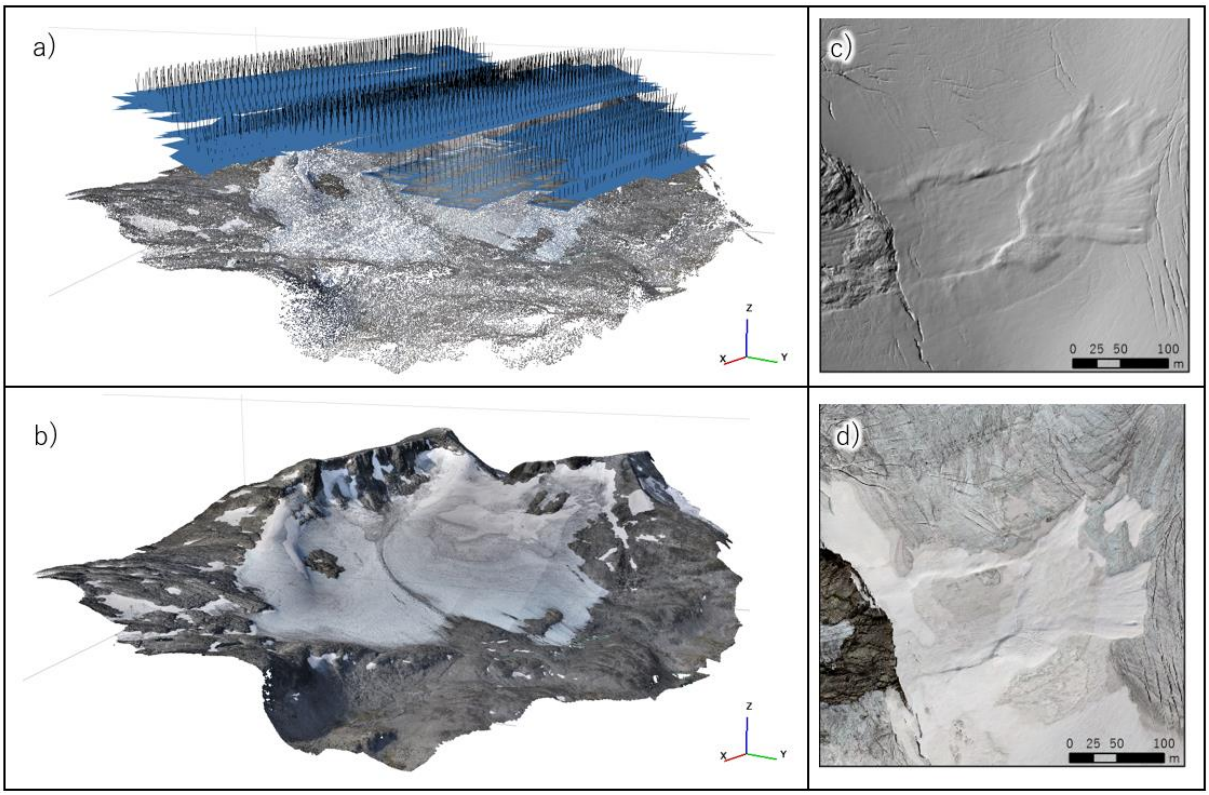

Figure 5.4: The main steps of SfM imagery processing with UAV imagery from September 2023 as an example. a) The first step is feature matching in the overlapping images and the generation of a sparse point cloud representing the initial surface model in three dimensions, as well as camera positions. b) The dense point cloud with colours as recorded in photographs. c) The extracted DEM represented as hillshade generated in ArcGIS Pro and d) an orthomosaic showing the location of a snow avalanche.

5.1.3 DEM calibration and cleaning

During image processing, it has been noted that elevation values between some of the DEMs had a constant mean difference of 47.7 meters over stable terrain. The reason for this were

different vertical datums used for the UAV and LiDAR datasets, with the latter having been used for reference. By default, UAVs utilises WGS84 coordinate system referenced to ellipsoid height (*h*) (NGA, 2014), while Kartverket's LiDAR dataset that has been used for georeferencing of historical data, is referenced to the Norwegian vertical reference frame NN2000 that reads elevation from the geoid, referring to orthometric height (*H*) (Figure 5.5) (Kartverket, 2020b).

The difference between the two is the heigh of the geoid, needed to be subtracted from the ellipsoidal values to estimate orthometric height. Based on the height reference model provided by Kartverket (2016), the value for the area of interest is 47.47 m (see Figure 4.3a). Since the RTK and PPK corrections also utilised the NN2000 datum for vertical referencing, only the UAV dataset from 2022 required adjustment by subtracting this value. This was necessary to account for the difference and facilitate comparison with other datasets.

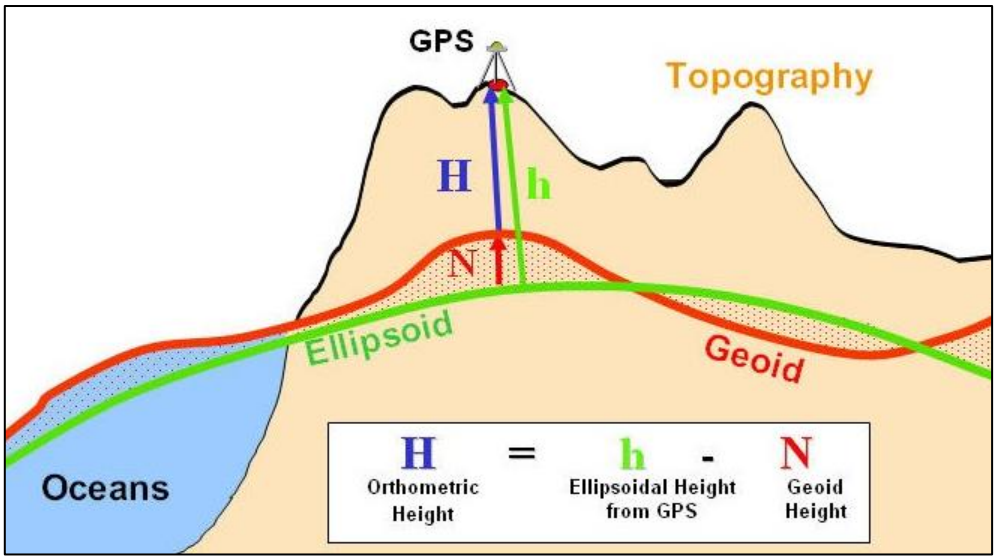

Figure 5.5: An illustration of the difference between vertical reference systems used by vertical datums. The WGS84 datum uses ellipsoidal height (h), whereas orthometric height (H) is measured from the geoid for the NN2000 datum. The difference between them is referred to as the geoid height, which varies across the Earth's crust (figure from Al Shouny et al., 2017).

In addition to correction for the different datums used, pixels with a correlation score of 0 in Figure 5.6b that resulted from low surface contrast seen in Figure 5.6a were removed from the final DEMs. This was accomplished utilising an additional product generated in CATALYST Professional OrthoEngine that holds information on pixel quality. Other areas that visually appeared erroneous in the shaded representation of DEMs were subjects for manual removal. Although interpolated values normally appeared over lakes, areas lacking contrast due to shadows or overexposure, also needed to be removed. It was attempted to remove all interpolated areas from the final DEMs using the additional pixel score product as a mask.

However, a decision to keep some smaller clusters of interpolated values and remove larger manually has been made (as seen in the Figure 5.7 a, b, c), to avoid large gaps being left.

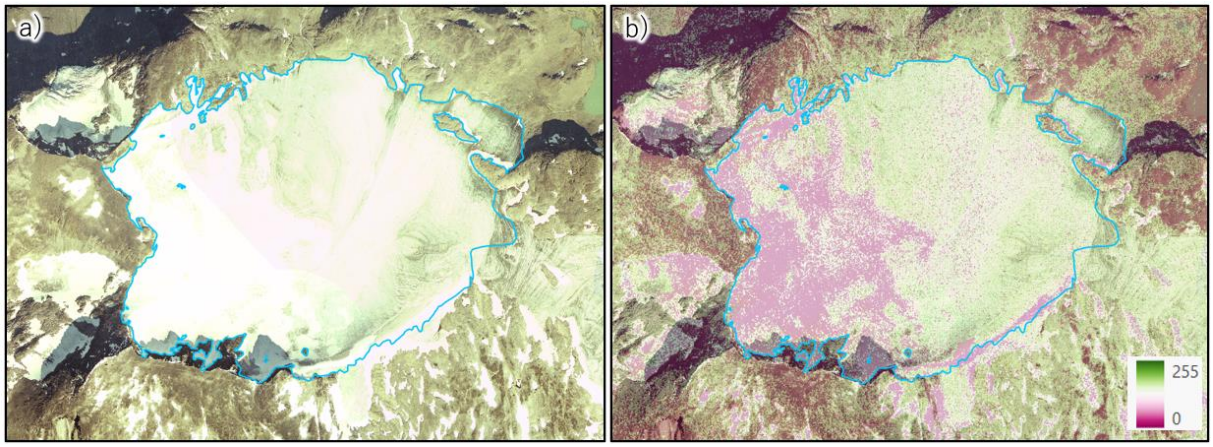

Figure 5.6: a) An orthoimage from 2004; b) a visualisation of the quality of each DEM pixel with 0 showing to pixels with the lowest score which were attempted to be removed. Pixel score is an additional product generated automatically in CATALYST Professional OrthoEngine.

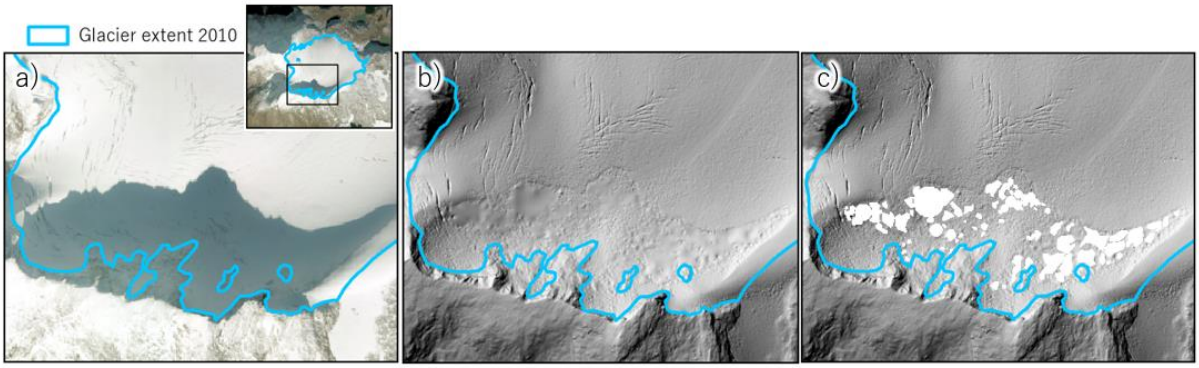

Figure 5.7: Manual DEM cleaning of interpolated areas. a) An orthomosaic of the Fannaråkbreen in 2017 with dark shadows casted on its surface. b) Smooth areas in the corresponding hillshade of the DEM derived from the imagery. c) White regions show to areas that were manually removed from the DEM.

5.2 Assessment of glacier surface change

Having modelled glacier surface elevations for each date, the difference between them was quantified in several steps. The first step involved different approaches for DEM alignment, followed by bias correction for achieving best possible accuracy, and interpolation of the resulting difference DEMs (DoDs).

5.2.1 DEM Co-registration

Glacier surface changes between two DEMs can be estimated by comparing spatially corresponding pixel values (Nuth & Kääb, 2011). First, two DEMs are subtracted and the difference between them over terrain assumed stable is determined (Nuth & Kääb, 2011). If there is no significant difference present, the resulting DoD is the final output and can be

further used for estimation of the average change for the area of interest. However, if elevation differs, a co-registration, or alignment of DEMs along with bias corrections may be necessary (Figure 5.8). The misalignments can be caused due to linear or non-linear systematic errors (biases) that need to be corrected before calculations of elevation change (Nuth & Kääb, 2011), even if inner orientations have already been assessed during the photogrammetric processing. By addressing displacements between two DEMs, accurate absolute orientation can be assured and the risk for elevation changes being affected by unrelated discrepancies across the datasets, can be eliminated.

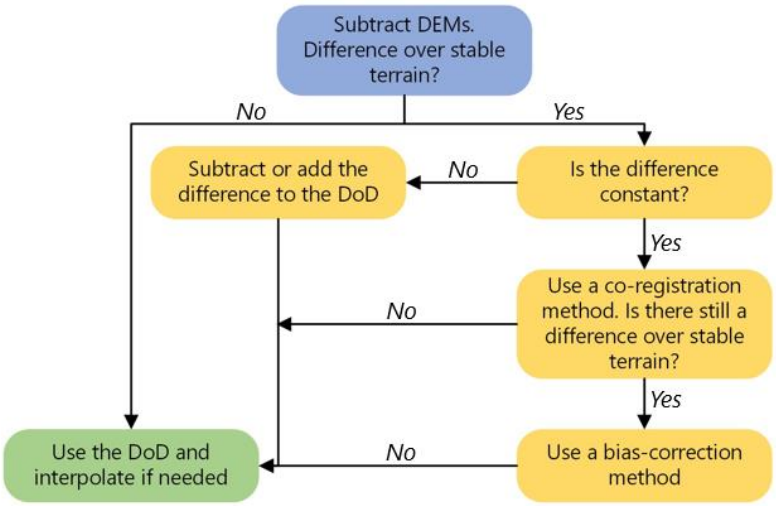

Figure 5.8: A decision tree for generation of a final DEM of difference (DoD). If there is a difference in elevation over what is assumed to be stable terrain, a co-registration and/or bias corrections may be needed. Blue colour represents the initial step, yellow – the decisions that must be made, green – the final step utilising the desired outcome.

To estimate glacier surface change and calculate mass balance for each time period, each pair of succeeding DEMs was differentiated between (Table 5.3) and the bias attempted to be removed using co-registration. This has been accomplished by employing glacier area and snow vector files (the generation of which is described in section 5.3) to exclude unstable ice and snow surfaces. This allowed for the utilisation of various DEM analysis methods available in the xDEM Python toolkit, developed by Mannerfelt et al. (2021). This package provides several methods for DEM co-registration to address bias in stable terrain. It also offers bias-correction techniques, tools for interpolation of DoDs based on glacier hypsometry, and the estimation of mean elevation change and the uncertainty. Other packages such as Anaconda, Numpy, Geopandas, Pandas, Geoutils, Rasterio and Datetime were also utilised in this analysis.

Table 5.3 summarises the co-registration and bias-correction methods that were fitted for each pair. The *Nuth and Kääb (2011)* approach adjusts the position of a DEM that is being aligned by identifying where it is slightly misaligned. It begins with comparing two DEMs to estimate the difference and generate a DoD, followed by a generation of slope and aspect maps based on the DEM used as a reference. These maps together with the DoD are utilised for the generation of a cosine function that is applied to assess offset direction, allowing for horizontally shifting a DEM to better fit the reference. The process repeats iteratively until either the maximum number of tries is reached or the improvement of the normalised median absolute deviation (NMAD), which measures statistical dispersion used to handle extreme elevation values (Höhle & Höhle, 2009), between the DEMs becomes insignificant. Although addressing horizontal biases, this method disregards rotational misalignments.

Table 5.3: A list of all DEM pairs that were aligned, the time period between data acquisitions and methods used for removal of biases using tools available in the xDEM package. N/r – not relevant.

DEM pair for co-registration	Year span	Area reference year	Methods for co-registration and bias removal	Error (m) (median; NMAD)
1966 - 1981	15	1966	Nuth and Kääb + Deramp, 2nd dgr. polynomial	-1.16; 1.98
1981 - 2004	23	1981	Nuth and Kääb + Deramp, 2nd dgr. polynomial	-1.59; 1.89
2004 - 2010	6	2004	Nuth and Kääb	-0.01; 1.56
2010 – 2017	7	2010	Deramp, 2nd dgr. polynomial	0.03; 1.0
2017 – 2020	3	2017	Deramp, 3rd dgr. polynomial	0.09; 0.55
2020 – 2022	2	2017	-	0.78; 1.35
2022 – 2023	1	2022	Deramp, 3rd dgr. polynomial	-0.02; 0.54
1966 – 2023 Sept	57	1966	-	0; 1.70
Season DEMs				
2022 Sept – 2023 June	0.5	2022	Deramp, 3rd dgr. polynomial	-0.02; 0.54
2023 June – 2023 Sept	0.5	2022	Constant bias of -3.64m	Not estimated
Slope DEMs				
Nadir – LiDAR 2020	N/r	N/r	Nuth and Kääb	0.0; 0.01
DJI's Smart Oblique – LiDAR 2020	N/r	N/r	Nuth and Kääb	0.0; 0.13

Instead, *Iterative Closest Point (ICP)* method can perform rotational corrections by treating DEMs as point clouds and adjusting the data multiple times until the best possible alignment

is reached (Besl & McKay, 1992). It compares the points of one DEM to the nearest points of the other, calculates how far off they are and then shifts the DEM to reduce this distance. Similarly to the Nuth and Kääb method described above, the process is repeated until improvements are no longer significant or the iteration limit is exceeded. This method also removes outlier points that do not fit well in order to avoid large errors.

Another method referred to as *Tilt,* accounts for 2-dimensional tilted misalignments by calculating a 1st order polynomial function based on the values of the entire DoD (Mannerfelt et al., 2021). It can account for small rotations or non-linear differences that are not uncommon for DEMs derived using Structure-from-Motion photogrammetry (e.g., Rosnell & Honkavaara, 2012; Javernick et al., 2014; Girod et al., 2017). Lastly, a supplementary function addressing vertical misalignments called *Vertical shift*. This xDEM function adjusts the model that is to be aligned based on e.g., mean or median value of elevation difference and should be used as an addition to another approach (Mannerfelt et al., 2021).

5.2.2 Bias correction

If relocation or rotation of a DEM does not fix the deviation measured over stable terrain, several other methods that include DEM transformations such as scaling, bending or warping in order to reduce or remove the differences between two datasets can be applied. xDEM allows biases to be identified and corrected by estimation of statistical measures (e.g., mean or median), or fitting of a parametric function for each terrain variable such as elevation, slope and/or aspect. The following description of different bias-correction approaches refers to Mannerfelt et al., (2021).

One of the biases can arise by residuals of the camera model that was calculated during photogrammetric processing. By applying a polynomial correction of a certain degree, *deramping* method can correct for these across the entire DoD. However, as it does not address horizontal shifts, it should be used as an addition to another approach. *Terrain bias* correction also employs polynomial functions to correct for systematic errors which result from the process of DEM rescaling, needed to perform in cases of different spatial resolutions. Lastly, biases that vary depending on the direction or orientation (e,g, flight direction during image acquisition) and repeat in a certain pattern, can be corrected by fitting of a sinusoid function of an appropriate frequency.

5.2.3 Interpolation of DoDs

Avoiding interpolation of the photogrammetric DEMs led to the presence of holes in some outputs. The Python package xDEM offers a tool for filling these holes on the glacier surface, utilising glacier hypsometry estimated from a reference DEM (McNabb et al., 2019). In this case, the reference used for each differentiation was a LiDAR DEM from 2020. This interpolation method relied on the assumption that surface elevation change relates to elevation, since ablation areas usually experience more lowering than upper glacier parts. This relationship is established from the difference and reference DEMs (Figure 5.9), and expressed as a linear or polynomial function, which is then used for filling of gaps. The figures detailing surface change plotted against glacier hypsometry for other time periods can be found in the section 2 of the Appendix. Once the holes withing the DoDs were interpolated, they were exported, and their values divided by the number of years that span between data acquisitions to derive values of elevation change per year for that specific period.

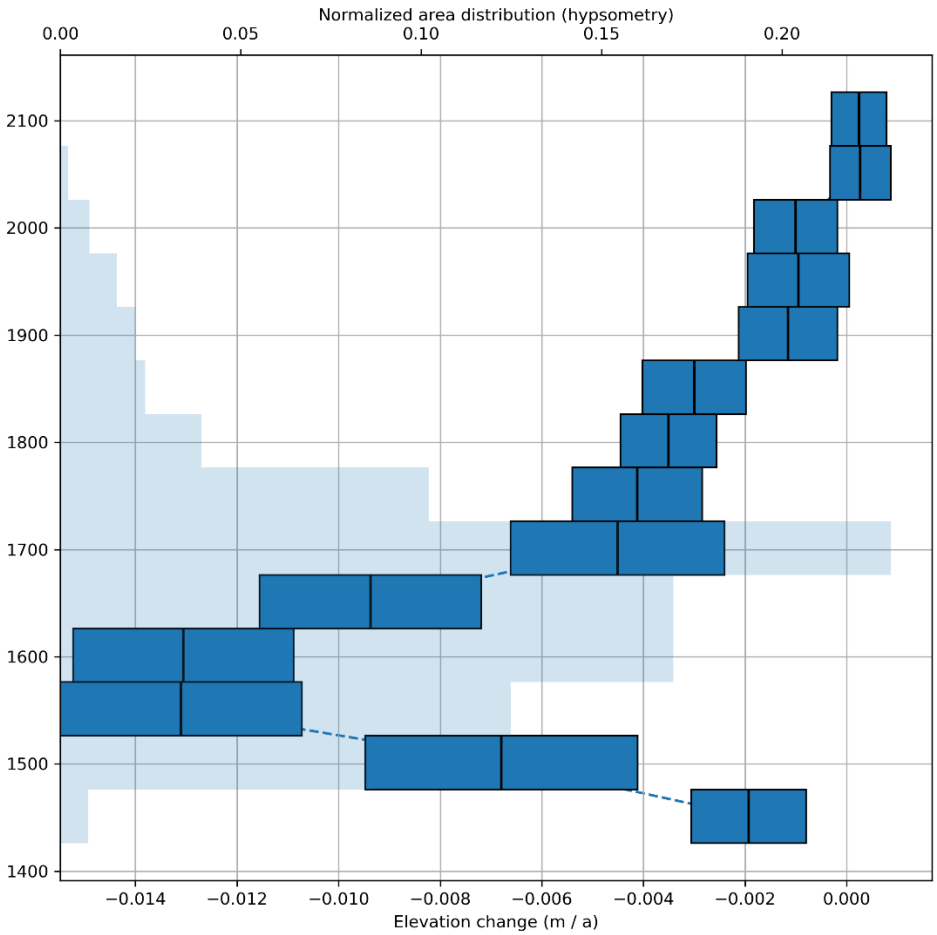

Figure 5.9: A figure showing glacier surface elevation differences at different glacier altitudes between 1966 and 2023. The transparent bars in the background shows glacier area distribution with elevation.

5.2.4 Surface change and precision

In the last step of DEM differentiation, the average annual glacier surface change for each period and its uncertainty were calculated. This was done by modelling spatial correlation of standardised error for stable ground, which was then used to infer data precision on the glacier surface (Mannerfelt et al., 2021). The input difference DEM had already been corrected for systematic errors, which values represented residuals after the removal of systematic biases. The analysis was performed employing spatial statistics tools provided by Hugonnet et al. (2022) and Rolstad et al. (2009), developed to analyse DEMs. Tool execution was based on the xDEM and *scikit-gstat* (Mälicke, 2022) Python packages, allowing to compute variograms that help depicting spatial data covariance and thus, assess the precision of the final value.

The precision of elevation measurements over stable rocky ground and smooth glacier surface may vary due to the influence of different terrain types and surface albedo (especially important for glaciers) (Figure 2.13). To address this in the assessment of elevation change uncertainty, spatial correlation and heteroscedasticity (spatial measurement error variation) needed to be quantified. The process began by estimation of a variogram (Figure 5.11a) defining spatial dependencies in order to calculate the number of independent observations (N), as shown in equation 5.1, by addressing number of pixels (N_{tot}), pixel size (PS) and the range of spatial correlation (d).

$$N = \frac{N_{tot} \times PS}{2d}, \qquad 5.1$$

It continued with the calculation of standard elevation error ($\sigma_{\overline{dh}}$) across space (equation 5.2). This estimation considered the variance of elevation difference samples (σ_{dh}) and the number of independent observations (pixels, N):

$$\sigma_{\overline{dh}} = \frac{\sigma_{dh}}{\sqrt{N}}, \qquad 5.2$$

The standard elevation error was used to derive normalised median absolute deviation values (NMAD) for the DoD data which had been grouped into bins. The NMAD was then assessed against a variety of stable terrain attributes (such as slope, aspect or terrain curvature, Figure 5.10) calculated from an independent DEM, which in this study is LiDAR elevation dataset from 2020. Since this reference DEM was known to be the most precise among all DEMs in possession, it was presumed that this analysis reveals solely the precision of the coarser DEM within the pair.

This step was necessary to identify variables that could explain changes in the variance of errors (heteroscedasticity). For the period of 1966 - 2023 (as for the rest of the time intervals, see figures in section 1 of the Appendix), these variables were slope and maximum absolute curvature (the maximum values for both absolute profile and planform curvatures (Zevenbergen & Thorne, 1987)) (Figure 5.10 a, c), as NMAD and aspect failed to show a systematic variance (Figure 5.10 b). Thus, when plotting the NMAD together with the two explanatory variables, the heteroscedasticity could be identified and a predicative function for the elevation error could be established. This function allowed for data standardisation - a step necessary for appropriate scaling as elevation errors from the stable terrain are inferred on the glacier (Figure 5.11b).

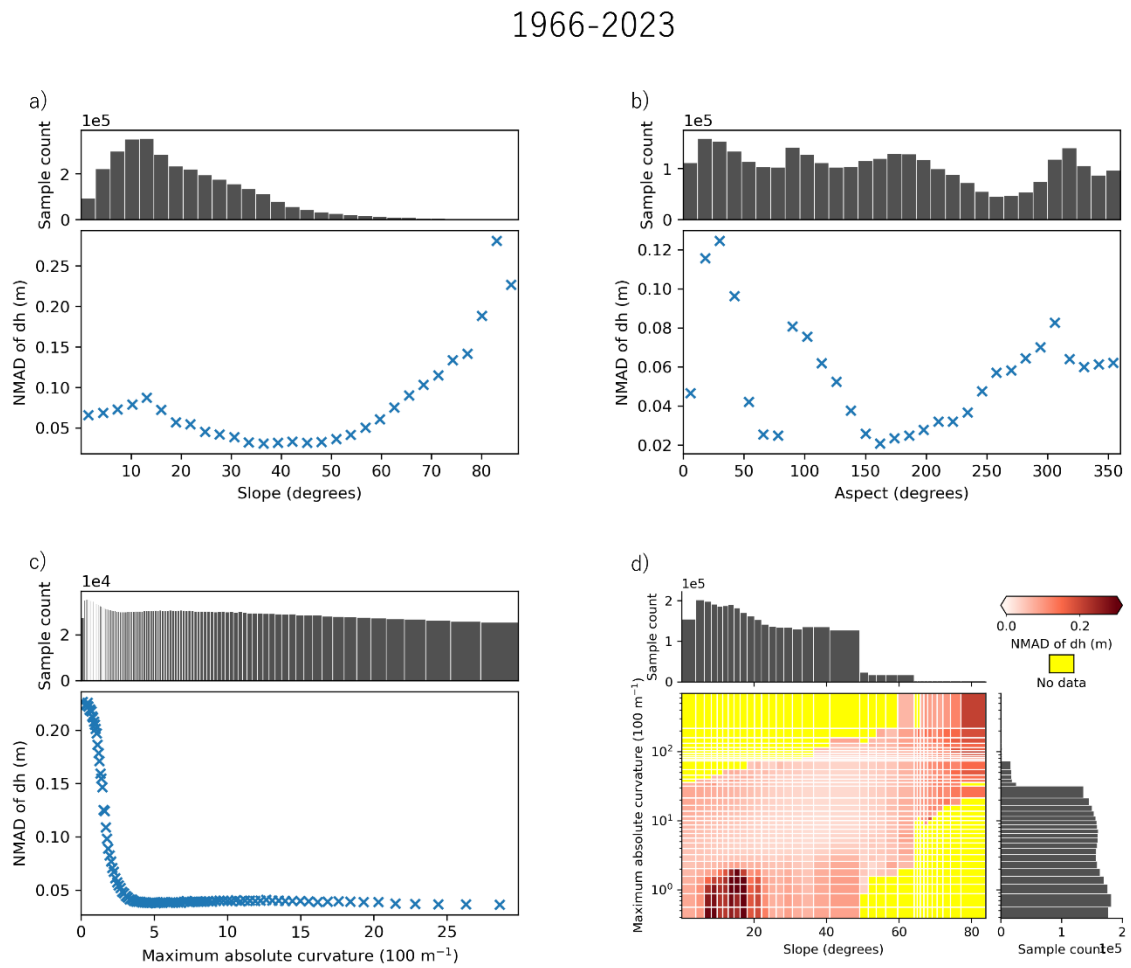

Figure 5.10: Modelling elevation error heteroscedasticity, required to assess the precision of difference DEM, which may vary with a) slope, b) aspect, and c) curvature. After identification of explanatory variables errors are plotted against them (d). The figures produced with tools available in the xDEM package.

Next, the spatial error correlation and the count of effective samples for results to be significant were determined with the help of a variogram analysis (Figure 5.11a). The spatially integrated errors were then re-scaled using the measurement error which were

dependent on the terrain variables explaining it (Figure 5.11b), thereby estimating the uncertainty of the average elevation change across the glacier surface (Figure 5.11c). Table 6.2 summarises the glacier surface elevation change for each period of time and its uncertainty.

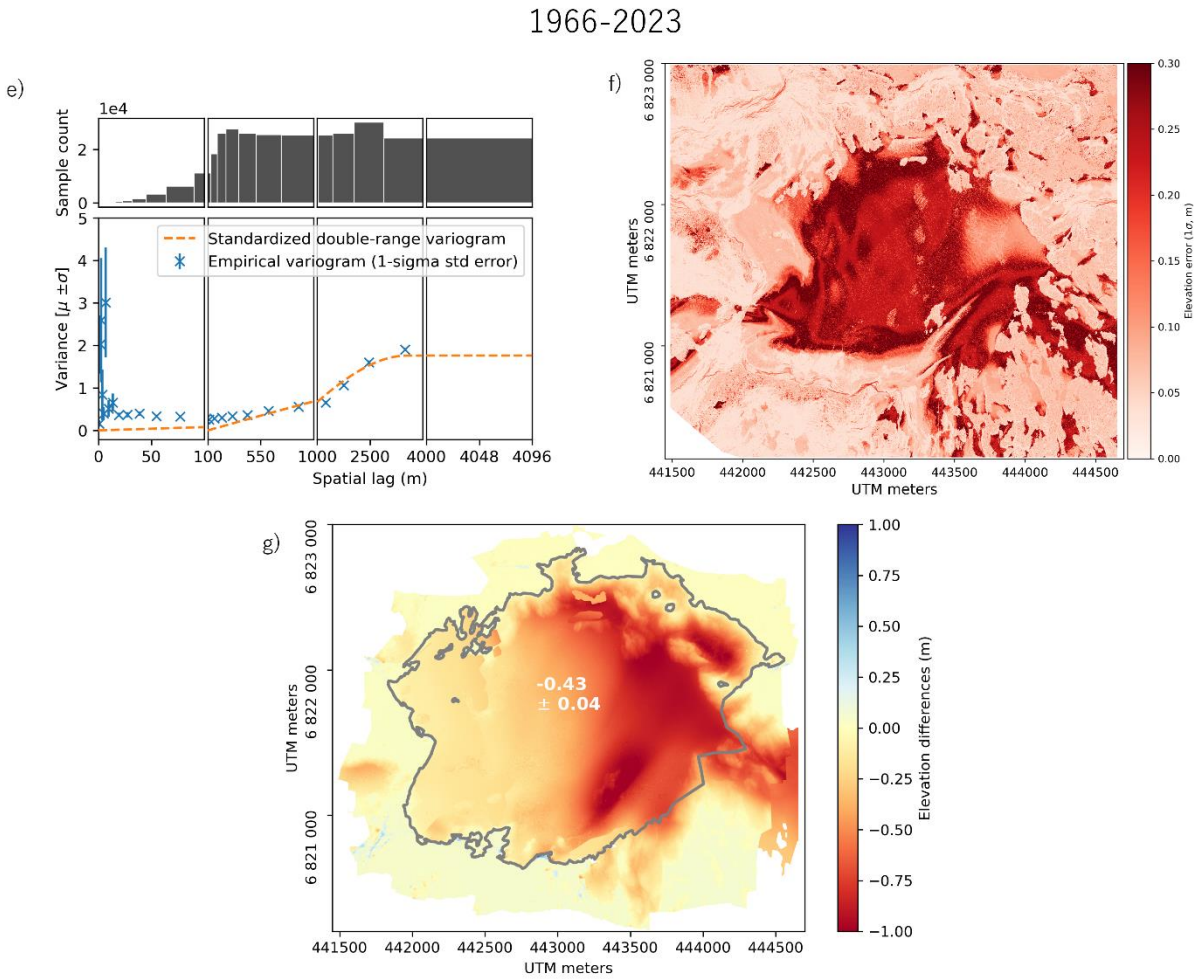

Figure 5.11: a) A variogram generated with a goal to estimate the number of effective samples and assess spatial correlation; b) a heatmap of elevation difference dispersion; c) the difference DEM with plotted glacier outline and the resulting mean elevation difference and its uncertainty.

5.3 Area change

As outlined in section 2.3.2, geodetic mass balance estimation requires glacier area. Since glacier surface was mapped using optical images, the same data was suitable to determine glacier area for each time epoch. Both analogue and digital data has been georeferenced and orthorectified to produce orthomosaics. These products were then used in ArcGIS Pro v. 3.2.0 (ESRI, 2024) for manual delineation of glacier area.

Determination of glacier boundaries for small glaciers in mountainous areas can bring challenges (Leigh et al., 2019). Due to Fannaråkbreen having been a large unit in the 1950's

that broke into several smaller units during retreat, only the largest coherent unit belonging to the same watershed was considered (area based on watershed, Figure 5.12). Difficulties in delineation occurred when separating the glacier from snow patches connected to the main glacier unit and identification of the drainage basin defined by the terrain. The LiDAR DEM from 2020 was used to generate contour lines and flow direction raster of the underlying terrain that was used for guidance during glacier delineation from other datasets as well.

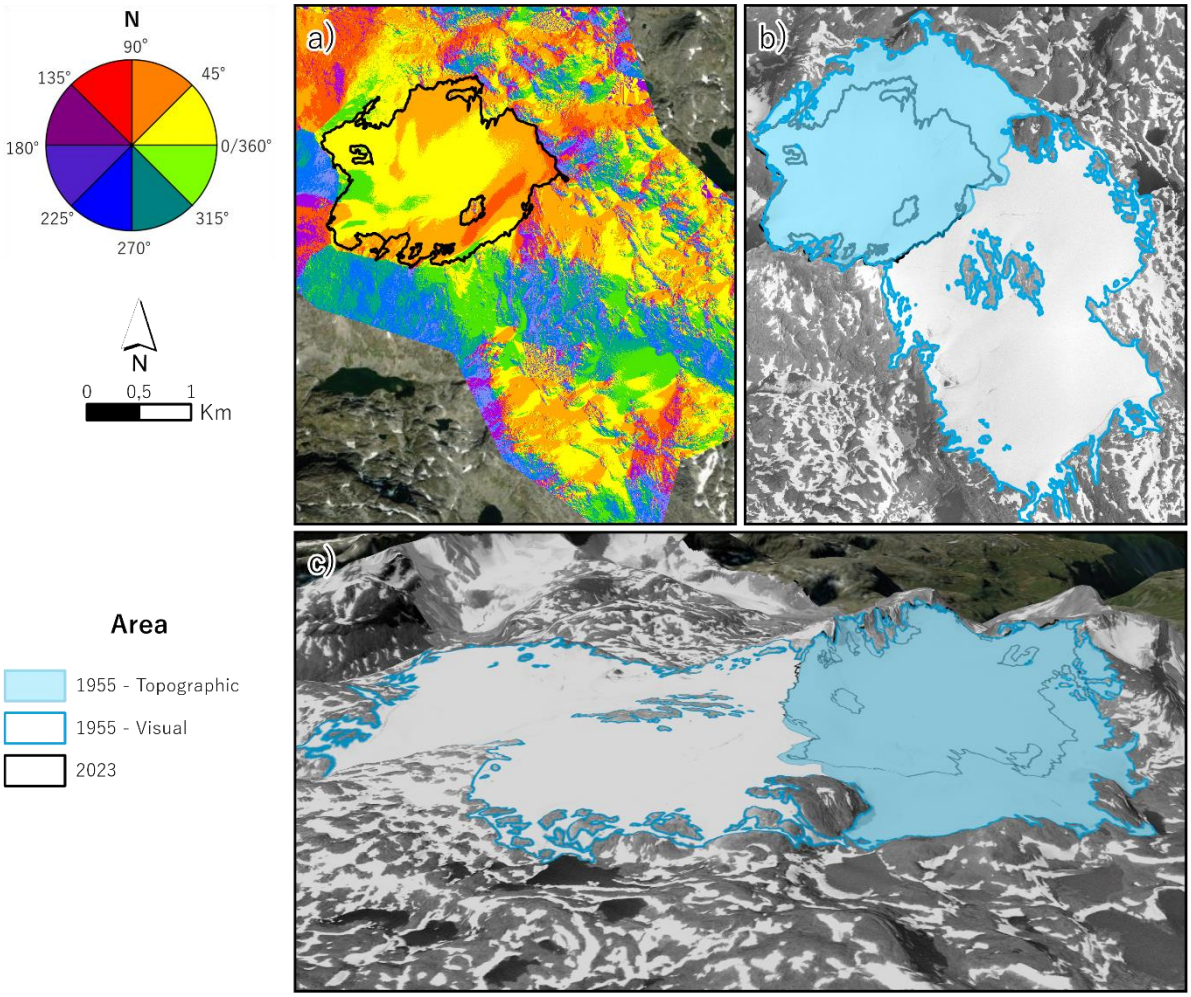

Figure 5.12: a) Aspect of the surrounding terrain estimated based on LiDAR DEM from 2020, visualised with colours and arrows, with glacier extent in 2023 (black line). b) Glacier extent in 1955, visually interpreted from images (blue outline) and based on topography (light blue polygon); c) a 3-D visualisation of the terrain and glacier area. This study is based on glacier area determined by topography (the watershed of the current glacier).

5.3.1 Snow masks

Additional vector files were obtained specifically for differentiation between DEMs to exclude ice and snow patches surrounding the glacier in the co-registration (section 5.2.1). Such masks were produced for the LiDAR DEM from year 2020 using a hillshade model in ArcGIS Pro (Figure 5.13a), by manually delineating all areas that appeared smooth and

merging them into a single vector file. Another such mask was generated for the DEM derived from the 2023 June imagery, using orthomosaic as a reference (Figure 5.13b). In this case, all pixels with the brightness value of >95 were reclassified into a binary raster mask and converted to a vector.

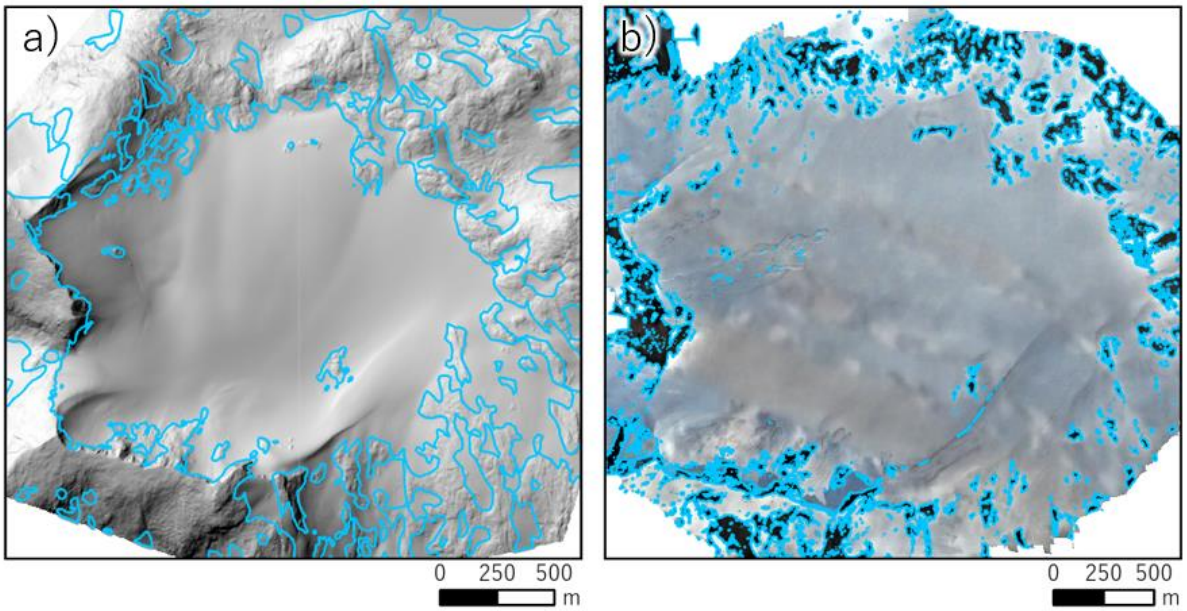

Figure 5.13: Vector masks used for DEM alignment to exclude ice and snow patches from the procedure. a) Manually delineated polygon based on smooth surfaces of the LiDAR 2020 DEM visualised as a hillshade in ArcGIS Pro; b) polygon extracted by reclassifying brightness values of the orthomosaic from June 2023.

5.3.2 Area change uncertainty

The uncertainty in the glacier area (E_a, see equation 5.4) originates from imagery resolution used during the process of manual delineation and was assessed using the method of buffering (Bolch et al., 2010; Robson et al., 2022). Glacier area was buffered by the width of orthoimage's resolution, resulting in two additional areas both larger and smaller by a certain magnitude, than the original polygon. This area difference was subsequently expressed as a percentage, the value then used for the estimation of the total volume change uncertainty (section 5.4.1).

5.4 Estimation of geodetic mass balance

With having estimated mean change in glacier elevation between the paired DEMs, it was possible to derive annual change in geodetic mass balance. This was accomplished by first estimating the alteration in glacier volume by multiplying glacier surface change by the glacier area. Once volume change was known, it was converted to meters of water equivalents using values for ice density of 850 ± 60 kg/m^3 (Huss, 2013), as showed with the equation 2.3.

However, for the period between September 2022 and June 2023, the volume change was assessed as accumulation of snow. Since snow density is not possible to measure remotely, an independent value of 421 kg/m^{-3} was adapted, measured for Storbreen in April, 2022 at around 1700 m a.s.l. by Andreassen, Elvehøy and Kjøllmoen (2023).

5.4.1 Mass balance uncertainty estimation

The accuracy of volumetric glacier balance for each time period ($E\Delta v_i$) was determined based on the approach used by Falaschi et al. (2019) (equation 5.3). First, the initial value of volume uncertainty was derived by multiplying the standard elevation error ($E\Delta h_i$) estimated in 5.2.4 by the glacier area (A_i)*:*

$$E\Delta v_i = E\Delta h_i \times A_i \qquad 5.3$$

However, as the result of total volume change is also affected by other uncertainty factors originating from area delineation (the percentage for each survey date estimated in 5.3.2) and density estimations (± 60 and ±15 kg/m^3 for ice and snow density respectively), a further error propagation is necessary. Thus, the total uncertainty value ($E\Delta v_{tot}$) was quantified as follows:

$$E\Delta v_{tot} = \sqrt{E^2\Delta v_i + E^2\rho + E^2 a} \qquad 5.4$$

5.5 A comparison of slope mapping methods

An additional comparison of two methods that can be applied for data acquisition with the DJI Mavic 3 Pro UAV was performed. The first way for image capturing, which was also applied for mapping of glacier surface in this study, was by having a constant camera angle at 90° (Figure 5.14a). The second approach was offered by the producer, integrated in the mission planning software, based on mapping the area of interest from both nadir and 45° angle (Figure 5.14b).

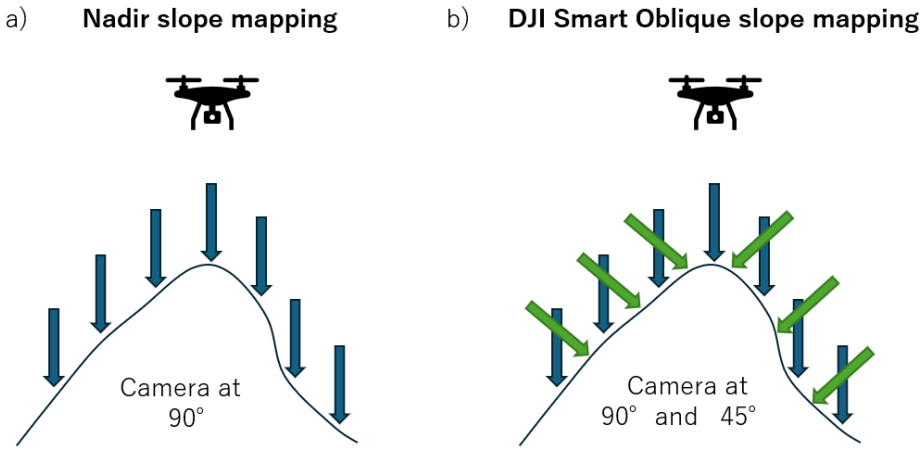

Figure 5.14: Two modes of camera position for terrain mapping. a) True vertical camera position, b) DJI's feature of Smart Oblique based on capturing images in both nadir and fixed oblique angles.

Using the Smar Oblique Capture function, the scene is captured from up to five angles by rotating the gimbal with a single-lens camera. The flight plan to be followed is segmented into several sections (Figure 5.15), with each sub-area corresponding to the number of angles images will be taken from. Sections along the edges are covered from fewer angles than the innermost parts within the survey area shortening the time required to accomplish the mission by reducing the amount of data which may not be necessary for the analysis (DJI-Enterprise, 2021).

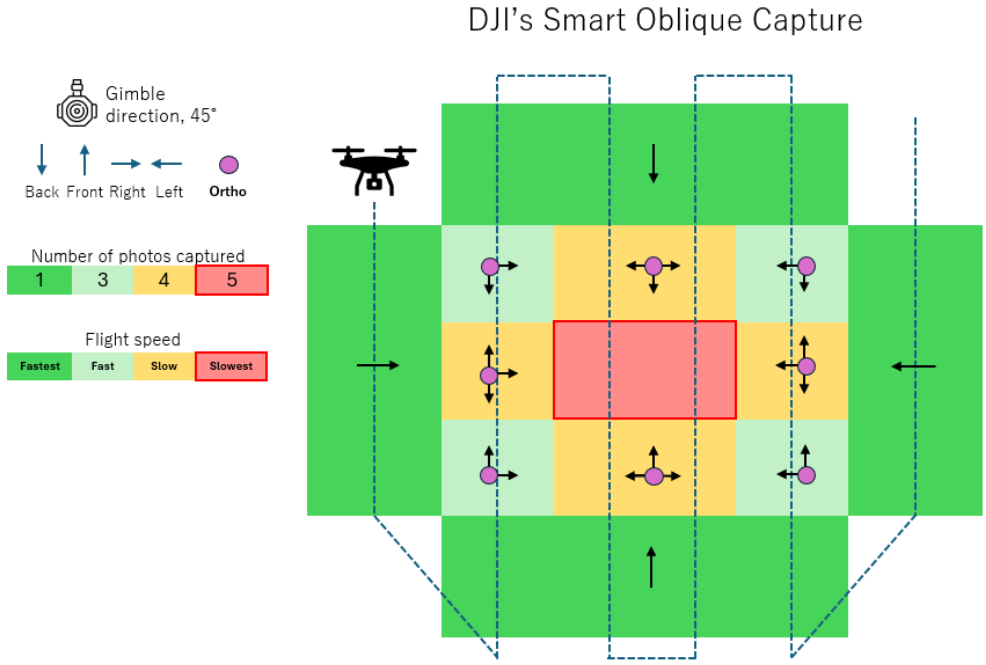

Figure 5.15:A visual representation of the DJI's Smart Oblique flight execution. The area of interest is divided into subareas with different flying speed and varying number of images that are taken from different angles (figure modified from an animation in DJI-Enterprise, 2021).

The two sets of images were used to generate two different slope DEMs. To determine their quality, they were aligned and co-registered to LiDAR data from 2020, excluding unstable ground. The difference DEMs of both comparisons were then used to estimate the NMAD utilising their pixel values.

6. Results

6.1 Changes in area

The analysis of glacier area span from 1955 until 2023, showing a general declining trend with some episodes of area increase (Table 6.1). Over this period of 68 years, the glacier area from 3.9 km^2 was reduced by 36.6 %, to the total of 2.47 km^2 (Figure 6.2b). Initially, the glacier surface area decreased to 3.58 km^2 by 1966, representing an 8.12% decline over 11 years, with an average annual decline rate of approximately -0.74%. A further decline continued until 1981, at a slower annual change of -0.28%.

Table 6.1: Table summarising the results of glacier area change over the period between 1955 and 2023.

Year	Area (km^2)	Area change a^{-1} (%)	Area change a^{-1} (km)
1955	3,90 ± 0,94%	-	-
1966	3,58 ± 0,84%	-0,74	-0,029
1981	3,44 ± 0,47%	-0,28	-0,010
1993	3,66 ± 0,58%	0,55	0,019
2004	3,17 ± 0,91%	-1,23	-0,045
2010	2,89 ± 0,38%	-1,47	-0,046
2017	2,87 ± 0,70%	-0,10	-0,003
2022	2,46 ± 0,31%	-2,84	-0,081
2023	2,47 ± 0,05%	0,40	0,010
1955-2023	-	**-0,54**	**-0,021**

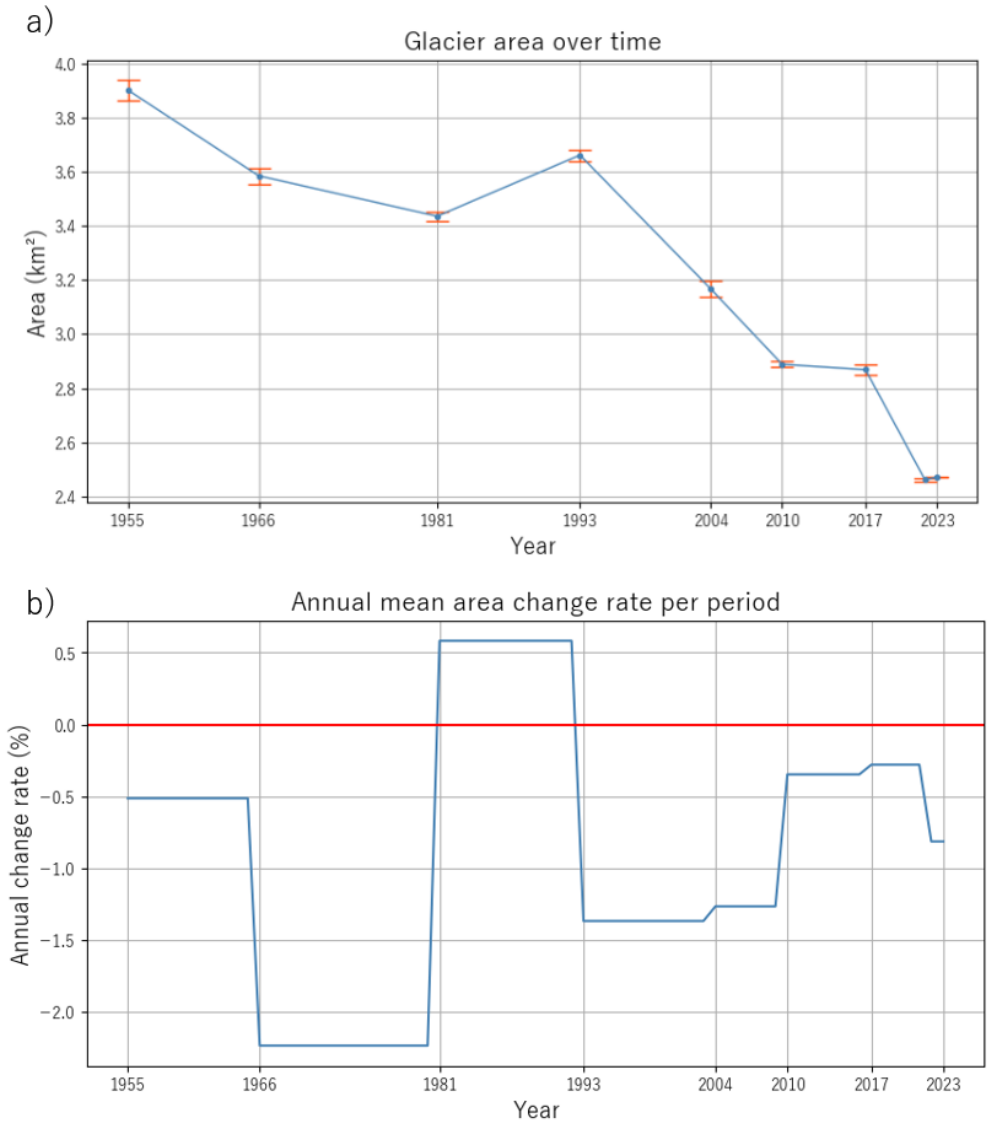

Figure 6.1: a) Glacier area in km² and estimation uncertainty (red bars) over time; b) Mean area change rate (%) estimated for each period of time.

However, the area increased to 3.66 km^2 by 1993, showing a 6.57% increase since 1981, at an average annual rate of 0.55%. Nonetheless, significant declines can be noted in the later periods. By the 2004, the area had reduced to 3.17 km^2 and further decreased to 2.89 km^2 by 2010, with an annual decline rate of -1.47% during this six year period. The area remained relatively stable until 2017, reaching 2.87 km^2, followed by a sharp decrease to 2.46 km^2 in 2022. A slight increase was observed in 2023, resulting in area of 2.47 km^2. Overall, during the observational period, the glacier shrank at an average annual rate of -0.54%. A visualisation of the glacier area changes throughout the respective periods can be seen in Figure 6.2a, c.

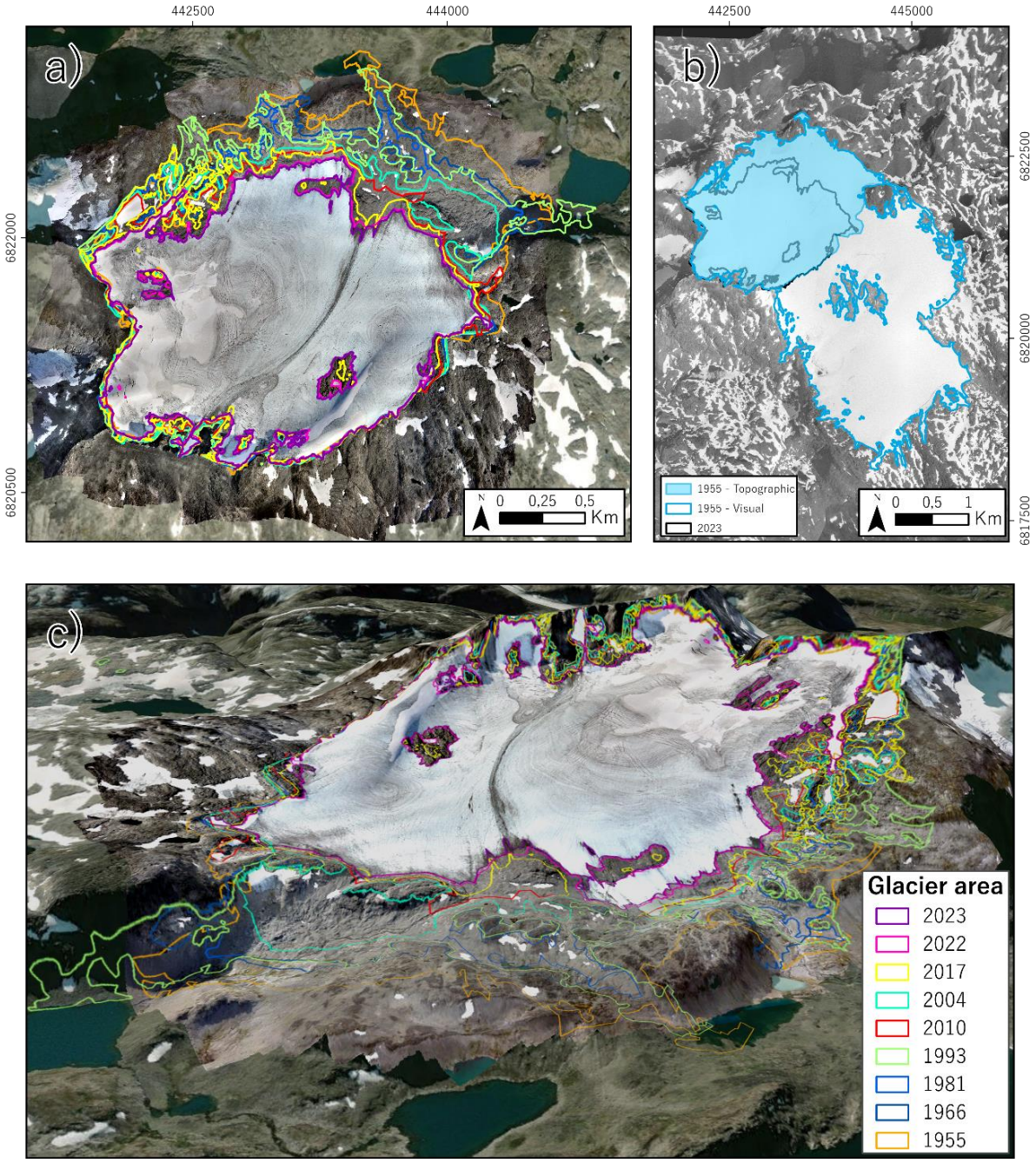

Figure 6.2: a) An orthoimage from 2023 with glacier outlines from each survey period; b) an orthoimage from 1955 with glacier extent vectors from 1955 and 2023 for comparison; c) a 3D-scene of the study area with orthoimage from 2023 draped over the LiDAR DEM. Background satellite image sourced from ESRI, Maxar, Earthstar Geographics and the GIS User Community, generated with ArcGIS Pro.

6.2 Surface elevation

6.2.1 Annual surface fluctuations

The basis for geodetic mass balance estimation was the difference in glacier surface elevation measured in subsequent time intervals between 1966 and 2023 (Table 6.2). Over this 57-year period, the average rate of glacier thinning was -0,43 ± 0,05 m annually. However, the rates of

elevation change varied greatly, not only across different periods, but also across different areas of the glacier (Figure 6.3).

From 1966 until 2004, the glacier experienced a relatively steady thinning rate of -0.25/-0.28 ± 0.01 m a^{-1} over the period of 38 years. The pace increased between 2004 and 2010, with a mean surface lowering of -1.11 ± 0.10 m annually. A slower thinning was detected in the next seven-year period between 2010 and 2017, with an average rate of -0.65 ± 0.03 per year. The next period from 2017 to 2020 exhibited faster surface lowering again, at rate of -1.06 ± 0.05 m a^{-1}.

The time frame with the fastest thinning was between 2020 and 2022, when the surface elevations declined sharply, by -2.55 ± 0.19 per year. Contrasting with the previous two years, the development during last period between 2022 and 2023 was considerably less dramatic, detailing a decrease of -1.26 ± 0.10 m a^{-1}.

Table 6.2: The summary of annual glacier surface change for each period of time and the uncertainty.

DEM pair for co-registration	Year span	DoD resolution (m)	Mean elevation difference (m a^{-1})
1966 - 1981	15	2	-0.25 ± 0.02
1981 - 2004	23	2	-0.28 ± 0.01
2004 - 2010	6	1	-1.11 ± 0.10
2010 – 2017	7	0.3	-0.65 ± 0.03
2017 – 2020	3	1	-1.06 ± 0.05
2020 – 2022	2	1	-2.55 ± 0.19
2022 – 2023	1	0.15	-1.26 ± 0.10
1966 – 2023	**57**		**-0,43 ± 0,05**
Seasonal elevation changes			
2022 Sept – 2023 June	0.5	0.15	+2.60 ± 0.26 m
2023 June – 2023 Sept	0.5	0.15	-4.08 ± 0.51 m

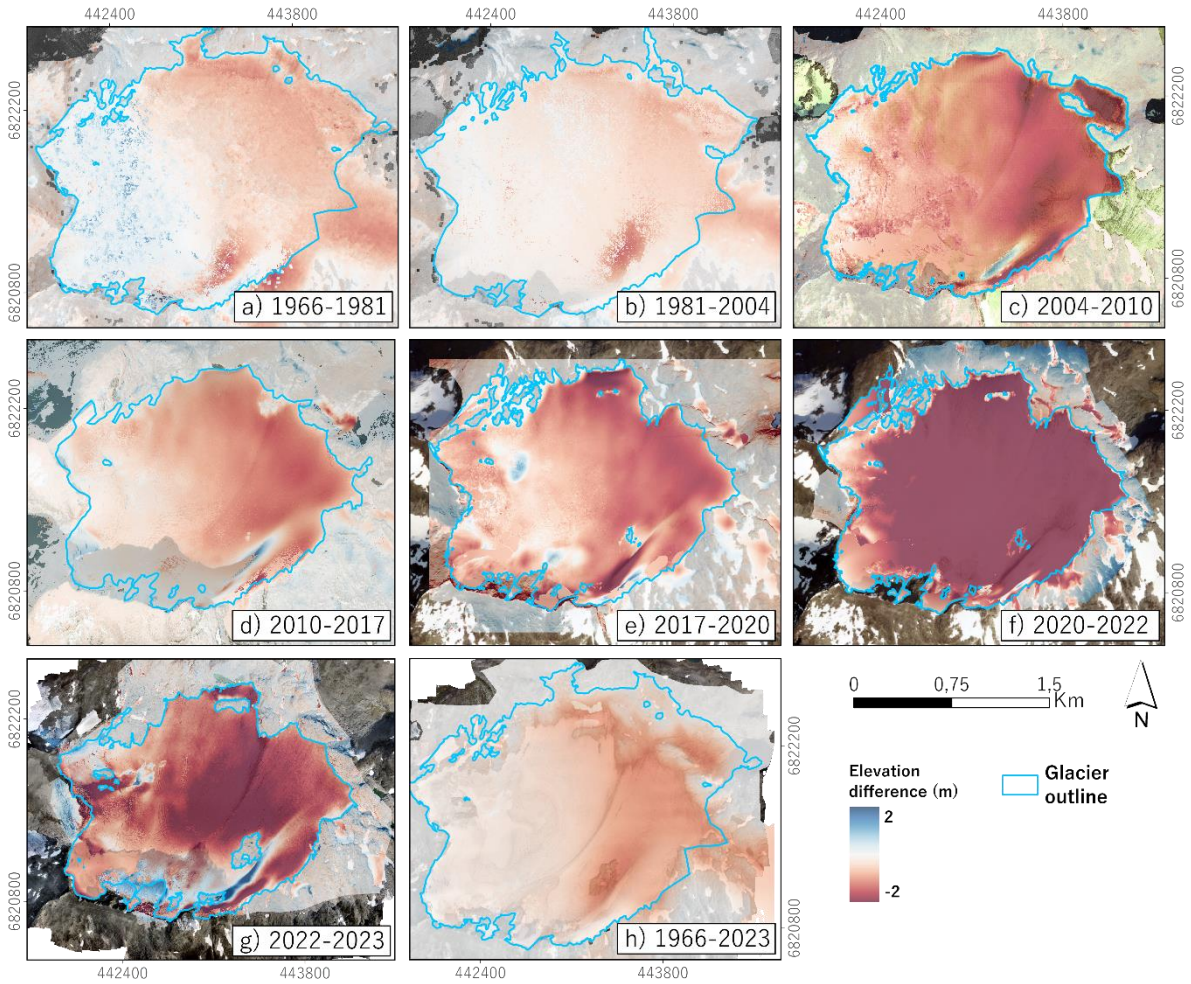

Figure 6.3: a) - h) Maps depicting glacier surface elevation change per year estimated for each period of time, with glacier boundaries (blue line) that were used for DEM differentiation. Orthomosaics are from the same year as the outline, with an exception being h), where the outline is from 1966 and orthomosaic is from 2023. Generated in ArcGIS Pro.

Each elevation change profile (Figure 6.4) shows negative development of glacier surface elevations, with the lowest glacier parts thinning the most, except for the period between 1966 and 1981, when glacier experienced some increase in surface elevation above 1670 m a.s.l. Moreover, in the last survey period between 2022 and 2023, the elevation seems to have decreased the most in the uppermost altitudes. The least surface change was registered for the earliest period, between 1966 and 2004.

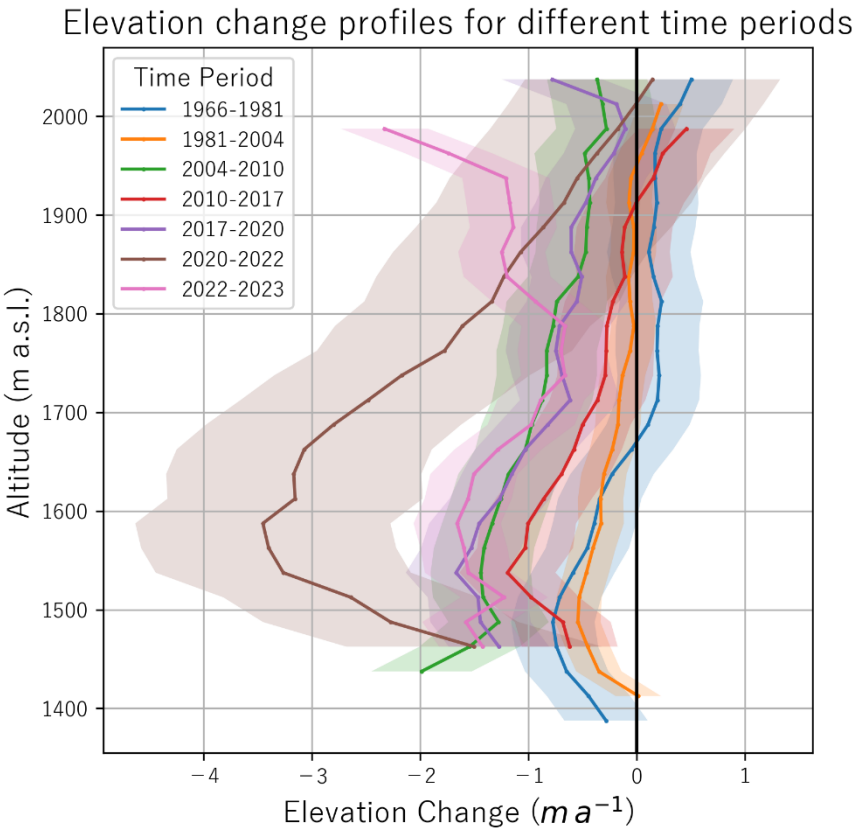

Figure 6.4: Mean annual glacier elevation change for every 25-meter band for each time period measured, with standard deviation plotted as shadowed area along the profiles.

6.2.2 Seasonal surface elevation change

During the period of accumulation, glacier shows to have thickened by on average 2.60 ± 0.26 m and lowered again by -4.08 ± 0.51 m during the melting months. The surface change that occurred due to winter accumulation was not homogenous across the entire glacier area. For instance, the accumulation data clearly indicates areas where surface height changed due to avalanche events (Figure 6.5a), also less accumulation seems to have happened at glacier front, at altitude from around 1540 to approximately 1600 m a.s.l. (Figure 6.6). Summer surface lowering, however, seems to have been relatively uniform (Figure 6.5b), with the most decrease having occurred along the mid-moraine and at the lowest parts at the glacier front (Figure 6.6).

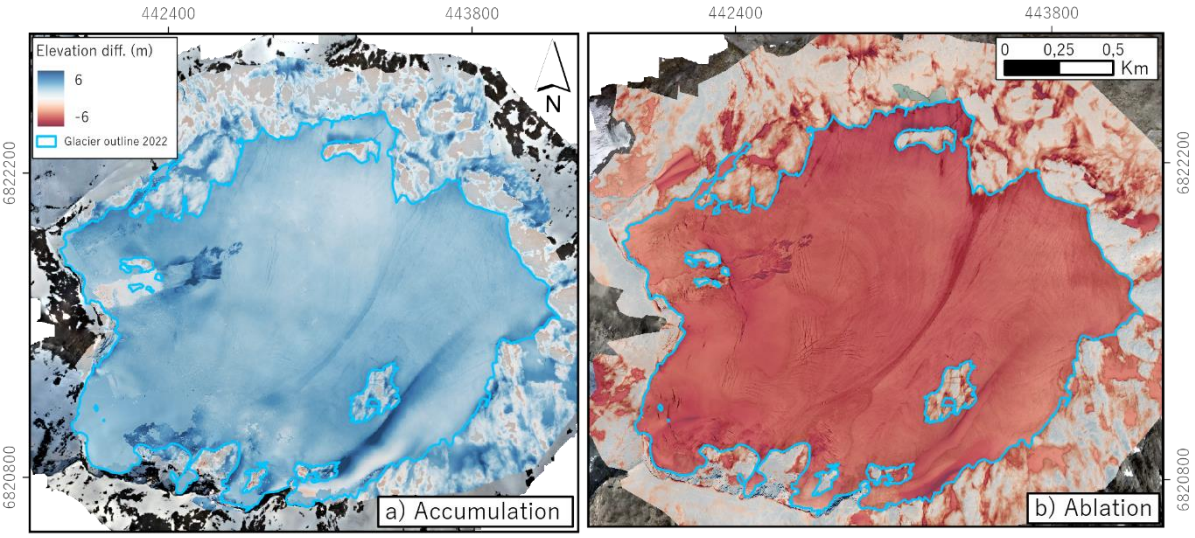

Figure 6.5: a) Increase in surface elevation during winter accumulation (September 2022 – June 2023); b) surface lowering caused by summer ablation (June 2023 – September 2023).

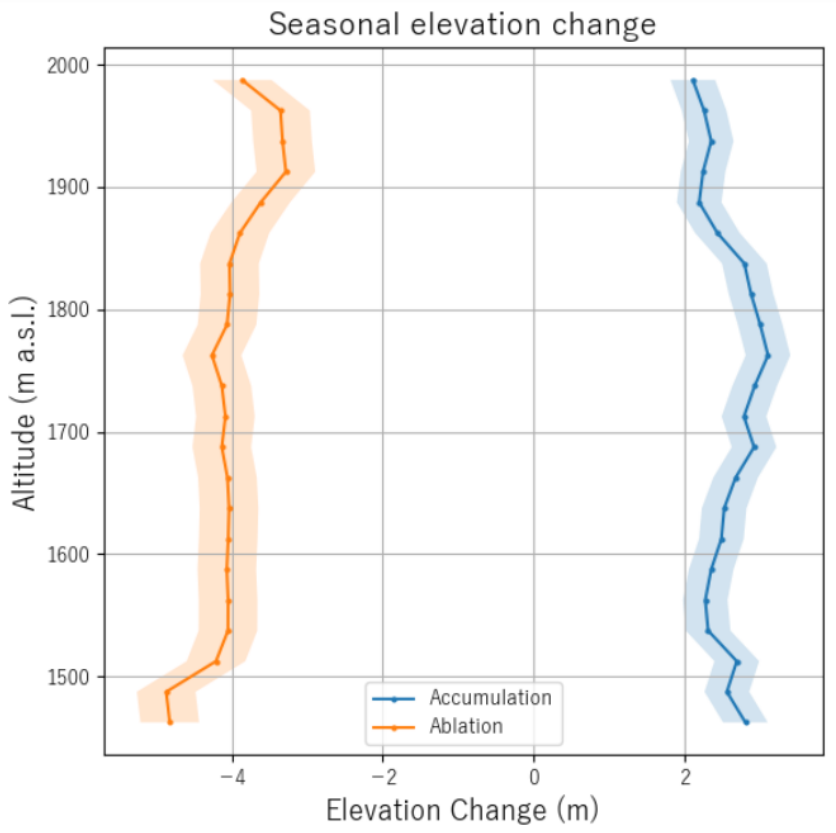

Figure 6.6: Mean seasonal glacier elevation change, measured every 25 meters of altitude with plotted uncertainty of one standard deviation. Yellow represents the ablation profile, while blue shows vertical accumulation.

6.3 Volume alterations and geodetic mass balance

Fluctuations of the glacier surface for the available datasets were transformed into volume changes using glacier area values from the beginning of the respective periods. These volumes were then converted to mass changes by applying the density for ice and snow and, finally, these mass changes were converted to water equivalents, as described in section 5.4 (for cumulative mass balance see Figure 6.8).

Figure 6.7 illustrates annual rates of volume change and Table 6.3 summarises these rates along with the estimated mass balance. A trend of negative annual volume change and mass balance trend is evident for the entire observational period. For this period of 57 years, the dataset shows an average annual volume change of -1.06 ± 1.12 m^3 x 10^6 and mass balance of -0.37 ± 0.02 m w. e., denoting glacial retreat for almost six decades.

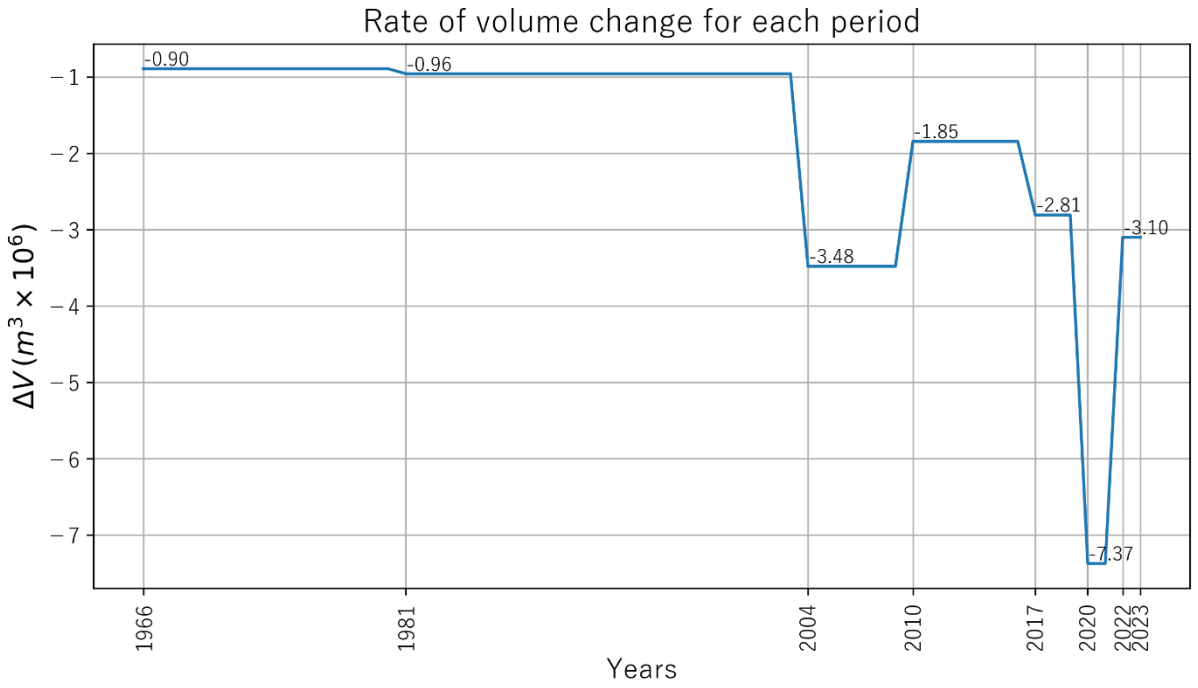

Figure 6.7: A figure illustrating the changing rate of glacier volume loss from 1966 to 2023. The rate has been accelerating dramatically with each period, except for 2010-2017, when the acceleration decreased by 3.16 m^3 x 10^6 per year yet continuing being negative. Note that the fastest rate of -7.37 m^3 x 10^6 may be an overestimation.

During the first 15 years of observation, the glacier has been losing -0.90 ± 0.07 million m^3 of volume each year, resulting in negative annual mass balance of -0.21 ± 0.01 m w. e. during this period. From 1981 to 2004, the reduction in both volume and mass balance were at the lowest, with volume changes of -0.96 ± 0.03 m^3 x 10^6 per year, yielding mass balance of -0.24 ± 0.01 m w. e per year. However, a significant increase in rate of volume loss can be seen between 2004 and 2010 as it accelerated to -3.48 ± 0.06 m^3 x 10^6 annually and the mass

balance also becomes increasingly more negative, reaching -0.94 m w. e. a^{-1}. This acceleration somewhat slows down between 2010 and 2017, yet still resulting in annual volume losses of -1.85 ± 0.12 m^3 x 10^6 and further loss of mass by -0.54 ± 0.03 m w. e. each year for three years.

Nonetheless, in the subsequent time intervals between 2017 and 2020, and 2020 - 2022, further increases in loss rates were observed. Especially in the latter period, when the volume changes reach -7.37 ± 0.54 m^3 x 10^6 per year and the mass balance rate measures less than -2 m w. e. a^{-1} during this interval. This constitutes the highest rates of loss in the entire dataset, which is followed by a slowdown in the annual volume loss (-3.10 ± 0.25 m^3 x 10^6) and a less negative mass balance (-1.07 ± 0.05 m w. e.) in 2023.

Table 6.3: A summary of annual volume change for each period and conversion to geodetic mass balance.

Time period	ΔV a^{-1} (m^3 x 10^6)	Mass balance (m w. e. a^{-1})
1966 - 1981	-0,90 ± 0.07	-0.21 ± 0.01
1981-2004	-0,96 ± 0.03	-0.24 ± 0.01
2004 - 2010	-3.48 ± 0.06	-0.94 ± 0.05
2010 - 2017	-1.85 ± 0.12	-0.54 ± 0.03
2017 - 2020	-2.81 ± 0.23	-0.83 ± 0.04
2020 - 2022	-7.37 ± 0.54	-2.18 ± 0.11
2022 - 2023	-3.10 ± 0.25	-1.07 ± 0.05
1966 - 2023	**-1,06 ± 0.12**	**-0.37 ± 0.02**
Seasonal volume change		
Accumulation	6,42 ± 0,64	1.10 ± 0.05
Ablation	-10,02 ± 1,28	-1.71 ± 0.09

The distinct seasonal patterns contrasting to the annual trends show how the accumulated mass is distributed across the glacier during winter and snow melting patterns during summer. There is an increase in volume by 6.42 ± 0.64 x 10^6 m^3 in the accumulation months, resulting in winter balance of 1.10 ± 0.05 m w. e. In the brief summer months from June 2023 to September, the experienced loss of volume was -10.02 ± 1.28 x 10^6 m^3, turning summer balance to -1.71 m w. e., highlighting large seasonal variation.

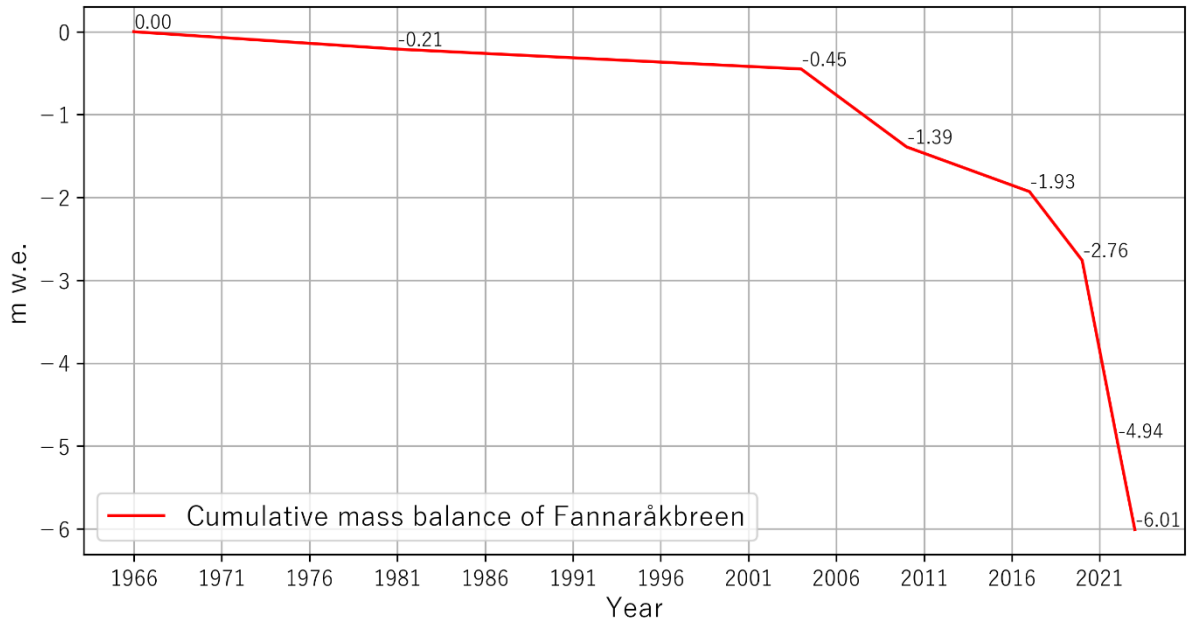

Figure 6.8: Cumulative geodetic mass balance estimated as changes since 1966. For the uncertainty values see table 6.3, as they were too small to be depicted using the scale of this figure.

6.4 Topographic slope mapping

The statistical NMAD values were calculated for the difference DEMs, which were derived by differentiating the data acquired using the two different slope mapping methods and the LiDAR dataset. A slight difference between these values were exhibited where the slope was at approximately 20° - 30° and between 40° and 60°. Overall, the NMAD appears to be lower for the DJI's Smart Oblique method.

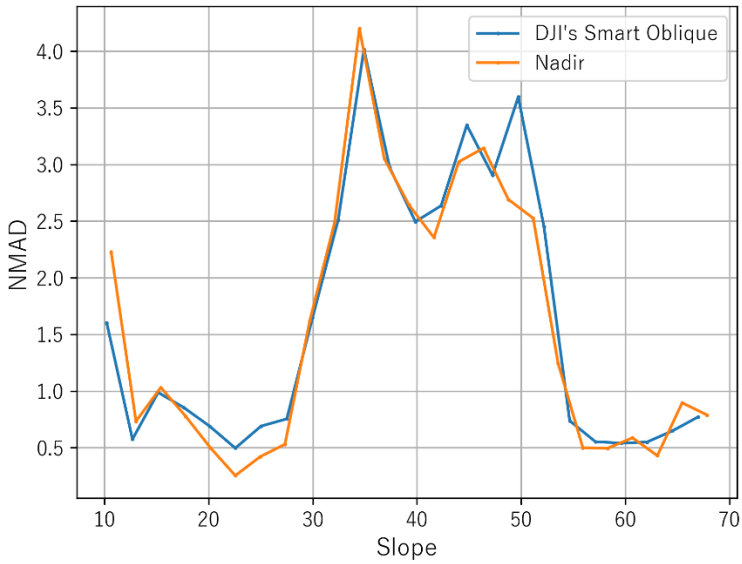

Figure 6.9: A figure comparing NMAD values estimated for differences between the tested methods when compared to LiDAR data. The plot shows similar results, with DJI's Smart Oblique producing slightly more dispersion from normal values with the slope between 20- 30° as well as between 40-60°.

7. Discussion

This section will discuss the significance and relevance of the results, and place the glacier change estimates from this study within a broader context. Since methodology was the primary factor influencing the results, it will be discussed first. Following this, the estimated parameters of Fannaråkbreen will be compared with those of other glaciers and examine the findings in relation to other studies.

7.1 Method limitation and error assessment

Due to the use of different sources to evaluate glacier changes over the period of 68 years, a number of challenges having an effect on the results were faced (e.g., Andreassen, Robson, et al., 2023). With the focus of this study being the assessment of the geodetic method using remote sensing to estimate glacier mass balance, this section presents challenges related to data collection, photogrammetric processing and estimation of surface elevation change using DEM co-registration.

7.1.1 Photogrammetry precision on steep terrain

The additional test which aimed to evaluate how the accuracy of photogrammetric datasets was affected by the steepness of the terrain revealed that neither method produced significantly better results, as detailed in section 6.4. However, as the DJI's Smart Oblique method resulted in slightly more dispersed errors, it was concluded that there was no particular advantage in using this data-intensive method for mapping sloping terrain.

The reason why capturing terrain from four different angles using the DJI's method did not prove to be more beneficial is presumably that some of these angles were not optimal. A more effective approach might have been to allow for flexible camera adjustments based on the slope of the undelaying terrain.

7.1.2 Area delineation

Implementation of correct glacier area to assess volumetric changes is important, as it has a direct effect on calculations of the glacier's total volume change over time. Inaccurate area measurements can lead to incorrect further estimations of mass balance, producing significantly erroneous results. However, utilising accurate and up-to-date area information is not always possible, as analyses over extended periods of time often require the use of various sources with differing spatial resolutions to estimate area changes (Andreassen, Robson, et al., 2023).

In this study, orthomosaics from aerial photographs were utilised to manually delineate glacier area vectors, which were used to analyse area change and geodetic mass balance, as outlined in section 5.4. Relatively fine image resolution resulted in inaccuracies being less than 1% (Table 6.1), showing to the most accurate delineation ever performed on this glacier. After visual inspection of historical photographs, it became clear that the glacier consisted of several units, with Fannaråkbreen being the predominant ice body today (Figure 6.2b). This presented a challenge in making a decision on what should be included in the area change analysis, as was also the case for some outlets of Jostedalsbreen in Andreassen, Robson et al. (2023), resulting in discrepancies of change rates due to different divisions of the glacier cap. A comparative analysis of Fannaråkbreen images from 1955 and 2004 (Figure 4.1), revealed that the southeastern parts of the glaciated area were undergoing vertical wastage, thus considered being dynamically inactive. Moreover, for an ice mass to be classified as a glacier, it must show signs of past or present flow. Thus, the presence of a medial moraine on the main unit indicating the direction of ice and debris movement (Benn & Evans, 2010, p. 346) provided an evidence of Fannaråkbreen being dynamic. This served as the argument for solely including the active glacier unit for the study, based on the current glacier watershed. However, if the excluded part was to be included, the total area change between 1955 to 2023 would have been -73.72%, a way more dramatic development from 9.40 km^2 to 2.47 km^2

7.1.3 Quality of the DEMs

The precision of surface models significantly influences the total uncertainty in mass balance calculations, particularly when estimating changes over short periods as they tend to be of smaller magnitude and require precise data to be detected (Beraud et al., 2023). Besides processing factors, DEM quality also depends on the quality of the data used for extraction of elevations. In this study, three distinct sources were utilised – historical analogue and digital imagery, LiDAR surface elevation model and UAV imagery. The images from 1955 presented significant challenges during processing due to the presence of artefacts such as scratches and dust (Figure 7.1a), as well as low surface contrast on the glacier, both affecting feature matching. Moreover, the calibration report accompanying the photographs contained mistakes, and the radial distortion values had to be extracted from a plotted curve, which reduced the precision in determining exterior orientation. Consequently, the attempts to produce a DEM were unsuccessful (Figure 7.1b) and the images were only orthorectified and used for area estimation.

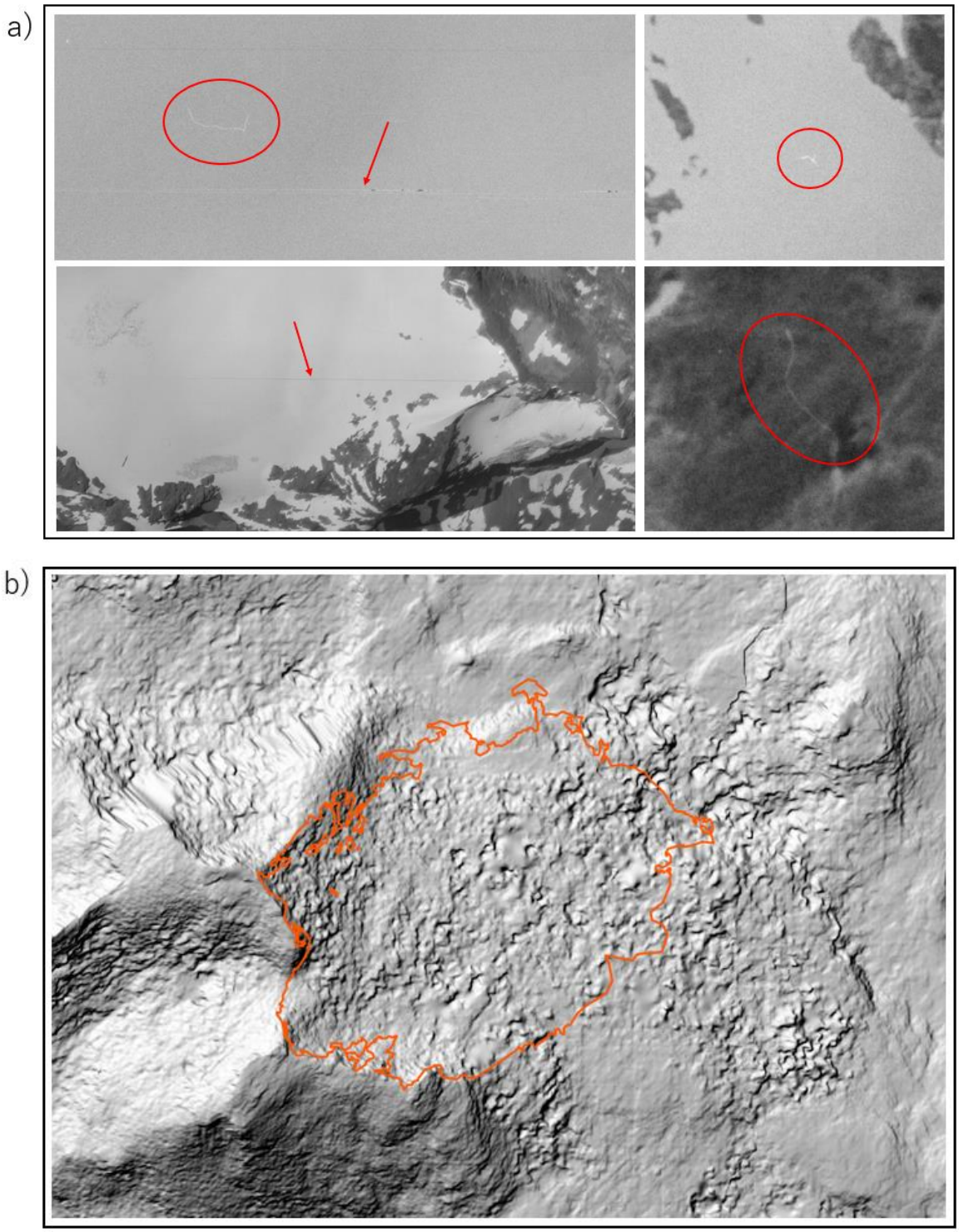

Figure 7.1: a) The artefacts in imagery from 1955 that may have had an effect on feature matching during photogrammetric processing; b) a shaded representation of a resulting DEM (2m of resolution, generated with ArcGIS Pro) with large errors, thus being unsuitable for DEM differencing (orange line – glacier area in 1955).

Furthermore, the availability of more images of the scene enhances parallax estimation during photogrammetric processing. For the years 1955 and 2004 three images were available, while only 2 were available for 1966 and 1981 (Table 4.1). Although three images are generally sufficient, two images may not adequately support the production of high-quality DEMs.

Nonetheless, an attempt was made, and DEMs were produced. Additionally, the high surface albedo of ice in the latter dataset resulted in almost featureless glacier surface in the images, complicating the extraction of elevation data. Many pixels on the glacier had a correlation score of zero (Figure 5.6), and they were removed during DEM cleaning (section 5.1.3). Another challenge related to optical data was shadows; the largest shadow cast by the southern glacier headwall in the 2010 imagery (Figure 5.7), necessitated interpolation of elevation values, which were ultimately manually removed.

7.1.4 Assessment of surface elevation change through DEM co-registration

Aligning surface models was essential for identifying biases determined by the stable bedrock surrounding the glacier and for their removal. Consequently, the co-registration of models significantly influenced the final mass balance results. The longer the interval over which elevation change is estimated, the easier it becomes to detect through comparison to the surrounding terrain. For this reason, the co-registration of each DEM pair derived from historical sources yielded low error margins, making it easier to clearly identify changes in the glacier surface.

However, aligning the 2020 LiDAR and the 2022 UAV datasets proved to be the most challenging. None of the bias removal techniques available within the xDEM package were effective in eliminating the differences observed over the surrounding rock. Consequently, the difference DEM without any co-registration was used in further analysis. As shown in Figure 6.3f, the elevation bias on stable terrain exhibited a decreasing trend radially towards the centre of the dataset, with little to no difference at the glacier boundary. This trend could not be confirmed for the glacier area, suggesting that surface lowering may have been overestimated towards the middle of the glacier as shown in Figure 6.4, and resulted in the highest value of uncertainty (Table 5.2).

Several factors may have contributed to these errors. Firstly, the type of UAV, which was not specifically designed for topographic surveys, posing challenges in covering large areas in high altitudes. Consequently, there was insufficient stable ground behind the glacier's headwall for proper model alignment. However, these issues were mitigated with the DJI Mavic 3 and Wingtra UAVs due to easier mission planning opportunities, lenses without causing distortions (such as fish-eye), longer lasting batteries and overall UAV size, making them being more stable in windy conditions. Secondly, a snowmask used for co-registration (Figure 5.12a) was manually delineated based on the surface smoothness in the shaded

LiDAR DEM, as no imagery from that year was available. This method may not have been precise enough to exclude snow patches effectively, leading to attempts to align the two surfaces over areas that in reality were not stable. Finally, the need to rescale the 2022 DEM down to 1 meter to compare the two DEMs may have introduced this bias, which in addition to X, Y and Z errors of the model itself (Table 4.2), could not be corrected due to too limited data available over the stable ground.

June 2023 and September 2023 were the other two datasets to which the 2022 DEM was aligned. In June, although little of the surrounding ground was free from snow, it was sufficient for co-registration and bias identification, as shown in Figure 6.5a. The same co-registration method was successfully applied to the September 2020 – September 2023 pair (Figure 6.3g). The success of these two independent alignments with the UAV data from 2022 suggests a possible issue with the LiDAR data, which was produced using only two laser measurements per 1 m^2 (Kartverket, 2020a). However, this explanation seems less likely, given the successful alignment of LiDAR DEM with the 2017 model.

7.1.5 Heteroscedasticity and spatial correlation of elevation errors

The elevation uncertainties of glacier DEMs cannot be adequately evaluated by solely using DEM differencing, as the stable ground and glacier surfaces exhibit different characteristics (e.g., contrast, albedo and slope) that lead to various inaccuracies. Therefore, the remaining uncertainties were assessed using geostatistical methods (Rolstad et al., 2009). Slope and maximum absolute curvature were identified as the two main factors affecting the precision of vertical measurements, correlating with the changes in the variance of elevation errors. Larger deviations from normal error values were observed with increasing terrain steepness, and in areas with low curvatures. Consistent with the findings from other studies (e.g., Bolstad & Stowe, 1994), the precision of photogrammetric elevation measurements was also shown to decrease with steeper slopes in this study.

Regarding curvature, significant error deviations were observed in some of the flattest areas, as shown in Figure 5.10c (and additional figures in section 1 of the Appendix). This may be attributed to the type of surveyed landscape, which included ice remnants and snow patches that were likely not excluded from the analysis of stable terrain. Since photogrammetry depends on feature matching to estimate the parallax (illustrated in Figure 2.7), having a surface with sufficient texture is therefore crucial. Typically, such areas have more optically uniform surface and are less curvaceous than bedrock. Additionally, the quality of the images

must be adequate to identify and match surface features belonging to the object of interest in stereo pairs. However, the historical photographs were not captured with optimal settings for recording ice and snow, causing them to appear completely white due to overexposure.

In other cases, the NMAD values decrease with decreasing curvature, probably indicating measurements of stable ground, and increase again with larger curvatures, which typically correlate with steepening slopes. Consequently, as depicted in the heatmaps of this dispersion (Figure 5.11b), the largest errors were inferred to occur on the glacier, where the surface is relatively flat. In cases involving UAV data, error variance was more significantly influenced by slope rather than curvature (see figures for other intervals in section 1 of the Appendix). This variation may be due to smaller DEM extents used, which included fewer snow fields and patches. Consequently, these features had little to no impact on large error deviations associated with low curvatures.

The assessment of spatial correlation was also employed to estimate mass balance uncertainties due to its significant impact on the total values. Considering that bare rock and ice surfaces possess different physical properties that affect photogrammetrically derived elevation data, employing semi-variograms (Figure 5.11a) to identify distance-dependent variance aids in improving uncertainty estimates (Rolstad et al., 2009; Magnússon et al., 2016). As shown by the variograms in the section 1 of the Appendix, dissimilarities increase with distance, revealing different scales of spatial correlation linked to various potential sources of error. Variance correlated with shorter distances (e.g., a couple hundred meters for the 2004-2010 dataset) likely originates from photogrammetric feature matching used to extract surface elevations. Meanwhile, variance at an intermediate scale of a couple of kilometres (e.g., for the 1966-2023 in Figure 5.11a, as well as accumulation and ablation DoDs in the Appendix) likely results from unresolved orientations relative to the image coordinate system (Rolstad et al., 2009).

7.2 Mass balance

7.2.1 Mass balance uncertainty

One source of uncertainty for the geodetic mass balance was the uncertainties arising from elevation measurements, evaluated through DEM differencing. Given focus of this study on the application of photogrammetry in the geodetic method, the uncertainties arising from this source are discussed in more detail in the previous section. The impacts of other error sources

on the final mass balance values have also been evaluated utilising the standard error propagation and are detailed in section 5.4.1 (equation 5.4), presented as a total uncertainty of mass change.

However, an additional uncertainty that was not accounted for is the ice density value proposed by Huss (2013), possibly introducing further inaccuracies if applied to mass conversions over periods shorter than five years. In this study, there were four such periods (the four most recent), suggesting that the uncertainties for the mass balance of these intervals may be somewhat higher than estimated.

Moreover, the snow density measured at Storbreen in April 2022 may not have been representative of Fannaråkbreen in June 2023, and the uncertainty of this measurement likely exceeded the uncertainty of the scales used for weighing snow. Possible mass loss due to ice melt was not addressed, and it was assumed that the ablated snow maintained the same density it had at the end of the accumulation period. Considering that snowpack densifies over time, it is reasonable to believe that seasonal ablation may have been underestimated, as the calculated volume loss might have involved mass with a higher density. This can be evidenced by comparing the sum of seasonal volume changes (-3.6 m^3 x 10^6) with the annual change in volume estimated to have occurred between 2022 and 2023 (-3.10 ± 0.25 m^3 x 10^6). Moreover, the value of combined summer and winter balances (-0.61 m w. e.) is significantly smaller than the observed annual balance (-1.07 ± 0.05 m w. e.), indicating that density variations may have significantly affected these estimates.

7.2.2 Connection with climate

The main driver for changes in mass balance in maritime glaciers is precipitation during the accumulation season, while the average ablation temperature is the main factor influencing the mass of those that exhibit more continental behaviour (Andreassen et al., 2005; Marzeion et al., 2012; Trachsel & Nesje, 2015). Since Fannaråkbreen is situated near the east-west transect, there is a possibility for the influence of both factors. Winter precipitation, summer temperature (extracted specifically for the study area from *seNorge_2018* interpolation) and Storbreen mass balance values have been averaged to match the intervals for which Fannaråkbreen data was available for and plotted together in Figure 7.2.

Similarly to Storbreen, the mass balance of Fannaråkbreen is inversely correlated with mean ablation temperatures. During the first two periods, Fannaråkbreen has been relatively stable, while Storbreen experienced an increase in rate of mass loss in 1981, likely due to slightly

increased summer temperatures and less snowfall. A faster mass loss was registered at both glaciers starting in 2004, however, after 2010, the rate somewhat increased for Fannaråkbreen, while Storbreen continued to melt. This difference may be attributed to both glaciers having more sensitivity to different drivers, e.g., even with less winter precipitation, only slightly colder summer temperatures were enough to slow down the rate of mass loss of Fannaråkbreen, while Storbreen's rate continued to accelerate. Despite an increase in the amount of snowfall, a slight increase in the temperatures of the summer months in 2017 resulted in both glaciers melting faster than the previous period, with Storbreen exceeding Fannaråkbreen, which may be due to Fannaråkbreen receiving more precipitation during months of accumulation.

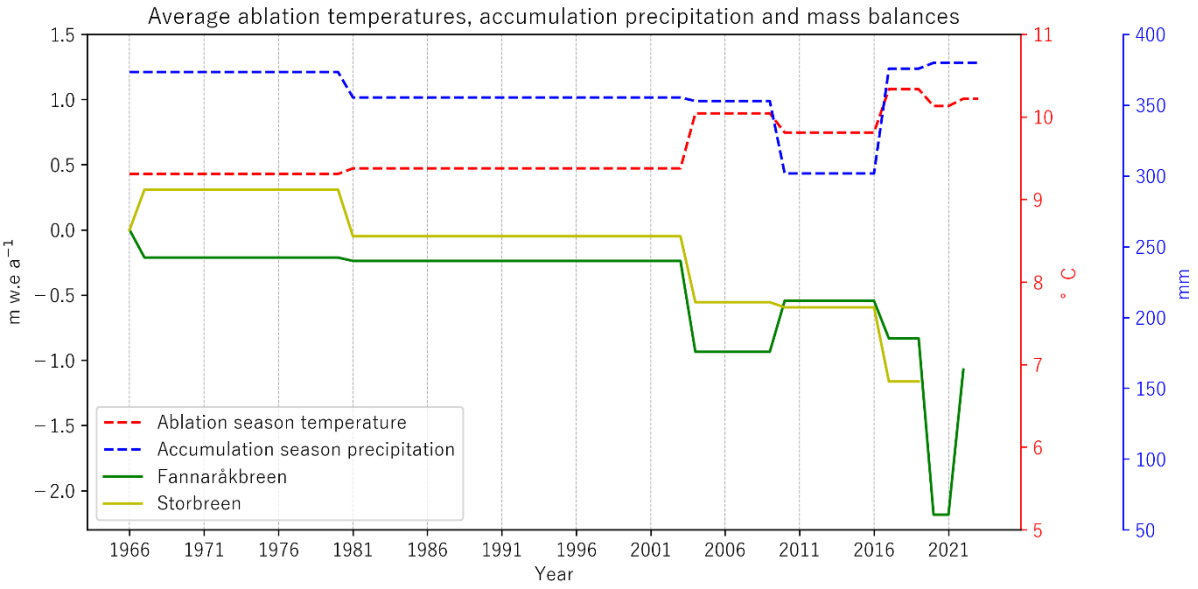

Figure 7.2: Averaged mass balance values for Fannaråkbreen and Storbreen plotted with mean ablation temperatures and winter precipitation over respective periods. Note that the dramatic increase in rate of mass loss between 2020 and 2022 may be overestimated due to large errors within the DoD from that time interval.

The variation between the two glaciers may be due to differences in their geometry or local climate causing glaciers that appear to be similar and located at different basins, to behave differently (Granshaw & Fountain, 2006; Fountain et al., 2009; Shindell & Faluvegi, 2009; Brown et al., 2010). Moreover, this comparison between geodetic and glaciological mass balances does not account for the inherent discrepancies inherent of both methods. Potential differences in survey dates, internal and basal ablation which are not accounted in the glaciological measurements (e.g., Schneider & Jansson, 2004), as well as interpolation between glaciological points (e.g., Zemp et al., 2013), may affect the results. Additionally, density uncertainties are relevant for both methods, and their validation is challenging due to the scarcity of firn density measurements in Norway (Andreassen, Robson, et al., 2023).

Thus, the results of Fannaråkbreen mass balance may show to substantial amounts of mass gained internally through refreezing, especially in the period between 2004 and 2010, what is not uncommon for temperate glaciers (see section 2.2.2). As Dyurgerov (2002) suggests, at least one measurement of internal mass gain for the glaciers being surveyed should be carried out to evaluate its influence to the total balance.

Glaciological mass balance could also have been affected by the uncertainties of the method (see section 2.3.1). Nonetheless, showing to the biases present in the DoD from the 2020 – 2022 period, it is reasonable to suggest that the sharpest acceleration of mass loss correlating with the same period may be due to overestimation of glacier surface lowering (Figure 6.3f).

7.2.3 Seasonal changes

The snow accumulated during the winter season of 2022 - 2023 exhibited a heterogeneous distribution, resulting in an increase of mass by +1.10 ± 0.05 m w. e. This pattern of snow allocation may be due to glacier's north-eastern aspect, which allows the prevailing westerlies to blow snow from the surrounding areas into the immediate hollow where the glacier is situated. A fresh snow avalanche observed in June 2023 originating from within the glacier area, indicates active slope processes and suggests that these are important for factors influencing patterns of accumulation (Figure 6.5b).

In total, the glacier had lost more mass during summer than it had gained, with the difference showing to annual balance of -0.61 m. w. e., what is almost 40% less than quantified by differencing the DEMs from September 2022 and September 2023. This again show to the possibility that the modelled surface of 2022 may have been lower than the actual elevations (what the bias trend also shows to, Figure 6.3f), what led to an overestimation of surface change and thus, mass balances for periods ending or starting with the year 2022. Another explanation is related to conversion of volume lost during ablation to mass, using snow density, causing this underestimation (as discussed in section 7.2.1).

The short-term geodetic mass balance of Fannaråkbreen was compared to the seasonal mass balance fluctuations of Storbreen measured utilising traditional field-based approaches (NVE, 2024) in Figure 7.3. Storbreen is the closest glacier having such long mass balance records and it has been shown to correlate with other glaciers of the region (Rasmussen et al., 2007). However, due to the unavailability of Storbreen data from 2023, it is not possible to directly compare the accumulation (Bw) and ablation (Bs) between the sites. Nonetheless, when compared to the previous measurements, the values from Fannaråkbreen fall within the range

of variation observed for Storbeen, which may indicate that Fannaråkbreen experiences a lower seasonal mass turnover.

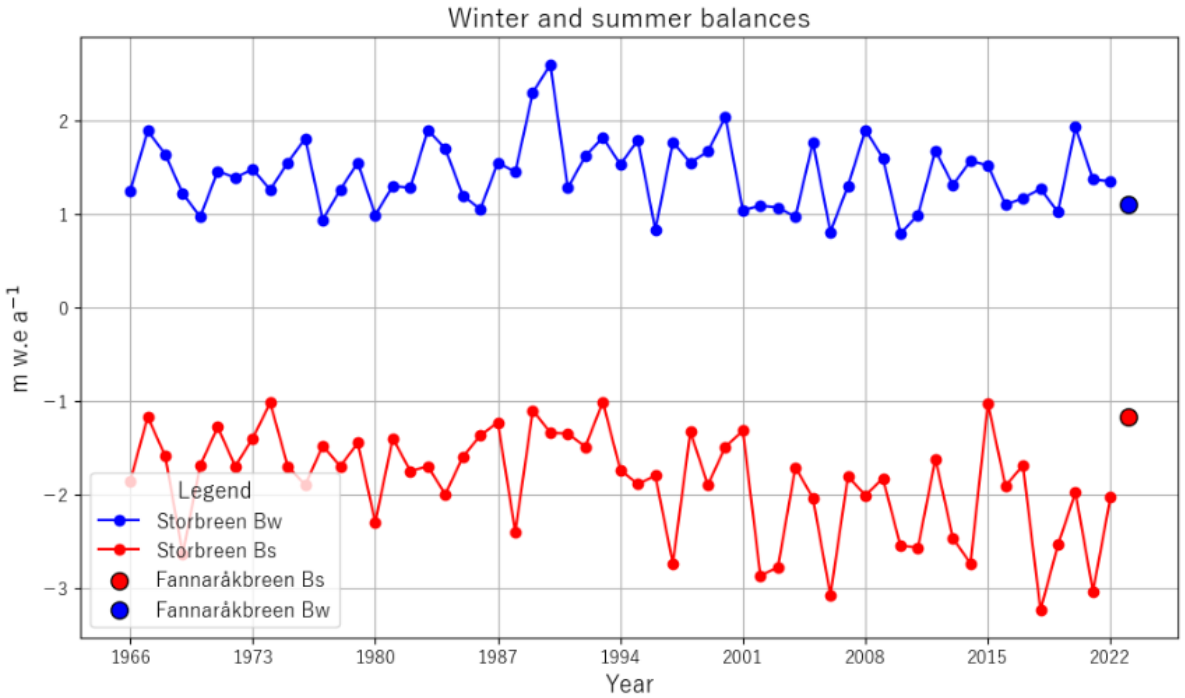

Figure 7.3: Glaciological winter (Bw) and summer (Bs) balances of Storbreen over the period of 1966 – 2022 and seasonal balances measured for Fannaråkbreen in and June and September 2023, visualised as points.

7.2.4 Regional context

Cumulative mass balance of Fannaråkbreen was plotted together with the glaciological mass balances of four other southern glaciers for comparison in Figure 7.4 - Nigardsbreen (a maritime outlet glacier of Jostedalsbreen), Storbreen, Gråsubreen, Hellstugubreen (more continental glaciers situated in Jotunheimen, east for Fannaråkbreen) (for glacier location refer to Figure 3.1). The surveys were conducted and published by The Norwegian Water Resources and Energy Directorate (NVE, 2024).

The last decade of the 20th century is characterised by advancements of Norwegian coastal glaciers due to high snowfall, influenced by high NAO and AO values (Nesje et al., 2008; Andreassen, Elvehøy, & Kjøllmoen, 2023), what is also marked by decreased rates of mass loss of the three glaciers used in this comparison. As this period fall between the surveys conducted in 1981 and 2004, it is not possible to observe the response of Fannaråkbreen. However, only a slight decrease in rate of mass loss observed between these dates may indicate that this period may also be possible to identify through the data if annual mass balances were measured. At around 2004, the rates of mass loss increased dramatically for the eastern glaciers including Fannaråkbreen, caused by smaller amounts of winter precipitation

and high summer temperatures (Nesje et al., 2008). This trend continued further, except for the maritime Nigardsbreen, which had only experienced a surplus since the period of advancement. Glacier size could be one of the explaining factors to this trend as well, since smaller glaciers are more sensitive to climatic forcing than larger systems (Grudd, 1990; Oerlemans, 1994; Nesje et al., 2008; Federici & Pappalardo, 2010). For the area of these glaciers refer to Table 7.1.

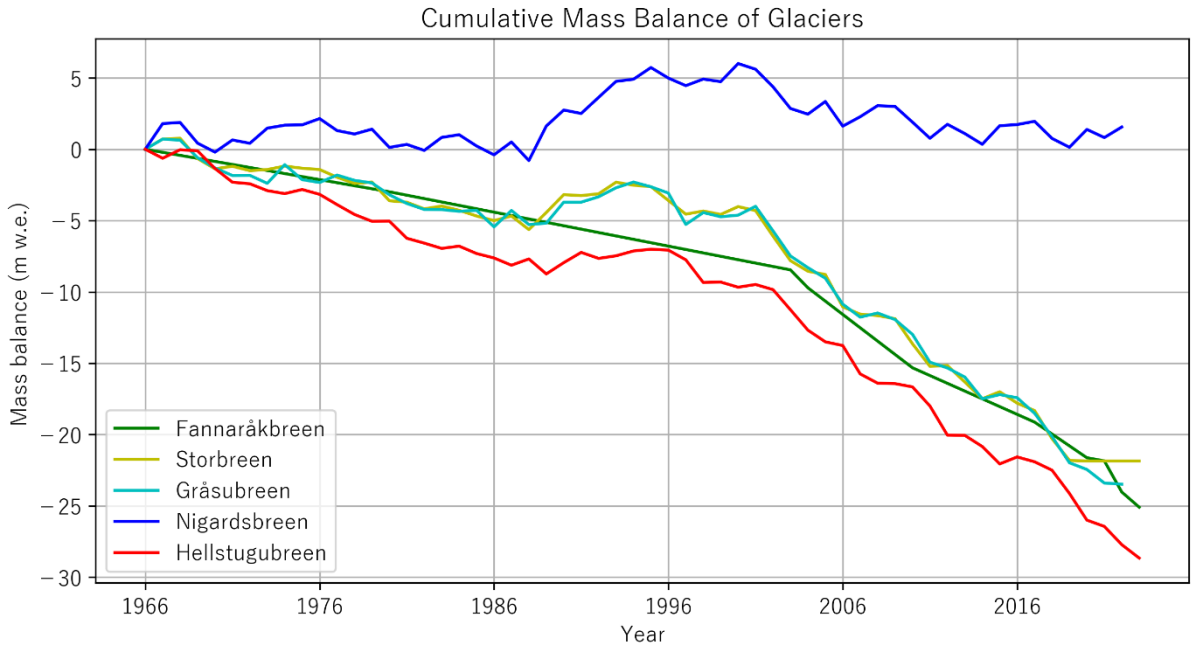

Figure 7.4: A comparison of cumulative geodetic mass balance of Fannaråkbreen with glaciological balances of the four other glaciers, also situated in southern Norway (NVE, 2024). Refer to Figure 3.1 for glacier locations.

On a national scale, between the years 1966 and 2023, Fannaråkbreen has been losing mass by on average -0.37 ± 0.02 m w. e. per year, what is a slightly faster rate than the estimated mean thinning for all Norwegian glaciers, -0.27 ± 0.02 m w. e. a^{-1} for the time period between 1960 and 2018 (Andreassen et al., 2020). This discrepancy may be explained by the difference in time periods for which mass balances were estimated. It is known that glaciers have been losing mass at increasing rates (Hugonnet, McNabb, et al., 2021), and the most recent years may have risen the average values for country's glaciers. Moreover, this may also be due to the differences in glacier geometry, topography, and regional factors such as continentality.

7.2.5 Comparison with global glacier change datasets

In this section, high-resolution surface elevation change data from 2004 to 2020 is compared to changes measured from 100 m DEMs derived from ASTER stereo-imagery covering the

period from 2000 to 2020, which were used in a global analysis of glacier change (Hugonnet, McNabb, et al., 2021). The changes of the study glacier were estimated based on photogrammetric and LiDAR surface models and were plotted for every 50 m of elevation in Figure 7.5, along with the changes estimated using satellite imagery. To evaluate these changes in a broader context, ASTER-derived elevation change was averaged across all glaciers in southern Norway for each elevation bin and plotted alongside the changes observed on Fannaråkbreen. Following the approach used in the aforementioned global study, which is based on glacier outlines generated during the Randolph Glacier Inventory in 2006 (RGI 6.0) (RGI Consortium, 2017), the average regional surface lowering was estimated at -0.56 m annually. Meanwhile, the study glacier exhibited average yearly thinning of -0.84 m, based on the satellite data.

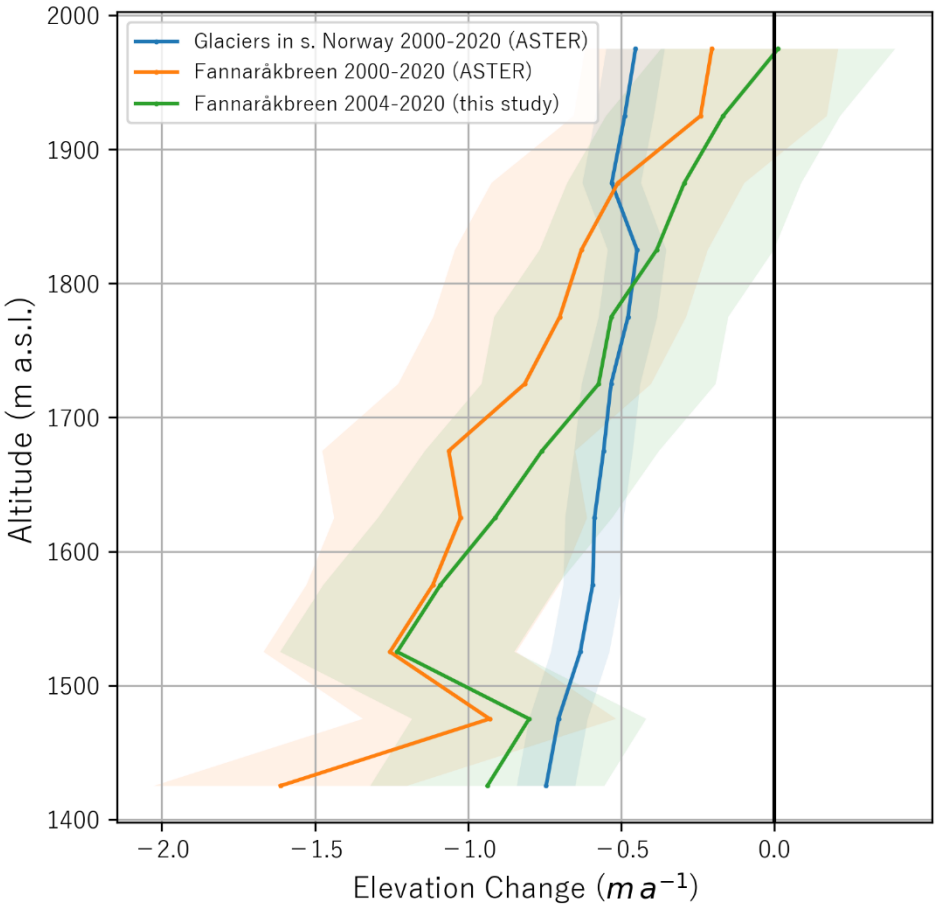

Figure 7.5: Glacier surface elevation changes per elevation bin of 50 m, based on ASTER data (blue and yellow, data from Hugonnet, McNabb, & Berthier, 2021) and a DoD, sourced from historical aerial imagery from 2004) and LiDAR data from 2020 (green line). The shaded area is a visualisation of one standard deviation.

Similar to the study area, the glaciers of southern Norway also experienced the most thinning at the lowest altitudes. However, the regional dataset indicates a somewhat smaller average glacier surface lowering at altitudes between 1820 – 1880 m a.s.l., which is not observed for

Fannaråkbreen. According to both datasets, Fannaråkbreen shows a slightly decreasing trend at the highest altitudes. Nonetheless, it also exhibits at least one such incident at the lower altitudes of its profile (1480 – 1520 m a.s.l.).

The changes on Fannaråkbreen are slightly overestimated in the ASTER dataset, averaging to -0,84 m per year, which is 0.26 m a^{-1} lower than the values derived from high-resolution data. However, the two datasets show good agreement between altitudes 1525 - 1625 m a.s.l. The majority of the glacier area is lies within these elevations (see hypsometry depicted in the Appendix, section 2), likely allowing the large pixels to capture changes more precisely than at higher altitudes. Compared to the regional thinning patterns, Fannaråkbreen exhibits a steeper slope of elevation changes, possibly due to its continentality, while the regional average is mostly influenced by the largest caps of Jostedalsbreen and Folgefonna, located in maritime climates.

7.3 The shrinkage of Fannaråkbreen in regional context

As seen in Figure 6.1, the area of Fannaråkbreen has been reducing at varying rates, except for the period 1981 and 2004, during which it increased by 6,57%. This increase is also attributed to more pronounced NAO index values during that period, which contributed to glacier mass gain, as described in section 7.2.3.

Area changes of the study glacier were compared to other glaciers form the region – Storbreen, Gråsubreen and Nigardsbreen (NVE, 2024). The area of these glaciers were surveyed on different dates and from different sources, thus annual change rate was estimated in order to make the changes comparable, as presented in Table 7.1. In Norway, as a consequence of glaciers having a negative mass budget between approximately 1960 and 2018, the total glaciated area shrunk by 10% on average (Andreassen et al., 2020). In the study region, with an exception being Nigardsbreen, all glaciers have also been reducing in size, however, at higher rates than the national average. Fannaråkbreen has been shrinking the fastest, which may be attributed to the use of high-resolution orthoimages for its delineation. In contrast, the area delineations of other glaciers might have been less accurate due to the reliance on old maps and coarser satellite images during glacier inventories (e.g., Andreassen et al., 2008; Andreassen et al., 2012; Andreassen, Nagy, et al., 2022).

Moreover, its relatively small size could have also played a role, as for instance, Gråsubreen has had a similar retreat rate and has the smallest area, again showing to the sensitivity of small-sized glaciers to climatic forcing. Nigardsbreen is the largest glacier and is a part of a

much larger glacier system of Jostedalsbreen, what may explain the lowest change rate. In addition, the topography of glacier bedrock plays a role in how quickly the area is lost, as it affects the ice thickness, what in turn results in some areas becoming free from ice quicker than others (Stokes et al., 2018). Also, this factor has a larger effect on smaller glaciers (Demuth et al., 2008; DeBeer & Sharp, 2009; Evans, 2009), what may explain this trend.

It should be noted that if all glacier units of Fannaråkbreen which appeared to belong to the same system based on imagery from 1955 – 1993 were included in the area analysis, the calculated loss would have been much larger. However, a decision was made to treat these areas separately because they exhibited signs of stagnation and vertical melting without immediate signs of significant movement, thus not meeting the criteria to be defined as a glacier (see section 2).

Table 7.1: Area change for the study glacier and the four other glaciers from the same region for comparison (refer to Figure 3.1 for locations of these glaciers).

Glacier	Period	Area at the beginning (km^2)	Area at the end (km^2)	Change, %	Annual change, %
Fannaråkbreen	1955-2023	3,9	2,47	-36,67	-0,54
Storbreen	1951-2019	5,73	4,87	-15,01	-0,21
Gråsubreen	1962-2019	2,36	1,744	-26,10	-0,46
Hellstugubreen	1962-2019	3,38	2,656	-21,42	-0,38
Nigardsbreen	1964-2017	48,31	44,94	-6,98	-0,13

7.4 The overall state of Fannaråkbreen

The assessment of changes in glacier mass balance over time must address the change in glacier area (Elsberg et al., 2001). In accordance to the global glacier observations, increasingly negative mass balance measured on a smaller glacier surface at each survey provides a clear evidence of climate becoming more and more unstable, causing higher amounts of glacier mass to be lost (WGMS, 2023).

With increasing melting rates, glacier surface thins and lowers the driving stresses that creates glacier flow. This normally cause the retreat of glacier front, however, as they slow down, vertical glacier wasting and fragmentation of the entire glacier may take place (WGMS, 2023). As seen from the images 1955 – 2004, a dissolution of one glacier unit to several seem to be the case here, causing a dilemma when delineating glacier area. This show that the glacier has been in negative balance for quite some time prior to the first image acquisition, and with the same trend continuing, it is very likely to disappear within the next decades.

This conclusion applies to several other glaciers from the observational network with long mass balance records, detailing the importance of improving the strategy to make sure that glacier monitoring can continue to be used in climate studies in the future. To do so, it is suggested to keep on monitoring the glaciers that has the longest records and include previously unmeasured glaciers – most importantly in regions that are not represented with enough samples (Hoelzle et al., 2017; Nussbaumer et al., 2017; Gärtner-Roer et al., 2019), alongside with an employment of numerical assessments of the available data using remote sensing (e.g., Huss & Hock, 2018; Hock et al., 2019; Rounce et al., 2023).

7.5 Remote sensing as a method for quantifying glacier change

Unmanned Aerial Vehicles (UAVs) have been increasingly used in glaciological investigations (Bhardwaj et al., 2016), and together with photogrammetry, it has been shown to be an effective and low-cost way to survey glaciers remotely (Hugenholtz et al., 2013). The results of this study also prove that the use of UAVs can be used to map glacier surface in high accuracy and high spatio-temporal resolution.

However, a care should be taken when choosing a type of UAV from the variety available. The choice should depend on the size of the glacier and the surrounding terrain as these factors influence the performance of different aircraft and the time needed to conduct the survey. Comparing the performance of the three different types of UAV used in this study, it can be concluded that those equipped with their own software for flight management and cameras suitable for surveying performed the best under cold and windy conditions, and provided data with minimal distortions.

To extract elevation information from the optical data, both UAV and historical aerial photographs alongside with photogrammetric methods were applied. As shown in section 2.5, the quality of the output DEM depends heavily on the sensor, accurate positioning, and external factors, such as sufficient surface texture needed for successful feature matching. The ice surface is normally relatively homogenous, what in some cases may result in low pixel scores. However, having flexibility in choosing the date to perform a UAV survey may help mitigate this. Nonetheless, it becomes more problematic when analysing archival data acquired in coarser resolution, without customisation of parameters to fit glacier monitoring and overexposing snow and ice areas.

Good alignment of surface models is another crucial factor influencing uncertainties of the geodetic method based on remotely sensed data. However, co-registration seeking to align

two models may not always be successful with the available tools, and as discussed in section 7.1.4, the bias in the 2022 DEM may have led to an overestimation of mass balance. This dataset was very important for estimation of seasonal mass balance and taken early in the master's program. Under other circumstances, it would be excluded from the analysis and a new attempt would have been made utilising an UAV more suitable for mapping large areas.

7.6 Further work

Based on the current experience, a repetition of this study using an UAV of the same type and specifically developed for mapping large areas, may be beneficial. For improved accuracy of cumulative mass balance values, it is recommended to combine field measurements of snow density at taken at various glacier altitudes in June, as density conversion is identified as a source of error when comparing seasonal and annual volumes and mass (section 7.2.1). Additionally, it can be advised to ensure that datasets to be georeferenced indirectly using GCPs cover more stable terrain for better model co-registration. Additionally, a more thorough analysis linking seasonal glacier variations to fluctuations of climate may be of interest, as it would allow estimation of glacier response time, allowing to evaluate its sensitivity to climatic forcing. Lastly, given the series of lakes downstream of the glacier, further study of sediment cores from these lakes could reveal glacier fluctuations and associated climatic changes throughout the Holocene.

8. Conclusion

Based on the surface models derived from high-resolution aerial imagery it has been estimated that Fannaråkbreen has been losing an average of -1.06 ± 0.12 million m^3 of its volume, or -0.37 ± 0.02 m w. e. each year from 1966 to 2023 putting it in line with the national average of -0.27 ± 0.02 m w. e. a^{-1} (1960 - 2018). During the same time, it experienced an area reduction of -0.74% a^{-1}. The period with the fastest observed melt rate was 2020 - 2022, during which the annual geodetic mass balance was quantified to be -2.18 ± 0.11 m w. e. This figure, however, may be an overestimation due to biases in the 2022 DEM. Additionally, seasonal balances were quantified with high accuracy, with winter accumulation estimated at 1.10 ± 0.05 m w. e., and summer mass loss totalling -1.71 ± 0.09 m w. e., indicating a negative development for the last survey period.

It has been shown that the glacier has been losing mass at increasing rates, consistent with findings of the global and regional-scale study on glacier change. Compared to other glaciers

within the area, Fannaråkbreen's response to atmospheric changes showed similarities with other continental glaciers of similar size, highlighting size being an important factor in climate sensitivity. A relatively good agreement was found between the patterns of glaciological mass balance for Storbreen and the geodetic balance of Fannaråkbreen, although some deviations have been caused by differences in size and local climate variations. However, it remains an open question how including disintegrated glacier parts in the analysis and handling significantly decreased glacier areas during DEM differencing would affect the results.

Historical aerial imagery can be combined with other high-resolution optical data to reconstruct mass balance over time, provided there is sufficient surface contrast required for photogrammetric processing. Data acquisition using UAVs with direct image georeferencing eliminated the need for resources required to establish GCPs, making surveying of small and hard-to-access glaciers feasible, providing more accurate results than coarser satellite data. Moreover, the utilisation of Structure-from-Motion photogrammetric algorithms, allows for processing of large quantities of imagery and the extraction of elevation data form historical photographs lacking camera calibration reports by solving interior orientations.

Overall, measuring glacier mass balance is important, as it offers valuable information about the state of the current and past climates across a variety of scales. Furthermore, assessing the patterns of mass accumulation and ablation in high-resolution helps understand critical factors influencing glacial responses and can aid in modelling glacier behaviour in remote areas to assess the impacts on sea-level rise, fresh-water availability and related geo-hazards.

9. References

Agisoft LLC (2024). *Features: professional edition*. Retrieved 26.03.2024 from https://www.agisoft.com/features/professional-edition/

Ahlmann, W. H. (1919). Geomorphological studies in Norway. *Geografiska Annaler*, *1*(1), 193-255.

Ahlmann, W. H. (1922). Glaciers in Jotunheimen and their physiography. *Geografiska Annaler*, *4*, 1-57.

Ahlmann, W. H. (1948). Glaciological Research on the North Atlantic Coasts No. I, pp. 84. Royal Geographical Society, London. *R.G.S. Research Series* (1), 83. https://doi.org/10.1002/qj.49707532317

Al Shouny, A., Yakoub, N., & Hosny, M. (2017). Evaluating the Performance of Using PPK-GPS Technique in Producing Topographic Contour Map. *Marine Geodesy*, *40*. https://doi.org/10.1080/01490419.2017.1321594

Andreassen, L. M., & Elvehøy, H. (2021). *Norwegian Glacier Reference Dataset for Climate Change Studies* (NVE Rapport, Issue 33/2021) https://publikasjoner.nve.no/rapport/2021/rapport2021_33.pdf

Andreassen, L. M., Elvehøy, H., & Kjøllmoen, B. (2002). Using aerial photography to study glacier changes in Norway. *Annals of Glaciology*, *34*, 343-348. https://doi.org/10.3189/172756402781817626

Andreassen, L. M., Elvehøy, H., & Kjøllmoen, B. (2023). *Glaciological investigations in Norway 2022* (23/2023).

Andreassen, L. M., Elvehøy, H., Kjøllmoen, B., & Belart, J. M. C. (2020). Glacier change in Norway since the 1960s – an overview of mass balance, area, length and surface elevation changes. *Journal of Glaciology*, *66*(256), 313-328. https://doi.org/10.1017/jog.2020.10

Andreassen, L. M., Elvehøy, H., Kjøllmoen, B., & Engeset, R. V. (2016). Reanalysis of long-term series of glaciological and geodetic mass balance for 10 Norwegian glaciers. *The Cryosphere*, *10*(2), 535-552. https://doi.org/10.5194/tc-10-535-2016

Andreassen, L. M., Elvehøy, H., Kjøllmoen, B., Engeset, R. V., & Haakensen, N. (2005). Glacier mass-balance and length variation in Norway. *Annals of Glaciology*, *42*, 317-325. https://doi.org/10.3189/172756405781812826

Andreassen, L. M., Elvehøy, H., Kjøllmoen, B., & Storheil, S. (2022). *Glaciological investigations in Norway* (27/2022). https://publikasjoner.nve.no/rapport/2022/rapport2022_27.pdf

Andreassen, L. M., Nagy, T., Kjøllmoen, B., & Leigh, J. R. (2022). An inventory of Norway's glaciers and ice-marginal lakes from 2018–19 Sentinel-2 data. *Journal of Glaciology*, 1-22. https://doi.org/10.1017/jog.2022.20

Andreassen, L. M., & Oerlemans, J. (2009). Modelling long-term summer and winter balances and the climate sensitivity of storbreen, norway. *Geografiska Annaler: Series A, Physical Geography*, *91*(4), 233-251. https://doi.org/10.1111/j.1468-0459.2009.00366.x

Andreassen, L. M., Paul, F., Kääb, A., & Hausberg, J. E. (2008). Landsat-derived glacier inventory for Jotunheimen, Norway, and deduced glacier changes since the 1930s. *The Cryosphere*, *2*, 131-145. www.the-cryosphere.net/2/131/2008/

Andreassen, L. M., Robson, B. A., Sjursen, K. H., Elvehøy, H., Kjøllmoen, B., & Carrivick, J. L. (2023). Spatio-temporal variability in geometry and geodetic mass balance of Jostedalsbreen ice cap, Norway. *Annals of Glaciology*, *64*(90), 26-43. https://doi.org/10.1017/aog.2023.70

Andreassen, L. M., Winsvold, S. H., Paul, F., & Hausberg, J. E. (2012). *Inventory of Norwegian glaciers*. NVE.

Aune, B. (1993). *Temperaturnormaler, normalperiode 1961–1990* (2/93). (Klima, Issue 2/93). https://ia800504.us.archive.org/16/items/temperaturnormaler-1961-1990/temperaturnormaler-1961-1990_text.pdf

Bakke, J., & Nesje, A. (2011). Equilibrium-Line Altitude (ELA). In V. P. Singh, P. Singh, & U. K. Haritashya (Eds.), *Encyclopedia of Snow, Ice and Glaciers. Encyclopedia of Earth Sciences Series* (pp. 268-277). Springer. https://doi.org/10.1007/978-90-481-2642-2_140

Baltsavias, E. P., Favey, E., Bauder, A., Bosch, H., & Pateraki, M. (2001). Digital Surface Modelling by Airborne Laser Scanning and Digital Photogrammetry for Glacier Monitoring. *The Photogrammetric Record*, *17*(98), 243-273. https://doi.org/10.1111/0031-868x.00182

Bamber, J. L., Krabill, W., Raper, V., & Dowdeswell, J. A. (2004). Anomalous recent growth of part of a large Arctic ice cap: Austfonna, Svalbard. *Geophysical Research Letters*, *31*(12). https://doi.org/10.1029/2004GL019667

Bamber, J. L., & Rivera, A. (2007). A review of remote sensing methods for glacier mass balance determination. *Global and Planetary Change*, *59*(1-4), 138-148. https://doi.org/10.1016/j.gloplacha.2006.11.031

Basantes-Serrano, R., Rabatel, A., Vincent, C., & Sirguey, P. (2018). An optimized method to calculate the geodetic mass balance of mountain glaciers. *Journal of Glaciology*, *64*(248), 917-931. https://doi.org/10.1017/jog.2018.79

Base, W. K. (2024). *PPK geotagging*. Retrieved 29.04.2024 from https://knowledge.wingtra.com/en/ppk-geotagging

Bash, E., Moorman, B., & Gunther, A. (2018). Detecting Short-Term Surface Melt on an Arctic Glacier Using UAV Surveys. *Remote Sensing*, *10*(10). https://doi.org/10.3390/rs10101547

Baurley, N. R., & Hart, J. K. (2022). Evolution of the seasonal dynamics of the lake-terminating glacier Fjallsjökull, southeast Iceland, inferred using high-resolution repeat UAV imagery. https://eartharxiv.org/repository/view/4842/

Belart, J. M. C., Berthier, E., Magnússon, E., Anderson, L. S., Pálsson, F., Thorsteinsson, T., Howat, I. M., Aðalgeirsdóttir, G., Jóhannesson, T., & Jarosch, A. H. (2017). Winter mass balance of Drangajökull ice cap (NW Iceland) derived from satellite sub-meter stereo images. *The Cryosphere*, *11*, 1501–1517. https://doi.org/10.5194/tc-11-1501-2017

Benn, D. I., & Evans, D. J. A. (2010). *Glaciers & glaciation* (2 ed.). Hodder Education.

Beraud, L., Cusicanqui, D., Rabatel, A., Brun, F., Vincent, C., & Six, D. (2023). Glacier-wide seasonal and annual geodetic mass balances from Pléiades stereo images: application to the Glacier d'Argentière, French Alps. *Journal of Glaciology*, *69*(275), 525-537. https://doi.org/10.1017/jog.2022.79

Berthier, E., Vincent, C., Magnússon, E., Gunnlaugsson, Á. Þ., Pitte, P., Le Meur, E., Masiokas, M., Ruiz, L., Pálsson, F., Belart, J. M. C., & Wagnon, P. (2014). Glacier topography and elevation changes derived from Pléiades sub-meter stereo images. *The Cryosphere*, *8*(6), 2275-2291. https://doi.org/10.5194/tc-8-2275-2014

Besl, P. J., & McKay, N. D. (1992). A method for registration of 3-D shapes. *IEEE Transactions on Pattern Analysis and Machine Intelligence*, *14*(2), 239-256. https://doi.org/10.1109/34.121791

Bhardwaj, A., Sam, L., Akanksha, Martín-Torres, F. J., & Kumar, R. (2016). UAVs as remote sensing platform in glaciology: Present applications and future prospects. *Remote Sensing of Environment*, *175*, 196-204. https://doi.org/10.1016/j.rse.2015.12.029

Bishop, M. P., Olsenholler, J. A., Shroder, J. F., Barry, R. G., Raup, B. H., Bush, A. B. G., Copland, L., Dwyer, J. L., Fountain, A. G., Haeberli, W., Kääb, A., Paul, F., Hall, D. K., Kargel, J. S., Molnia, B. F., Trabant, D. C., & Wessels, R. (2004). Global Land Ice Measurements from Space (GLIMS): Remote Sensing and GIS Investigations of the Earth's Cryosphere. *Geocarto International*, *19*(2), 57-84. https://doi.org/10.1080/10106040408542307

Bojinski, S., Verstraete, M., Peterson, T. C., Richter, C., Simmons, A., & Zemp, M. (2014). The Concept of Essential Climate Variables in Support of Climate Research, Applications, and Policy. *Bulletin of the American Meteorological Society*, *95*(9), 1431-1443. https://doi.org/10.1175/bams-d-13-00047.1

Bolch, T., Yao, T., Kang, S., Buchroithner, M. F., Scherer, D., Maussion, F., Huintjes, E., & Schneider, C. (2010). A glacier inventory for the western Nyainqentanglha Range and the Nam Co Basin, Tibet, and glacier changes 1976–2009. *The Cryosphere*, *4*(3), 419-433. https://doi.org/10.5194/tc-4-419-2010

Bolstad, P. V., & Stowe, T. J. (1994). An evaluation of DEM accuracy: elevation, slope, and aspect. *Photogrammetric Engineering and Remote Sensing*, *60*, 1327-1332. https://api.semanticscholar.org/CorpusID:130633210

Braithwaite, R. J. (2002). Glacier mass balance: the first 50 years of international monitoring. *Progress in Physical Geography*, *26*(1), 76-95. https://doi.org/10.1191/0309133302pp326ra

Braithwaite, R. J. (2009). After six decades of monitoring glacier mass balance we still need data but it should be richer data. *Annals of Glaciology*, *50*(50), 191-197. https://doi.org/10.3189/172756409787769573

Braithwaite, R. J., & Zhang, Y. (1999). Modelling changes in glacier mass balance that may occur as a result of climate changes. *Geografiska Annaler, Series A: Physical Geography*, *81*(4), 489-496. https://doi.org/10.1111/j.0435-3676.1999.00078.x

Brown, J., Harper, J., & Humphrey, N. (2010). Cirque glacier sensitivity to 21st century warming: Sperry Glacier, Rocky Mountains, USA. *Global and Planetary Change*, *74*(2), 91-98. https://doi.org/10.1016/j.gloplacha.2010.09.001

Cao, B., Guan, W., Li, K., Pan, B., & Sun, X. (2021). High-Resolution Monitoring of Glacier Mass Balance and Dynamics with Unmanned Aerial Vehicles on the Ningchan No. 1 Glacier in the Qilian Mountains, China. *Remote Sensing*, *13*(14). https://doi.org/10.3390/rs13142735

Carrivick, J. L., Andreassen, L. M., Nesje, A., & Yde, J. C. (2022). A reconstruction of Jostedalsbreen during the Little Ice Age and geometric changes to outlet glaciers since then. *Quaternary Science Reviews*, *284*. https://doi.org/10.1016/j.quascirev.2022.107501

Carrivick, J. L., Smith, M. W., & Quincey, D. J. (2016). *Structure form motion in geosciences*. Wiley-Blackwell.

CATALYST.Earth. (2024a). *Catalyst Professional*. Retrieved 26.03.2024 from https://catalyst.earth/solutions/catalyst-professional/

CATALYST.Earth. (2024b). *Extracting a digital elevation model from epipolar pairs*. Retrieved 15.03.2024 from https://catalyst.earth/catalyst-system-files/help/tasks/orthoengine_t/Chapter_611a.html

CATALYST.Earth. (2024c). *Understanding camera calibration data*. Retrieved 19.03.2024 from https://catalyst.earth/catalyst-system-files/help/concepts/orthoengine_c/Chapter_43.html

Che, Y., Wang, S., Yi, S., Wei, Y., & Cai, Y. (2020). Summer mass balance and surface velocity derived by unmanned aerial vehicle on debris-covered region of Baishui

River Glacier No. 1, Yulong Snow Mountain. *Remote Sensing*, *12*(20), 3280. https://www.mdpi.com/2072-4292/12/20/3280
Clarke, G. K. C., Jarosch, A. H., Anslow, F. S., Radić, V., & Menounos, B. (2015). Projected deglaciation of western Canada in the twenty-first century. *Nature Geoscience*, *8*(5), 372-377. https://doi.org/10.1038/ngeo2407
Cogley, G. J. (1999). Effective sample size for glacier mass balance. *Geografiska Annaler*, *81A*, 497-507. https://doi.org/10.1111/1468-0459.00079
Cogley, G. J., Hock, R., Rasmussen, L. A., Arendt, A. A., Bauder, A., Braithwaite, R. J., Jansson, P., Kaser, G., Möller, M., Nicholson, L., & Zemp, M. (2011). *Glossary of Glacier Mass Balance and Related Terms.* https://unesdoc.unesco.org/ark:/48223/pf0000192525
Collins, D. N. (1984). Water and mass balance measurements in glacierised drainage basins. *Geografiska Annaler*, *66A*(3), 197-214. https://doi.org/10.1080/04353676.1984.11880109
Consortium, R. (2017). *Randolph Glacier Inventory (RGI) - A Dataset of Global Glacier Outlines: Version 6.0.* [Technical Report] (Global Land Ice Measurements from Space). https://www.glims.org/RGI/00_rgi60_TechnicalNote.pdf
Cox, L. H., & March, R. S. (2004). Comparison of geodetic and glaciological mass-balance techniques, Gulkana Glacier, Alaska, U.S.A. *Journal of Glaciology*, *50*(170), 363-370. https://doi.org/10.3189/172756504781829855
Csatho, B. M., Schenk, A. F., van der Veen, C. J., Babonis, G., Duncan, K., Rezvanbehbahani, S., van den Broeke, M. R., Simonsen, S. B., Nagarajan, S., & van Angelen, J. H. (2014). Laser altimetry reveals complex pattern of Greenland Ice Sheet dynamics. *Proceedings of the National Academy of Sciences*, *111*(52), 18478-18483. https://doi.org/10.1073/pnas.1411680112
Cuffey, K. M., & Paterson, W. S. B. (2010). *The physics of glaciers* (Fourth edition. ed.). Butterworth-Heinemann.
Dahl, S. O., & Nesje, A. (1992). Paleoclimatic implications based on equilibrium-line altitude depressions of reconstructed Younger Dryas and Holocene cirque glaciers in inner Nordfjord, western Norway. *Palaeogeography, Palaeoclimatology, Palaeoecology*, *94*(1), 87-97. https://doi.org/10.1016/0031-0182(92)90114-K
Dahl, S. O., & Nesje, A. (1994). Holocene glacier fluctuations at Hardangerjoekulen, central southern Norway: a high-resolution composite chronology from lacustrine and terrestrial deposits. *The Holocene*, *4*, 436-468. https://doi.org/10.1177/095968369400400306
DeBeer, C. M., & Sharp, M. J. (2009). Topographic influences on recent changes of very small glaciers in the Monashee Mountains, British Columbia, Canada. *Journal of Glaciology*, *55*(192), 691-700. https://doi.org/10.3189/002214309789470851
Dehecq, A., Gardner, A. S., Alexandrov, O., McMichael, S., Hugonnet, R., Shean, D., & Marty, M. (2020). Automated Processing of Declassified KH-9 Hexagon Satellite Images for Global Elevation Change Analysis Since the 1970s. *Frontiers in Earth Science*, *8*. https://doi.org/10.3389/feart.2020.566802
Demuth, M., Pinard, V., Pietroniro, A., Luckman, B., Hopkinson, C., Dornes, P., & Comeau, L. (2008). Recent and past-century variations in the glacier resources of the Canadian Rocky Mountains: Nelson River system. *Terra Glacialis* Special issue(12), 27-52.
DJI-Enterprise. (2021). *Aerial Surveying Just Got Smart*. Retrieved 12.04.2024 from https://enterprise-insights.dji.com/blog/smart-oblique-capture
Dyurgerov, M. (2002). *Glacier mass balance and regime: data of measurements and analysis* (M. F. Meier & R. L. Armstrong, Eds. Vol. 55). Citeseer. https://instaar.colorado.edu/uploads/occasional-papers/OP55_glaciers.pdf

Dyurgerov, M. B., & Meier, M. F. (1999). Analysis of Winter and Summer Glacier Mass Balances. *Geografiska Annaler: Series A, Physical Geography*, *81*(4), 541-554. https://doi.org/10.1111/1468-0459.00082

Dyurgerov, M. B., & Meier, M. F. (2000). Twentieth century climate change: evidence from small glaciers. *Proceedings of the National Academy of Sciences USA*, *97*(4), 1406-1411. https://doi.org/10.1073/pnas.97.4.1406

Easy, M. M. (2024). *Map Pilot Pro, Superior Data Collection for Professionals*. Retrieved 29.04.2024 from https://www.mapsmadeeasy.com/map_pilot/

Ekaso, D., Nex, F., & Kerle, N. (2020). Accuracy assessment of real-time kinematics (RTK) measurements on unmanned aerial vehicles (UAV) for direct geo-referencing. *Geo-spatial Information Science*, *23*(2), 165-181. https://doi.org/10.1080/10095020.2019.1710437

Eker, R., Alkan, E., & Aydın, A. (2021). A Comparative Analysis of UAV-RTK and UAV-PPK Methods in Mapping Different Surface Types. *European Journal of Forest Engineering*, *7*(1), 12-25. https://doi.org/10.33904/ejfe.938067

Elsberg, D. H., Harrison, W. D., Echelmeyer, K. A., & Krimmel, R. M. (2001). Quantifying the effects of climate and surface change on glacier mass balance. *Journal of Glaciology*, *47*(159), 649-658. https://doi.org/10.3189/172756501781831783

Eltner, A., Baumgart, P., Maas, H.-G., & Faust, D. (2014). Multi-temporal UAV data for automatic measurement of rill and interrill erosion on loess soil. *Earth Surface Processes and Landforms*, *40*. https://doi.org/10.1002/esp.3673

Eltner, A., Kaiser, A., Castillo, C., Rock, G., Neugirg, F., & Abellán, A. (2016). Image-based surface reconstruction in geomorphometry – merits, limits and developments. *Earth Surf. Dynam.*, *4*(2), 359-389. https://doi.org/10.5194/esurf-4-359-2016

Eltner, A., & Sofia, G. (2020). Structure from motion photogrammetric technique. In *Remote Sensing of Geomorphology* (pp. 1-24). https://doi.org/10.1016/b978-0-444-64177-9.00001-1

ESRI. (2024). *2D, 3D & 4D GIS Mapping - ArcGIS Pro*. Retrieved 25.03.2024 from https://www.esri.com/en-us/arcgis/products/arcgis-pro/overview

Evans, I. S. (2009). A brief report on recent change in small glaciers in British Columbia, Canada. *Quaternary Newsletter*, *118*, 28-31.

Falaschi, D., Lenzano, M. G., Villalba, R., Bolch, T., Rivera, A., & Lo Vecchio, A. (2019). Six Decades (1958–2018) of Geodetic Glacier Mass Balance in Monte San Lorenzo, Patagonian Andes. *Frontiers in Earth Science*, *7*. https://doi.org/10.3389/feart.2019.00326

Federici, P. R., & Pappalardo, M. (2010). Glacier retreat in the Maritime Alps area. *Geografiska Annaler: Series A, Physical Geography*, *92*(3), 361-373.

Fischer, A. (2010). Glaciers and climate change: Interpretation of 50 years of direct mass balance of Hintereisferner. *Global and Planetary Change*, *71*(1-2), 13-26. https://doi.org/10.1016/j.gloplacha.2009.11.014

Fischer, A. (2011). Comparison of direct and geodetic mass balances on a multi-annual time scale. *The Cryosphere*, *5*(1), 107-124. https://doi.org/10.5194/tc-5-107-2011

Flaticon. (2024). *Access 14.8M+ vector icons & stickers.* Retrieved 08.04.2024 from https://www.flaticon.com/

Forel, F. A. (1895). *International Commission on Glaciers, Les variations periodiques des glaciers, discours preliminaire.* (Archives des sciences physiques et naturelles). https://doi.org/10.1017/S0016756800179038

Fountain, A. G., Hoffman, M. J., Granshaw, F. D., & Riedel, J. L. (2009). The 'benchmark glacier' concept – does it work? Lessons from the North Cascade Range, USA. *Annals of Glaciology*, *50*, 163 - 168. https://doi.org/10.3189/172756409787769690

Fox, A. J., & Nuttall, A. M. (1997). Photogrammetry as A Research Tool for Glaciology. *The Photogrammetric Record*, *15*(89), 725-737. https://doi.org/10.1111/0031-868x.00081
Furukawa, Y., & Ponce, J. (2010). Accurate, Dense, and Robust Multiview Stereopsis. *IEEE Transactions on Pattern Analysis and Machine Intelligence*, *32*(8), 1362-1376. https://doi.org/10.1109/TPAMI.2009.161
Gardelle, J., Berthier, E., & Arnaud, Y. (2012). Impact of resolution and radar penetration on glacier elevation changes computed from DEM differencing. *Journal of Glaciology*, *58*(208), 419-422. https://doi.org/10.3189/2012JoG11J175
Gardelle, J., Berthier, E., Arnaud, Y., & Kääb, A. (2013). Region-wide glacier mass balances over the Pamir-Karakoram-Himalaya during 1999–2011. *The Cryosphere*, *7*(4), 1263-1286. https://doi.org/10.5194/tc-7-1263-2013
Giesen, R. H., Andreassen, L. M., Broeke, M. R. v. d., & Oerlemans, J. (2008). Compraison of the meteorology and surface energy balance at Storbreen and Midtdalsbreen southern norway. *The Cryosphere Discussions*, *2*, 873-916. https://doi.org/10.5194/tc-3-57-2009
Girod, L., Nuth, C., Kääb, A., McNabb, R., & Galland, O. (2017). MMASTER: Improved ASTER DEMs for Elevation Change Monitoring. *Remote Sensing*, *9*(7). https://doi.org/10.3390/rs9070704
Gisnås, K., Etzelmüller, B., Farbrot, H., Schuler, T. V., & Westermann, S. (2013). CryoGRID 1.0: permafrost distribution in Norway estimated by a spatial numerical model. *Permafrost and Periglacial Processes*, *24*, 2-19. https://doi.org/10.1002/ppp.1765
Gisnås, K., Etzelmüller, B., Lussana, C., Hjort, J., Sannel, B. K., Isaksen, K., Westermann, S., Kuhry, P., Christiansen, H. H., Frampton, A., & Åkerman, J. (2017). Permafrost map for Norway, Sweden and Finland. *Permafrost and Periglacial Processes*, *28*, 359-378. https://doi.org/10.1002/ppp.1922
Gjessing, J. (1967). Norway's paleic surface. *Norsk Geografisk Tidsskrift*, *21*, 69-132. https://doi.org/10.1080/00291956708621854
Gjessing, J. (1978). *Norges landformer*. Universitetsforlaget Oslo/Bergen/Tromsø.
Gomarasca, M. A. (2009). Elements of Photogrammetry. In *Basics of Geomatics*. Springer. https://doi.org/10.1007/978-1-4020-9014-1_3
Gonçalves, J. A. (2016). Automatic orientation and mosaicing of archived aerial photography using structure from motion. *The International Archives of the Photogrammetry, Remote Sensing and Spatial Information Sciences*, *XL-3/W4*, 123-126. https://doi.org/10.5194/isprs-archives-XL-3-W4-123-2016
Granshaw, F. D., & Fountain, A. G. (2006). Glacier change (1958-1998) in the North Cascades National Park Complex, Washington, USA. *Journal of Glaciology*, *52*, 251-256. https://doi.org/10.3189/172756506781828782
Granshaw, S. I. (1980). Bundle adjustment methods in engineering photogrammetry. *The Photogrammetric Record*, *10*(56), 181-207. https://doi.org/10.1111/j.1477-9730.1980.tb00020.x
Gruber, A., Wessel, B., Huber, M., & Roth, A. (2012). Operational TanDEM-X DEM calibration and first validation results. *ISPRS Journal of Photogrammetry and Remote Sensing*, *73*, 39-49. https://doi.org/10.1016/j.isprsjprs.2012.06.002
Grudd, H. (1990). Small Glaciers as Sensitive Indicators of Climatic Fluctuations. *Geografiska Annaler*, *72*(1), 119-123. https://doi.org/10.1080/04353676.1990.11880305
Gruen, A. (2012). Development and Status of Image Matching in Photogrammetry. *The Photogrammetric Record*, *27*(137), 36-57. https://doi.org/10.1111/j.1477-9730.2011.00671.x

Gärtner-Roer, I., Nussbaumer, S., Hüsler, F., & Zemp, M. (2019). Worldwide Assessment of National Glacier Monitoring and Future Perspectives. *Mountain Research and Development*, *39*. https://doi.org/10.1659/MRD-JOURNAL-D-19-00021.1

Haeberli, W. (1998). Historical evolution and operational aspects of worldwide glacier monitoring. *Studies and reports in hydrology*, *56*, 35-51. http://pascal-francis.inist.fr/vibad/index.php?action=getRecordDetail&idt=1736303

Haeberli, W. (2011). Glacier Mass Balance. In V. P. Singh, P. Singh, & U. K. Haritashya (Eds.), *Encyclopedia of Snow, Ice and Glaciers* (pp. 399-408). Springer. https://doi.org/10.1007/978-90-481-2642-2_341

Haeberli, W., & Holzhauser, H. (2003). Alpine glacier mass changes during the past two millennia. *Pages News*, *11*(1), 13-15. https://doi.org/10.22498/PAGES.11.1.13

Hanssen-Bauer, I. (2015). *Klima i Norge 2100 - Kunnskapsgrunnlag for klimatilpasning, oppdatert i 2015.* https://www.met.no/kss/_/attachment/download/4140d58a-d368-4145-9c1f-e85de3d5fe74:1760c9f2c4acae80b91f61299dcf9e1187ce81cb/klima-i-norge-2100-opplag2.pdf

Hanssen-Bauer, I., & Førland, E. J. (1998). *Annual and seasonal precipitation variations in Norway 1896-1997* (Report 27/98). https://www.met.no/publikasjoner/met-report/met-report-1998/_/attachment/download/f8fca59d-91d9-4c9c-8bc0-970c0ba4ef26:64d94ddd7b00c6046c1a5b8fa5568508f9092553/MET-report-27-1998.pdf

Haug, T., Rolstad, C., Elvehøy, H., Jackson, M., & Maalen-Johansen, I. (2009). Geodetic mass balance of the western Svartisen ice cap, Norway, in the periods 1968–1985 and 1985–2002. *Annals of Glaciology*, *50*(50), 119-125. https://doi.org/10.3189/172756409787769528

Hock, R., Bliss, A., Marzeion, B. E. N., Giesen, R. H., Hirabayashi, Y., Huss, M., RadiĆ, V., & Slangen, A. B. A. (2019). GlacierMIP – A model intercomparison of global-scale glacier mass-balance models and projections. *Journal of Glaciology*, *65*(251), 453-467. https://doi.org/10.1017/jog.2019.22

Hock, R., & Jensen, H. (1999). Application of kriging interpolation for glacier mass balance computations. *Geografiska Annaler*, *81A*(4), 611-619. https://doi.org/10.3189/S0260305500012192

Hock, R., & Noezli, C. (1997). Areal melt and discharge modelling of Storglaciären, Sweden. *Annals of Glaciology*, *24*, 211-216. https://doi.org/10.3189/S0260305500012192

Hoelzle, M., Azisov, E., Barandun, M., Huss, M., Farinotti, D., Gafurov, A., Hagg, W., Kenzhebaev, R., Kronenberg, M., Machguth, H., Merkushkin, A., Moldobekov, B., Maxim, P., Saks, T., Salzmann, N., Schöne, T., Tarasov, Y., Usubaliev, R., Vorogushyn, S., & Zemp, M. (2017). Re-establishing glacier monitoring in Kyrgyzstan and Uzbekistan, Central Asia. *Geoscientific Instrumentation, Methods and Data Systems Discussions*, 1-36. https://doi.org/10.5194/gi-2017-31

Hoinkes, H. (1970). Methoden und Möglichkeiten von Massenhaushaltsstudien auf Gletschern: Ergebnisse der Messreihe Hintereisferner (Ötztaler Alpen) 1953–1968. *Zeitschrift für Gletscherkunde und Glazialgeologie*, *6*(1-2), 37-89. http://repository.uibk.ac.at/viewer.alo?objid=1021565&page=1&viewmode=fulltextview

Holmlund, E. S. (2021). Aldegondabreen glacier change since 1910 from structure-from-motion photogrammetry of archived terrestrial and aerial photographs: utility of a historic archive to obtain century-scale Svalbard glacier mass losses. *Journal of Glaciology*, *67*(261), 107-116. https://doi.org/10.1017/jog.2020.89

Holmlund, E. S., & Holmlund, P. (2019). Constraining 135 years of mass balance with historic structure-from-motion photogrammetry on Storglaciären, Sweden.

Geografiska Annaler: Series A, Physical Geography, *101*(3), 195-210. https://doi.org/10.1080/04353676.2019.1588543
Holmlund, P., Karlén, W., & Grudd, H. (1996). Fifty Years of Mass Balance and Glacier Front Observations at the Tarfala Research Station. *Geografiska Annaler: Series A, Physical Geography*, *78*(2-3), 105-114. https://doi.org/10.1080/04353676.1996.11880456
Hormes, A. (2009). Radiocarbon wiggle-match dating of proglacial lake sediments – Implications for the 8.2 ka event. *Quaternary Geochronology*, *4*(4), 267-277. https://doi.org/10.1016/j.quageo.2008.12.004
Huber, J., McNabb, R. W., & Zemp, M. (2020). Elevation Changes of West-Central Greenland Glaciers From 1985 to 2012 From Remote Sensing. *Frontiers in Earth Science, 8*(35). https://doi.org/10.3389/feart.2020.00035
Hugenholtz, C. H., Whitehead, K., Brown, O. W., Barchyn, T. E., Brian, J., Moorman, LeClair, A., Riddell, K., & Hamilton, T. K. (2013). Geomorphological mapping with a small unmanned aircraft system (sUAS): Feature detection and accuracy assessment of a photogrammetrically-derived digital terrain model. *Geomorphology*, *194*, 16-24. https://doi.org/10.1016/j.geomorph.2013.03.023
Hugonnet, R., Brun, F., Berthier, E., Dehecq, A., Mannerfelt, E. S., Eckert, N., & Farinotti, D. (2022). Uncertainty Analysis of Digital Elevation Models by Spatial Inference From Stable Terrain. *IEEE Journal of Selected Topics in Applied Earth Observations and Remote Sensing*, *15*, 6456-6472. https://doi.org/10.1109/jstars.2022.3188922
Hugonnet, R., McNabb, R., & Berthier, E. (2021). *Accelerated global glacier mass loss in the early twenty-first century - Dataset.* Theia publication products. https://doi.org/10.6096/13
Hugonnet, R., McNabb, R., Berthier, E., Menounos, B., Nuth, C., Girod, L., Farinotti, D., Huss, M., Dussaillant, I., Brun, F., & Kaab, A. (2021). Accelerated global glacier mass loss in the early twenty-first century. *Nature*, *592*(7856), 726-731. https://doi.org/10.1038/s41586-021-03436-z
Huss, M. (2011). Present and future contribution of glacier storage change to runoff from macroscale drainage basins in Europe. *Water Resources Research*, *47*(7). https://doi.org/10.1029/2010wr010299
Huss, M. (2013). Density assumptions for converting geodetic glacier volume change to mass change. *The Cryosphere*, *7*(3), 877-887. https://doi.org/10.5194/tc-7-877-2013
Huss, M., & Bauder, A. (2009). 20th-century climate change inferred from four long-term point observations of seasonal mass balance. *Annals of Glaciology*, *50*(50), 207-214. https://doi.org/10.3189/172756409787769645
Huss, M., Bauder, A., & Funk, M. (2017). Homogenization of long-term mass-balance time series. *The Cryosphere*, *7*(4), 877-887. https://doi.org/10.5194/tc-7-877-2013
Huss, M., Bauder, A., Funk, M., & Hock, R. (2008). Determination of the seasonal mass balance of four Alpine glaciers since 1865. *Journal of Geophysical Research: Earth Surface*, *113*(F1). https://doi.org/10.1029/2007jf000803
Huss, M., & Hock, R. (2018). Global-scale hydrological response to future glacier mass loss. *Nature Climate Change*, *8*(2), 135-140. https://doi.org/10.1038/s41558-017-0049-x
Höhle, J., & Höhle, M. (2009). Accuracy assessment of digital elevation models by means of robust statistical methods. *ISPRS Journal of Photogrammetry and Remote Sensing*, *64*(4), 398-406. https://doi.org/10.1016/j.isprsjprs.2009.02.003
Haakensen, N. (1989). *Akkumulasjon på breene i Norge vinteren 1988-89*. https://publikasjoner.nve.no/meddelelse/1989/meddelelse70.pdf
Immerzeel, W. W., Kraaijenbrink, P. D. A., Shea, J. M., Shrestha, A. B., Pellicciotti, F., Bierkens, M. F. P., & de Jong, S. M. (2014). High-resolution monitoring of Himalayan

glacier dynamics using unmanned aerial vehicles. *Remote Sensing of Environment*, *150*, 93-103. https://doi.org/10.1016/j.rse.2014.04.025

IPCC. (2023). Sections. In: *Climate Chage 2023: Synthesis Report. Contribution of Working Groups I, II and III to the Sixth Assessment Report of the Intergovernmental Panel on Clmate Change* [Core Writing Team, H. Lee and J. Romero (eds.)]. IPCC, Geneva, Switzerland, pp. 35-115. https://doi.org/10.59327/IPCC/AR6-9789291691647

James, M. R., & Robson, S. (2012). Straightforward reconstruction of 3D surfaces and topography with a camera: Accuracy and geoscience application. *Journal of Geophysical Research: Earth Surface*, *117*(F3). https://doi.org/10.1029/2011JF002289

James, M. R., Robson, S., d'Oleire-Oltmanns, S., & Niethammer, U. (2017). Optimising UAV topographic surveys processed with structure-from-motion: Ground control quality, quantity and bundle adjustment. *Geomorphology*, *280*, 51-66. https://doi.org/10.1016/j.geomorph.2016.11.021

Jansson, P. (1999). Effect of uncertainties in measured variables on the calculated mass balance of Storglaciären. *Geografiska Annaler*, *81A*(4), 633-642. https://doi.org/10.1111/1468-0459.00091

Javernick, L., Brasington, J., & Caruso, B. (2014). Modeling the topography of shallow braided rivers using Structure-from-Motion photogrammetry. *Geomorphology*, *213*, 166-182. https://doi.org/10.1016/j.geomorph.2014.01.006

Jóhannesson, T., Björnsson, H., Magnússon, E., Guðmundsson, S., Pálsson, F., Sigurðsson, O., Thorsteinsson, T., & Berthier, E. (2013). Ice-volume changes, bias estimation of mass-balance measurements and changes in subglacial lakes derived by lidar mapping of the surface of Icelandic glaciers. *Annals of Glaciology*, *54*(63), 63-74. https://doi.org/10.3189/2013AoG63A422

Kartverket. (2016). *Height reference model (HREF NN2000)* [Height model]. Geonorge. https://kartkatalog.geonorge.no/metadata/height-reference-model-href-nn2000/71a73064-59a5-4f03-a0b8-fa5c649c3fc9

Kartverket. (2020a). *NDH Jostedalsbreen 2pkt 2020 Project Report*. https://hoydedata.no/LaserServices/REST/DownloadPDF.ashx?filePath=\\statkart.no\hoydedata_orig\vol10\4706\metadata\NDH%20Jostedalsbreen%202pkt%202020_Prosjektrapport.pdf

Kartverket. (2020b). *The Norwegian vertical reference frame NN2000* (19-04811-4). https://www.kartverket.no/globalassets/til-lands/posisjon/the-norwegian-vertical-reference-frame-nn2000.pdf

Kartverket. (2023). *Guide to CPOS*. Retrieved 10.03.2024 from https://www.kartverket.no/en/on-land/posisjon/guide-to-cpos

Kartverket. (2024a). *Fastmerker og Basestasjoner* [WMS]. Geonorge. https://kartkatalog.geonorge.no/metadata/fastmerker-and-basestajoner-wms/8c2c434b-07f7-4ebc-9bc6-9c15cdd75c4c

Kartverket. (2024b). *Flyfoto*. Retrieved 02.20.2024 from https://www.kartverket.no/til-lands/flyfoto

Kartverket. (2024c). *Guide to ETPOS*. Retrieved 01.05.2024 from https://www.kartverket.no/en/on-land/posisjon/guide-to-etpos

Kartverket. (2024d). *Høydedata*. Retrieved 11.02.2023 from https://www.hoydedata.no/

Kartverket. (2024e). *Norge i bilder*. Retrieved 01.09.2023 from https://www.norgeibilder.no/

Karušs, J., Lamsters, K., Ješkins, J., Sobota, I., & Džeriņš, P. (2022). UAV and GPR Data Integration in Glacier Geometry Reconstruction: A Case Study from Irenebreen, Svalbard. *Remote Sensing*, *14*(3). https://doi.org/10.3390/rs14030456

Kasser, P. (1967). Fluctuations of glaciers, 1959-1965: A contribution to the International Hydrological Decade.
Kavan, J. (2020). Early twentieth century evolution of Ferdinand glacier, Svalbard, based on historic photographs and structure-from-motion technique. *Geografiska Annaler: Series A, Physical Geography*, *102*(1), 57-67. https://doi.org/10.1080/04353676.2020.1715124
Klug, C., Bollmann, E., Galos, S. P., Nicholson, L., Prinz, R., Rieg, L., Sailer, R., Stötter, J., & Kaser, G. (2018). Geodetic reanalysis of annual glaciological mass balances (2001–2011) of Hintereisferner, Austria. *The Cryosphere*, *12*(3), 833-849. https://doi.org/10.5194/tc-12-833-2018
Krabill, W., Abdalati, W., Frederick, W., Manizade, S., Martin, C., Sonntag, J., Swift, R., Thomas, R., Wright, W., & Yungel, J. (2000). Greenland ice sheet: high-elevation balance and peripheral thinning. *Science*, *289*(428-430). https://doi.org/10.1126/science.289.5478.428
Krimmel, R. M. (1999). Analysis of Difference Between Direct and Geodetic Mass Balance Measurements at South Cascade Glacier, Washington. *Geografiska Annaler, Series A: Physical Geography*, *81*(4), 653-658. https://doi.org/10.1111/j.0435-3676.1999.00093.x
Krimmel, R. M., & Meier, M. F. (1975). Glacier applications of ERTS -1 images. *Journal of Glaciology*, *15*(73), 391-402. https://doi.org/10.3189/S002214300003450X
Kronenberg, M., Barandun, M., Hoelzle, M., Huss, M., Farinotti, D., Azisov, E., Usubaliev, R., Gafurov, A., Petrakov, D., & Kääb, A. (2016). Mass-balance reconstruction for Glacier No. 354, Tien Shan, from 2003 to 2014. *Annals of Glaciology*, *57*(71), 92-102. https://doi.org/10.3189/2016AoG71A032
Kulp, S. A., & Strauss, B. H. (2019). New elevation data triple estimates of global vulnerability to sea-level rise and coastal flooding. *Nature Communications*, *10*(1), 4844. https://doi.org/10.1038/s41467-019-12808-z
Kääb, A., Winsvold, S. H., Altena, B., Nuth, C., Nagler, T., & Wuite, J. (2016). Glacier Remote Sensing Using Sentinel-2. Part I: Radiometric and Geometric Performance, and Application to Ice Velocity. *Remote Sensing*, *8*(7). https://doi.org/10.3390/rs8070598
Larsen, C. F., Motyka, R. J., Arendt, A. A., Echelmeyer, K. A., & Geissler, P. E. (2007). Glacier changes in southeast Alaska and northwest British Columbia and contribution to sea level rise. *Journal of Geophysical Research*, *112*(F01007). https://doi.org/10.1029/2006JF000586
Leigh, J. R., Stokes, C. R., Carr, R. J., Evans, I. S., Andreassen, L. M., & Evans, D. J. A. (2019). Identifying and mapping very small (<0.5 km2) mountain glaciers on coarse to high-resolution imagery. *Journal of Glaciology*, *65*(254), 873-888. https://doi.org/10.1017/jog.2019.50
Leigh, J. R., Stokes, C. R., Evans, D. J. A., Carr, R. J., & Andreassen, L. M. (2020). Timing of Little Ice Age maxima and subsequent glacier retreat in northern Troms and western Finnmark, northern Norway. *Arctic, Antarctic, and Alpine Research*, *52*(1), 281-311. https://doi.org/10.1080/15230430.2020.1765520
Leprince, S., Barbot, S., Ayoub, F., & Avouac, J.-P. (2007). Automatic and Precise Orthorectification, Coregistration, and Subpixel Correlation of Satellite Images, Application to Ground Deformation Measurements. *IEEE Transactions on Geoscience and Remote Sensing*, *45*(6), 1529-1558. https://doi.org/10.1109/tgrs.2006.888937
Lie, Ø., Dahl, S. O., & Nesje, A. (2003a). A theoretical approach to glacier equilibrium-line altitudes using meteorological data and glacier mass balance records from southern Norway. *The Holocene*, *13*(3), 365-372. https://doi.org/10.1191/0959683603hl629rp

Lie, Ø., Dahl, S. O., & Nesje, A. (2003b). Theoretical equilibrium-line altitudes and glacier buildup sensitivity in southern Norway based on meteorological data in a geographical information system. *The Holocene*, *13*(3), 373-380. https://doi.org/10.1191/0959683603hl630

Liestøl, O. (1967). *Storbreen glacier in Jotunheimen, Norway.* http://hdl.handle.net/11250/173862

Liestøl, O. (2000). *Glaciology* (2nd ed., Vol. no. 6/2000). Unipub forl.

Lillesand, T., Kiefer, R. W., & Chipman, J. (2015). *Remote Sensing and Image Interpretation*. Wiley.

Lucieer, A., Jong, S. M. d., & Turner, D. (2013). Mapping landslide displacements using Structure from Motion (SfM) and image correlation of multi-temporal UAV photography. *Progress in Physical Geography: Earth and Environment*, *38*(1), 97-116. https://doi.org/10.1177/0309133313515293

Lussana, C. (2020). *seNorge observational gridded datasets. seNorge_2018, version 20.05* (MET report No. 07/20). https://www.met.no/publikasjoner/met-report/met-report-2020/_/attachment/download/9f79d391-62d8-4fc1-a61a-9f0e7f1de389:8c74ebf2118593aa75272e6aff416ce66f86e73f/MET-report-07-2020.pdf

Lussana, C. (2021). *seNorge observational gridded datasets. seNorge_2018, version 21.09* (MET report No. 07/2021). https://www.met.no/publikasjoner/met-report/met-report-2021/_/attachment/download/5abd0cf0-9a45-4c38-8ee2-1484150009f9:aa5a68ca6035f7baa3856a0d371f6a822c23c29b/MET-report-7-2021.pdf

Lussana, C., Tveito, O. E., Dobler, A., & Tunheim, K. (2019). seNorge_2018, daily precipitation, and temperature datasets over Norway. *Earth System Science Data*, *11*(4). https://doi.org/10.5194/essd-11-1531-2019

Lutro, O. (2002). *Berggrunnskart SYGNEFJELL 1518 III, M 1:50 000. Provisional ed.* https://www.ngu.no/upload/Publikasjoner/Kart/B50/sygnefjell.pdf

Magnússon, E., Muñoz-Cobo Belart, J., Pálsson, F., Ágústsson, H., & Crochet, P. (2016). Geodetic mass balance record with rigorous uncertainty estimates deduced from aerial photographs and lidar data – Case study from Drangajökull ice cap, NW Iceland. *The Cryosphere*, *10*(1), 159-177. https://doi.org/10.5194/tc-10-159-2016

Mannerfelt, E., Hugonnet, R., & Dehecq, A. (2021). *Python package xDEM for the analysis of DEM*. https://xdem.readthedocs.io/en/stable/about_xdem.html

Marshak, S., & Repcheck, J. (2009). *Essentials of Geology*. WW Norton.

Marzeion, B., Champollion, N., Haeberli, W., Langley, K., Leclercq, P., & Paul, F. (2017). Observation-Based Estimates of Global Glacier Mass Change and Its Contribution to Sea-Level Change. *Surv Geophys*, *38*(1), 105-130. https://doi.org/10.1007/s10712-016-9394-y

Marzeion, B., Jarosch, A. H., & Hofer, M. (2012). Past and future sea-level change from the surface mass balance of glaciers. *The Cryosphere*, *6*(6), 1295-1322. https://doi.org/10.5194/tc-6-1295-2012

Marzeion, B., & Nesje, A. (2012). Spatial patterns of North Atlantic Oscillation influence on mass balance variability of European Glaciers. *The Cryosphere Discussions*, *6*, 1-35. https://doi.org/10.5194/tcd-6-1-2012

Matthews, J. A. (2005). 'Little Ice Age' glacier variations in Jotunheimen, southern Norwvay: a study in regionally controlled lichenometric dating of recessional moraines with implications for climate and lichen growth rates. *The Holocene*, *15*(1), 1-19. https://doi.org/.1191/0959683605hl779rp

Matthews, J. A., Olaf Dahl, S., Nesje, A., Berrisford, M. S., & Andersson, C. (2000). Holocene glacier variations in central Jotunheimen, southern Norway based on distal glaciolacustrine sediment cores. *Quaternary Science Reviews*, *19*(16), 1625-1647. https://doi.org/10.1016/S0277-3791(00)00008-1

Maune, D. F. (2007). *Digital Elevation Model Technologies and Applications: The DEM Users Manual* (D. F. Maune, Ed. 2nd ed.). American Society for Photogrammetry and Remote Sensing.

Maussion, F., Butenko, A., Champollion, N., Dusch, M., Eis, J., Fourteau, K., Gregor, P., Jarosch, A. H., Landmann, J., Oesterle, F., Recinos, B., Rothenpieler, T., Vlug, A., Wild, C. T., & Marzeion, B. (2019). The Open Global Glacier Model (OGGM) v1.1. *Geosci. Model Dev.*, *12*(3), 909-931. https://doi.org/10.5194/gmd-12-909-2019

McNabb, R., Nuth, C., Kääb, A., & Girod, L. (2019). Sensitivity of glacier volume change estimation to DEM void interpolation. *The Cryosphere*, *13*(3), 895-910. https://doi.org/10.5194/tc-13-895-2019

Meier, M. F. (1965). Glaciers and Climate. In *The Quaternary of the U.S* (pp. 795-806). Princeton University Press. https://doi.org/10.1515/9781400876525-051

Meier, M. F. (1984). Contribution of Small Glaciers to Global Sea Level. *Science*, *226*(4681), 1418-1421. https://doi.org/10.1126/science.226.4681.1418

Mertes, J. R., Gulley, J. D., Benn, D. I., Thompson, S. S., & Nicholson, L. I. (2017). Using structure-from-motion to create glacier DEMs and orthoimagery from historical terrestrial and oblique aerial imagery. *Earth Surface Processes and Landforms*, *42*(14), 2350-2364. https://doi.org/10.1002/esp.4188

Mesa-Mingorance, J. L., & Ariza-López, F. J. (2020). Accuracy Assessment of Digital Elevation Models (DEMs): A Critical Review of Practices of the Past Three Decades. *Remote Sensing*, *12*(16). https://doi.org/10.3390/rs12162630

MET. (2023). *Dataset: average/seNorge2018_version_23.09_tgmean_mon_1957-2022.nc* Version 23.09). https://thredds.met.no/thredds/catalog/senorge/seNorge_2018/indices/version_23.09/average/catalog.html?dataset=senorge/seNorge_2018/indices/version_23.09/average/seNorge2018_version_23.09_tgmean_mon_1957-2022.nc

MET. (2024a). *Dataset: 12/seNorge2018_rr_monthly_202312.nc*. https://thredds.met.no/thredds/catalog/senorge/seNorge_2018/aggregated_products/rr/2023/12/catalog.html?dataset=senorge/seNorge_2018/aggregated_products/rr/2023/12/seNorge2018_rr_monthly_202312.nc

MET. (2024b). *Dataset: 12/seNorge2018_tg_monthly_202312.nc*. https://thredds.met.no/thredds/catalog/senorge/seNorge_2018/aggregated_products/tg/2023/12/catalog.html?dataset=senorge/seNorge_2018/aggregated_products/tg/2023/12/seNorge2018_tg_monthly_202312.nc

MET. (2024c). *Dataset: precipitation/seNorge2018_version_23.09_prcptot_mon_1957-2022.nc* Version 23.09. https://thredds.met.no/thredds/catalog/senorge/seNorge_2018/indices/version_23.09/precipitation/catalog.html?dataset=senorge/seNorge_2018/indices/version_23.09/precipitation/seNorge2018_version_23.09_prcptot_mon_1957-2022.nc

Micheletti, N., Chandler, J. H., & Lane, S. N. (2015). Investigating the geomorphological potential of freely available and accessible structure-from-motion photogrammetry using a smartphone. *Earth Surface Processes and Landforms*, *40*(4), 473-486. https://doi.org/10.1002/esp.3648

Miljødirektoratet. (2024). *Naturvernområder* Version 20141001) [Vector]. https://kartkatalog.miljodirektoratet.no/Dataset/Details/0

Mosbrucker, A. R., Major, J. J., Spicer, K. R., & Pitlick, J. (2017). Camera system considerations for geomorphic applications of SfM photogrammetry. *Earth Surface Processes and Landforms*, *42*(6), 969-986. https://doi.org/10.1002/esp.4066

Mukherjee, K., Menounos, B., Shea, J., Mortezapour, M., Ednie, M., & Demuth, M. N. (2023). Evaluation of surface mass-balance records using geodetic data and physically-based modelling, Place and Peyto glaciers, western Canada. *Journal of Glaciology*, *69*(276), 665-682. https://doi.org/10.1017/jog.2022.83

Mukherjee, S., Joshi, P. K., Mukherjee, S., Ghosh, A., Garg, R. D., & Mukhopadhyay, A. (2013). Evaluation of vertical accuracy of open source Digital Elevation Model (DEM). *International Journal of Applied Earth Observation and Geoinformation*, *21*, 205-217. https://doi.org/10.1016/j.jag.2012.09.004

Mälicke, M. (2022). SciKit-GStat 1.0: a SciPy-flavored geostatistical variogram estimation toolbox written in Python. *Geosci. Model Dev.*, *15*(6), 2505-2532. https://doi.org/10.5194/gmd-15-2505-2022

Mölg, N., & Bolch, T. (2017). Structure-from-Motion Using Historical Aerial Images to Analyse Changes in Glacier Surface Elevation. *Remote Sensing*, *9*(10). https://doi.org/10.3390/rs9101021

Nesje, A. (2023). Future state of Norwegian glaciers: Estimating glacier mass balance and equilibrium line responses to projected 21st century climate change. *The Holocene*, *33*(10), 1257-1271. https://doi.org/10.1177/09596836231183069

Nesje, A., Bakke, J., Dahl, S. O., Lie, Ø., & Matthews, J. A. (2008). Norwegian mountain glaciers in the past, present and future. *Global and Planetary Change*, *60*(1-2), 10-27. https://doi.org/10.1016/j.gloplacha.2006.08.004

Nesje, A., Lie, Ø., & Dahl, S. O. (2000). Is the North Atlantic Oscillation reflected in Scandinavian glacier mass balance records? *Journal of Quaternary Science*, *15*(6), 587-601. https://doi.org/10.1002/1099-1417(200009)15:6<587::Aid-jqs533>3.0.Co;2-2

NGA. (2014). Department of Defense, World Geodetic System 1984, Its Definition and Relationships with Local Geodetic Systems [Technical Report], 3 ed. https://geodesy.unr.edu/hanspeterplag/library/geodesy/wgs84fin.pdf

Nolan, M., Larsen, C., & Sturm, M. (2015). Mapping snow depth from manned aircraft on landscape scales at centimeter resolution using structure-from-motion photogrammetry. *The Cryosphere*, *9*(4), 1445-1463. https://doi.org/10.5194/tc-9-1445-2015

Norsk Klimaservicesenter (2024). *Seklima*. Retrieved 06.03.2024 from https://seklima.met.no/

Nussbaumer, S. U., Hoelzle, M., Hüsler, F., Huggel, C., Salzmann, N., & Zemp, M. (2017). Glacier Monitoring and Capacity Building: Important Ingredients for Sustainable Mountain Development. *Mountain Research and Development*, *37*, 141 - 152. https://www.jstor.org/stable/90001389

Nuth, C., Kohler, J., Aas, H. F., Brandt, O., & Hagen, J. O. (2007). Glacier geometry and elevation changes on Svalbard (1936–90): a baseline dataset. *Annals of Glaciology*, *46*, 106 - 116. https://doi.org/10.3189/172756407782871440

Nuth, C., & Kääb, A. (2011). Co-registration and bias corrections of satellite elevation data sets for quantifying glacier thickness change. *The Cryosphere*, *5*(1), 271-290. https://doi.org/10.5194/tc-5-271-2011

NVE. (2023). *Storbreen*. Retrieved 05.03.2024 from https://www.nve.no/hydrology/glaciers/glacier-monitoring/storbreen/

NVE. (2024). *Climate indicator products* https://glacier.nve.no/Glacier/viewer/CI/en/

Nye, J. F. (1960). The response of glaciers and ice-sheets to seasonal and climatic changes, . *Proceedings of the Royal Society of London*, *256*(1287), 559-584. https://doi.org/10.1098/rspa.1960.0127
Oerlemans, J. (1994). Quantifying global warming from the retreat of glaciers. *Science*, *264*(5156), 243-245. https://doi.org/10.1126/science.264.5156.243
Ohmura, A. (2011). Observed Mass Balance of Mountain Glaciers and Greenland Ice Sheet in the 20th Century and the Present Trends. *Surveys in Geophysics*, *32*(4), 537-554. https://doi.org/10.1007/s10712-011-9124-4
Paterson, W. S. B. (1994). *The physics of glaciers*. Pergamon.
Pelto, B. M., Menounos, B., & Marshall, S. J. (2019). Multi-year evaluation of airborne geodetic surveys to estimate seasonal mass balance, Columbia and Rocky Mountains, Canada. *The Cryosphere*, *13*(6), 1709-1727. https://doi.org/10.5194/tc-13-1709-2019
PSFG - Permanent Service on the Fluctuations of Glaciers (1973). *Fluctuations of glaciers 1965–1970* (923101045X). https://archive.org/details/fluctuationsofgl0000kass
PSFG - Permanent Service on the Fluctuations of Glaciers (1977). *Fluctuations of glaciers 1970–1975* (Vol. 3). International Commission on Snow and Ice of the International Association of Scientific Hydrology/UNESCO. https://doi.org/10.1002/qj.49710544522
PSFG - Permanent Service on the Fluctuations of Glaciers (1985). *Fluctuations of glaciers, 1975-1980* (Vol. 4). International Commission on Snow and Ice of the International Association of Hydrological Sciences/UNESCO. https://doi.org/10.2307/633124
Pix4D. (2020). *Introducing Pix4Dmatic: mapping at a larger scale*. Retrieved 29.04.2029 from https://www.pix4d.com/blog/new-pix4dmatic-release/
Rasmussen, L. A., Andreassen, L. M., & Conway, H. (2007). Reconstruction of mass balance of glaciers in southern Norway back to 1948. *Annals of Glaciology*, *46*, 255-260. https://doi.org/10.3189/172756407782871242
Raup, B., Kääb, A., Kargel, J. S., Bishop, M. P., Hamilton, G., Lee, E., Paul, F., Rau, F., Soltesz, D., Khalsa, S. J. S., Beedle, M., & Helm, C. (2007). Remote sensing and GIS technology in the Global Land Ice Measurements from Space (GLIMS) Project. *Computers & Geosciences*, *33*(1), 104-125. https://doi.org/10.1016/j.cageo.2006.05.015
Remondino, F., Spera, M. G., Nocerino, E., Menna, F., & Nex, F. (2014). State of the art in high density image matching. *The Photogrammetric Record*, *29*(146), 144-166. https://doi.org/10.1111/phor.12063
Reucsh, H. (1901). Nogle bidrag till forstaaelsen af hvorledes Norges dale og fjelde er blevne til. *Norges Geologiske Undersoekelse*, *32*, 124-263. https://hdl.handle.net/11250/2675030
Rignot, E., Rivera, A., & Casassa, G. (2003). Contribution of the Patagonia icefields of South America to sea level rise. *Science*, *302*(5644), 434-437. https://doi.org/10.1126/science.1087393
Robson, B. A., MacDonell, S., Ayala, Á., Bolch, T., Nielsen, P. R., & Vivero, S. (2022). Glacier and rock glacier changes since the 1950s in the La Laguna catchment, Chile. *The Cryosphere*, *16*(2), 647-665. https://doi.org/10.5194/tc-16-647-2022
Roe, G. H. (2011). What do glaciers tell us about climate variability and climate change? *Journal of Glaciology*, *57*(203), 567-578. https://doi.org/10.3189/002214311796905640
Roe, Gerard H., Baker, Marcia B., & Herla, F. (2017). Centennial glacier retreat as categorical evidence of regional climate change. *Nature Geoscience*, *10*(2), 95-99. https://doi.org/10.1038/ngeo2863

Roe, G. H., & O'Neal, M. (2009). The response of glaciers to intrinsic climate variability: observations and models of late Holocene variations in the Pacific Northwest. *Journal of Glaciology*, *55*, 839-854. https://doi.org/ 10.3189/002214309790152438

Rolstad, C., Haug, T., & Denby, B. (2009). Spatially integrated geodetic glacier mass balance and its uncertainty based on geostatistical analysis: application to the western Svartisen ice cap, Norway. *Journal of Glaciology*, *55*(192), 666-680. https://doi.org/10.3189/002214309789470950

Rosnell, T., & Honkavaara, E. (2012). Point Cloud Generation from Aerial Image Data Acquired by a Quadrocopter Type Micro Unmanned Aerial Vehicle and a Digital Still Camera. *Sensors*, *12*(1), 453-480. https://www.mdpi.com/1424-8220/12/1/453

Rounce, D. R., Hock, R., Maussion, F., Hugonnet, R., Kochtitzky, W., Huss, M., Berthier, E., Brinkerhoff, D., Compagno, L., Copland, L., Farinotti, D., Menounos, B., & McNabb, R. W. (2023). Global glacier change in the 21st century: Every increase in temperature matters. *Science*, *379*(6627), 78-83. https://doi.org/10.1126/science.abo1324

Sapiano, J. J., Harrison, W. D., & Echelmeyer, K. A. (1998). Elevation, volume and terminus changes of nine glaciers in North America. *Journal of Glaciology*, *44*(146), 119-135. https://doi.org/10.3189/S0022143000002410

Schenk, T. (2005). Introduction to photogrammetry. *The Ohio State University, Columbus*, *106*. https://www.academia.edu/download/58585147/IntroPhoto.pdf

Schenk, T., & Csatho, B. (2012). A New Methodology for Detecting Ice Sheet Surface Elevation Changes From Laser Altimetry Data. *IEEE Transactions on Geoscience and Remote Sensing*, *50*(9), 3302-3316. https://doi.org/10.1109/TGRS.2011.2182357

Schiefer, E., Menounos, B., & Wheate, R. (2007). Recent volume loss of British Columbian glaciers, Canada. *Geophysical Research Letters*, *34*(L16503). https://doi.org/10.1029/2007GL030780

Schneider, T., & Jansson, P. (2004). Internal accumulation in firn and its significance for the mass balance of Storglaciären, Sweden. *Journal of Glaciology*, *50*(168), 25-34. https://doi.org/ 10.3189/172756504781830277

Schnorbus, M., Werner, A., & Bennett, K. (2014). Impacts of climate change in three hydrologic regimes in British Columbia, Canada. *Hydrological Processes*, *28*(3), 1170-1189. https://doi.org/10.1002/hyp.9661

Schytt, V. (1962). Mass balance studies in Kebnekajse. *Journal of Glaciology*, *4*(33), 281-286. https:/doi.org/10.3189/S002214300002757X

Seehaus, T., Malz, P., Sommer, C., Lippl, S., Cochachin, A., & Braun, M. (2019). Changes of the tropical glaciers throughout Peru between 2000 and 2016 – mass balance and area fluctuations. *The Cryosphere*, *13*(10), 2537-2556. https://doi.org/10.5194/tc-13-2537-2019

Seitz, S. M., Curless, B., Diebel, J., Scharstein, D., & Szeliski, R. (2006). A Comparison and Evaluation of Multi-View Stereo Reconstruction Algorithms. *2006 IEEE Computer Society Conference on Computer Vision and Pattern Recognition* (CVPR'06) New York, NY, USA, 2006, pp. 519-528, https://doi.org/10.1109/CVPR.2006.19

Shakesby, R. A., Matthews, J. A., Winkler, S., Fabel, D., & Dresser, P. Q. (2020). Early-Holocene moraine chronology, Sognefjell area, southern Norway: evidence for multiple glacial and climatic fluctuations within the Erdalen Event (~10.2–9.7 ka). *Norwegian Journal of Geology*. https://doi.org/10.17850/njg100-3-2

Shindell, D., & Faluvegi, G. (2009). Climate response to regional radiative forcing during the twentieth century. *Nature Geoscience*, *2*(4), 294-300. https://doi.org/10.1038/ngeo473

Sissons, J. B. (1979). Palaeoclimatic inferences from former glaciers in Scotland and the Lake District. *Nature*, *278*, 518-521. https://doi.org/10.1038/278518a0

Smith, M. W., Carrivick, J. L., & Quincey, D. J. (2016). Structure from motion photogrammetry in physical geography. *Progress in Physical Geography: Earth and Environment*, *40*(2), 247-275. https://doi.org/10.1177/0309133315615805

Sold, L., Huss, M., Hoelzle, M., Andereggen, H., Joerg, P. C., & Zemp, M. (2013). Methodological approaches to infer end-of-winter snow distribution on alpine glaciers. *Journal of Glaciology*(59), 1047–1059. https://doi.org/10.3189/2013JoG13J015

SSB. (2024). *Electricity* https://www.ssb.no/en/energi-og-industri/energi/statistikk/elektrisitet

Stoffel, M., & Huggel, C. (2012). Effects of climate change on mass movements in mountain environments. *Progress in Physical Geography: Earth and Environment*, *36*(3), 421-439. https://doi.org/10.1177/0309133312441010

Stokes, C. R., Andreassen, L. M., Champion, M. R., & Corner, G. D. (2018). Widespread and accelerating glacier retreat on the Lyngen Peninsula, northern Norway, since their 'Little Ice Age' maximum. *Journal of Glaciology*, *64*(243), 100-118. https://doi.org/10.1017/jog.2018.3

Szelski, R. (2011). *Computer vision: Algorithms and applications*. Springer.

Sælthun, N. R. (1973). Space variation of summer precipitation in a highland basin. *Vannet i Norden*, *1973*(1), 30-42.

Thibert, E., Blanc, R., Vincent, C., & Eckert, N. (2008). Glaciological and volumetric mass-balance measurements: error analysis over 51 years for Glacier de Sarennes, French Alps. *Journal of Glaciology*, *54*(186), 522-532. https://doi.org/10.3189/002214308785837093

Thibert, E., Eckert, N., & Vincent, C. (2013). Climatic drivers of seasonal glacier mass balances: an analysis of 6 decades at Glacier de Sarennes (French Alps). *The Cryosphere*, *7*(1), 47-66. https://doi.org/10.5194/tc-7-47-2013

Thibert, E., & Vincent, C. (2009). Best possible estimation of mass balance combining glaciological and geodetic methods. *Annals of Glaciology*, *50*(50), 112-118. https://doi.org/10.3189/172756409787769546

Thorarinsson, S. (1940). Present glacier shrinkage, and eustatic changes of sea-level. *Geografiska Annaler*, *22*, 131-159. https://doi.org/10.1080/20014422.1940.11880686

Tonkin, T. N., & Midgley, N. G. (2016). Ground-Control Networks for Image Based Surface Reconstruction: An Investigation of Optimum Survey Designs Using UAV Derived Imagery and Structure-from-Motion Photogrammetry. *Remote Sensing*, *8*, 16-19. https://doi.org/10.3390/rs8090786

Trachsel, M., & Nesje, A. (2015). Modelling annual mass balances of eight Scandinavian glaciers using statistical models. *The Cryosphere*, *9*(4), 1401-1414. https://doi.org/10.5194/tc-9-1401-2015

Triggs, B., McLauchlan, P. F., Hartley, R. I., & Fitzgibbon, A. W. (2000). Bundle Adjustment — A Modern Synthesis. Vision Algorithms: Theory and Practice, Berlin, Heidelberg. https://www.cs.jhu.edu/~misha/ReadingSeminar/Papers/Triggs00.pdf

Tuffen, H., James, M. R., Castro, J. M., & Schipper, C. I. (2013). Exceptional mobility of an advancing rhyolitic obsidian flow at Cordón Caulle volcano in Chile. *Nat Commun*, *4*, 2709. https://doi.org/10.1038/ncomms3709

Ullman, S., & Brenner, S. (1979). The interpretation of structure from motion. *Proceedings of the Royal Society of London. Series B. Biological Sciences*, *203*(1153), 405-426. https://doi.org/10.1098/rspb.1979.0006

Vaughan, G. D. (2014). *Observations: Cryosphere, in IPCC (ed.)* Climate Change 2013 – The Physical Science Basis: Working Group I Contribution to the Fifth Assessment Report of the Intergovernmental Panel on Climate Change., C. U. Press. https://www.ipcc.ch/report/ar5/wg1/observations-cryosphere/

Vaze, J., Teng, J., & Spencer, G. (2010). Impact of DEM accuracy and resolution on topographic indices. *Environmental Modelling & Software*, *25*(10), 1086-1098. https://doi.org/10.1016/j.envsoft.2010.03.014

Vincent, C., Kappenberger, G., Valla, F., Bauder, A., Funk, M., & Le Meur, E. (2004). Ice ablation as evidence of climate change in the Alps over the 20th century. *Journal of Geophysical Research: Atmospheres*, *109*(D10). https://doi.org/10.1029/2003JD003857

Vivero, S., Bodin, X., Farías-Barahona, D., MacDonell, S., Schaffer, N., Robson, B. A., & Lambiel, C. (2021). Combination of Aerial, Satellite, and UAV Photogrammetry for Quantifying Rock Glacier Kinematics in the Dry Andes of Chile (30°S) Since the 1950s. *Frontiers in Remote Sensing*, *2*. https://doi.org/10.3389/frsen.2021.784015

Wagnon, P., Brun, F., Khadka, A., Berthier, E., Shrestha, D., Vincent, C., Arnaud, Y., Six, D., Dehecq, A., Ménégoz, M., & Jomelli, V. (2020). Reanalysing the 2007–19 glaciological mass-balance series of Mera Glacier, Nepal, Central Himalaya, using geodetic mass balance. *Journal of Glaciology*, *67*(261), 117-125. https://doi.org/10.1017/jog.2020.88

Wagnon, P., Vincent, C., Arnaud, Y., Berthier, E., Vuillermoz, E., Gruber, S., Ménégoz, M., Gilbert, A., Dumont, M., Shea, J. M., Stumm, D., & Pokhrel, B. K. (2013). Seasonal and annual mass balances of Mera and Pokalde glaciers (Nepal Himalaya) since 2007. *The Cryosphere*, *7*(6), 1769-1786. https://doi.org/10.5194/tc-7-1769-2013

Wang, P., Li, Z., Li, H., Wang, W., & Yao, H. (2014). Comparison of glaciological and geodetic mass balance at Urumqi Glacier No. 1, Tian Shan, Central Asia. *Global and Planetary Change*, *114*, 14-22. https://doi.org/10.1016/j.gloplacha.2014.01.001

Weber, P., Andreassen, L. M., Boston, C. M., Lovell, H., & Kvarteig, S. (2020). An ~1899 glacier inventory for Nordland, northern Norway, produced from historical maps. *Journal of Glaciology*, *66*, 259-277. https://doi.org/10.1017/jog.2020.3

Weber, P., Lovell, H., Andreassen, L. M., & Boston, C. M. (2020). Reconstructing the Little Ice Age extent of Langfjordjøkelen, Arctic mainland Norway, as a baseline for assessing centennial-scale icefield recession. *Polar Research*, *39*. https://doi.org/10.33265/polar.v39.4304

Westoby, M. J., Brasington, J., Glasser, N. F., Hambrey, M. J., & Reynolds, J. M. (2012). 'Structure-from-Motion' photogrammetry: A low-cost, effective tool for geoscience applications. *Geomorphology*, *179*, 300-314. https://doi.org/10.1016/j.geomorph.2012.08.021

WGMS. (1988). *Fluctuations of Glaciers 1980-1985*. International Commission on Snow and Ice of the International Association of Scientific Hydrology/UNESCO. https://wgms.ch/downloads/wgms_1993_fogVI.pdf

WGMS. (2008). *Global glacier changes: facts and figures*. W. G. M. S. UNEP. http://dx.doi.org/10.5167/uzh-4173

WGMS. (2023). *Global Glacier Change Bulletin No. 05 (2020-2021)*. Zemp, M., Gärtner-Roer, I., Nussbaumer, S.U., Welty, E.Z., Dussaillant, I., and Bannwart, J. (eds.), ISC(WDS)/IUGG(IACS)/UNEP/UNESCO/WMO, World Glacier Monitoring Service, Zurich, Switzerland, 134 pp., publication based on database version: https://doi.org/10.5904/wgms-fog-2023-09

WGMS. (2024). *"Reference glaciers" for mass balance*. Retrieved 27.04.2024 from https://wgms.ch/products_ref_glaciers/

Wigmore, O., & Mark, B. (2017). Monitoring tropical debris-covered glacier dynamics from high-resolution unmanned aerial vehicle photogrammetry, Cordillera Blanca, Peru. *The Cryosphere*, *11*(6), 2463-2480. https://doi.org/10.5194/tc-11-2463-2017

Wingham, D. J., Ridout, A. J., Scharroo, R., Arthern, R. J., & Shum, C. K. (1998). Antarctic elevation change from 1992 to 1996. *Science*, *282*(5388), 456-458. https://doi.org/10.1126/science.282.5388.456

Wingtra. (n.d.). *WingtraOne PPK*. Retrieved 10.03.2024 from https://knowledge.wingtra.com/en/wingtraone-ppk

Winkler, S. (2001). *Untersuchungen zur Klima- und Morphodynamik in skandinavischen Gebirgsregionen während des Holozän - ein Vergleich ihrer Wechselwirkungen und Prozeßsysteme im überregionalen Kontext kaltgemäßigter maritimer Gebirgsregionen* [Habilitation thesis (unpublished), University of Trier]. https://gepris.dfg.de/gepris/projekt/5091232?context=projekt&task=showDetail&id=5091232&

Winkler, S., Donner, A., & Tintrup gen. Suntrup, A. (2020). Periglacial Landforms in Jotunheimen, Central Southern Norway, and Their Altitudinal Distribution. In *Landscapes and Landforms of Norway* (pp. 169-202). https://doi.org/10.1007/978-3-030-52563-7_8

Winsvold, S. H., Andreassen, L. M., & Kienholz, C. (2014). Glacier area and length changes in Norway from repeat inventories. *The Cryosphere*, *8*(5), 1885-1903. https://doi.org/10.5194/tc-8-1885-2014

Winsvold, S. H., Kääb, A., Nuth, C., Andreassen, L. M., Van Pelt, W. J. J., & Schellenberger, T. (2017). Using SAR satellite data time-series for regional glacier mapping. *The Cryosphere*, *12*, 867-890. https://doi.org/10.5194/tc-12-867-2018

WMO. (2011). Guide to climatological practices. *Meteorological Organization Rep.*, *100*, 117. https://www.uncclearn.org/resources/library/guide-to-climatological-practices/

WMO. (2023). *The Global Climate 2011-2020*. WMO. https://library.wmo.int/idurl/4/68585

Wolf, P. R., & Dewitt, B. A. (2000). *Elements of photogrammetry: with applications in GIS* (3rd ed.). McGraw-Hill.

Yuan, X. (2009). Geometric Processing Models For Remotely Sensed Imagery And Their Accuracy Assessment. In (pp. 105-139). https://doi.org/10.1007/978-1-4419-0050-0_5

Zemp, M., Frey, H., Gärtner-Roer, I., Nussbaumer, S. U., Hoelzle, M., Paul, F., Haeberli, W., Denzinger, F., Ahlstrøm, A. P., Anderson, B., Bajracharya, S., Baroni, C., Braun, L. N., Cáceres, B. E., Casassa, G., Cobos, G., Dávila, L. R., Delgado Granados, H., Demuth, M. N., . . . Vincent, C. (2015). Historically unprecedented global glacier decline in the early 21st century. *Journal of Glaciology*, *61*(228), 745-762. https://doi.org/10.3189/2015JoG15J017

Zemp, M., Thibert, E., Huss, M., Stumm, D., Rolstad Denby, C., Nuth, C., Nussbaumer, S. U., Moholdt, G., Mercer, A., Mayer, C., Joerg, P. C., Jansson, P., Hynek, B., Fischer, A., Escher-Vetter, H., Elvehøy, H., & Andreassen, L. M. (2013). Reanalysing glacier mass balance measurement series. *The Cryosphere*, *7*(4), 1227-1245. https://doi.org/10.5194/tc-7-1227-2013

Zevenbergen, L. W., & Thorne, C. R. (1987). Quantitative analysis of land surface topography. *Earth Surface Process Landforms*, *12*(1), 47-56. https://doi.org/10.1002/esp.3290120107

Zhou, Q.-Y., Park, J., & Koltun, V. (2016). *Fast Global Registration* (Vol. 9906). https://doi.org/10.1007/978-3-319-46475-6_47

Zuo, Z., & Oerlemans, J. (1997). Contribution of glacier melt to sea-level rise since AD 1865: a regionally differentiated calculation. *Climate Dynamics*, *13*(12), 835-845. https://doi.org/10.1007/s003820050200

Østrem, G., & Brugman, M. (1991). *Glacier mass-balance measurements: A manual for field and office work* (Scientific Report 4, S. a. N. V. o. E. Environment Canada, Oslo.

https://globalcryospherewatch.org/bestpractices/docs/%C3%98strem-Brugman_1991_Glacier-Mass-Balance-Meas.pdf
Østrem, G., & Haakensen, N. (1993). Glaciers of Norway. In R. S. Williams & J. G. Ferrigno (Eds.), *Satellite image atlas of glaciers of the world* (1386-E-3 ed., pp. 53): US Geological Survey. https://pubs.usgs.gov/pp/p1386e/norway.pdf
Østrem, G., & Haakensen, N. (1999). Map comparison or traditional mass-balance measurements: which method is better? *Geografiska Annaler*, *81A*(4), 703-711. https://www.jstor.org/stable/521508

Appendix

1. Plots used for estimation of surface change precision

This section contains plots form the remaining datasets generated using the xDEM Python package, introduced in section 6.2.4. The scale between figures varies to better visualise the data, thus they should not be directly compared.

1.1 1966 - 1981

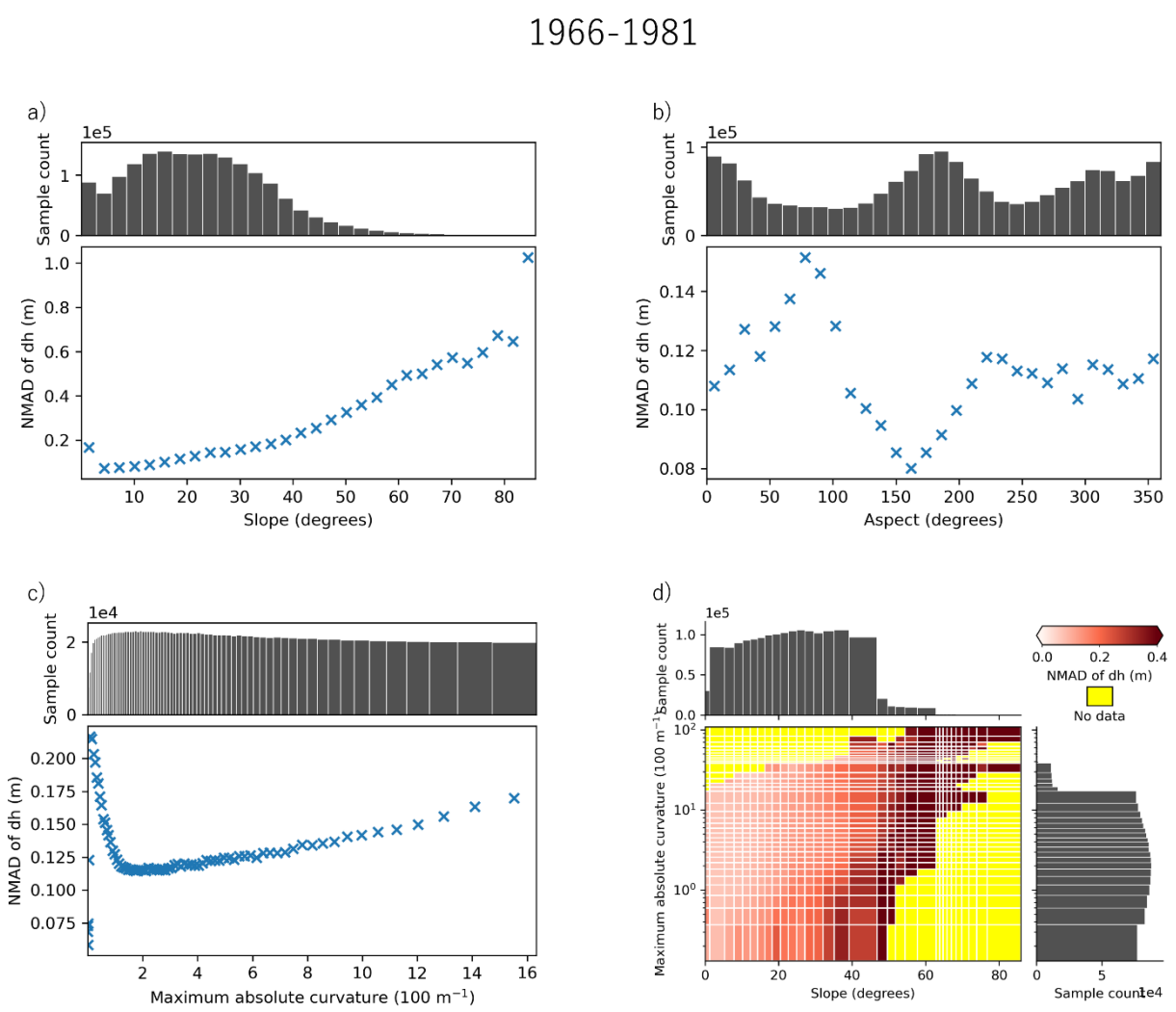

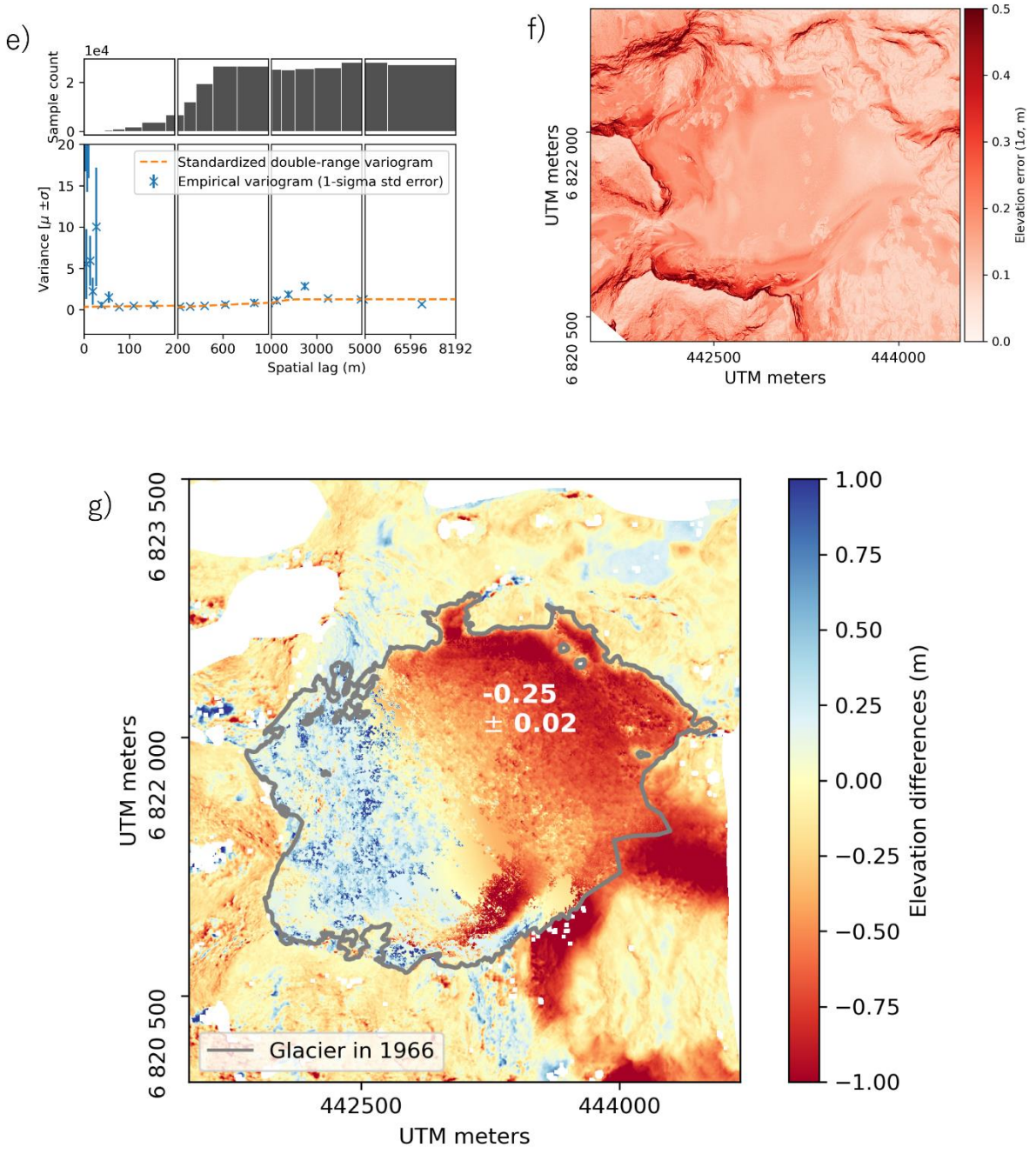
e)
1e4
Sample count
Standardized double-range variogram
Empirical variogram (1-sigma std error)
Variance [$\mu \pm \sigma$]
Spatial lag (m)
f)
UTM meters
6 822 000
6 820 500
442500
444000
UTM meters
Elevation error (1σ, m)
g)
6 823 500
6 822 000
6 820 500
UTM meters
-0.25
± 0.02
Glacier in 1966
442500
444000
UTM meters
Elevation differences (m)

1.2 1981 - 2004

1981-2004

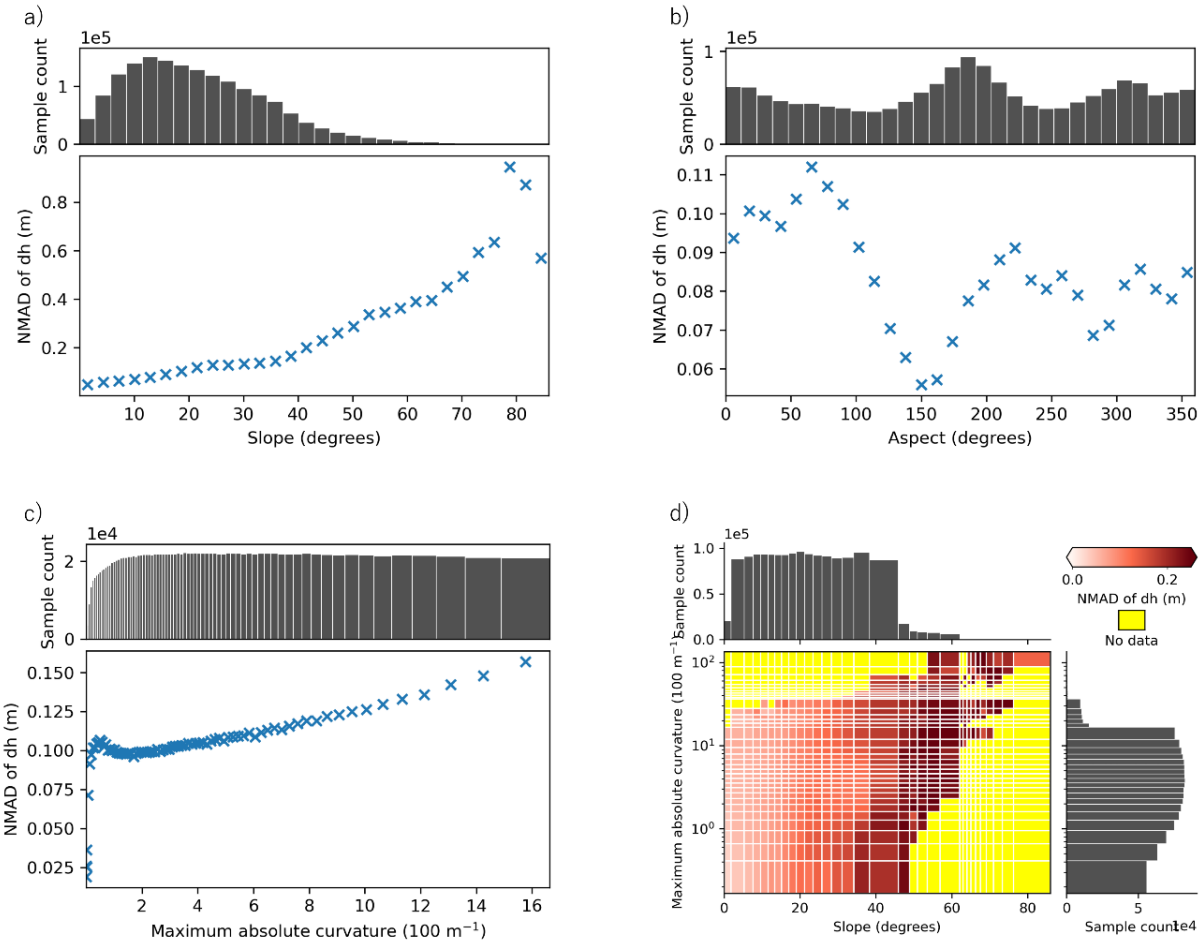

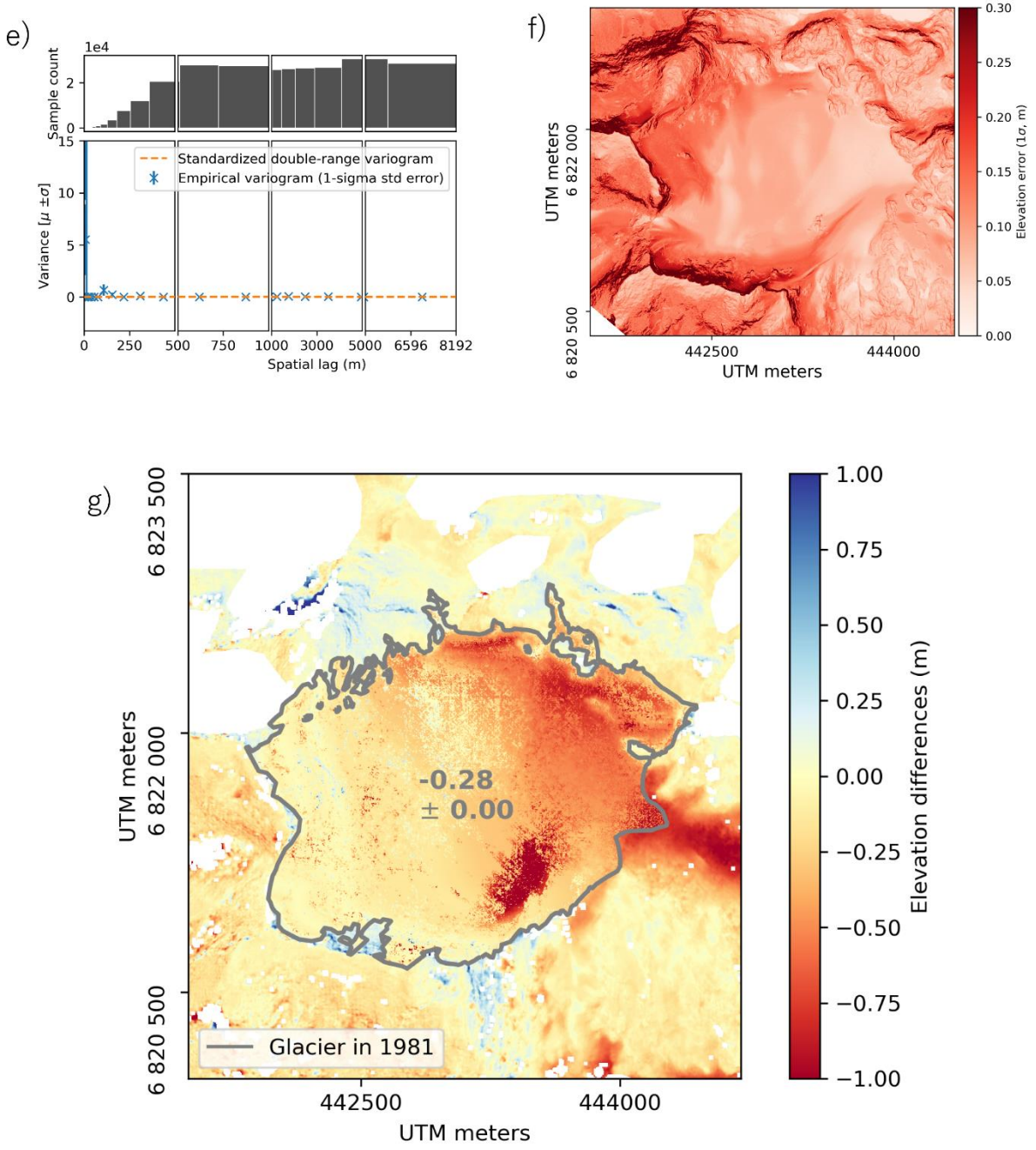
e)
1e4
Sample count
Standardized double-range variogram
Empirical variogram (1-sigma std error)
Variance [$\mu \pm \sigma$]
Spatial lag (m)
f)
UTM meters
UTM meters
Elevation error (1σ, m)
g)
-0.28
± 0.00
Glacier in 1981
UTM meters
UTM meters
Elevation differences (m)

1.3 *2004 – 2010*

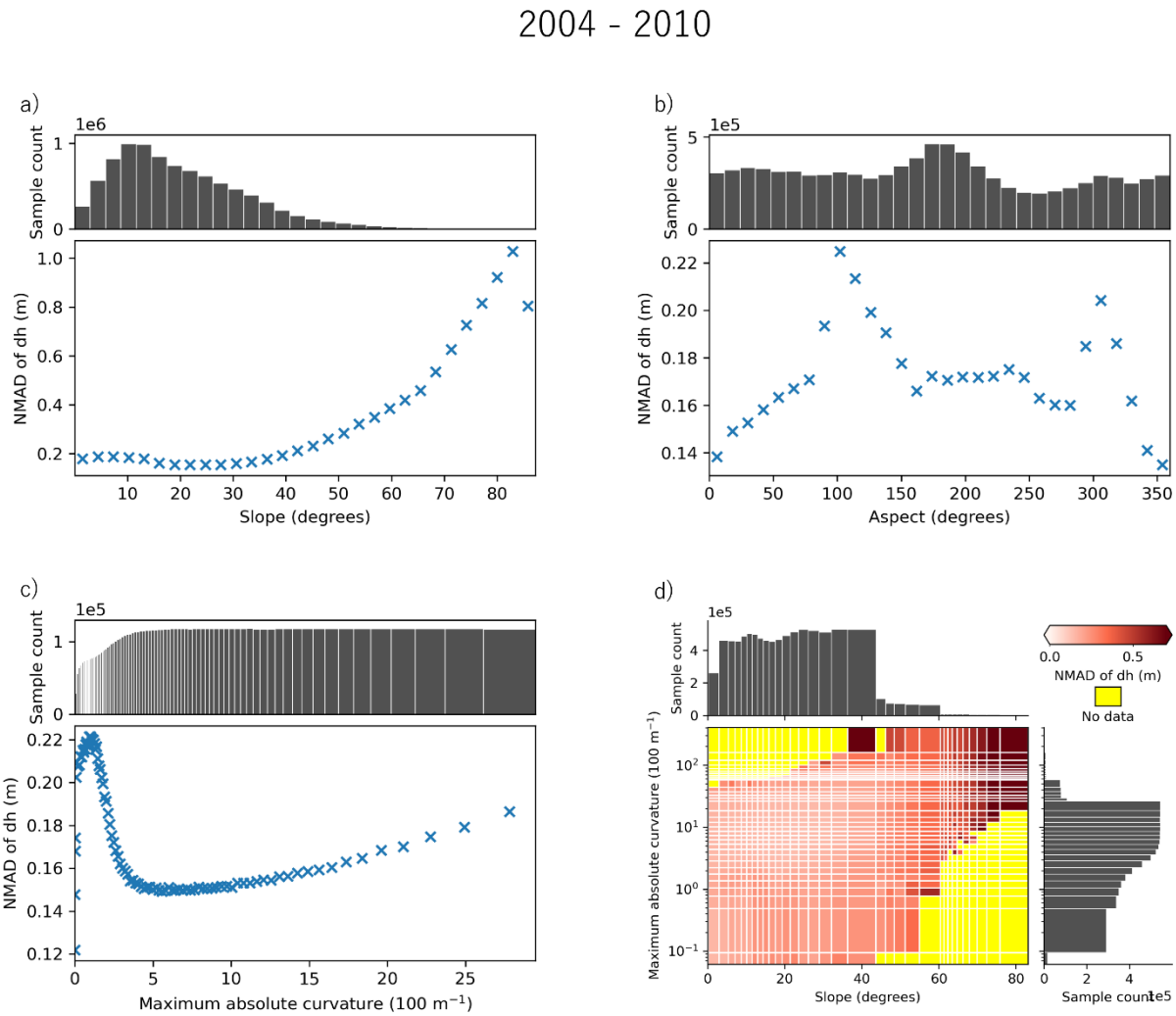
2004 - 2010
a)
1e6
Sample count
NMAD of dh (m)
Slope (degrees)
b)
1e5
Sample count
NMAD of dh (m)
Aspect (degrees)
c)
1e5
Sample count
NMAD of dh (m)
Maximum absolute curvature (100 m⁻¹)
d)
1e5
Sample count
0.0
0.5
NMAD of dh (m)
No data
Maximum absolute curvature (100 m⁻¹)
Slope (degrees)
Sample count
1e5

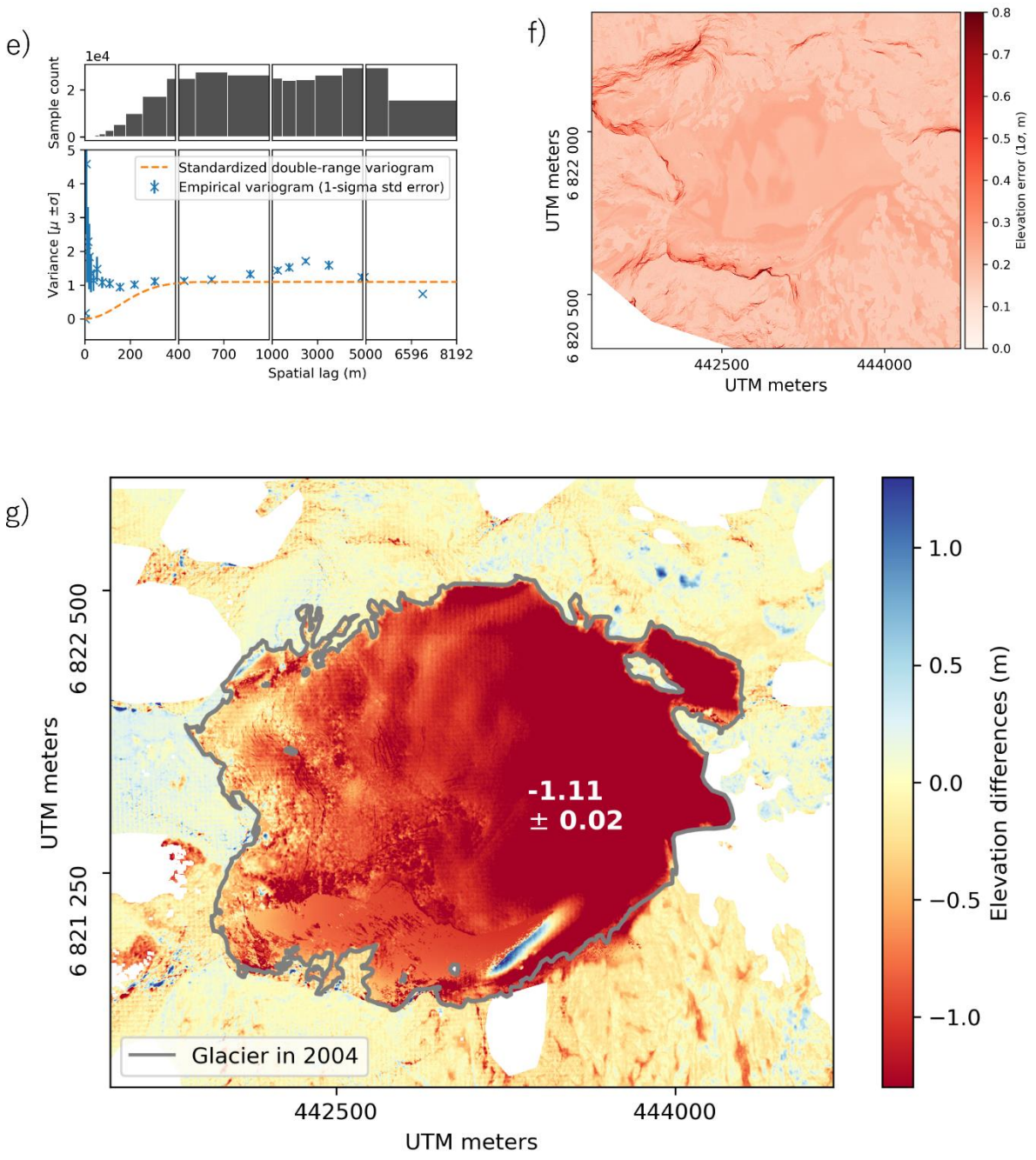
e)
1e4
Sample count
Standardized double-range variogram
Empirical variogram (1-sigma std error)
Variance [$\mu \pm \sigma$]
Spatial lag (m)
f)
UTM meters
6 822 000
6 820 500
442500
444000
Elevation error (1σ, m)
g)
6 822 500
6 821 250
UTM meters
442500
444000
-1.11
± 0.02
Glacier in 2004
Elevation differences (m)

1.4 2010 - 2017

2010-2017

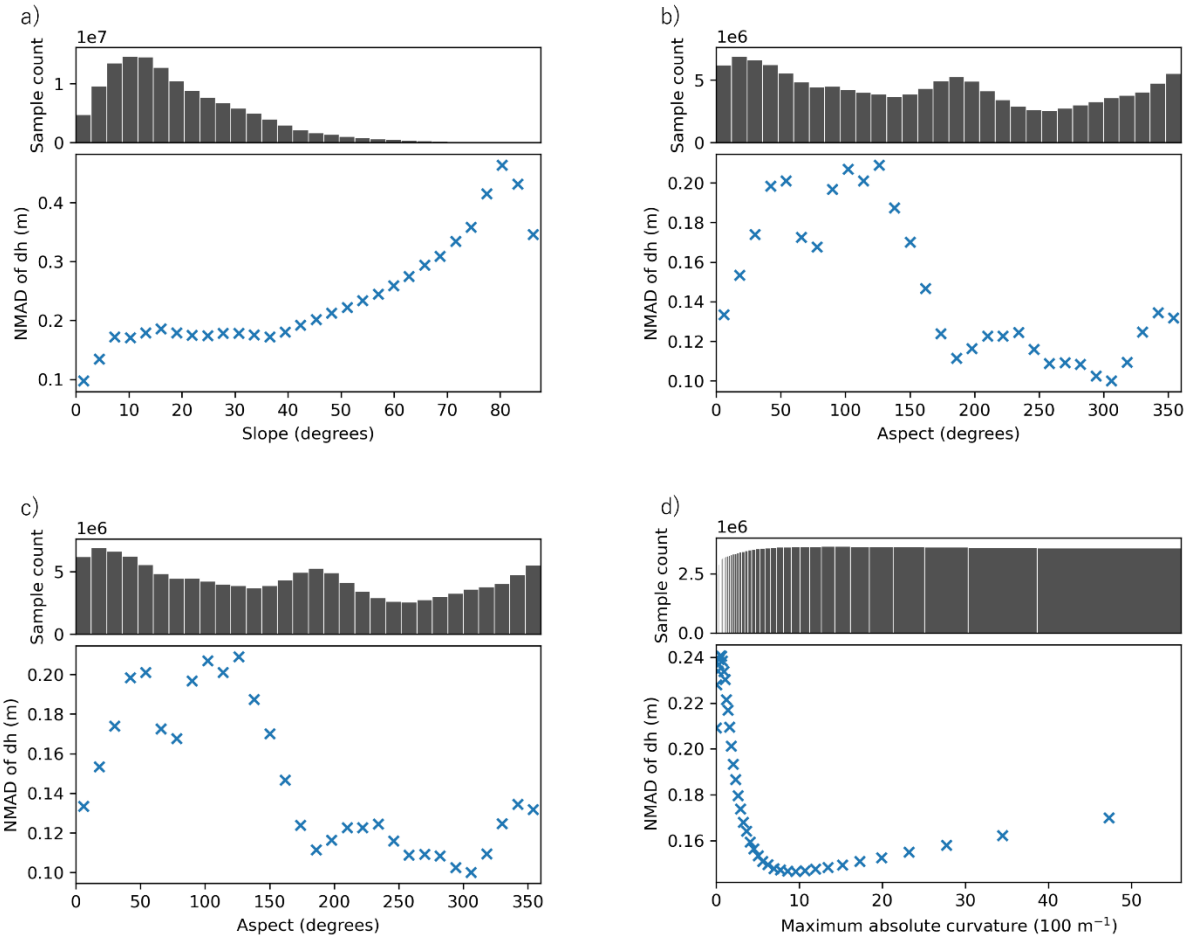

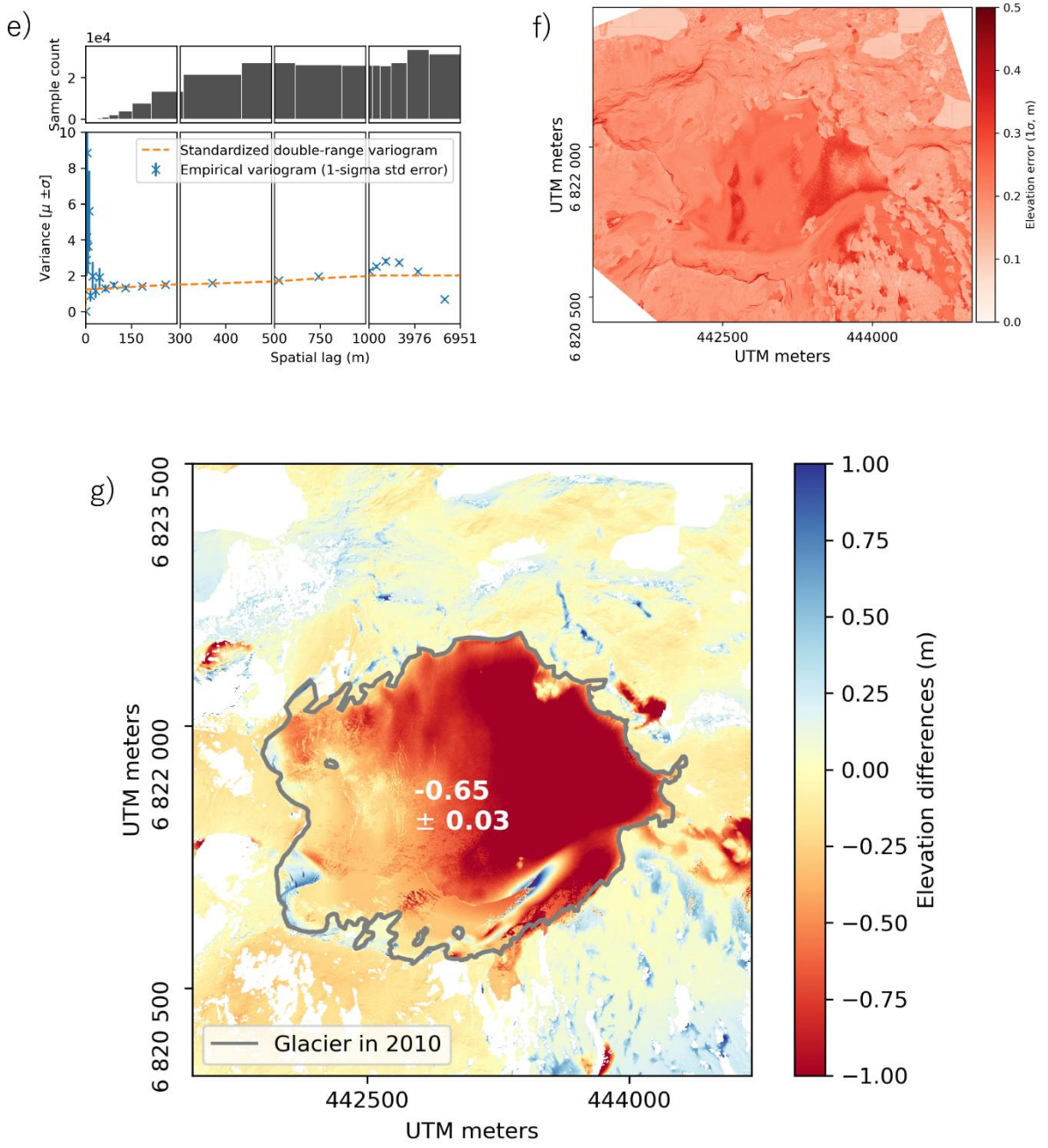
e)
1e4
Sample count
Standardized double-range variogram
Empirical variogram (1-sigma std error)
Variance [$\mu \pm \sigma$]
Spatial lag (m)
f)
UTM meters
UTM meters
Elevation error (1σ, m)
g)
-0.65
± 0.03
Glacier in 2010
UTM meters
UTM meters
Elevation differences (m)

1.5 2017 - 2020

2017-2020

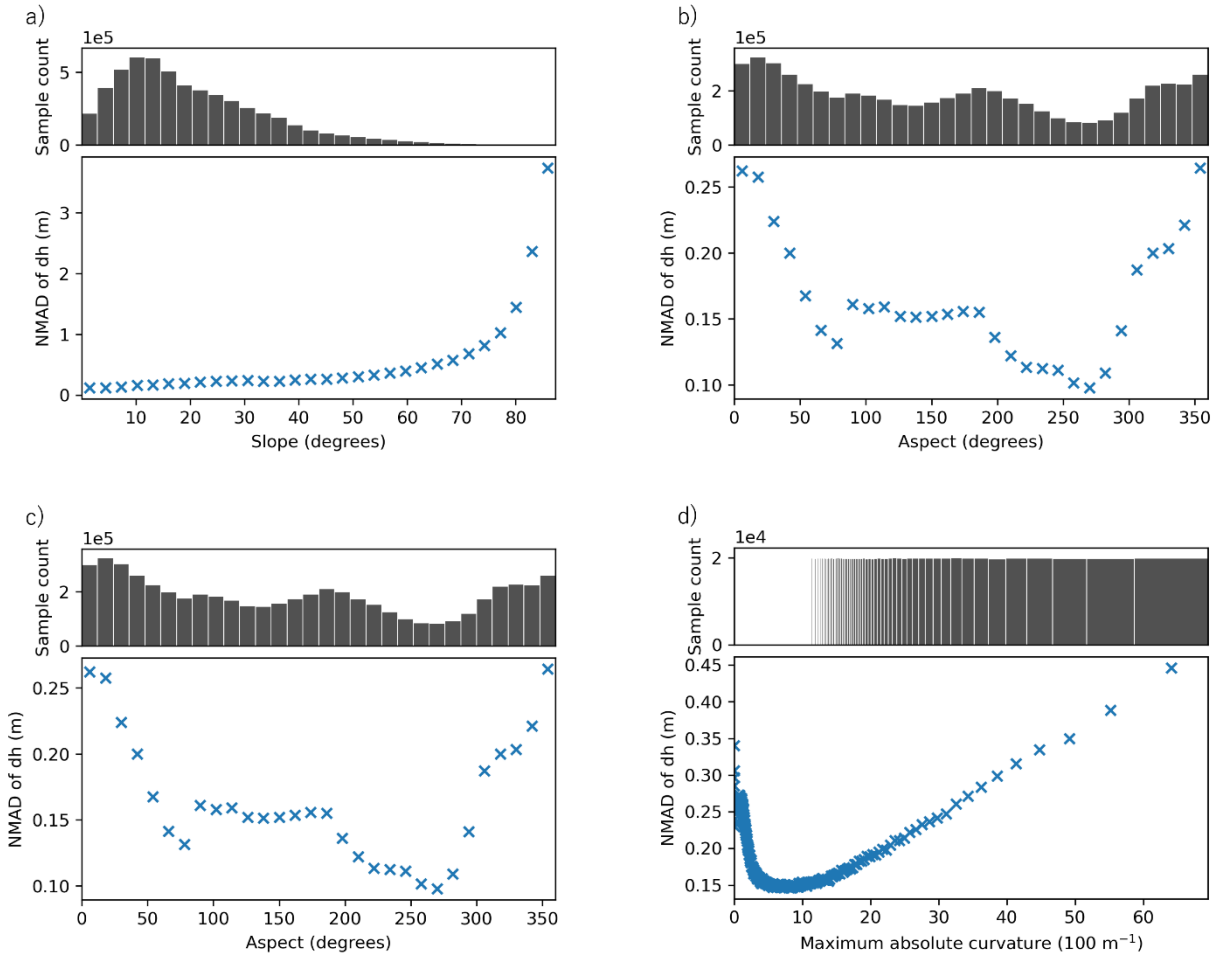

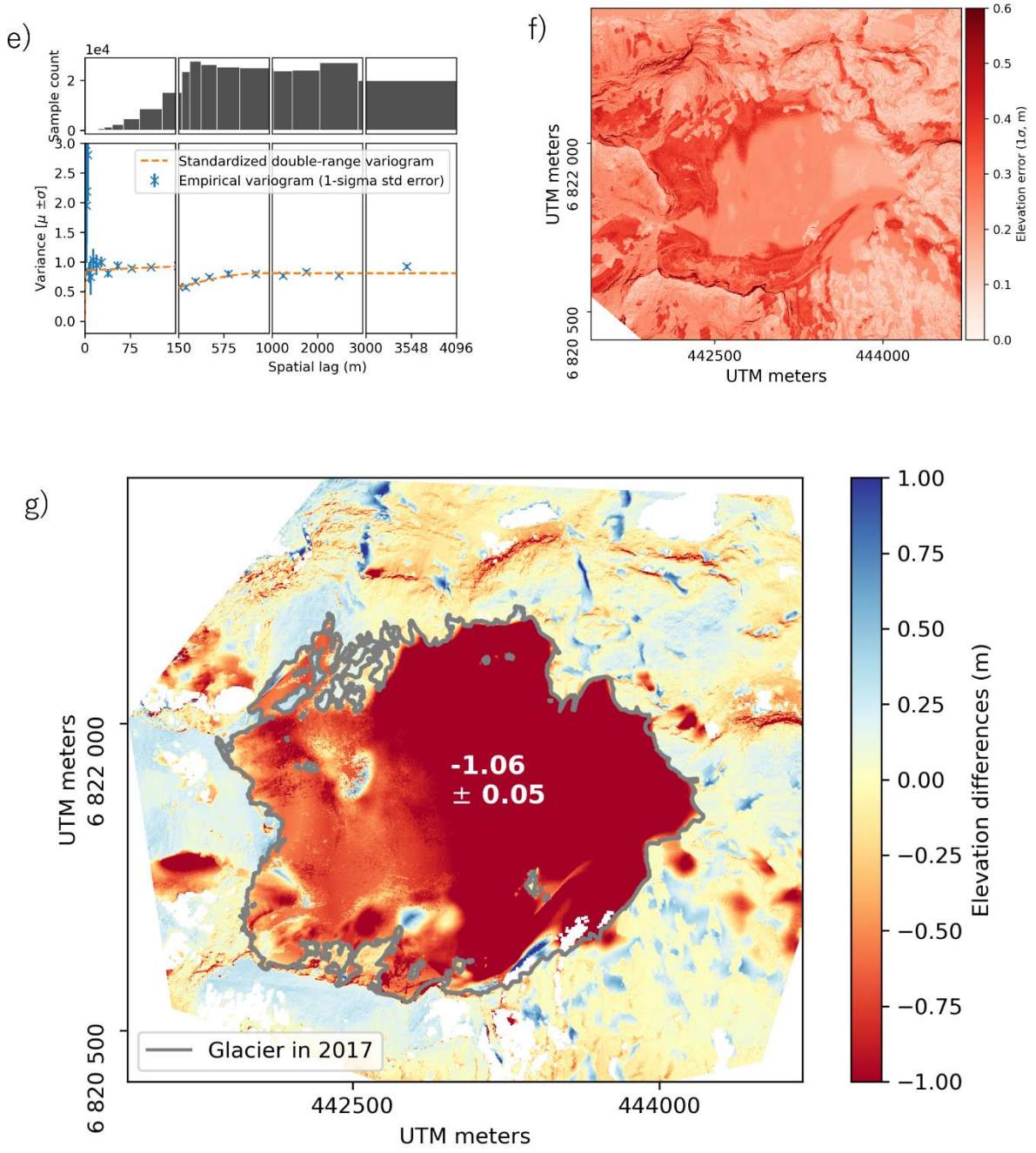
e)
1e4
Sample count
Standardized double-range variogram
Empirical variogram (1-sigma std error)
Variance [$\mu \pm \sigma$]
Spatial lag (m)
f)
UTM meters
6 822 000
6 820 500
442500
444000
Elevation error (1σ, m)
g)
-1.06
± 0.05
Glacier in 2017
Elevation differences (m)

1.6 2020 - 2022

2020-2022

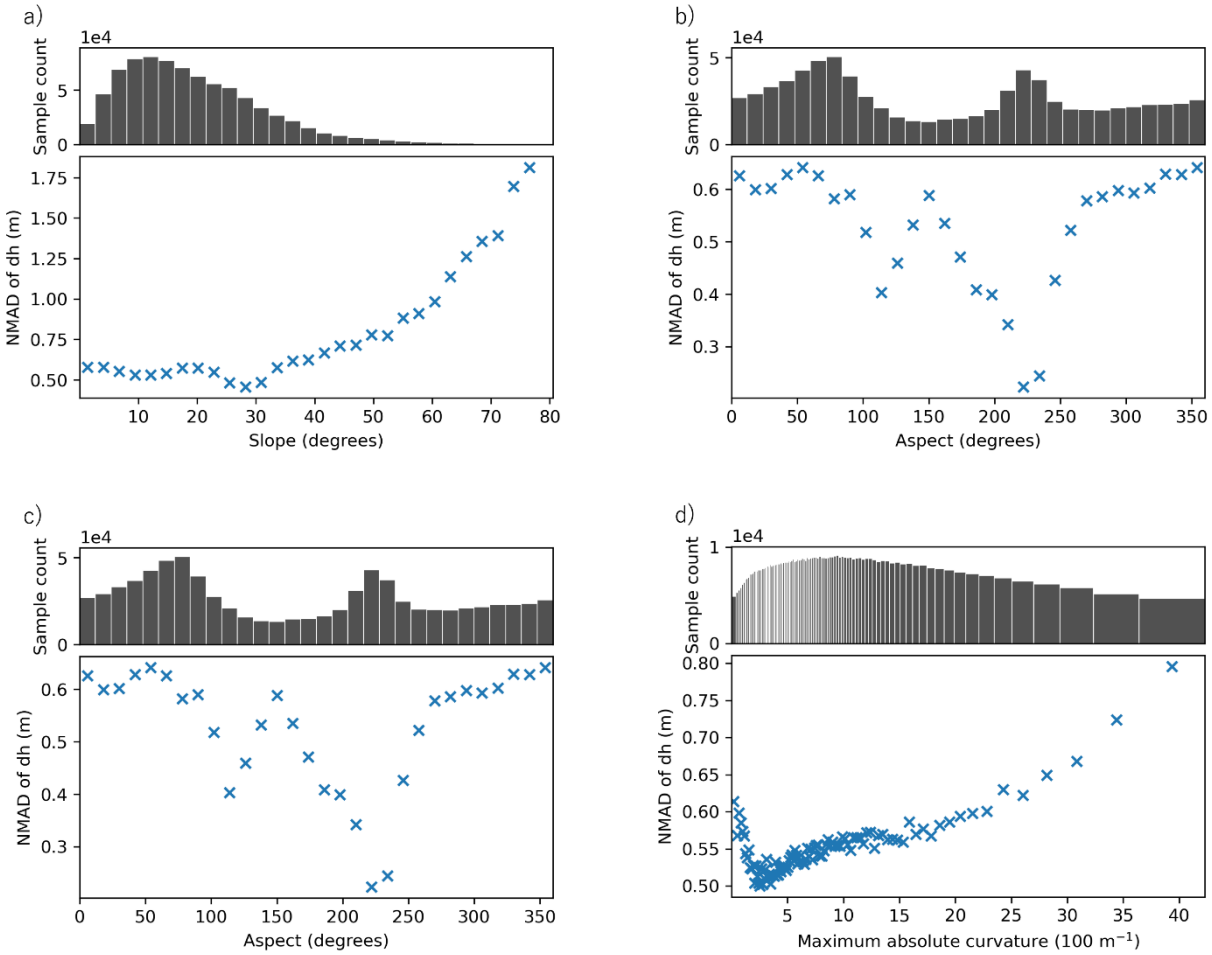

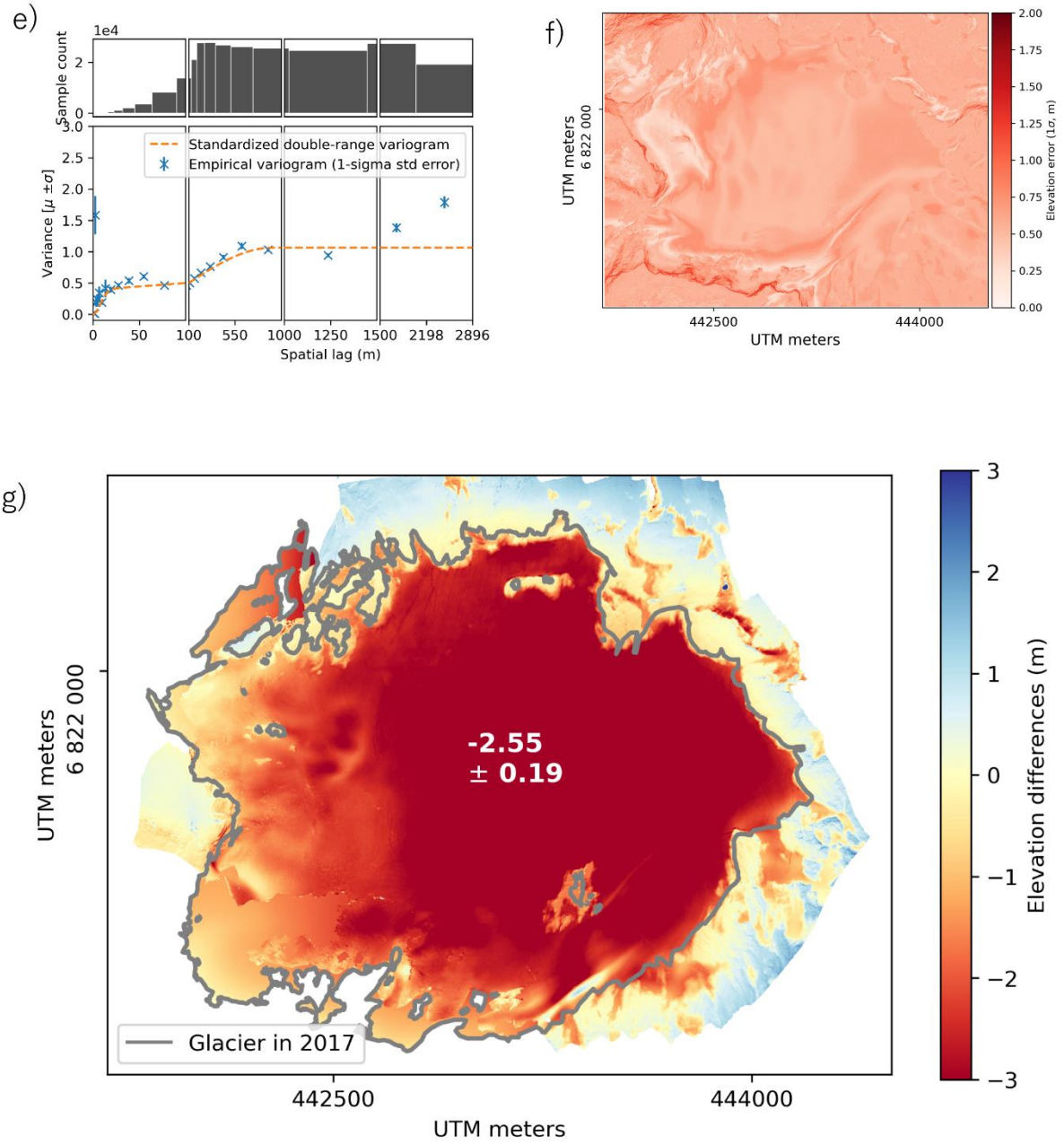
e)
1e4
Sample count
Standardized double-range variogram
Empirical variogram (1-sigma std error)
Variance [$\mu \pm \sigma$]
Spatial lag (m)
f)
UTM meters
6 822 000
442500
444000
UTM meters
Elevation error (1σ, m)
g)
-2.55
± 0.19
Glacier in 2017
UTM meters
6 822 000
442500
444000
UTM meters
Elevation differences (m)

1.7 2022 - 2023

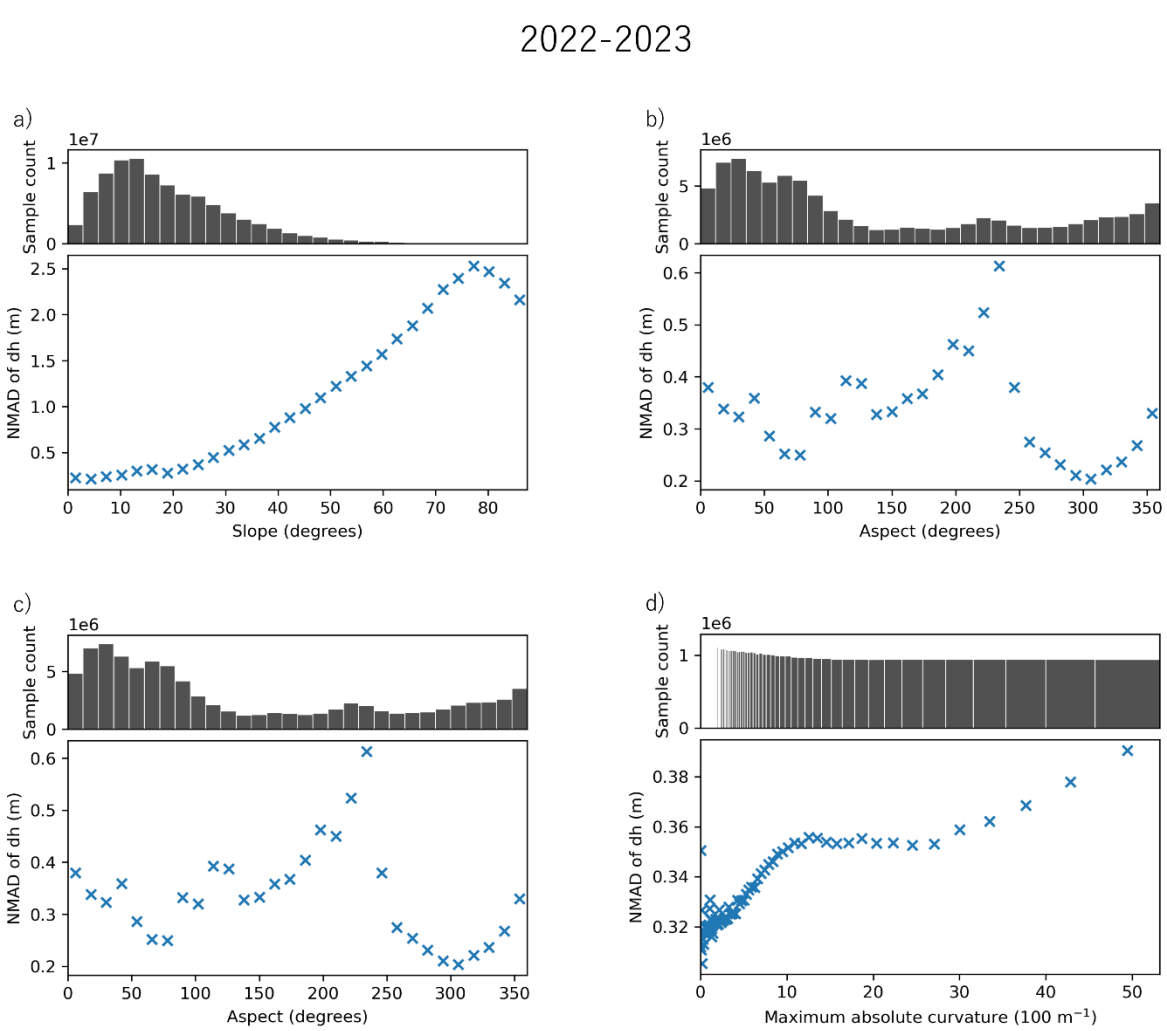
2022-2023
a)
1e7
Sample count
NMAD of dh (m)
Slope (degrees)
b)
1e6
Sample count
NMAD of dh (m)
Aspect (degrees)
c)
1e6
Sample count
NMAD of dh (m)
Aspect (degrees)
d)
1e6
Sample count
NMAD of dh (m)
Maximum absolute curvature (100 m^{-1})

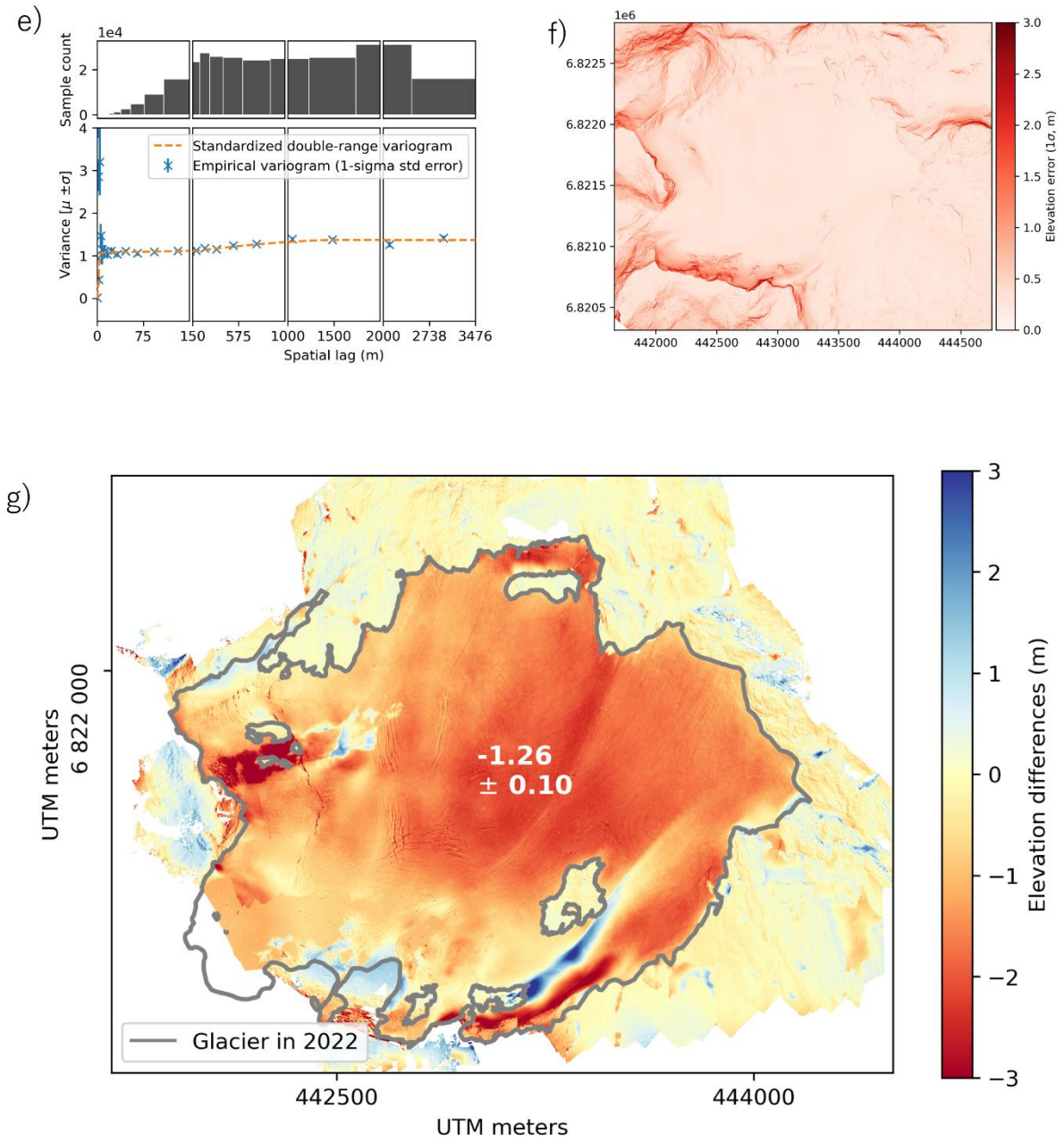
e)
1e4
Sample count
Standardized double-range variogram
Empirical variogram (1-sigma std error)
Variance [$\mu \pm \sigma$]
Spatial lag (m)
f)
1e6
Elevation error (1σ, m)
g)
-1.26
± 0.10
Glacier in 2022
UTM meters
6 822 000
442500
444000
UTM meters
Elevation differences (m)

1.8 Accumulation (September 2022 – June 2023)

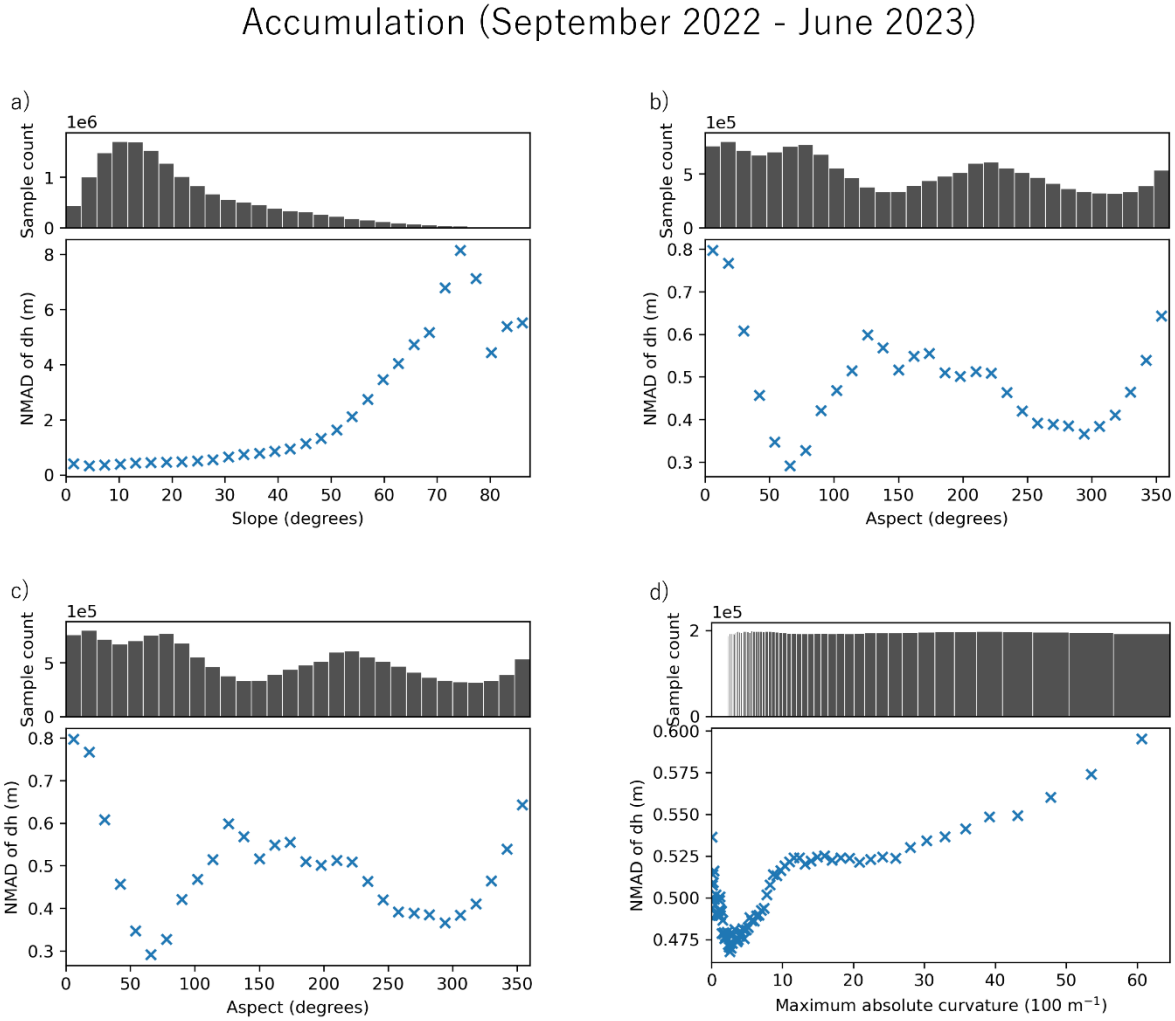

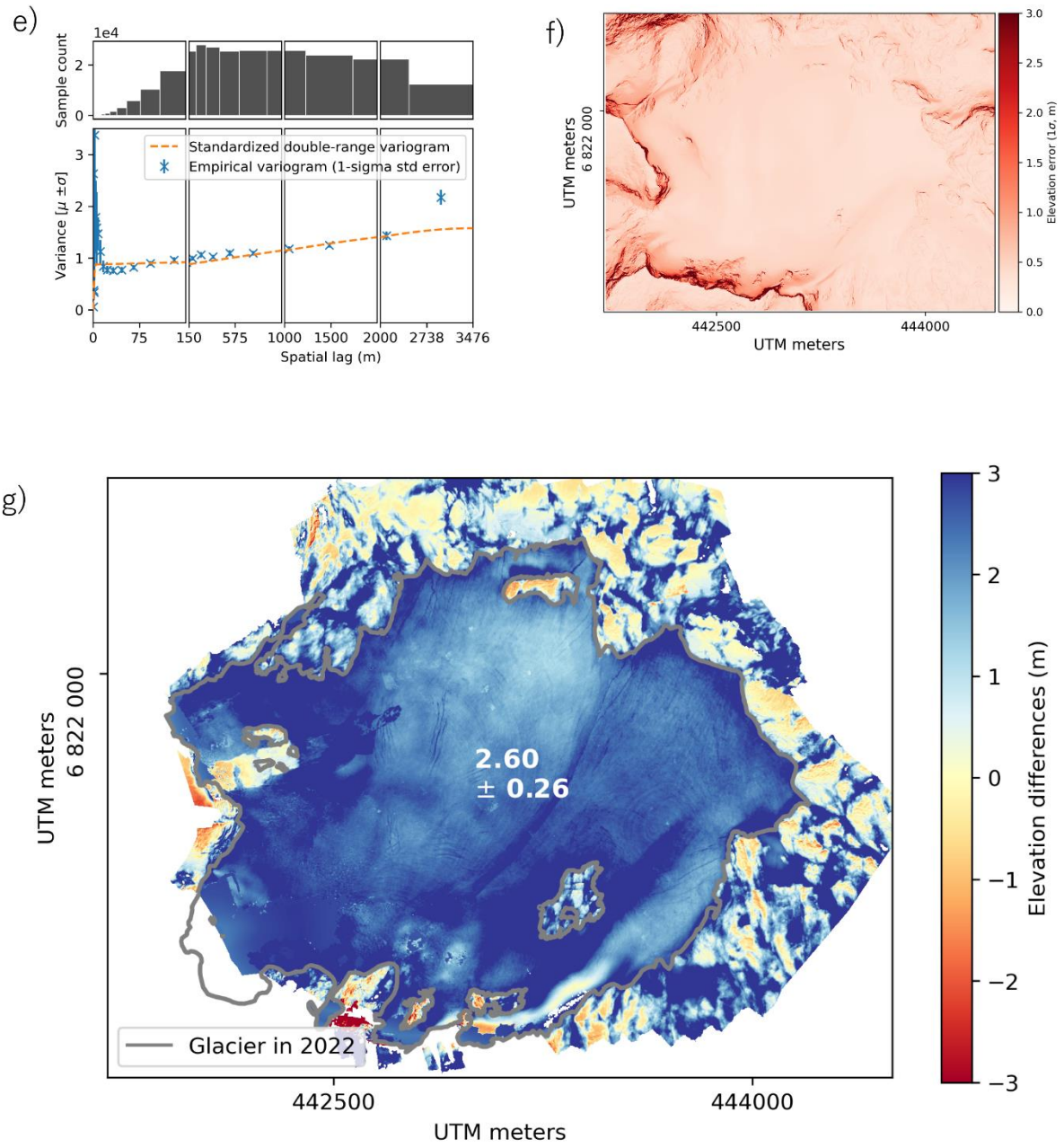
e)
1e4
Sample count
Standardized double-range variogram
Empirical variogram (1-sigma std error)
Variance [μ ±σ]
Spatial lag (m)
f)
UTM meters
6 822 000
442500
444000
UTM meters
Elevation error (1σ, m)
g)
UTM meters
6 822 000
2.60
± 0.26
Glacier in 2022
442500
444000
UTM meters
Elevation differences (m)

1.9 Ablation (June 2023 – September 2023)

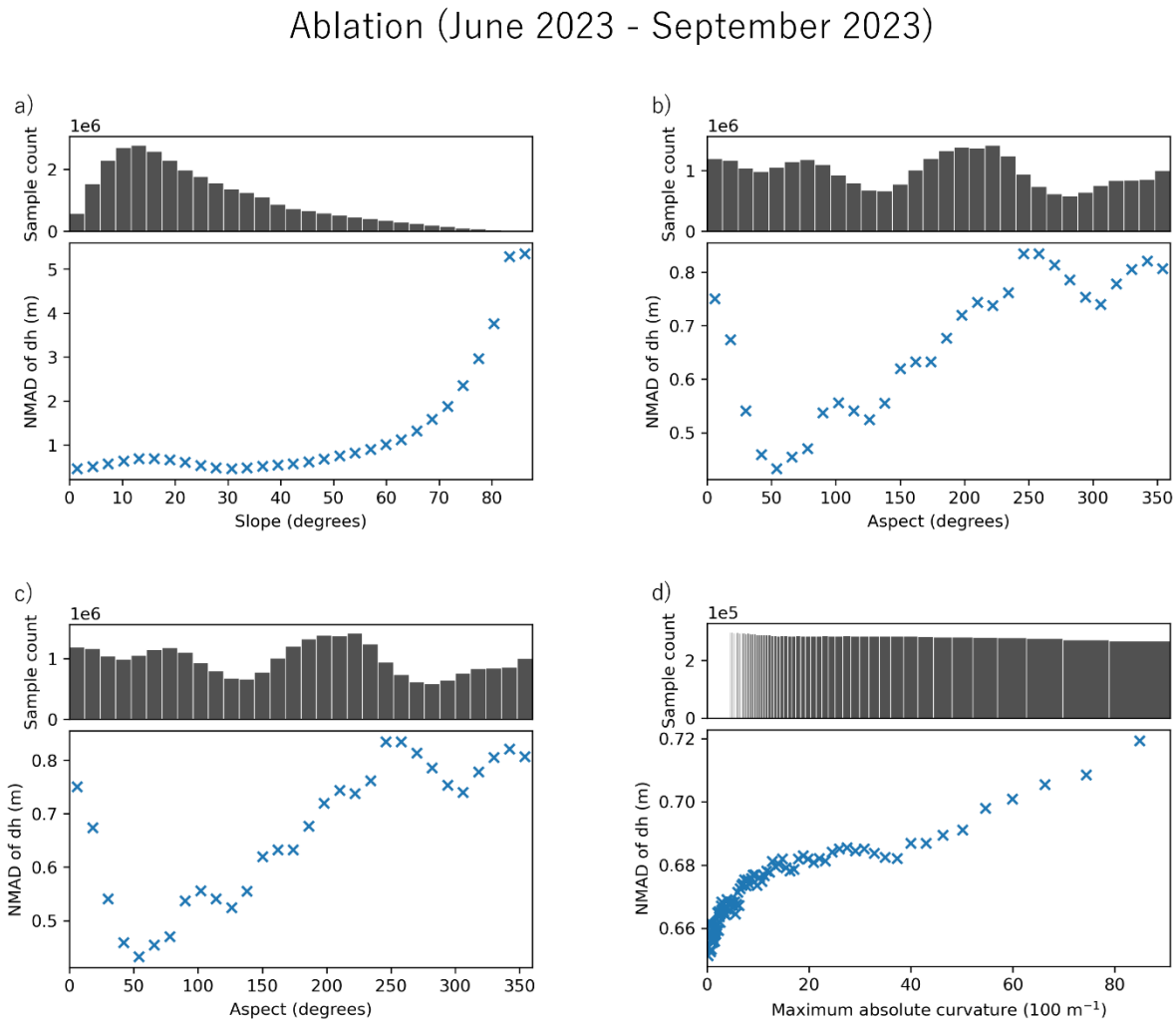

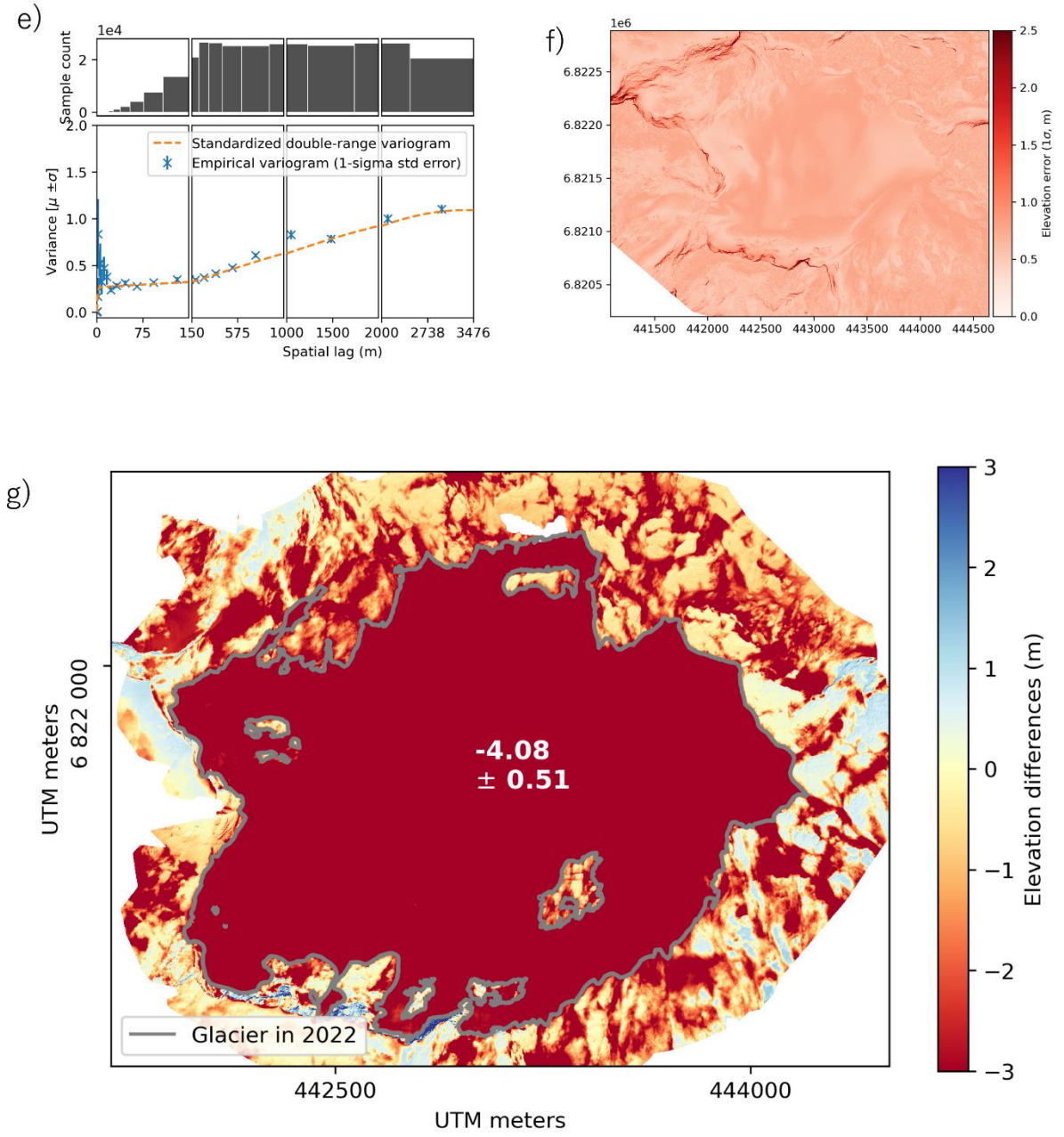
e)
1e4
Sample count
Standardized double-range variogram
Empirical variogram (1-sigma std error)
Variance [$\mu \pm \sigma$]
Spatial lag (m)
f)
1e6
Elevation error (1σ, m)
g)
-4.08
± 0.51
Glacier in 2022
UTM meters
6 822 000
442500
444000
UTM meters
Elevation differences (m)

2. Surface elevation changes and glacier hypsometry

In this section, the figures depicting annual changes for different glacier altitudes as well as glacier hypsometry (shaded bins) are presented. Plots for seasonal changes are at the end of the section.

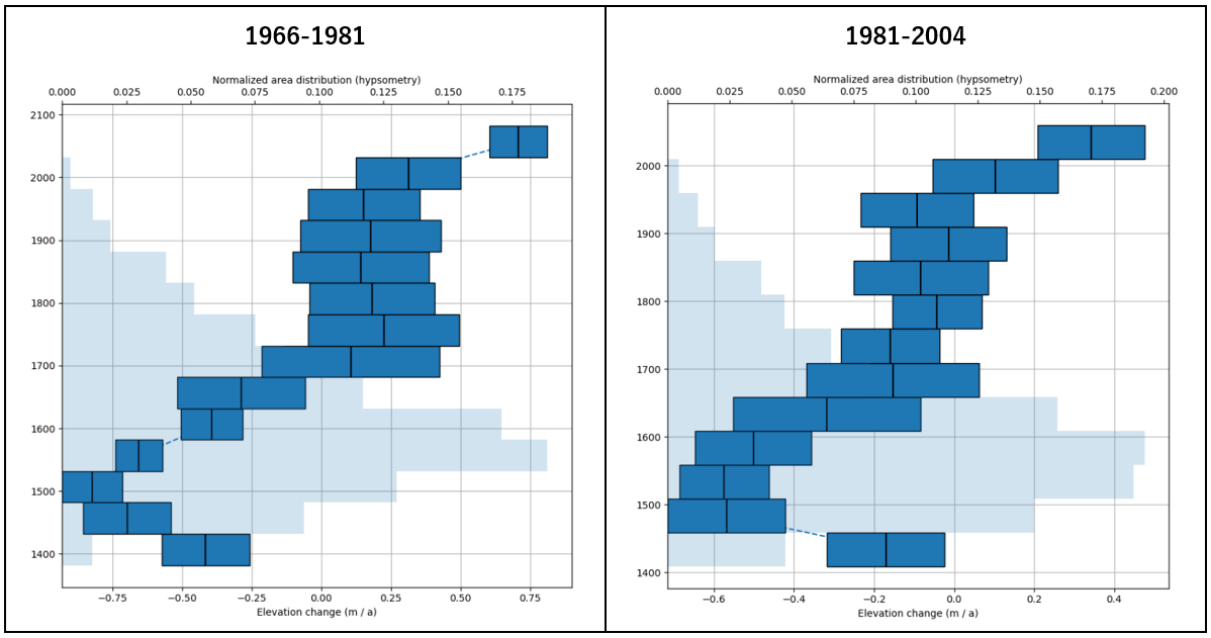

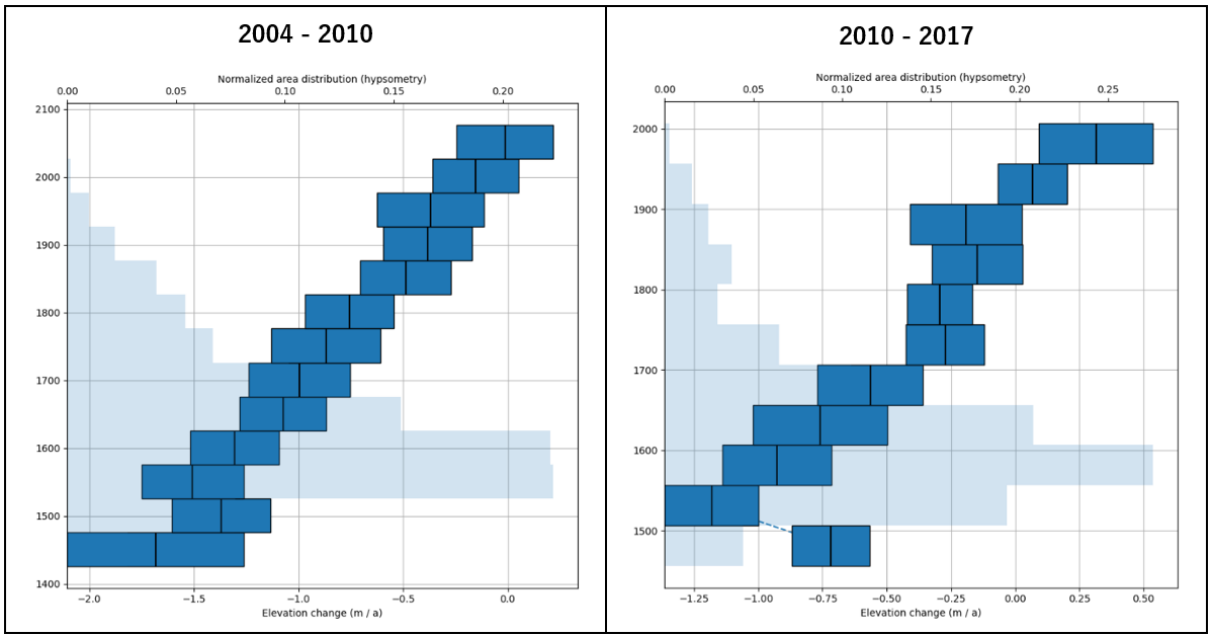

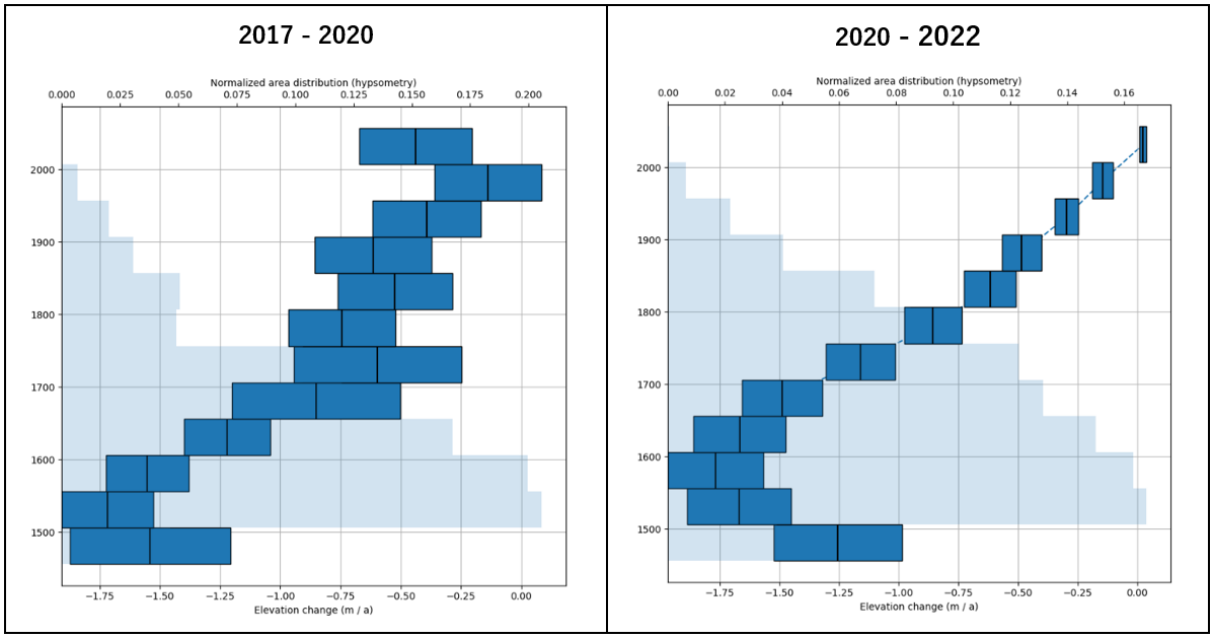
2017 - 2020
Normalized area distribution (hypsometry)
0.000 0.025 0.050 0.075 0.100 0.125 0.150 0.175 0.200
2000
1900
1800
1700
1600
1500
−1.75 −1.50 −1.25 −1.00 −0.75 −0.50 −0.25 0.00
Elevation change (m / a)
2020 - 2022
Normalized area distribution (hypsometry)
0.00 0.02 0.04 0.06 0.08 0.10 0.12 0.14 0.16
2000
1900
1800
1700
1600
1500
−1.75 −1.50 −1.25 −1.00 −0.75 −0.50 −0.25 0.00
Elevation change (m / a)

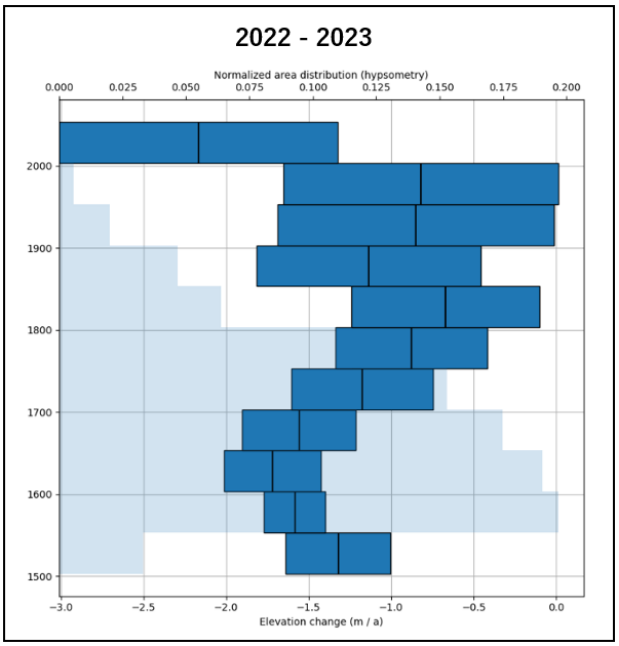
2022 - 2023
Normalized area distribution (hypsometry)
0.000 0.025 0.050 0.075 0.100 0.125 0.150 0.175 0.200
2000
1900
1800
1700
1600
1500
−3.0 −2.5 −2.0 −1.5 −1.0 −0.5 0.0
Elevation change (m / a)

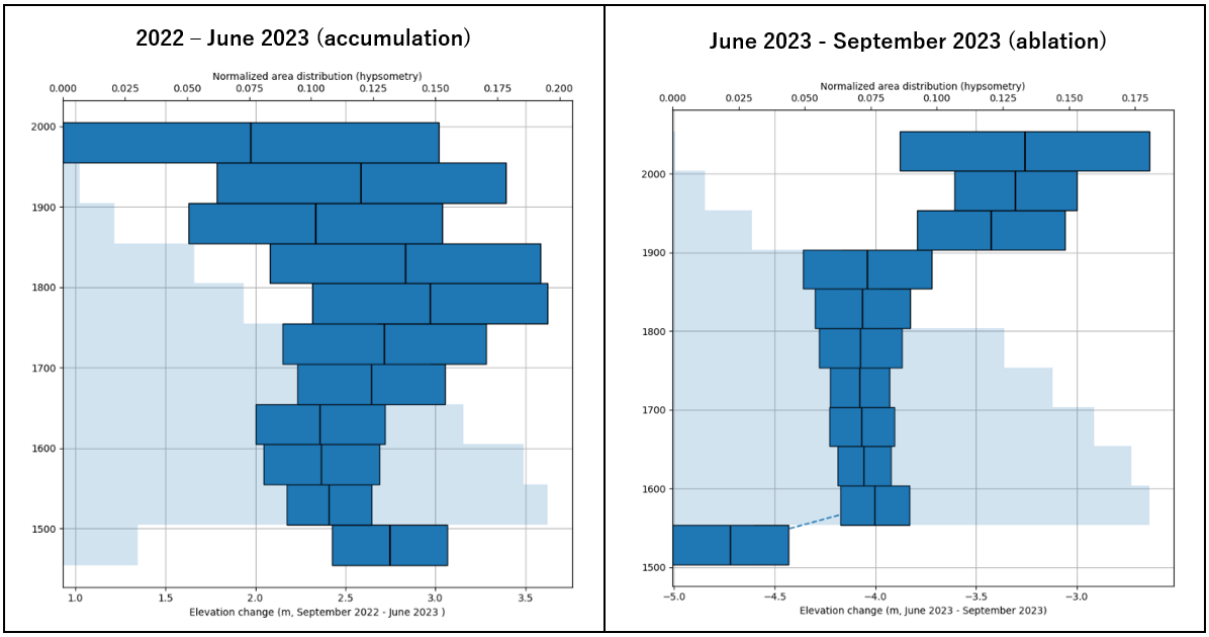
2022 – June 2023 (accumulation)
Normalized area distribution (hypsometry)
0.000
0.025
0.050
0.075
0.100
0.125
0.150
0.175
0.200
2000
1900
1800
1700
1600
1500
1.0
1.5
2.0
2.5
3.0
3.5
Elevation change (m, September 2022 - June 2023)
June 2023 - September 2023 (ablation)
Normalized area distribution (hypsometry)
0.000
0.025
0.050
0.075
0.100
0.125
0.150
0.175
2000
1900
1800
1700
1600
1500
−5.0
−4.5
−4.0
−3.5
−3.0
Elevation change (m, June 2023 - September 2023)